Nucleation, Growth and Transformation Phenomena of Vivianite

Dissertation submitted for the degree of

Doctor rerum naturalium

(Dr. rer. nat.)

To

The Department of Earth Sciences

Freie Universität Berlin

By

Alice Paskin

Berlin, 2024

Erklärung

Hiermit erkläre ich, Alice Paskin, dass diese Arbeit mit dem Titel „Nucleation, Growth and Transformation Phenomena of Vivianite“ ausschließlich auf Grundlage der angegebenen Hilfsmittel und Hilfen selbstständig von mir verfasst wurde. Diese Arbeit ist nicht in einem früheren Promotionsverfahren eingereicht worden.

Berlin, den 23. April 2024

Alice Paskin

Thesis Reviewers

Prof. Dr. Liane G. Benning (first reviewer)

Department of Earth Sciences, Freie Universität Berlin, 12249 Berlin, Germany

GFZ German Research Centre of Geosciences, 14473 Potsdam, Germany

Prof. Dr. Thomas Neumann (second reviewer)

Department of Applied Geochemistry, Technischen Universität Berlin, 10587 Berlin, Germany

PhD Disputation Commission

Prof. Dr. Liane G. Benning

Department of Earth Sciences, Freie Universität Berlin, 12249 Berlin, Germany

GFZ German Research Centre of Geosciences, 14473 Potsdam, Germany

Prof. Dr. Thomas Neumann

Department of Applied Geochemistry, Technischen Universität Berlin, 10587 Berlin, Germany

Prof. Dr. Dirk Scherler

Department of Earth Sciences, Freie Universität Berlin, 12249 Berlin, Germany

GFZ German Research Centre of Geosciences, 14473 Potsdam, Germany

Prof. Dr. Friedhelm von Blanckenburg

Department of Earth Sciences, Freie Universität Berlin, 12249 Berlin, Germany

Dr. Jeffrey Paulo H. Perez

GFZ German Research Centre of Geosciences, 14473 Potsdam, Germany

Date of defense: 10th July 2024

Zusammenfassung

Vivianit, ein hydratisiertes Fe^{2+} Phosphat ($Fe_3(PO_4)_2 \cdot 8H_2O$), ist ein weltweit vorkommendes Mineral in anoxischen limnischen oder marinen Sedimenten, Böden, in Verbindung mit organischen Stoffen und in Grundwasserströmen. Es ist eine Schlüsselphase, die den Kreislauf und die Immobilisierung von Fe^{2+} und Phosphor in diesen Systemen steuert. Die Bildung von Vivianit kann die Rückgewinnung von Phosphor aus Abwässern unterstützen; daher ist es ein wichtiges Mineral für Anwendungen in der Kreislaufwirtschaft. Diese Dissertation bietet neue Einblicke in die komplexen Prozesse, die die Keimbildung, das Wachstum und die Phasenumwandlungen von Vivianit steuern. Die Keimbildung von Vivianit erfolgt über eine vorübergehende Zwischenphase – amorphes Eisenphosphat (AFEP), über einen nichtklassischen Weg. AFEP ist eine metastabile Vorläuferphase, die eine deutlich andere lokale Struktur und Zusammensetzung ($Fe_3(PO_4)_2 \cdot 4.7H_2O$) im Vergleich zu Vivianit aufweist. Durch Laborversuche und Ex-situ-Techniken habe ich gezeigt, dass AFEP aus übersättigten Lösungen ausfällt, anschließend hydratisiert wird und strukturelle Transformationen durchläuft, um in thermodynamisch stabiles Vivianit umgewandelt zu werden. Die entscheidende Rolle von Wasser in dieser Transformation wird ebenfalls hervorgehoben. Die Stabilität von AFEP ist umgekehrt proportional zur systemischen (Vivianit-) Übersättigung und Temperatur, was darauf hindeutet, dass das Auftreten von AFEP in nahezu ausgewogenen (Umwelt-) Systemen weit verbreitet ist. Experimente zur Röntgenklein- und -weitwinkelstreuung an Synchrotronquellen bieten neue Einblicke in die zeitliche Entwicklung der Vivianitkristallisation über AFEP-Nanopartikel, wobei Beobachtungen auf gleichzeitige Prozesse der AFEP-Transformation und des Vivianitwachstums in Lösung hinweisen – was einen direkten Zusammenhang zwischen diesen beiden Prozessen offenbart. Darüber hinaus zeigen Untersuchungen der Vivianit-Bildungskinetik temperaturabhängige Dynamik und eine direkte Korrelation zwischen Temperatur und Transformationsrate. Die Wachstumsrate von Vivianit konnte mit dem JMAK-Modell modelliert werden, um die scheinbare Aktivierungsenergie (~ 51 kJ/mol) dieser Transformation abzuleiten. Temperaturabhängige Variationen der Kristallsplitterung geben auch neue Einblicke in unterschiedliche Vivianitkristallmorphologien. Zusätzlich werden hier erstmals die thermisch induzierten Phasenumwandlungen von Vivianit (Amorphisierung und Rekristallisation in eine völlig neue Mineralphase), insbesondere unter Hochtemperaturbedingungen, einschließlich des entscheidenden Einflusses der Atmosphäre auf die resultierenden umgewandelten Phasenzusammensetzungen, berichtet. Diese Forschung bietet neue und bedeutende Einblicke in die Mechanismen der Vivianit-/Mineralkeimbildung und des -wachstums in wässrigen Lösungen, die Materialsynthese und die thermische Stabilität von Eisenphosphaten.

Abstract

Vivianite, a hydrated Fe^{2+} phosphate ($Fe_3(PO_4)_2 \cdot 8H_2O$), is a mineral found globally in anoxic lacustrine or marine sediments, soils, associated with organic matter and in groundwater streams. It is a key phase controlling the cycling and immobilization of Fe^{2+} and phosphorus in these systems. Vivianite formation can aid in phosphorus recovery from wastewater; therefore, it is an important mineral for circular economy applications. This dissertation presents novel insights into the intricate processes governing the nucleation, growth, and phase transformations of vivianite. The nucleation of vivianite occurs via a transient intermediate phase – amorphous ferrous phosphate (AFEP), via a nonclassical pathway. AFEP is a metastable precursor phase which has a distinctly different local structure and composition ($Fe_3(PO_4)_2 \cdot 4.7H_2O$), compared to vivianite. Through laboratory experiments and *ex situ* techniques, I demonstrated that AFEP precipitates from supersaturated solutions, undergoes subsequent hydration and structural transformations to transform into thermodynamically stable vivianite. The crucial role of water in this transformation is also highlighted. The stability of AFEP is inversely proportional to systemic (vivianite) supersaturation and temperature, suggesting AFEP occurrence to be a widely prevalent phenomenon in near-equilibrium (environmental) systems. Synchrotron-based small and wide-angle X-ray scattering experiments provide novel insights into the temporal evolution of vivianite crystallization via AFEP nanoparticles, with observations indicating concomitant processes of AFEP transformation and vivianite growth in solution – revealing a direct link between these two processes. Furthermore, the investigation of vivianite growth kinetics shows temperature-dependent dynamics, and a direct correlation between temperature and transformation rate. The rate of vivianite growth could be modeled via the JMAK model to derive the apparent activation energy (~ 51 kJ/mol) of this transformation. Temperature-dependent variations in crystal splitting also reveal new insights into varying vivianite crystal morphologies. Additionally, the thermally induced phase transformations of vivianite (amorphization and recrystallization into a distinctly new mineral phase), particularly under high-temperature conditions, including the critical influence of atmosphere on the resultant transformed phase compositions, is also reported here for the first time. This research provides new and significant insights for vivianite/mineral nucleation and growth mechanisms in aqueous solutions, materials synthesis and thermal stability of iron phosphates.

Acknowledgments

I express my sincere gratitude to Prof. Liane G. Benning for accepting and supervising me as her doctoral student, for the encouragement of new ideas, inspirational guidance and confidence in the success of this work. I thank Prof. Thomas Neumann for reviewing this thesis. I acknowledge the Helmholtz Association for providing the project funding and the German Research Centre of Geosciences (GFZ) for institutional facilities.

I would like to particularly thank my mentors and collaborators at GFZ, which contributed to the development and conceptualization of this work – Jeffrey Paulo H. Perez for guidance with structural modeling by means of X-ray absorption spectroscopy, inductively-coupled plasma - optical emission spectroscopy and mineral synthesis; Thaïs Couasnon for valuable insights related to experimental design, performing transmission electron microscopy and collaborative synchrotron work; Roberts Blukis for guidance with *in situ* X-ray diffraction measurements, pair-distribution function analyses and Rietveld refinements; Sergey Lobanov for optical spectroscopy and modeling; I also am greatly indebted to each of them for thoughtful discussions, constructive criticism and help in manuscript preparations.

I am grateful to Stefan Reinsch for thermogravimetry-calorimetry and helpful discussions on phase transformations. Vladimir Roddatis, Marcin Syczewski, Chiara Bahl and Gerardo A. Siller are acknowledged for help with electron microscopy and for insightful discussions. Brian Pauw is thanked for advice on modeling small angle X-ray scattering data. The team at Diamond Light Source UK – Thomas Zinn, Andy Smith, Tim Snow and Nick Terrill, are thanked for their hospitality and guidance during our beamtime. Rebecca Volkmann and Karim Altona are thanked for experimental assistance at I22 beamline. I appreciate Sandy Herrmann, Marc Paje and Caitlin Berryman for constantly helping me with bureaucratic and laboratory-related issues. I want to thank Ruth Delina for being a supportive friend, and the entire Section 3.5 team, for the positive and collaborative working atmosphere.

Finally, I would like to thank my family – my dear sister Martha and my parents, for their care and concern for me despite the distance. I am very grateful to Philipp for his steadfast support and bright optimism.

Thesis Structure and Outline

The presented thesis is a cumulative work of scientific papers, either published in peer reviewed journals (Chapter 3) or in the final stages of preparation for submission (Chapters 4 and 5). In this section the specific contributions from the co-authors to the final chapters have been outlined as follows.

Chapter 1. 'Introduction' This chapter introduces the open questions and challenges of understanding vivianite formation, fundamental nucleation pathways of mineral phases, the scope of this work and research objectives as well as the proposed hypotheses.

Chapter 2. 'Literature Review' provides an up-to-date literature review of vivianite formation, occurrences and identification. It also has sections on ferruginous ocean chemistry on early Earth and the fundamental theories of nucleation and growth of minerals.

Chapter 3. 'Nucleation and Crystallization of Vivianite via an Amorphous Intermediate' is adapted from the article published in *Journal of the American Chemical Society,* 2023 Vol. 145 Issue 28 Pages 15137-15151. (DOI. 10.1021/jacs.3c01494)

A. Paskin, T. Couasnon, J. P. H. Perez, S. S. Lobanov, R. Blukis, S. Reinsch, L. G. Benning

This chapter reports a novel nonclassical phase transformation of amorphous ferrous phosphate (AFEP) to vivianite, via a hydration induced pathway through structural changes in the transient AFEP phase.

Author contributions: The first author AP performed the syntheses (vivianite and AFEP), prepared samples for microscopic and spectroscopic measurements, performed data analysis (UV-vis, SEM, IR, optical spectroscopy, pre-edge XANES analyses), thermochemical modeling on PHREEQC, conceptualized, and wrote the initial manuscript under the supervision of LGB, TC and JPHP. TC was responsible for TEM measurements and performed XAS measurements at DESY, Hamburg. JPHP helped in acquiring and analyzing ICP-OES data at the HELGES facility at GFZ Potsdam. JPHP also performed structural modeling of the amorphous intermediate by EXAFS *shell-by-shell* fitting from XAS data. SSL performed optical spectroscopy, SR performed TGA-DSC measurements and RB performed PDF measurements, respectively. All co-authors helped in manuscript preparations and provided constructive feedback with data analysis.

Chapter 4. 'Kinetics of Vivianite Nucleation and Growth' is adapted from the article aimed for future submission to a peer-reviewed journal.

A. Paskin, T. Couasnon, L. G. Benning

This chapter reports a small- and wide-angle X-ray scattering experimental study of the *in situ* nucleation and growth pathway of vivianite at a range of environmentally relevant temperatures (10 – 60 ˚C) performed at Diamond light source UK, the variations in morphology and crystal splitting are shown by means of *ex situ* SEM measurements. The concomitant processes of AFEP transformation and vivianite growth are shown to be inherently linked.

Author contributions: AP, TC and LGB conceptualized this project and AP wrote the proposal to perform synchrotron measurements at Diamond Light Source with the help of TC and LGB. AP designed the *in situ* experimental setup, planned and executed the *in situ* SAXS-WAXS experiments at Diamond Light Source with support from TC and LGB. The I22 beamline scientists (Thomas Zinn, Andy Smith, Tim Snow & Nick Terrill) helped in using the I22 beamline. Rebecca Volkmann and Karim Altona provided experimental assistance at I22. AP wrote the initial manuscript and performed the (*in situ* SAXS-WAXS) data analysis on Python and Origin, theoretical modeling the temperature resolved kinetics and constructed all the figures. LGB provided helpful insights with data processing, writing and figure construction. Brian Pauw helped with McSAS software for modeling SAXS data. Chiara Bahl helped in performing SEM measurements. All co-authors helped in manuscript preparations.

Chapter 5. 'High-Temperature Induced Amorphization and Phase Transformation of Vivianite' is adapted from the article aimed for future submission to a peer reviewed journal.

A. Paskin, T. Couasnon, R. Blukis, J. P. H. Perez, S. Reinsch, V. Roddatis, M. Syczewski, L. G. Benning

This chapter shows a high temperature induced transformation pathway of vivianite, and a novel phase transformation to crystalline graftonite ($Fe_3(PO_4)_2$) (T > 500˚C) and anoxic atmosphere is shown by means of *in situ* measurements such as *in situ* IR, SEM and TGA-DSC. This transformation is pseudomorphic and follows separate pathways depending on the anaerobicity of the system. In the presence of oxygen, complete Fe^{2+} oxidation takes place and a new phase called rodolicoite forms instead of graftonite. The fundamental transformation pathways, role of water and structural changes during this transformation are highlighted.

Author contributions: The first author, AP conceptualized this project, with help from SR, TC and LGB. AP performed all the material synthesis experiments, XRD, IR spectroscopy, phase identification on QUALX, data analysis, interpretation and writing of this manuscript based on the help and supervision from LGB. TC performed TEM measurements and SAED data analysis. RB and AP performed *in situ* XRD measurements of vivianite in a STOE high-temperature furnace accessory, RB helped with Rietveld refinements and constructed *in situ* XRD figure 5.2. JPHP helped in XAS sample preparation, performed *shell-by-shell* fitting of Fe-K edge EXAFS data and constructed EXAFS Figure A3S7, table A3T3 shown in appendix III. SR performed TGA-DSC measurements and project conceptualization. VR performed TEM-EELS measurements and helped in data interpretation. MS performed in SEM-EDX of the samples and also *in situ* SEM in collaboration with VR. Case van Genuchten accommodated 2 samples during their allocated beamtime (proposal number: I-20230052) at DESY Hamburg. XAS measurements were carried out at PETRA III, and Kaifeng Wang assisted AP in using the P65 beamline for XAS measurements. All co-authors helped in manuscript preparations.

Chapter 6. 'Conclusions and Outlook' highlights the final conclusions and outlook of this work from a geoscientific, environmental, and fundamental (nucleation and growth) perspective. The open questions arising from this work and future research directions are proposed.

In addition to scientific papers included in as the main chapters of this dissertation, the candidate also wrote and contributed to the appendix chapters IV and V, which were adapted from the publication in Geochemical Perspective Letters 2023, 28, 20–26 (DOI: 10.7185/geochemlet.2339).

A. Vuillemin, M. Morlock, A. Paskin, L. G. Benning, C. Henny, J. Kallmeyer, J. M. Russell, and H. Vogel

AP performed SEM-EDX of the sedimentary mineral (vivianite, siderite and millerites) samples for morphological investigation and elemental point analyses. AP also contributed to manuscript writing and preparation.

List of Abbreviations

ACC	Amorphous calcium carbonate
AFEP	Amorphous ferrous phosphate
CN	Coordination number
CNT	Classical nucleation theory
DSC	Differential scanning calorimetry
EDS	Energy dispersive X-ray
EXAFS	Extended X-ray absorption fine structure
FFT	Fast Fourier-transform
FTIR	Fourier transform infrared
HAP	Hydroxyl-apatite
HR-TEM	High resolution transmission electron microscopy
ICP-OES	Inductively coupled plasma optical emission spectroscopy
JMAK	Johnson−Mehl−Avrami−Kolmogorov
K_{sp}	Solubility product
Ma	Mega annum (1 million years ago)
PDF	Pair distribution function
PFA	Perfluoroalkoxy alkane
QC	Quality control
RSD	Relative standard deviation
SEM	Scanning electron microscopy
SAED	Selected area electron diffraction
SAXS	Small-angle X-ray scattering
SD	Standard deviation
SI	Saturation index
TEM	Transmission electron microscopy
TGA	Thermogravimetric analysis
UV-vis	Ultraviolet-visible

WAXS	Wide-angle X-ray scattering
XAS	X-ray absorption spectroscopy
XANES	X-ray absorption near-edge structure
XRD	X-ray diffraction

List of Figures

36. **Figure A1F2**. STEM-EDS analysis of precursor indicating an iron phosphate phase (SI 10.19), the Cu signal comes from the copper grid background. SI 10.19 – 30 s.
37. **Figure A1F3**. (A) TEM micrograph of solids obtained from batch reaction at 100 s with squared areas representing the locations of HRTEM analysis for B and C; (B) HR-TEM of area B showing amorphous intermediate (*inset* FFT pattern); (C) HR-TEM of area C with corresponding crystalline FFT pattern for vivianite indexed in (D). SI 10.19.
38. **Figure A1F4.** *Ex situ* TEM micrographs of solids from a vivianite precipitation experiment at a SI of 7.16: 20 min showing spherical aggregated nanoparticles (~ 50 nm in diameter) and corresponding SAED pattern showing diffuse rings characteristic of an amorphous material.
39. **Figure A1F5**. STEM-EDS analysis showing aggregated spherical nanoparticles of iron phosphate (SI 7.16) at 20 min.
40. **Figure A1F6.** XRD pattern of solids from a vivianite precipitation experiment at SI 7.16 48 h after filter quenching (*above*). TEM micrographs of the solids from the reaction mixture at 48 h showing vivianite crystals with aggregated amorphous precursor on its surface (*below*).
41. **Figure A1F7.** In situ time resolved pH metric measurements of vivianite precipitation at different supersaturations at pH 7.2.
42. **Figure A1F8.** XRD pattern of solids from a vivianite precipitation experiment at SI 12.86 immediately after filter quenching, time taken for filtration ~ 20 s.
43. **Figure A1F9**. (A) Normalized Fe K-edge XANES; (B) k^3-weighted $\chi(k)$ EXAFS spectra; (C) Radial distribution function via FT-EXAFS spectra; (D) First derivative of $\chi(k)$; for AFEP and vivianite respectively.
44. **Figure A1F10.** Pre-edge extraction from Fe-K edge XANES spectrum of AFEP via subtraction of a modeled arctangent function
45. **Figure A1F11.** Thermogravimetric (TGA) measurement and the first derivative of the TGA plot (dTG) of two AFEP samples under Ar gas flow. Sample 1 was dried under vacuum for 6 h and sample 2 was dried for 24 h, prior to analysis.
46. **Figure A1F12.** Thermogravimetric (TGA) measurement of AFEP (repeat) and vivianite samples under Ar gas flow.
47. **Figure A1F13.** SEM micrograph of synthetic vivianite collected from an experiment at SI 12.86 (20 ± 10 s) showing micrometer ranged platy rosette
48. **Figure A1F14. (A)** TEM micrograph of aggregated AFEP nanoparticles and crystalline vivianite; **(B)** TEM micrograph showing the observed beam damage
49. **Figure A1F15**. FTIR spectra of dried solid obtained after suspending AFEP (10 mg) in 50 ml anoxic deionized water in crimped vials inside the anaerobic chamber after 24 h and 5 d.
50. **Figure A2S1.** Experimental scheme of the *in situ* SAXS WAXS experiments performed at beamline I22 at the Diamond Light Source. UK.
51. **Figure A2S2.** *In situ* SAXS patterns from a vivianite precipitation experiment at 21˚C.
52. **Figure A2S3.** Details of linear JMAK fits obtained from the WAXS data at different temperatures
53. **Figure A2S4.** Time resolved SEM micrographs showing vivianite crystals sampled from experiments: 10˚C at 3 min – small platelets (left) and at 21˚C at 10 min

List of Tables

Table of Contents

Chapter 1. Introduction

Vivianite is a hydrated Fe^{2+} phosphate mineral with the chemical formula $Fe_3(PO_4)_2.8H_2O$. It is the thermodynamically stable Fe^{2+} orthophosphate and is widely found in anoxic soils, associated with organic remains and sediments [1-6]. Studies in various aquatic systems (*e.g.* lake sediments [3, 6] and anoxic soils [7]) have documented that vivianite is linked to, and at times even controls, the closely linked Fe^{2+} and phosphorus cycling and immobilization in aquatic systems and soils [4, 8-10], where it forms under reducing, anoxic and slightly acidic-to-neutral pH conditions [2]. Overall high Fe^{2+}, P and low sulfur (S) activities are required for its stabilization [1]. However, despite increasing evidence of vivianite being present in many modern and ancient settings, its origin and occurrence in these environments are still not fully understood and there exists a significant knowledge gap in its formation pathways.

1.1. The challenges of understanding vivianite formation

When using thermodynamic saturation index (SI) calculations to predict mineral occurrences in various systems, the results reveal many inconsistencies between theoretical calculations and experimental observations [3, 7, 9, 11, 12]. In case of vivianite, laboratory studies [11] showed that vivianite crystallization only occurred at much higher supersaturations (SI > 4) and even after precipitation, the system remained oversaturated with respect to it. Crystalline vivianite has been documented as being metastable within a wide SI range of 0 – 11, making the thermodynamic predictions of its stability unreliable [12].

Sedimentary cores from Potomac river (Columbia, USA), when analyzed for their pore water chemistry [9], have indicated that despite being highly oversaturated with respect to vivianite, it was not found in several regions of the core. This suggests that either phases other than vivianite were contributing to the Fe^{2+} and phosphate speciation in these locations, or the analytical techniques employed failed to characterize it [9]. Such discrepancies were also confirmed by Rothe *et al* [3] whose natural pore water data of lake Groß-Glienicke (Berlin, Germany), suggested that SI calculations were unreliable indicators of vivianite presence. In addition, Walpersdorf *et al* [7] reported that vivianite incubation experiments from anoxic meadow soils in Nørreå river valley (Jutland, Denmark), contained high concentrations of dissolved Fe^{2+} and PO_4^{3-} ions , yet they did not reach vivianite solubility (SI ~ 0) even after weeks of incubation experiments. They also reported that despite high supersaturations, vivianite did not solely contribute to the Fe-P speciation in this system, as it was

only partially present [7]. Gschwend *et al* [13] have analyzed an anoxic ground water plume oversaturated with respect to vivianite in Cape Cod aquifer (Massachusetts, USA), and reported partially present vivianite and ferrous phosphate nanoparticles (~ 100 nm), whose origin was not ascertained.

Theoretically, vivianite formation should have been observed in the above systems, due to oversaturation (SI > 0). However, this was not, or only partially, observed. Therefore, it is evident that vivianite formation cannot be solely explained and predicted based-on thermodynamic calculations. The absences of vivianite, despite apparent supersaturation, in these systems can be explained by errors in its solubility constant, kinetic constraints *i.e.* slow reaction rates, or the presence of competing Fe-P phases that may potentially contribute or even control the Fe-P speciation. Furthermore, natural systems also remain quite difficult to predict due to processes occurring at mineral interfaces and organic complexation of ions [3]. Thus, thermodynamics, alone, cannot predict or explain vivianite formation in different systems. There is a need for further fundamental studies on the formation mechanism of vivianite and the useful insights required to fully elucidate the conditions for its formation, as well as its stability.

1.2. Classical versus non-classical nucleation pathways

The nucleation of small crystals from solution is described by the classical nucleation theory (CNT) as the spontaneous formation of crystalline nuclei that grow when larger than a critical size, which is primarily determined by the ratio of surface to bulk energy [14]. In addition, it is known (for nearly a century) that nucleation and growth often do not occur through the addition of single atoms/molecules to the critical nuclei, but may proceed through the aggregation of nanometric building blocks such as pre-nucleation clusters or nanoparticles. Mechanisms that involve such precursors have been termed 'non-classical', because they could not be explained within the framework of CNT.

In many sparingly soluble mineral systems (*e.g*. Ca-CO_3, [15-18] Ca-PO_4 [19-22] and Ca-SO_4 [23-25]), in the last two decades, significant amount of evidence has emerged showing that crystallization can occur via many different pathways with variable precursor from dense liquids/ionic complexes [26] [27], to nanocrystalline precursors [23] to amorphous precursors [15-17, 20, 21, 28-30] and that the crystallization process can proceed via different pathways including dehydration (*e.g.* Ca-CO_3 [15-18], Ca-SO_4 [23-25]) or a hydration (*e.g*. Zn-PO_4 [31], Co-PO_4 [32]) of these amorphous precursors. It is evident that water plays an important role in the transformation mechanism of the amorphous to crystalline phase [32]. In case of iron-(oxyhydr)oxides (*i.e.* magnetite, goethite) non-classical amorphous particle aggregation-based

pathways [33, 34], alongside oriented attachment pathways constituting of nanocrystalline particles [35]. In this context, time-resolved measurements (*in situ* or *ex situ*) by coupling the reaction systems with, spectroscopic, microscopic or diffractometric analytical methods can enable a better understanding of the nucleation and growth processes of nanoparticles and crystals via non-classical pathways [15, 16, 28, 36, 37]. In the non-sulfidic Fe^{2+} and phosphate rich settings where vivianite forms, similar nonclassical pathways can occur but to date there exist no direct evidences and thus, this is the scope of this thesis, as outlines below.

1.3. Scope of this work

The occurrence and formation of vivianite have been extensively studied from a geological, environmental (phosphate recovery) and structural perspective. However, its formation mechanism, its nucleation and growth mechanism, or its stability have not been addressed. Despite being a widely found mineral in anoxic geologic settings and lacustrine sediments, very few kinetic studies have been performed with vivianite and none of these can explain the discrepancies stemming from its thermodynamic predictions of formation and conditions for occurrence.

With the projects in my thesis, I aimed to unravel the fundamental nucleation and growth mechanism for the formation of vivianite, and assess its stability and temperature-dependent transformation behavior. This knowledge will help in deciphering its role in bio-geochemical cycles of iron and phosphorus in modern/ancient systems globally, its geologic occurrence and relevance for phosphorus recovery from wastewater.

1.4. Research Objectives and Hypotheses

The research objectives of this PhD are to fill the knowledge gaps related to the nucleation, growth and transformation mechanisms of vivianite, under anoxic conditions, relevant to its natural occurrence. The broader perspective of this work is to understand the reasons for discrepancies regarding the literature occurrence of this mineral in ancient and modern systems globally. These results would enable a better understanding of the formation conditions of vivianite, its role in Fe and P cycling/ immobilization and stability in these systems. The research objectives and hypotheses of this thesis are the following.

1. To elucidate the fundamental nucleation and growth pathway of vivianite (classical or non-classical)

2. To evaluate the kinetics and mechanism of vivianite growth at environmentally relevant temperatures
3. To observe the phase transformation behavior of vivianite at high temperatures, to offer a better understanding of its stability in natural/engineered systems

1.5. Thesis Outline

This thesis consists of six chapters, including the present 'Introduction' chapter. The following is a brief summary of all the chapters in this work.

Chapter 2 provides an up-to-date review on the existing literature on vivianite and a sub-section on fundamental nucleation and growth pathways of minerals.

Chapter 3 reports a nonclassical nucleation and growth mechanism of vivianite via a novel amorphous ferrous phosphate phase, which undergoes structural changes and hydration in solution, to transform to vivianite.

Chapter 4 reports the kinetics and mechanism of vivianite nucleation and growth (rate constants and activation energy), showing that the rate of this transformation is directly proportional temperature.

Chapter 5 reports an atmosphere dependent mineralogical transformation. This is the high temperature induced amorphization and solid-state phase transformation of vivianite, via an anhydrous and amorphous intermediate phase.

Chapter 6 reports the conclusions from the collective results of this work and provides a future research outlook.

Chapter 2. Literature Review

2.1. Introduction to vivianite

P. B. Moore has described transition metal phosphates as the most perplexing substances in the entire mineral kingdom [38]. Among these is the crystalline form of ferrous phosphate hydrate ($Fe_3(PO_4)_2{\cdot}8H_2O$) also known as vivianite or 'blue iron earth'. Vivianite is a member of the $A_3(XO_4)_2{\cdot}8H_2O$ (A = Fe, Mn, Co, Zn, Mg; B = As, P) series of minerals. It is an extensively studied mineral due to its importance in geochemical Fe and P cycling [4, 5, 10, 39], its relevance for P-recovery from wastewater [40-42] and its unusual physical and chemical properties [43-45]. The following sub-sections will cover the existing literature on vivianite, including its structure, occurrence, identification, relevance and thermodynamic stability constants, in greater detail.

2.1.1. Crystal structure

The X-ray crystal structure of vivianite was first reported by Mori and Ito [46, 47] in 1950. Its unit cell is monoclinic and space group is *C2/m*. It consists of two different types of octahedrally coordinated Fe^{2+} atoms liked by oxygens of phosphate tetrahedra and water molecules in its structure, forming complex sheets stretched infinitely along the (010) direction. This gives it a (010) preferred cleavage plane. As shown in Figure 2.1, the first type are the $Fe^{I}(H_2O)_4(O)_2$ octahedral units and these are inter-connected to neighboring octahedra by means of corner shared PO_4 groups. The second type are the dimeric $Fe^{II}(H_2O)_2(O)_4$ octahedra and these are interlinked to identical via a common O-O edge, and to neighboring groups via corner shared PO_4 groups (Figure 2.1). The *ac* direction sheets are primarily interlinked via weak bonds through water molecules, that form complex tetrahedral arrangements within its lattice [46, 47].

Its structure has been refined several times over the years and recent refinements by Capitelli *et al* [48] show that it forms a consistent O-H···O hydrogen bond network (Figure 2.1) via tetrahedrally arranged water molecules that link the octahedral Fe^{I} and Fe^{II} units in its lattice. They showed that hydrogen bonds lead to the formation of a complex 3D structure as shown in Figure 2.1. It is clear that vivianite forms a complex hydrated structure and H-bonding plays a role in stabilizing its structure [48]. As the crystal structure of vivianite is well known and studied, its identification by X-ray diffraction is one of its most common methods of identification [3, 4, 39, 47, 49]. Vivianite also exhibits strong pleochroism (α = bluish green, β = blue, γ = green) due to differences in $Fe^{2+} \rightarrow Fe^{3+}$ charge transfer interactions along different crystal planes [50, 51].

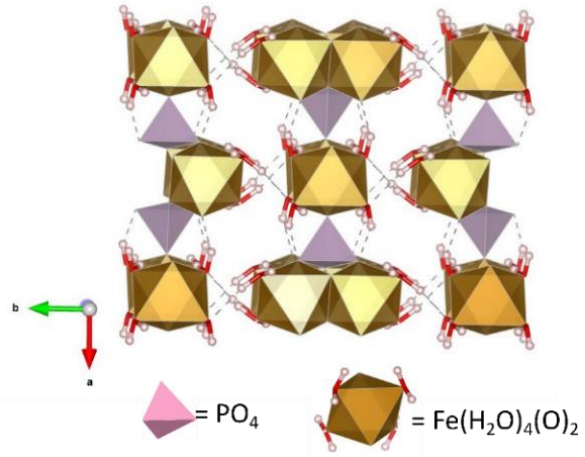

Figure 2.1. Crystal structure of vivianite showing FeO_6 octahedra (orange), PO_4 tetrahedra (pink) interlinked via water H-bonds (dashed lines), image constructed [52] from its *cif* file [48]

2.1.2. Natural occurrences

Vivianite most commonly occurs in anoxic aqueous environments that are rich in Fe^{2+} (ferruginous) and orthophosphate. The presence of sulfides can lead to the formation of pyrite (FeS_2) [1], hence non-sulfidic but ferruginous [49] conditions are essential for vivianite formation. There exist three main proposed mechanisms of vivianite formation in aquatic sediments. Firstly, vivianite might nucleate directly from pore solution, secondly its nucleation might be directed by biological templates like the cell wall of microorganisms and thirdly it might form through progressive conversion of Fe^{3+} compounds under orthophosphate and Fe^{2+} rich reductive conditions [4]. Some of the most common natural vivianite specimens are collected from freshwater lake sediments where it is the most stable diagenetic ferrous orthophosphate, as suggested by Nriagu [10]. Vivianite is commonly encountered as blue colored spherical agglomerates or millimeter sized grains/nodules in these lacustrine sediments [6, 9, 53, 54].

Marine sediments have also shown presence of authigenic vivianite below a sulfate transition zone, close to bottom anoxia [39]. Anoxic wetland soils also exhibit sponge-like blue vivianite, [7, 55, 56], particularly in the organic-rich gyttja layer of meadow soils with high Fe^{2+} concentrations [7]. Vivianite is also found in close association with organic remains of microbes [49] and larger organisms [57], wherein phosphate generally forms as a product of bacterial metabolism and bone decomposition. Vivianite forms readily in anaerobic groundwater [11], river bogs [58] and in wastewater sewage sludge [59]. Some of the most commonly co-occurring ferrous minerals with vivianite are pyrite and siderite ($FeCO_3$) [2, 58].

Vivianite also sometimes occurs as a secondary phase in altered granitic pegmatites [60-62] associated with primary Ca-, Fe- and Mn- phosphates.

2.1.2.1. Crystal habit and morphology

Vivianite commonly occurs in sediments, silt or fine clay in the form of nodules or small grains ranging up to 1 cm in diameter [10]. The nodules are composed of crystals having a roughly spherical morphology. Elongated platy, lath and needle shaped spherical crystal aggregates of vivianite, with diameter ranges of 200 – 300 µm, have also been reported [4].

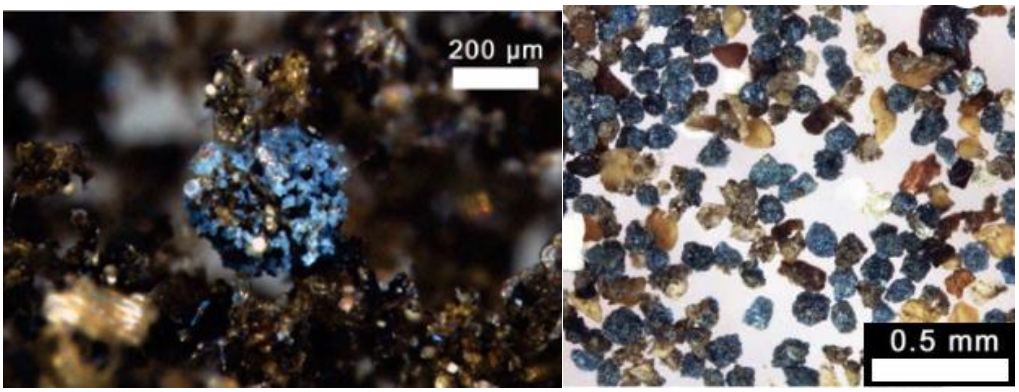

Figure 2.2. Reflected light microscope images of a vivianite nodules from Lake Stechlin sediments, Germany (modified from Rothe *et al.*, 2014 [3])

In a few cases vivianite has been known to occur with organic matter, comprising of carbohydrates and aliphatic carbon compounds, which are present due to the action of microorganisms [53]. Zelibor *et al* experimentally showed that the presence of gel-like organic debris may affect crystallization and morphology of vivianite nodules. It is suggested that the combination of the gel medium dynamics and influence of natural electric field in the upper sediments could explain the spherical aggregation of vivianite crystals [53]. The authigenic origin of vivianite can be inferred through inclusions of diatom shells and organic debris in its natural samples [3, 6] as well as the euhedral crystals on organic particle surfaces [9].

2.1.3. Identification and spectroscopic characterization of vivianite

2.1.3.1. Color changes upon Fe^{2+} oxidation caused by aerial exposure

Vivianite is colorless and translucent in its pure form. However, upon exposure to air partial oxidation of $Fe^{2+} \rightarrow Fe^{3+}$ takes place causing intervalence charge transfer via the bridging O^{2-} anion leading to the absorption of visible light [63]. This causes it to develop a bluish-green hue commonly observed in

its natural deposits. When Fe^{2+} is oxidized, the water molecules in the structure are replaced with hydroxyl ions according to the following reaction

$$2[Fe^{2+} - H_2O] + \frac{1}{2}O_2 \rightarrow 2[Fe^{3+} - OH^-] + H_2O$$

Therefore, it is unsurprising that one of the earliest methods to identify vivianite have been its observation by the naked eye [2, 44] because it shows a characteristic white (colorless) to pale blue-green color transition, gradually darkening upon continued aerial exposure.

Heating under vacuum can also cause oxidation of vivianite by decomposition of crystal water and release of hydrogen [64]. Inertly synthesized specimens are extremely sensitive to air and light and can contain significant amounts of Fe^{3+}, upon exposure. The oxidation of vivianite occurs at room temperature and proceeds till the total Fe^{3+} concentration is 50 % [43]. At higher than 50 % Fe^{3+} concentrations vivianite gets converted to metavivianite [65]. ^{57}Fe Mössbauer spectroscopy has been demonstrated to be an effective technique in the identification of iron containing minerals. It has been used to study the oxidation states of Fe in vivianite samples and also in determining the ratios of the Fe^{2+}/Fe^{3+} within the mineral phases [43, 64].

2.1.3.2. X-ray Diffraction (XRD)

Vivianite has been extensively studied by XRD techniques [3, 4, 39, 47, 49]. It shows a characteristic powder X-ray diffraction pattern that allows it to be identified among other crystalline and non-crystalline phases. The XRD detection of vivianite requires a ratio of at least 5 % by weight of the total mineral for the technique to show the three most intense characteristic peaks for vivianite at *d-values* of 6.79, 2.97, and 2.71 [4, 66]. When more than 40 % of the Fe has been oxidized the monoclinic vivianite lattice collapses to give the triclinic symmetry of metavivianite [43]. Thus, the XRD sample must be prepared anoxically and care must be taken while handling it.

2.1.3.3. Scanning Electron Microscopy with Dispersive X-Ray Spectroscopy (SEM-EDX)

The elemental composition of vivianite in fragments of naturally occurring samples can be qualitatively found by SEM-EDX technique [3, 49, 67]. The method has been used to study naturally occurring specimens from various sources to map the percentage composition of Fe, P and O in the sample. The percentage elemental composition of non-oxidized vivianite is Fe (33.4%), P (12.35%) and O (51.03%). It is important to mention that the elemental composition can only be determined semi-

quantitatively by SEM-EDX technique because the crystal surfaces have an unknown orientation. As expected, the Fe/P ratio is close to 1.5 for vivianite and has been considered by many sources for its EDX mapping [67]. SEM can reveal its morphology, crystallite sizes and provide an estimated elemental composition of the vivianite sample.

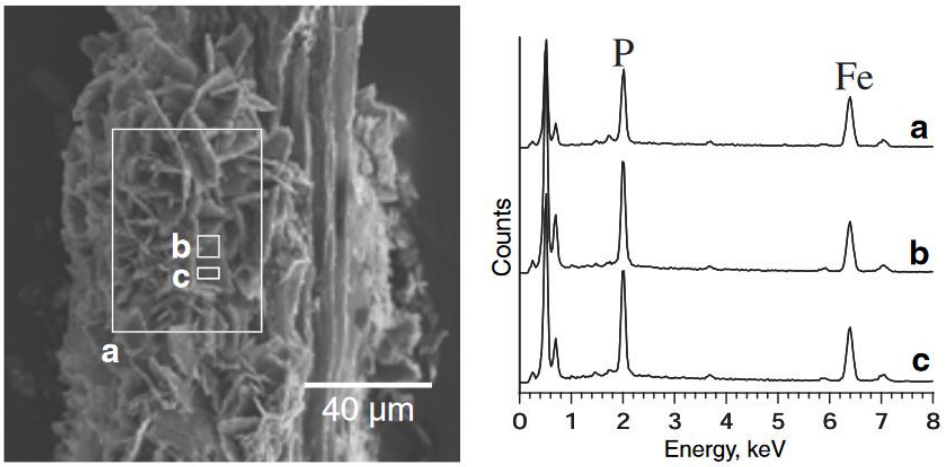

Figure 2.3. SEM image and EDX spectra of the selected regions for vivianite growing on paddy rice root tips (modified image from Nanzyo *et al*, 2010) [67]

2.1.3.4. Infrared (IR) and Raman Spectroscopy

Infrared [7, 54] and Raman [68] spectroscopy are also quite helpful in its identification. The IR spectrum of vivianite shows characteristic H-O-H stretching and bending modes at nearly 3430 cm^{-1} and 1690 cm^{-1} respectively, the tetrahedral phosphate group shows vibrations at 974 – 1037 cm^{-1}. IR analysis is an additional tool in the characterization of vivianite and has been widely used in identification of this mineral [54, 69]. An advantage of using Raman spectroscopy over IR is that data below 400 cm^{-1} can be obtained. Vivianite shows strong broad O-H stretching bands between 3000 to 3700 cm^{-1}. The strongest band in the Raman spectrum is at 3262 cm^{-1} attributable to the OH stretching. A strong band is observed at 951 cm^{-1} and is due to the Raman active PO stretching. Two intense bands are observed at 236 and 186 cm^{-1} and these bands are attributable to Fe-O stretching vibrations [69].

2.1.3.5. Fe K-edge X-ray absorption spectroscopy (XAS)

The determination of the oxidation state, coordination number and atomic environment of the Fe atoms in vivianite are possible through X-ray absorption spectroscopy. This technique can identify both crystalline and non-crystalline phases via comparison with standard spectra or by a linear combination of standard spectra, when more than one phase may be present [70]. The energy of the

absorption edge in the Fe *K*-edge spectra of vivianite shows that Fe^{2+} is the dominant state for iron in vivianite samples. The absorption edge is at an energy of 7121.5 eV for pure non-oxidized vivianite and at 7123.5 eV for oxidized samples bearing ferric ions [71]. The pre-edge features (centroid) in XANES is sensitive to the geometry and spatial arrangement of the Fe sites and correspond to 1s → 3d transition [72]. This can be used to determine the oxidation state and local symmetry of the Fe sites in natural samples, which may contain vivianite [72, 73].

2.2. Thermodynamic stability field and solubility of vivianite

Vivianite occurs globally under anoxic aqueous conditions at high Fe^{2+} and phosphate activities and at low sulfide activity [1, 10]. The favorable pH for vivianite formation lies between 6 – 9 [1]. As phosphate speciates in the HPO_4^{2-} and $H_2PO_4^-$ forms in the pH range of natural waters [66] , the solubility of vivianite in aqueous media is given by the following equilibrium [66]

$$Fe_3(PO_4)_2 \cdot 8H_2O + 2H^+ \rightarrow 3\ Fe^{2+} + 2\ HPO_4^{2-} + 8\ H_2O$$

Hence, the solubility product (K_{sp}) of vivianite can be defined as

$$K_{sp} = \frac{[(Fe^{2+})^3 \cdot \gamma_{Fe}^3] \cdot [(HPO_4^{2-})^2 \cdot \gamma_P^2]}{(H^+)^2 \cdot \gamma_H^2}$$

Where γ represents the activity coefficients of each species and parentheses represent the molal concentration of each species (subscripts Fe = iron, P = phosphate, H = protons).

In one of the earliest studies on vivianite solubility by Rosenvqvist [2] (1970), its solubility product was calculated from Holocene clay sediments. The reported K_{sp} values [2] were shown to lie between 10^{-39} to 10^{-40}. Later, Nriagu [1] (1972), also worked on the solubility of synthetic vivianite in aqueous phosphoric acid solution and suggested contributions from ion pair formation $FeH_2(PO_4)^+$ - $FeHPO_4^0$ that had been previously unacknowledged, reporting a value of 10^{-36}, which differed in several orders of magnitudes from the previously calculated value, by Rosenqvist [2]. Following this, Al Borno and Tomson [66] (1994) determined the K_{sp} of vivianite at a series of different temperatures and reported it as $10^{-35.75}$ at 25˚C. The latter K_{sp} values [1 66] are frequently used for calculation of vivianite saturation indices (SI) in different systems at variable physical and chemical parameters. However, such

thermodynamic calculations have several limitations and are unreliable indicators of vivianite´s actual occurrence.

2.3. Vivianite synthesis in the laboratory

Vivianite can be prepared in the laboratory by using deoxygenated water as a solvent, under anoxic conditions upon mixing of phosphate and ferrous salts under ambient temperature and pressure. The synthesis requires strictly anoxic conditions and nearly neutral pH. In the presence of oxygen and at alkaline pH (> 9), other crystalline/amorphous ferric phosphates or ferric-oxy-hydroxides may readily precipitate out preferentially over vivianite, which significantly hinders its formation [74]. For the synthesis, the most commonly used ferrous salts are Mohr's salt ($Fe(NH_4)_2(SO_4)_2.6H_2O$) [43, 66] and ferrous sulphate ($FeSO_4$) [65], both of which are relatively stable Fe^{2+} precursors.

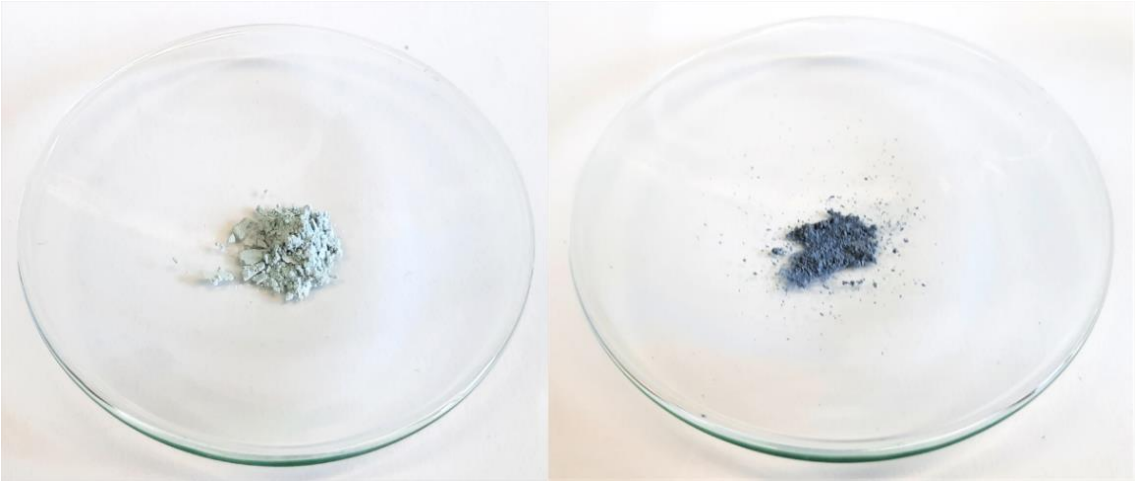

Figure 2.4. Picture showing synthetic vivianite samples from anoxic laboratory precipitation experiments and color changes upon aerial exposure; The light blue color of the freshly prepared anoxic sample *(left)* is a contrast to the darker indigo-blue color of the oxidized sample *(right)* after 1 week of aerial exposure.

The most commonly used phosphate salts for its synthesis are di- and mono-basic sodium/ammonium phosphate solutions, aqueous solubility of orthophosphate (PO_4^{3-}) precursors is quite low and this species is rarely encountered in natural waters, so mono or di-hydrogen phosphates are preferred. It has been reported that iron phosphate salts generally precipitate as strengite ($FePO_4.2H_2O$) under aerobic conditions [43]. Upon treating vivianite to high temperature and pressure conditions, it has been reported to show a buff tint, most likely due to partial oxidation of the ferrous ions [66]. The synthetically precipitated vivianite can be converted to a buff colored precipitate under acidic pH (3-5) and higher temperatures of 80˚C, as reported by Al-Borno et al. [66]. Ferric ions can be detected if the solid is

exposed to air and light, thus special care must be taken during the synthesis. It has also been shown that synthetic SO_4^{2-} intercalated green-rust ($Fe^{2+}_4 Fe^{3+}_2 (OH) \cdot 12\ SO_4 \cdot x\ H_2O$) can react with Na_2HPO_4 via anion-exchange to transform into vivianite [75].

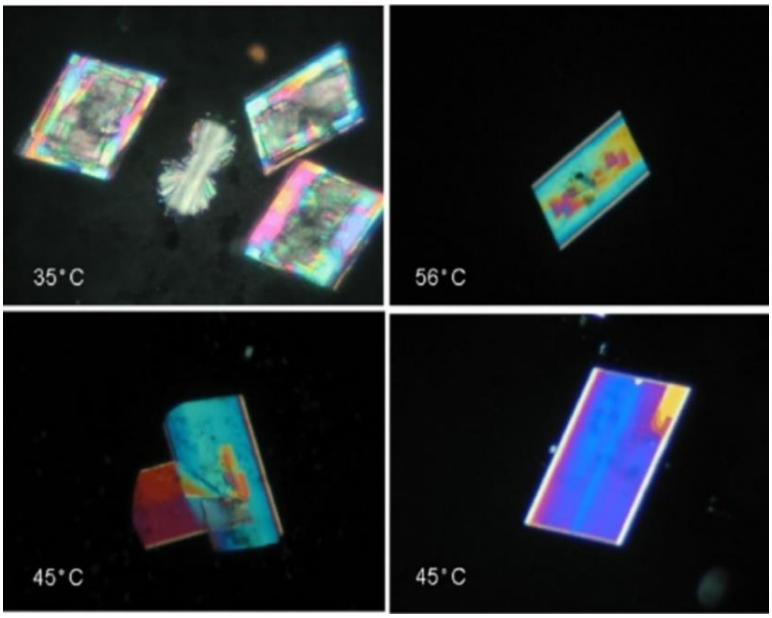

Figure 2.5. Polarized light microscope images of synthetically grown vivianite crystals at different temperatures by precipitation from aqueous solutions, reproduced with permission from Madsen, 2020 [76]; Copyright © John Wiley and Sons Inc.

2.4. Ferruginous ocean chemistry on early Earth

Ferruginous or 'Fe^{2+} rich' conditions are believed to be predominant in deep-oceans on early Earth, as well as through much of its history. The oxygenation of the Earth's Oceans is widely believed to occur in two major episodes: the Great Oxidation Event (2400-2200 Ma)[77] and the Neoproterozoic Oxygenation Event (800 – 540 Ma)[78]. This oxidation was a complex process and the Precambrian ocean chemistry remains debated. The development of modern Earth's environment and evolution of complex life probably were a direct consequence of the emergence of photosynthesizing cyanobacteria, which is expected to coincide with the major oxidation events in Earth's history [78].

The Proterozoic eon (2500 to 541 Ma) marks the expansion of eukaryotic life and the brisk onset of biological diversification towards its ending sub-era, known as the Neoproterozoic eon (1000 to 541 Ma). Some evidences of this phenomenon are the discovery of Fe^{2+} deposits in Neoproterozoic marine cements [79] and banded Fe rock formations in Western Australia [80]. These ferruginous conditions are also important factors to consider when illuminating early Earth's ocean chemistry and its possible

impact on evolution of life. Canfield and Poulton have analyzed well-preserved Neoproterozoic sedimentary rocks from seven different countries and they have reported evidence of ferruginous conditions in deep oceans [81].

If the ratio between geochemically highly reactive Fe and total Fe in sediments is greater than 0.38, it may indicate anoxic water conditions dominated by dissolved Fe^{2+} [81]. Influx through deep-sea hydrothermal vents is considered to be the main source of Fe^{2+} in the water column, along with anoxic diagenesis of sediments [82]. The change in the chemistry of oceanic mid-waters from sulfidic to ferruginous could have provided opportunities for the early eukaryotes to evolve and flourish in this changed environment [83].

Figure 2.6. Banded iron formation outcrop at Hamersley group, Australia *(right)* and a close-up of the banding from Canada *(left)*. Modified image from Poulton and Canfield, 2011 [81]. Reproduced with copyright © permission from Mineralogical Society of America.

However, one of the biggest challenges is to explain the source of highly-reactive and bioavailable Fe^{2+} in the water column, which is difficult to explain based on the thermodynamic predictions. A recent study suggested that cyanide and derivatives *i.e.* metal cyanide complexes, urea and formate, that transform insoluble iron and calcium minerals into more soluble reactive species, which may lead to the formation of organophosphates that may have played a pivotal role in early Earth's evolution [84].

Generally, the majority of Fe^{2+} produced from hydrothermal vents reacts with sulfides to form pyrite (FeS_2) or is oxidized to ferric (oxyhydr)oxides (*e.g.* ferrihydrite)[81]. Therefore, the sources of bioavailable reactive Fe^{2+}, in the ancient oceans remain uncertain. Furthermore, elevated phosphorus-to-iron ratios in Neoproterozoic iron formations dating 750 – 635 Ma, indicate unusually high dissolved phosphate concentrations. These conditions may have led to high primary productivity and organic C burial, ultimately followed by more oxidizing conditions in the ocean and atmosphere [85]. Given, the large amount of dissolved Fe^{2+} and phosphate in the early Earth's oceans particularly during the oxygenation events, the large-scale occurrences of vivianite may be very likely during that period [1]. Therefore, understanding the formation pathways of vivianite is an important step, to unravel its role in geochemical Fe\P cycling in these environments.

2.5. Fundamental theories of nucleation

The term 'nucleation' refers to the process of agglomeration of monomeric growth units (atoms, ions or molecules) to form macroscopic thermodynamically stable phases. There are different theories of crystal growth, broadly speaking the classical and non-classical theories. The driving force behind such transformations is the difference between the chemical potential of the monomers in the supersaturated solution and their chemical potential in the solid matrix. Thus, for crystallization to spontaneously occur, the difference in chemical potential between the initial and final states must be a positive quantity. This implies that the activity of the monomeric units needs to be higher in the liquid phase than the solid phase, if a crystal were to form in solution. Broadly, there exist two theories of nucleation namely the classical (CNT) and non-classical nucleation theories, these will be discussed in the following sub-sections.

2.5.1. Classical nucleation theory

The classical nucleation theory (CNT) was first introduced by Volmer and Weber in 1926 [86]. It was later developed by Becker and Döring through equations which provide simple kinetic models to describe the dynamics of phase transitions including metastability, nucleation and coarsening. Frenkel [87] also contributed to the development of this theory by describing pre-translation phenomena and hetero-phase fluctuations.

The CNT is based on assuming equilibrium behavior between solid-liquid phases in solution during crystallization. This theory suggests that the formation of macroscopic aggregates or crystals in solution is determined by the interfacial surface free-energy cost and volume free-energy release of

the aggregating nucleus. The surface free-energy term comprises of the total surface area of a sphere of radius r times the free energy change per unit area of the surface formed. The volume/bulk free-energy term comprises of the volume of the sphere times the change in free energy per unit volume (ΔG_v). One can add these two terms to obtain the total free energy of nucleation as

$$\Delta G = \frac{4}{3}\pi r^3(-\Delta G_v) + 4\pi r^2(\Delta G_S)$$

If one were to plot this summed up free energy ΔG vs the radius r, a barrier of free energy is observed with a global maximum. The position of the maxima is found by equating the partial derivative of ΔG with respect to r to be zero. Solving this equation for r gives us the value of the critical radius r_c.

$$\frac{\partial(\Delta G)}{\partial r} = 4\pi r^2(\Delta G_V) + 8\pi R(\Delta G_S) = 0$$

$$r_C = \frac{-2\Delta G_S}{\Delta G_V}\pi$$

Before the critical radius is achieved by the nucleus, its aggregation and growth are not favored thermodynamically due to the free energy cost of forming a new surface. However, once this radius has been achieved, its subsequent growth is a thermodynamically favorable process as the bulk/volume free energy term dominates, decreasing the overall free energy of the system and leading to larger particle size. In order to form aggregates the free-energy barrier must be crossed and the critical radius must be achieved.

If the nucleus radius is smaller than r_c then the particle will eventually dissolve in the surrounding solution. However, if the particle grows beyond the critical radius, the particle can grow to larger macroscopic dimensions. The universal applicability of the CNT has been questioned over the years due to increasing evidences of intermediates and multi-step nucleation pathways, leading to the so-called non-classical nucleation theory, which will be discussed further in the following sections.

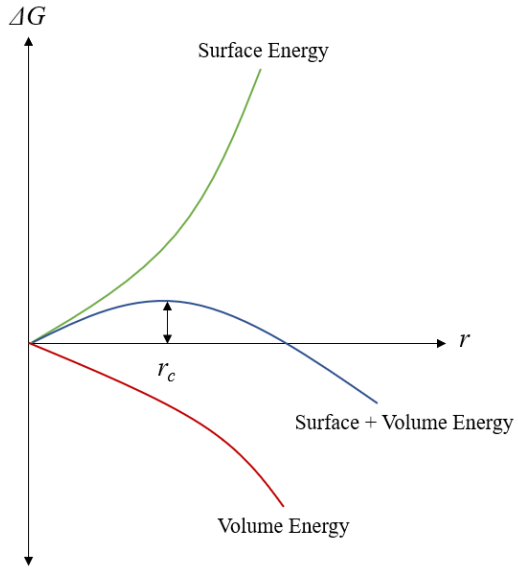

Figure 2.7. Variation of the total free energy of nucleation (*ΔG*) versus the radius (*r*) showing the surface and volume energy curves, the free-energy barrier, the critical radius (r_c) in the classical model.

2.5.2. Non-classical nucleation theory

CNT has a few oversimplified assumptions that the nuclei are spherical and their phase boundaries are sharp and well-defined. It also assumes that the solid-liquid interface is planar irrespective of the particle size and that the macroscopic properties of the nuclei and final phases are identical. These assumptions may or may not be applicable to many complex systems such as minerals, proteins, colloids and polymers. In classical nucleation theories, only interaction potentials (enthalpic effects) are considered but not entropic solvent effects. The non-classical theory of crystal growth accounts for the shortcomings of the CNT. As a precursor to this theory, the rule of stages given by Ostwald [88], that the formation of a thermodynamically stable phase does not occur in a single step from the metastable phase but proceeds in multiple steps having a free energy closer to the previous stage. The system which approaches the critical point shows density fluctuations and when local supersaturations become large enough, a solid phase nucleates. In some cases, [26] the first step is initiated by critical density fluctuations which cause the formation of a dense droplet which has a lower free energy than the surrounding medium and higher than the ordered solid phase. This is followed by a second, slower and rate determining, step of the formation of ordered nuclei. Non-classical pathway is favored when the sum of the two energy barriers is less than the barrier for CNT.

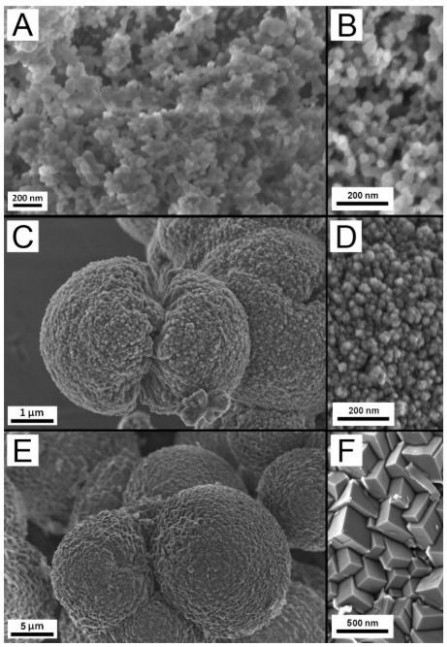

Figure 2.8. An example of multi-step nucleation process of dolomite shown via SEM images of different Mg-ACC phases showing amorphous intermediate stage (A,B), proto-dolomite (C,D) and crystalline dolomite (E.F), (modified image from Rodriguez-Blanco *et al* 2015 [28])

An example of this phenomenon is $CaCO_3$ nucleation, which is studied extensively and the pre-nucleation stage of amorphous calcium carbonate (ACC) has been reported by different sources [16, 17, 89]. The cluster formation can be characterized via the concept of equilibrium thermodynamics, applying a multiple-binding model. Stable clusters are the relevant species in $CaCO_3$ nucleation, the experiments are based on the measurement of Ca^{2+} concentrations at constant pH values, enabling a quantitative determination of all species present at the different stages of crystallization as supersaturation is slowly achieved [90]. In the CNT approximation, the critical nucleation energy barrier ΔG* needs to be overcome to form metastable clusters which initiate classical nuclei formation, however it has been observed that stable clusters are formed with an almost negligible energy barrier in accordance with the non-CNT. Studies have shown that the surface directed calcium phosphate crystallization proceeds through pre-nucleation clusters via the non-classical pathway through high resolution cryo-TEM [91].

The initial stage is the loose aggregation of pre-nucleation clusters, followed by their aggregation over a monolayer, then densification happens near the monolayer leading to the nucleation of amorphous spherical particles and the development of crystallinity [91]. Overall, nucleation is sensitive to small changes such as temperature, pressure, impurities and interaction potentials. Thus, advances in the

fundamental and comprehensive understanding of nucleation pathways, can allow us to create novel materials with useful properties for material science applications.

Chapter 3. Nucleation and Crystallization of Vivianite via an Amorphous Intermediate

Adapted from the published article:

Nucleation and Crystallization of Ferrous Phosphate Hydrate via an Amorphous Intermediate

A. Paskin, T. Couasnon, J. P. H. Perez, S. S. Lobanov, R. Blukis, S. Reinsch, L. G. Benning

J. Am. Chem. Soc. 2023, 145, 28, 15137-1515

DOI: https://doi.org/10.1021/jacs.3c01494

ABSTRACT. The fundamental processes of nucleation and crystallization are widely observed in systems relevant to material synthesis and biomineralization; yet most often their mechanism remains unclear. In this study we unravel the discrete stages of nucleation and crystallization of $Fe_3(PO_4)_2{\cdot}8H_2O$ (vivianite). We experimentally monitored the formation and transformation from ions to solid products by employing correlated, time-resolved in situ and ex situ approaches. We show that vivianite crystallization occurs in distinct stages via a transient amorphous precursor phase. The metastable amorphous ferrous phosphate (AFEP) intermediate could be isolated and stabilized. We resolved the differences in bonding environments, structure and symmetric changes of the Fe site during the transformation of AFEP to crystalline vivianite through synchrotron X-ray absorption spectroscopy at the Fe K-edge. This intermediate amorphous ferrous phosphate phase has a lower water content and less distorted local symmetry, compared to the crystalline end product vivianite. Our combined results indicate a non-classical, hydration-induced nucleation and transformation mechanism driven by the incorporation and rearrangement of water molecules and ions (Fe^{2+} and PO_4^{3-}) within the AFEP, is the dominating mechanism of vivianite formation at moderately high to low vivianite supersaturations (saturation index ≤ 10.19). We offer fundamental insights into the aqueous, amorphous-to-crystalline transformations in the ferrous phosphate system and highlight the different attributes of the ferrous phosphate precursor, compared to its crystalline counterpart.

3.1. Introduction

The process of crystallization of solid phases in an aqueous solution underlies and controls natural (*e.g.*, rock formations [92], biomineralization [93, 94]), as well as artificial (material synthesis and design [95,

[96]) systems. Therefore, this fundamental process has received a lot of recognition, particularly in material [97-99] and environmental sciences [100-102]. Classical nucleation theory (CNT) states that the thermodynamic barrier of interfacial free-energy needs to be overcome by crystalline nuclei to achieve critical sizes, which allows them to grow to macroscopic dimensions via monomer-by-monomer addition [86]. Although the CNT framework applies to crystallization of iron bearing phases such as magnetite [34], CNT is insufficient in describing many other systems, in which nucleation proceeds via transient amorphous stages, aggregation and clusters, unaccounted for by CNT [92, 103, 104]. Ostwald's law of stages states that the formation of a heterogeneous phase proceeds in multiple stages with each metastable stage having a higher stability than the previous stage, a process that continues until the most thermodynamically stable end state is reached [88, 105]. As a consequence, several studies have recently show that the formation of thermodynamically stable phases follows a non-classical pathway [92, 104, 106]. Among these are the calcium and magnesium carbonate (Ca-Mg-CO_3) phases calcite and dolomite [107], or calcium phosphate (apatite), which have all been shown to crystallize via the dehydration of amorphous calcium / or calcium - magnesium carbonate [108-111] and amorphous calcium phosphate (ACP) [112] precursors. The nucleation of hydroxyapatite (HAP) via ACP and the formation of $CaCO_3$ polymorphs (aragonite, vaterite and calcite) from ACC have been shown to have substantial implications for biomineralization [2, 25, 26]. In situ TEM studies have documented that the ACC to crystalline $CaCO_3$ transformation can occur simultaneously via non-classical and classical pathways [17, 113].

The di-hydrous gypsum ($CaSO_4 \cdot 2H_2O$) endmember of the Ca-SO_4 system, was shown to form via the hydration [114] and particle-mediated rearrangement of anhydrous nanocrystalline precursor [23]. It is thus clear that non-classical crystallization of thermodynamically stable phases can proceed via hydration or dehydration and that the pathway is dependent on the interplay between thermodynamic and kinetic factors. Nevertheless, for many sparingly soluble salt systems a comprehensive elucidation and structural analysis of kinetically controlled crystallization stages and possible intermediate phases remain scarce.

One such understudied system consists of iron phosphate phases and in particular ferrous phosphates. The thermodynamically stable ferrous phosphate is vivianite ($pK_{sp,25℃}$ = 35.416) [66]. Vivianite is a two-component hydrated solid phase that acts as a crucial mineral controlling the iron and phosphorus element cycles [59, 115] in modern and ancient ferruginous (Fe^{2+} rich) anoxic systems worldwide [4, 7, 10, 67]. In addition, vivianite has major economical relevance in phosphorus recovery from wastewater [40-42, 116] and removal of harmful contaminants like lead from the environment [117]. Vivianite is also a

precursor in synthesis of $LiFePO_4$ material used for battery (cathode) applications [118]. Yet, the mechanisms controlling vivianite nucleation and crystallization remain unstudied.

In the present study we unraveled the fundamental nucleation and growth pathway from solution leading to the formation of crystalline vivianite with a focus on the changes in aqueous and solid-state chemical environments. By combining *in situ* ultraviolet visible (UV-vis) spectrophotometric monitoring of the reaction progress with multiple complementary *ex situ* solution and solid analyses, we characterized the formation and transformation of all reaction stages as well as the changes in structure and bonding of iron and phosphorus and the fate of water in the formed solid phases. This allowed us to derive a mechanism for the crystallization of vivianite.

3.2. Experimental Section

3.2.1. Synthesis and thermochemical modeling

All experiments were performed at room temperature inside an anaerobic chamber (Coy Laboratory Products, Inc.) under a gas atmosphere of 97 % N_2 and 3 % H_2. Labware used for synthesis were soaked in 10 % HCl solution overnight and rinsed with ultrapure water (~18.2 M Ω·cm resistivity). All experimental solutions were prepared from ultrapure water that had been degassed by purging with CO_2-free Ar gas and heating (at 80˚ C) for at least 5 h.

Ferrous phosphate phases were synthesized in a perfluoroalkoxy alkane reactor by mixing equimolar (0.01 mol L^{-1}) solutions of ferrous ammonium sulfate ($Fe(NH_4)_2(SO_4)_2 \cdot 6H_2O$, 99.95 %, Alfa Aesar GmbH) and a mixed sodium potassium phosphate reagent ([HPO_4] = 0.01 mol L^{-1}) with the latter buffered at pH 7.2, (see section AIS1, appendix I for phosphate reagent preparation protocol). The experimental pH was continuously recorded every 1 s using a multi-purpose data logger board, “DrDAQ” (Pico Technology, Cambridgeshire, UK), equipped with a pH probe, calibrated with NIST pH buffers. The resulting suspension was stirred at 300 r.p.m on a stirrer plate throughout the reaction. After fixed time periods (30 s and 6 min) an aliquot of the solution was removed and filter-quenched immediately by fast vacuum filtration through a 0.2-µm membrane filter (Nucleopore polycarbonate membrane). The solids were rinsed with ultrapure water and isopropanol (≥ 99.5%, Sigma-Aldrich) to remove excess salts and water. The time taken to filter the solution was ≤ 30 s. The resulting solids were allowed to dry for 5 h inside the anaerobic chamber and transferred to an air-tight crimp sealed vial for storage until further characterization. Thermodynamic and geochemical modeling (Section AIS2, appendix I) of the system using the ionic concentrations, pH and temperature of the experiments were carried out using the PHREEQC program [119] (Version 3) via the Thermoddem database [120].

3.2.2. In situ UV-vis spectrophotometry

Time-dependent changes in UV-vis absorbance (turbidity) upon mixing of the solutions described above were monitored using an Evolution 220 spectrophotometer (Thermo Fischer Scientific, USA) equipped with an in-built stirrer / temperature control unit (Peltier accessory) and a 3.5 mL septa-sealed quartz cuvette (Sealable Cell 10 mm, Hellma GmbH), that was under continuous argon gas flow to maintain anaerobic conditions. The cuvette was filled with ultrapure water (~18.2 M Ω·cm resistivity) and measured as the blank. UV-vis measurements were started with 1.5 mL of the aqueous phosphate buffer reagent (0.01 mol L^{-1}) equilibrated inside the cuvette in the UV-vis spectrophotometer at room temperature. The UV-vis absorbance was recorded at a fixed wavelength of 450 nm as that wavelength corresponds to the lowest absorbance intensity for the initial solution. Once a stable reading was attained, 1.5 mL of the ferrous ammonium sulfate solution (0.01 mol L^{-1}) was quickly injected into the cuvette under constant stirring, and under argon flow. The absorbance was then recorded at the rate of 1 frame/s with experiments run for 16 minutes.

3.2.3. Characterization

Inductively coupled plasma – optical emission spectroscopy (ICP-OES). To determine the dissolved ion concentrations during the experiments, an aliquot of the reaction mixture was filtered through a syringe filter (0.1 µm, PTFE) and collected in acid-cleaned PP tubes. The liquid phase was acidified by conc. HCl (AristaAR®, VWR), and stored at 4˚C until analysis. To determine the resulting solid composition (i.e., Fe/P ratio), powdered solid samples were digested using conc HCl in acid cleaned flasks. Elemental concentrations in the acidified samples were analyzed using a Varian 720ES ICP-OES. The samples were spiked with 1 mg g^{-1} cesium as an ionization buffer, and scandium (1 µg g^{-1}) as an internal standard. Ionic concentrations were evaluated using the emission wavelengths of 261.382 nm (Fe) and 213.618 nm (P) respectively. The determined limits of detection (LoD) for iron and phosphorus are 0.014 µg L^{-1} and 4 µg L^{-1}, respectively. Refer to table A1T1 in the appendix I for quality control (QC) and analytical uncertainties.

Powder X-ray diffraction (XRD) and Pair-Distribution Function (PDF) analyses. The XRD samples were prepared inside the anaerobic chamber by grinding the dried powders with a mortar and pestle and transferring them into a glass capillary (Hilgenberg 4007805, 0.5 mm) sealed with a wax plug (Cristaseal Sealant Tray, Hawksley & Sons Ltd.) to prevent oxidation. XRD patterns were measured in Debye-Scherrer geometry on a STOE STADI P (STOE & Cie GmbH, Germany) diffractometer operating at 40 kV and 40 mA, using Ag K_α radiation (λ = 0.55941 Å), equipped with a curved Ge(111)

monochromator and two DECTRIS MYTHEN2 R detectors with a 0.015° step size and 1500 s per step. The 2θ values ranged from 1° to 70°. An empty capillary, measured under the same experimental conditions, was taken as the background. The background patterns were subtracted from the experimental patterns, prior to plotting and analysis. XRD data handling was performed on STOE WinXPOW software (Version 3.21.2) and OriginPro (2021) software (OriginLab Corporation, Northampton, MA, USA). The calculated XRD patterns were obtained from the respective crystallographic information file (cif) [121] and using the Vesta software [52].

Pair distribution function (PDF) analysis was done with the PDFGETX2 software [122] and using the powder XRD patterns measured up to 140°(2θ). Data treatment included background subtraction (0.5 mm empty capillary), polarization (Ge(111), d = 3.226 Å), Compton, multiple, diffuse scattering and absorption (μt = 0.3) corrections. PDFs were generated up to a maximum Q of 50 Å from Fourier transform of the Q[S(Q)-1].

Scanning electron microscopy (SEM). Samples were prepared inside the anaerobic chamber by suspending ~ 5 mg of a dried solid sample in degassed isopropanol and drop-casting onto SEM stubs. The isopropanol was allowed to evaporate, and then the samples were removed from the anaerobic chamber and immediately carbon coated (~ 20-nm layer) using a high-vacuum sputter coater (BAL-TEC MED 020 Leica Microsystems) prior to SEM analyses on a FEI Quanta 3D field-emission-SEM instrument at 20 kV. Particles were imaged and elemental maps were recorded using energy dispersive X-ray spectroscopic analyses (SEM-EDS).

Transmission electron microscopy (TEM). Inside the anaerobic chamber, aliquots of the reaction mixture were quenched at 30 s, 100 s, 6 min (SI 10.19) and 20 min and 48 h (SI 7.16). These samples were drop-casted onto lacy carbon-coated copper grids that were deposited on the filtration frit of a vacuum filtration assembly. The samples on the grids were rinsed with ultrapure water and isopropanol to remove salts and subsequently dried under vacuum. They were then transferred from the anaerobic chamber to a TEM sample holder, and inserted, within 1 min, into the TEM airlock and set under vacuum. Micrographs and analyses of the samples were acquired using a TECNAI F20 XTWIN TEM operated at 200 kV with a field emission gun electron source, and a Gatan Imaging Filter (GIF) Tridiem™ EDS X-ray analyzer. Imaging, selected area electron diffraction (SAED), and scanning-TEM coupled to EDS (STEM-EDS) were used to analyze particle morphology, crystallinity and qualitative chemical composition of the samples. The TEM image analysis was performed using the Image J, (US-National Institute of Health) and TIA (FEI Company © and digital micrograph, Gatan Inc.) software packages.

Fourier transform infrared spectroscopy (FTIR) spectra of the dried solids were acquired using the attenuated total reflection (ATR) mode on a Nicolet iS5 spectrometer (Thermo Fischer Scientific, USA) with an iD7 diamond ATR accessory and KBr beam optics. FTIR spectra were acquired within a range of 400 to 4000 cm^{-1} and 16 scans were averaged with a resolution of 4 cm^{-1}. Spectra were analyzed using the Thermo-Nicolet OMNIC version 1.02 software package (Thermo Fisher Scientific Inc).

Thermal Analyses. Thermo gravimetric measurements (TGA) were used to determine the water content of the samples. Data was acquired on a thermobalance SETARAM TAG 24 (Setaram, Caluire, France) system. The powdered samples were stored under nitrogen until insertion into open platinum crucibles (100 µL). Measurements were conducted under argon flow ($35 \cdot 10^{-5}$ L s^{-1}) after repeated evacuation cycles (~$3 \cdot 10^{-1}$ mbar) at a heating rate of 10 K/min up to a maximum temperature of 500°C. The data was analyzed using the OriginPro (2021) software (OriginLab Corporation, Northampton, MA, USA).

X-Ray Absorption Spectroscopy (XAS) data were collected at the Fe K-edge (7112 eV) on the P65 undulator beamline of the Deutsches Elektronen-Synchrotron (HASYLAB, DESY PETRA III, Hamburg, Germany) operated at 6.0 GeV with 100 mA current in multi bunch mode. Powdered samples were mixed with cellulose (2.5 % Fe) and pressed into ~1-mm thick and 13 mm Ø pellets, that were sealed inside the anaerobic chamber with 25 µm thick Kapton® tape that has a low O_2 diffusivity [123]. Samples were transferred and transported to DESY inside crimped vials.

At DESY these vials were reinserted and stored in a glovebox until just prior to measurement when they were transferred into the liquid helium flow cryostat (Oxford Instruments), that allowed for the samples and reference compounds (synthetic γ-FeO(OH) [124] and $Fe(OH)_2$ [125]) to be maintained at 20 K and 10^{-6} mbar and thus prevent oxidation and photo-reduction under the beam during the XAS measurements. Incoming photon flux energy was modulated with a Si(111) double crystal monochromator, with an energy resolution of ~ 0.7 eV at the Fe K-edge, and a beam size of 0.3·1.5 mm^2. The effective suppression of higher harmonics was achieved using Si-plane mirrors. The data were collected from -150 eV below the edge to +1000 eV above with a scan energy increment of ~ 0.6 eV in continuous mode. The time for each spectrum was 240 s and an average of 5 scans was used for the analysis. Spectra of reference compounds and samples were acquired in transmission mode, concomitantly with the spectrum of an Fe foil for energy calibration and alignment. The first inflection point in the first derivative of the adsorption threshold of the Fe foil was calibrated at 7112 eV. Incident and transmitted X-ray intensities were recorded using ion chambers with a path length of 5 cm. The ion chambers were filled with gas mixture of N_2, Ar and Kr to approximately obtain 15 %, 50 % and 100

% absorption for the incident beam I_0, the transmitted beam I_T and the beam transmitted through the reference foil I_{T2} respectively. X-ray absorption near edge structure (XANES) data handling and edge-analyses was done on Athena software [126]. Pre-peaks were obtained by programming and subtracting a fitted arctangent function on OriginPro (2021) software (OriginLab Corporation, Northampton, MA, USA). The pre-peak components were deconvoluted and fitted using Fityk software [127]. Extended X-ray absorption fine structure (EXAFS) modeling was done by fitting Fe-O/P paths on SIXpack software using IFFEFIT database [128].

Optical spectroscopy (ultraviolet to near infrared) was performed to characterize the *d-d* electronic transition bands in the solid phases. Data was recorded from 7000 – 14000 cm^{-1}. The spectra were collected on a Vertex 80v spectrometer (Bruker, USA) with exchangeable UV-vis and near IR beam-splitters. Samples were powdered by a mortar pestle and suspended in epoxy resin, inside the anaerobic chamber, and smeared on a glass slide for measurements. Then the sample was taken out of the anaerobic chamber and transported to the instrument for data collection. Background estimation included measurement of the glass slide and epoxy resin. UV bands were deconvoluted and fitted using Fityk software for Pseudo-Voigt profiles [127].

3.2.4. Stability of initial precipitates

The initial ferrous phosphate precipitates were filter quenched after 30 s of mixing equimolar (0.01 mol L^{-1}) solutions of ferrous ammonium sulfate ($Fe(NH_4)_2(SO_4)_2 \cdot 6H_2O$, 99.95 %, Alfa Aesar GmbH) and a mixed sodium phosphate reagent ($[HPO_4]$ = 0.01 mol L^{-1}) at pH 7.2, (see section S1, appendix I), as described in section 2.1. The solids were characterized by IR spectroscopy and ~ 30 mg aliquot of each solid was transferred into a crimped vial with 50 ml ultrapure water (~18.2 M Ω·cm resistivity). The mixture was crimp-sealed and kept at room temperature inside the anaerobic chamber for 5 d. An aliquot of the suspension was filtered and dried (see section 2.1 for filtration setup) inside the anaerobic chamber. IR and SEM analyses of the resulting products were performed after 24 h and 5 d respectively.

3.3. Results and Discussion

3.3.1. Detection of an amorphous iron phosphate intermediate during the crystallization of vivianite

Using the available thermodynamic data for vivianite (solubility product K_{sp} at 25℃: $1.75 \cdot 10^{-35}$) [66], at the equimolar ionic concentrations ($[Fe^{2+}] = [HPO_4^{2-}]$: 50, 0.005 and $5 \cdot 10^{-4}$ mol L^{-1} in the mixed solutions) our computational modeling showed that under the given conditions our experimental

solutions were supersaturated exclusively with respect to vivianite (saturation index (SI) = 10.19; for SI calculations see section S2, appendix I). However, immediately upon mixing of the equimolar solutions at SI 10.19 ($[Fe^{2+}] = [HPO_4^{2-}]$: 0.005 mol L^{-1}), we observed the formation of a pale green suspension that transformed with time into bluish-white precipitates, which, toward the end of the experiments (15 min) settled at the bottom of the PFA reactor. When the pale green suspension was filter-quenched after 30 s, the powder XRD analyses revealed a poorly ordered phase, evidenced by two broad peaks centered at Q values of 2.15 and 4.00 $Å^{-1}$ (Figure 3.1).

The increase in turbidity (measured as absorbance) in our *in situ* UV-vis spectrophotometric experiments, evidenced a step-wise increase that can be equated with the multi-stage formation of solid phases (Figure 3.2-A, black trace). Contrary to the sigmoidal shape of UV-vis spectrophotometric curves reported for single step mineral crystallization reactions [129, 130], the turbidity curve clearly suggested intermediate stages of nucleation and crystallization (Figure 3.2-A).

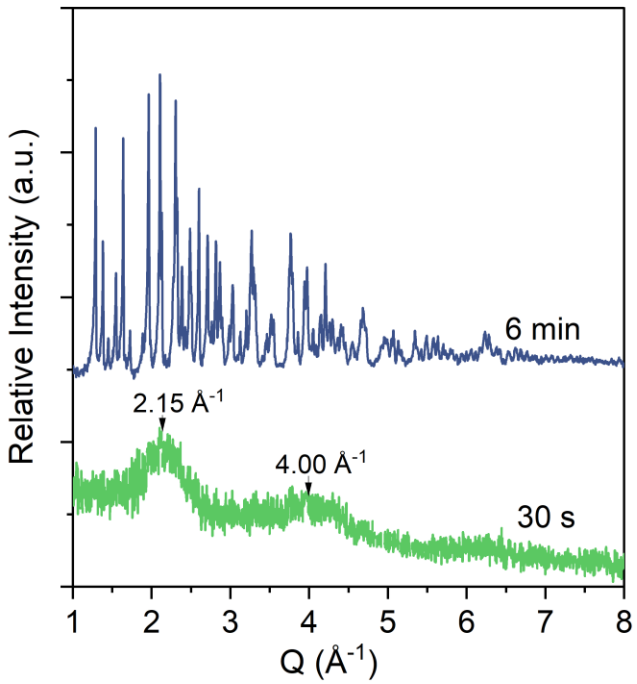

Figure 3.1. Powder X-ray diffraction patterns of filter-quenched solids collected from the reaction mixture after 30 s (green) and 6 min (blue); + 30 s for filtration respectively; SI vivianite is 10.19. Filter-quenching the mixed solutions after 6 min, the XRD pattern evidenced sharp Bragg reflections assignable to pure crystalline vivianite (Figure 1). Using the literature cif file for vivianite [121] we derived a calculated vivianite pattern and compared it with the spectra from our synthetic vivianite produced after 6 min and found a good match for all peaks (Figure F1, appendix I).

Immediately upon mixing, the turbidity increased indicating the instantaneous formation of a solid phase with higher scattering than the initial solutions. After ~ 30 s a first plateau was reached (1st black arrow in Figure 3.2-A) and the turbidity remained constant up to ~ 4 min.

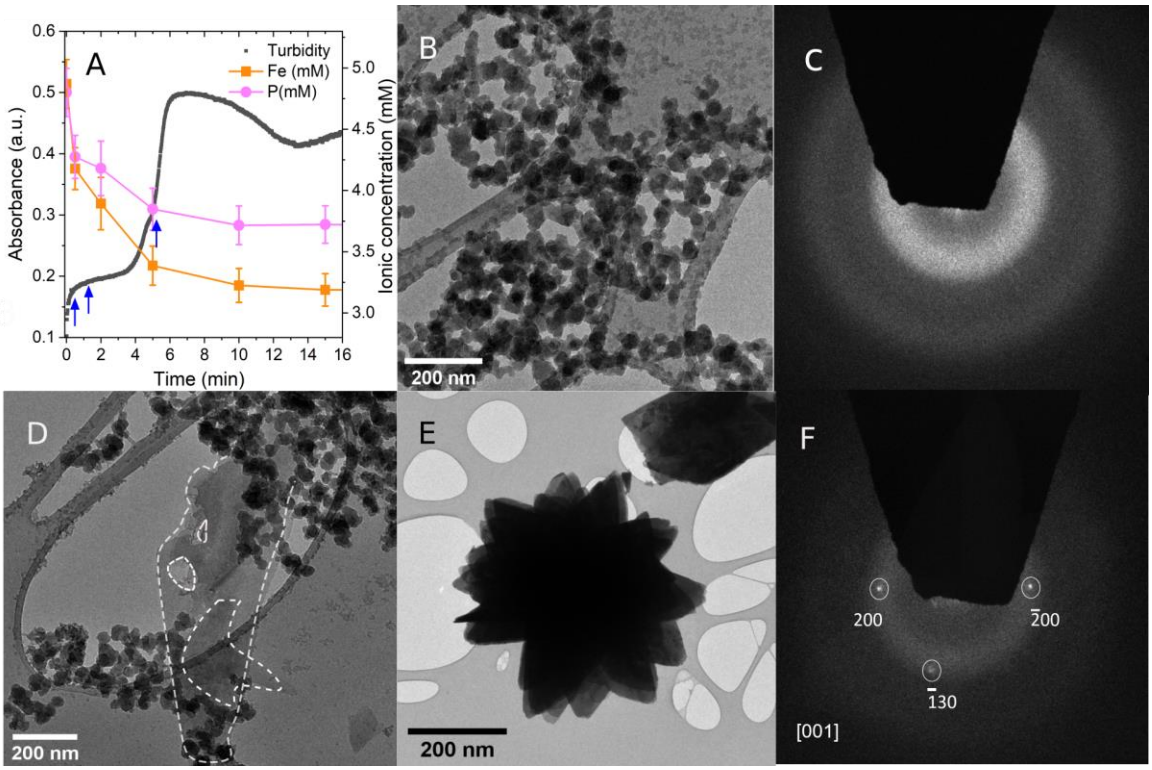

Figure 3.2. (A) In situ, time resolved turbidity (black curve) and ex situ ICP-OES analyses of dissolved species (Fe – orange and P – pink points) during a vivianite precipitation experiment at SI 10.19, with error bars representing values from three repeat measurements. Arrows in blue represent sampling points for TEM analysis; (B) TEM micrograph of solids after 30 s of reaction, showing aggregated nanoparticles; (C) Associated SAED pattern of B showing diffused scattering features indicating an amorphous phase; (D) TEM micrograph after 100 s of reaction showing both the amorphous nanoparticulate aggregates and the initial thin vivianite platelets (dashed white outline); (E) TEM micrograph of solids after 6 min showing radial platy florets of vivianite; (F) Associated SAED pattern of E indexed along [001] zone axis.

A second drastic increase in turbidity, clearly suggested a secondary stage in the phase formation reaction followed with a maximum having been reached at ~ 7 min with a shoulder on the sharp rise. Similar UV-vis spectrophotometric curves having an initial plateau and a second marked rise in turbidity have been reported for the crystallization of the ferrous carbonate mineral - siderite ($FeCO_3$) [101]. In their study, Mulders *et al.* showed that the initial rise of absorbance was a consequence of nucleation of a nanoscale amorphous ferrous carbonate precursor, followed by the second marked rise in turbidity due to the transformation of the amorphous precursor into crystalline siderite [101].

In our work, the plateau and sudden increase observed during the precipitation also suggested the presence of an intermediate phase immediately after mixing, and a secondary transformation to another phase between 4 and ~ 7 min when a 2nd plateau is reached.

The patterns were reproducible in repeat experiments. In all cases, after the 2nd plateau was reached, a gradual decrease in turbidity was observed, a decrease explainable by the gravitational settling of the growing precipitates. Such decreases, linked to settling, are common in turbidity patterns and have for example been reported for calcite crystallization via amorphous calcium carbonate (ACC), where the larger stable calcite crystals settled following their transformation from ACC [97].

We cross-correlated our turbidity observations with *ex situ* analyses of the changes in dissolved iron and phosphorus concentrations during the precipitation, at different time points (Figure 3.2-A, pink, orange points). The fast-initial turbidity increase was mirrored by a fast-initial decrease in dissolved iron and phosphate concentrations upon mixing. This confirmed the instantaneous formation of an iron phosphate phase. However, the first initial drop in ion concentrations did not precipitate all ions and did not reach vivianite solubility product values ($[Fe^{2+}] = 1.31 \cdot 10^{-7}$ mol L^{-1}, $[PO_4^{3-}] = 8.76 \cdot 10^{-8}$ mol L^{-1})[66]. After ~ 5 min, a second more minor decrease in Fe or P concentrations was observed, and apparent equilibrium was nearly achieved at the same time as the maximum in turbidity was reached. The two different rates of changes in aqueous Fe and P concentrations indicate the initial instantaneous nucleation of an Fe-P phase, which in the 2nd stage sequestered additional Fe and P ions from the surrounding medium to form the solids with different scattering, as evidenced by the 2nd increase in turbidity after ~ 4 minutes (Figure 3.2-A). Analysis of the acid-digested solids retrieved from the experiments after 30 s, revealed an Fe/P ratio of 1.41 ± 0.01, which matches the stoichiometric composition of a solid with formula $Fe_3(PO_4)_{2.12}$. Based on this stoichiometry one could infer the presence of a Fe^{2+} phosphate. However, since the ICP-OES technique analyzes total Fe content in the digested precipitates and cannot detect partial oxidation of Fe, we verified the oxidation state of Fe by synchrotron Fe-K edge X-ray absorption spectroscopy (XAS, see below). Not surprisingly, the analysis of the crystalline end product vivianite yielded an Fe/P ratio of 1.45 ± 0.01, matching vivianite's expected chemical composition.

The rapidly nucleated poorly ordered phase (green XRD pattern in Figure 3.1) remained stable for a few minutes prior to the secondary increase in turbidity. If its transformation would occur by dissolution and subsequent re-precipitation to vivianite, the turbidity curve should have indicated a temporary decrease in absorbance before the start of 2nd rapid absorbance rise at ~ 4 min. This was not observed, although from our XRD data (blue pattern in Figure 3.1) it is clear that crystalline

vivianite was formed. Although we cannot exclude some dissolution, our data seems to indicate that the amorphous precursor did not (or only partially) dissolve prior to vivianite crystallization. For monodisperse suspensions particles sizes can theoretically be correlated to turbidity measurements through Mie scattering approximations. However, in our experiments this is difficult due to the fast changes in the physical and chemical properties or our rapidly evolving suspension (i.e., changes in solution and solid compositions, refractive index, particle density and shape) – all parameters that are difficult to control, especially for fast reactions, such as this. However, we could derive particle morphologies and sizes as a function of time from TEM micrographs of *ex situ* filter quenched solids. At the time points indicated by arrows in Figure 3.2 A (30 s, 100 s and 6 min) samples were collected and analyzed. Corresponding TEM micrographs (Figure 3.2 B-F) revealed that the precipitates obtained after 30 s were nearly spherical nanoparticles of a fairly monodisperse particle size distribution of ~ 50 nm diameters, that were most often present as aggregates (Figure 3.2-B). Associated SAED patterns showed only diffuse rings characteristic of an amorphous material (Figure 3.2-C). The STEM-EDS analysis of these particles only evidenced the presence of iron, phosphorus and oxygen in the patterns, without any other impurities (Figure A1F2, appendix I).

The TEM micrographs of solids acquired within the time frame of the 1st plateau of the turbidity curve (at 100 s) revealed aggregated nanoparticles but also very thin platelets (white dotted outline in Figure 3.2-D). To unravel the variable structural order within this sample, we used high resolution TEM (HR-TEM) coupled to fast Fourier transform (FFT). The data indicated areas of variable structural order within the sample (Figure A1F3, appendix I). The very thin platelets (Figure 2D) were crystalline vivianite (Figure A1F3, appendix I), yet all nanoparticles surrounding the poorly formed vivianite platelets were amorphous (Figure A1F3, appendix I). This suggests that the first thin vivianite platelets may already form immediately after the instantaneous nucleation and stabilization of the amorphous nanoparticles as evidenced by the 1st plateau in the turbidity pattern (Figure 3.2-A).

On the other hand, the precipitates after 6 min consisted of larger, radial plate-shaped crystalline florets ranging between 0.5 and 5 µm in diameter (Figure 3.2-E, Figure). The associated SAED pattern was indexed and matched crystalline vivianite (along the [001] zone axis, Figure 3.2-F).

Our *in situ* turbidity data evidenced a nearly constant trend of ~ 2 min (1 – 3 min), despite the TEM data indicating the concomitant presence of minor vivianite and the initiation of the amorphous to crystalline transformation during the 1st plateau time point (100 s). This particular trend can be understood by a kinetic steady state approximation stating that a constant (time-independent) concentration of a reactive species can be approximated from varying concentrations of the reagents,

assuming equal rates of its formation and consumption [131]. Therefore, the formation rate of this intermediate and its rate of transformation to the first thin vivianite platelets can be assumed as approximately equal during the transition period, as evidenced by a nearly constant turbidity trend between 1 – 3 min. When all the solid phases have precipitated; the steady state is disrupted and the reaction is driven rapidly to the more thermodynamically stable end state. This is cross correlated by all the presented observations (XRD, *in situ* UV-vis spectrophotometry, ICP-OES, and TEM/SAED) which all confirm that an intermediate nanoparticulate amorphous Fe-P containing phase formed prior to vivianite crystallization. Since supersaturation is a very important aspect of nucleation and growth, we investigated the kinetic and mechanistic impact of varying vivianite supersaturation in this system.

3.3.2. Effect of supersaturation

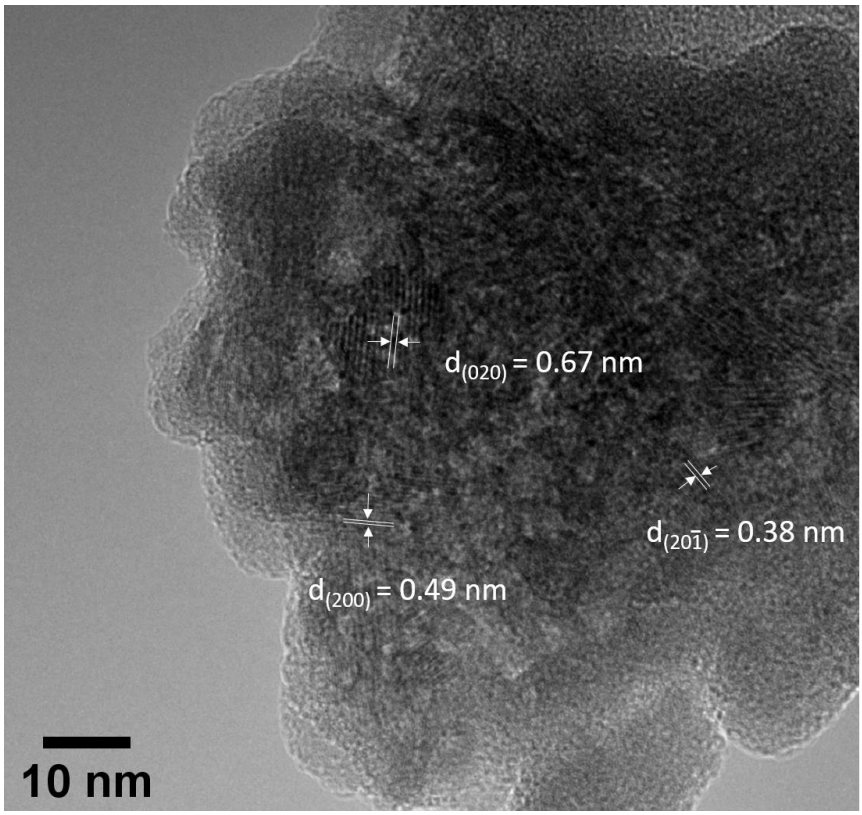

Figure 3.3. HR-TEM micrograph of aggregated iron phosphate nanoparticles and lattice fringes (d_{hkl}) corresponding to crystalline vivianite within the interior of the aggregates. Solids collected at SI 7.16 at 20 min.

The TEM micrographs (Figure A1F4, appendix I) from an experiment at a lower supersaturation (SI = 7.16), revealed the presence of homogeneous spherical and amorphous nanoparticles ~ 50 nm diameters, after 20 min.

The EDX analyses (Figure A1F5, appendix I) of these samples showed presence of only iron, phosphorus, and oxygen. Compared to SI 10.19 where the majority of the nanoparticles converted to vivianite in ~ 5 min, prolonged presence of the amorphous nanoparticles at this supersaturation (20 min), shows that the lifetime of the precursor increases at a lower SI. HR-TEM micrographs (Figure 3.3) of the precursor aggregates revealed presence of dispersed domains of short-range lattice fringes within their interior. These parallel fringes (d_{hkl}) were assignable to initially forming (020), (200) and ($20\bar{1}$) lattice planes of vivianite. The size range of these domains were ~ 10 nm and their shapes were irregular as shown in Figure 3. These micrographs indicate that vivianite crystallization could be initiated via a nanoscale atomic rearrangement within the interior of the aggregates. Since *ex situ* TEM can only offer a snapshot of a time-resolved process and can be prone to sample preparation artefacts, a nanoscale dissolution-reprecipitation process cannot be entirely excluded, but the TEM micrographs shown in Figure 3 point towards a solid-state transformation of the aggregated amorphous Fe-P precursor. The XRD analysis of solids at SI 7.16 at 48 h (Figure A1F6, appendix I) evidenced sharp Bragg peaks assignable to crystalline vivianite. The corresponding TEM micrographs (Figure A1F6, appendix I) from the sample at 48 h revealed micrometer-sized vivianite crystals and spherical nanoparticles with surprisingly larger sizes (80 - 100 nm diameter, Figure A1F6 appendix I – bottom image) on their surface. If the amorphous nanoparticles dissolved prior to vivianite crystallization, their sizes should have decreased with time. However, their sizes increased with time (Figure A1F6, appendix I) through a possible Ostwald ripening process [18] showing that lower supersaturations delay vivianite formation.

An experiment at SI 12.86 was performed to analyze the effect of a higher supersaturation. The XRD analyses (Figure A1F8 appendix I) from this experiment showed precipitation of crystalline vivianite immediately upon mixing and filter-quenching the suspension (~ 20 s). This may be caused by rapid homogeneous nucleation and a decrease in the nucleation induction period at very high supersaturations. SEM showed that most of the vivianite crystallized as radial platy florets with faceted crystals (Figure A1F13, appendix I). Noteworthy is nevertheless, that surface texture of these florets was smooth, within instrumental detection (Figure A1F13, appendix I), indicating crystal growth via ionic attachment [58].

Our data shows that the overall rate of vivianite formation was greatly enhanced at higher supersaturations (SI ≥ 12.86) and the growth of vivianite occurs via ionic attachment. The kinetics of nucleation, as a function of supersaturation, were also studied by in situ pH metric measurement at different vivianite saturation indices at an initial pH of 7.2 (Figure A1F7 appendix I). These results

(Section A1F3, appendix I) showed that the rate of nucleation and transformation was kinetically enhanced at higher supersaturations.

Previous studies based on in situ TEM studies of ACP transformation to HAP have shown the preferential formation of HAP nanocrystals on the surface of the ACP via a non-classical dissolution-reprecipitation pathway [27, 59]. He et al [27] also suggested a second independent pathway of HAP crystallization via the classical route involving HAP nucleation directly from solution. Thus, in the calcium phosphate both classical and non-classical dissolution-reprecipitation pathways occur concurrently during the crystallization of HAP. Similarly, Nielsen *et al* showed that multiple nucleation and growth pathways can occur simultaneously in the $CaCO_3$ system, at moderate to high supersaturations [28].

Based on the data presented above (TEM, SEM, XRD), concurrent pathways of vivianite nucleation and growth are suggested in this system, depending on the supersaturation. The focus of this work is the, previously unreported, amorphous iron phosphate intermediate, which converted to vivianite with time via a solid-state transformation at SI ≤ 10.19. Since the recovery of the precursor proved to be a challenge, all analyses of the were based on solids harvested at SI 10.19 at 30 ± 10 s. To understand the factors driving the transformation of the amorphous precursor to vivianite, we probed the nature, chemical composition and structure of the poorly ordered precursor and crystalline end member vivianite.

3.3.3. Structural variations in symmetry and bonding environments at the Fe site

To accurately determine the Fe oxidation state, possible variations in Fe bonding environments and symmetry in both phases, synchrotron Fe-K edge XAS measurements (XANES and EXAFS) were performed on the solid samples. The Fe-K edge XANES spectra of synthetic vivianite (blue pattern, Figure 4) showed an energy edge position (E_o) of 7121.61 eV based on the position of the maxima in the first derivative plot (Figure A1F9, appendix I), correlating well to the reported literature value of 7121.50 eV for naturally occurring vivianite [71]. The XANES spectrum of the amorphous intermediate indicated an E_o value of 7121.29 eV, suggesting the presence of Fe^{2+} as the dominant oxidation state. Comparisons between the E_o values of vivianite, the poorly ordered intermediate (green and blue spectra, Figure 3.4), to reference spectra of synthetic $Fe^{2+/3+}$ compounds (black and red spectra, Figure 3.4), confirmed Fe^{2+} as the dominant oxidation state in both samples. By combining all the so far presented data (XRD, TEM, EDS, ICP-OES and XANES) we can state that the amorphous intermediate phase is a ferrous phosphate, herewith designated as AFEP (amorphous ferrous phosphate).

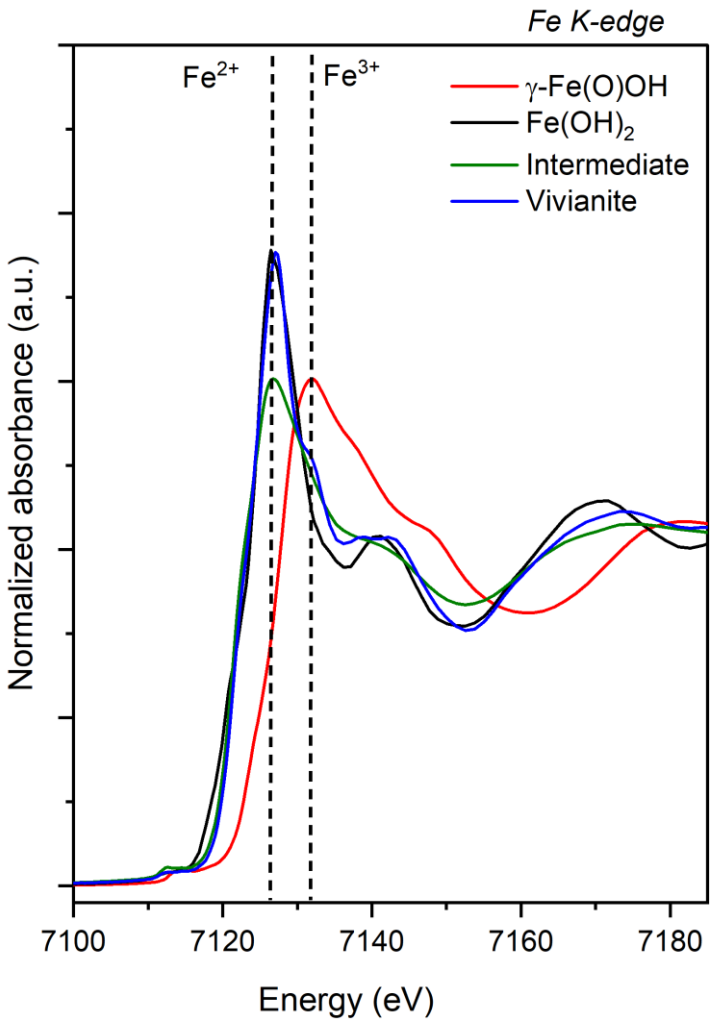

Figure 3.4. Normalized Fe-*K* edge XANES spectra collected for synthetic γ-Fe(O)OH (reference for Fe^{3+}), $Fe(OH)_2$ (reference for Fe^{2+}), amorphous intermediate and vivianite. Dashed lines represent energy edge positions for Fe^{2+} and Fe^{3+} oxidation states.

Furthermore, the pre-edge feature accounts for 1s → 3d (quadrupole) or 1s → 4p (dipole) electronic transitions in the Fe K-edge XANES spectra. The shape and position of the pre-edge depends strongly on the Fe oxidation state, spin, symmetry and coordination geometry [72, 73]. In the AFEP spectrum, the pre-edge feature was extracted by interpolating the background and modeling the contribution of the edge jump to the pre-edge using a spline function several eV before and after the pre-edge (Figure F10, appendix I). This method for pre-edge analysis has been used by Wilke *et al.* for studying oxidation states and coordination of iron bearing mineral phases [72]. We deconvoluted the pre-edges into Pseudo-Voigt components with equal Gaussian and Lorentzian (50:50) contributions and fitted the spectra for octahedrally coordinated Fe^{2+} compounds with three components based on theoretical predictions, symmetry considerations and 3d-4p orbital hybridizations [132, 133].

The position of the pre-edge 'centroid' or weighted average of the fitted peaks is centered at approximately 7113.00 eV for Fe^{2+} and at 7113.50 eV for Fe^{3+} mineral phases [72, 73]. A centrosymmetric and non-distorted Fe octahedra gives rise to three predicted features directly in the raw pre-edge data. This peak deconvolution revealed features at 7112.35, 7112.65 and 7114.45 eV (Figure 3.5). The weighted average or centroid of the deconvoluted peaks was extracted via integrated peak areas percentages and maxima of each component. The centroid was calculated to be at 7112.95 eV, which is positioned well within the range for Fe^{2+} oxidation state [73], reinforcing the edge-energy (E_o) XANES analysis. The pre-edge fitting of AFEP indicated a nearly non-distorted octahedral high spin (S = 2) Fe^{2+} center based on the fitting results. Predictable, marked differences were observed in the EXAFS spectra of vivianite and AFEP, with differences noticeable particularly in their FT-EXAFS spectra indicating a variable Fe coordination and composition (Figure F9, appendix I). To unravel the local structure of AFEP and study its coordination environment, shell-by-shell fittings for Fe-O and Fe-P paths were performed on the Fe K-edge data (Figure 3.6, Table A1T2, appendix I).

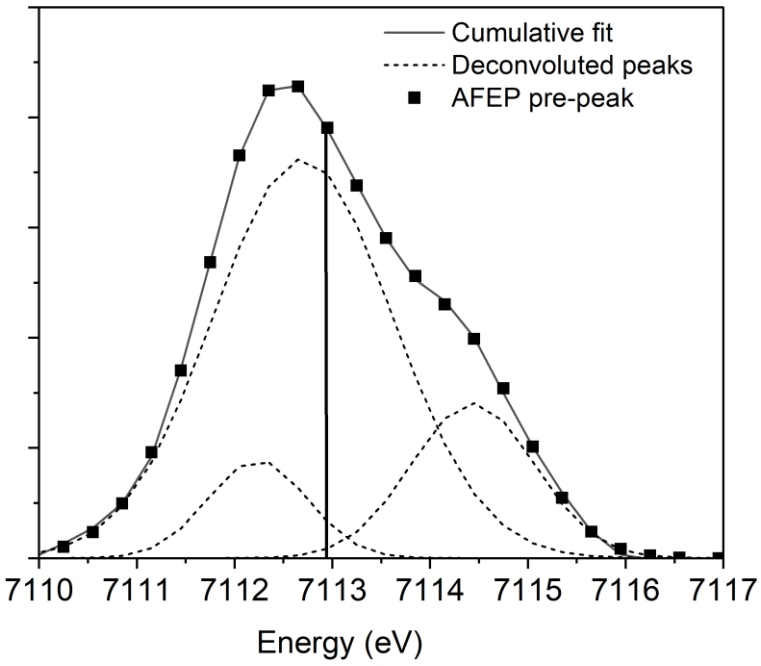

Figure 3.5. Deconvoluted pre-edge contributions for AFEP (amorphous ferrous phosphate) based on Pseudo-Voigt (50:50) function fitting. Vertical solid line represents centroid position.

Background subtracted, normalized and k^3-weighted EXAFS spectra and Fourier-transforms (FTs) of AFEP and the fits (Figure 6) revealed first neighbor contribution in AFEP being the Fe-O atomic correlation with an interatomic distance (R_{Fe-O}) of 2.10 ± 0.01 Å and a coordination number (CN) of ~

6. The second neighbor contribution was assigned to the Fe-P atomic correlation with an R_{Fe-P} of 3.34 ± 0.01 Å and CN_{Fe-P} of ~ 4.

This suggests an average local structure wherein four PO_4 tetrahedra and two H_2O molecules are octahedrally coordinated to the central Fe^{2+} atom. We used this data to model the local structure of AFEP based on the EXAFS fitting results (Figure 3.6). We can compare this with data from Mikutta *et al.* who modeled and fitted the first shell of EXAFS spectra of amorphous ferric phosphate and obtained an average Fe-O distance of 1.97 Å [134]. Unsurprisingly, the higher oxidation state of Fe in the ferric phosphate lead to a shortening of the Fe-O bond, and thus the shorter average bond distance as compared to 2.10 Å in our amorphous ferrous phosphate (AFEP).

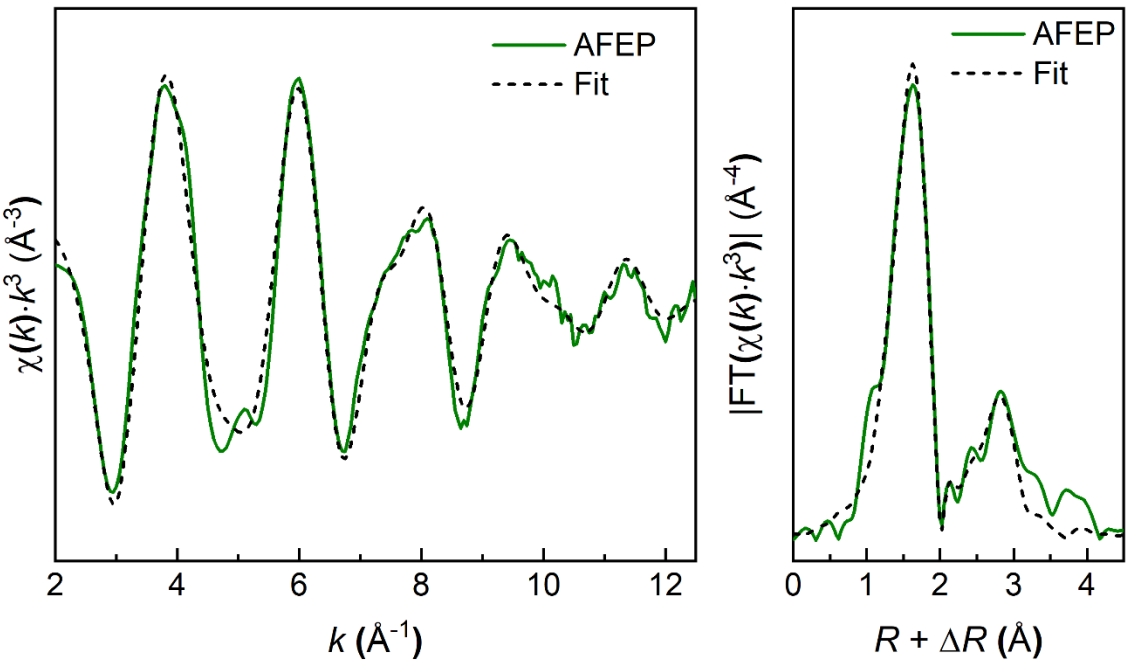

Figure 3.6. Fe K-edge normalized, background-subtracted, k^3-weighted EXAFS spectra and Fourier Transforms (FTs) of AFEP sample. Solid lines = experimental spectra; dashed lines = fitted spectra

We cross-confirmed the local ordering of both phases through reduced PDF (G(r)) analysis of AFEP and vivianite and determined the atomic structural correlations (Figure 3.8). The G(r) peaks (Figure 3.8) for average Fe-O distance (vivianite ~ 2.21 Å, and AFEP ~ 2.08 Å), and for Fe-P bonds.

Contrastingly, the published crystal structure of vivianite [66] consists of two different octahedrally coordinated Fe^{2+} environments within its lattice, designated as Fe^{2+}(A) and Fe^{2+}(B). The coordination at the Fe^{2+}(A) site shows tetragonal distortion and near-D_{4h} symmetry with four equatorial water ligands at Fe-O distances of 2.213 Å and two axial phosphates at Fe-O distances of 2.030 Å [47]. The

tetragonal compression at this site is evident from the large variation in axial and equatorial Fe-O bond distances [135]. The near-C_{2v} [51] symmetry of the Fe^{2+}(B) site indicates Fe-O distances of 2.157 Å and 2.147 Å for bridging and terminal oxygens of the water ligands and 2.101 Å for phosphate oxygens [47].

The PDF analyses indicated the bond distances Fe-O_{PO4} vivianite, ~ 3.33 Å, and AFEP ~ 3.34 Å. Fe-O_{PO4} distances (vivianite at ~ 4.08 Å and AFEP at 4.06 Å) were also discernible for both phases. However, Fe-Fe distances (vivianite at r ~ 4.64, 5.22 and 6.15 Å) [136] were quite weak or nearly absent for AFEP. The G(r) decays rapidly with increasing *r* for AFEP due to lack of long-range ordering, indicating the lack of coherence due to its amorphous nature. Contrastingly, the G(r) of vivianite shows coherent scattering domains to high distances, reflecting its crystalline nature. The results agree to XRD (Figure 3.1) and TEM-SAED (Figure 3.2) results described previously.

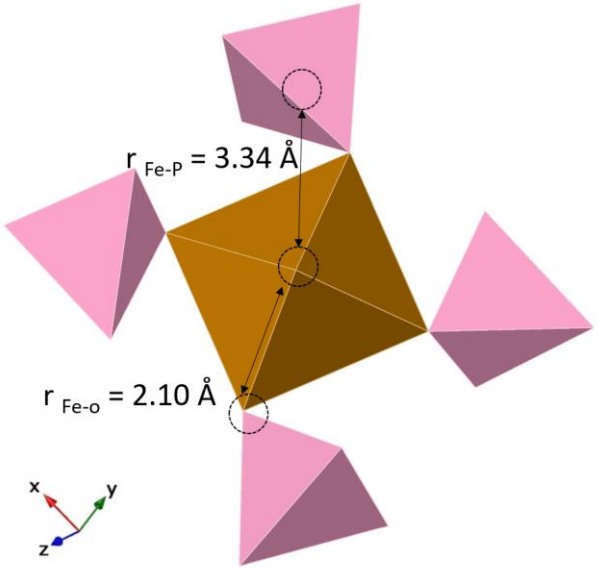

Figure 3.7. Average local structure of AFEP with four PO_4 tetrahedra bonded to an FeO_6 octahedra; bond distances modeled via EXAFS first and second shell-fits. Bond distances are shown in Angstrom (Å) units.

The Fe-O bond length variations in vivianite arise due to symmetric effects and variations in orbital hybridizations [133]. These variations are pronounced in the vivianite pattern (Figure 3.7) but almost negligible in the AFEP pattern, most likely due to variations in 4p-3d orbital hybridization of the Fe^{2+} ion. The shorter average Fe-O distances in AFEP was confirmed by both the PDF and EXAFS fitting data indicating changes in Fe-O structural geometry that occurred during the transformation.

To further contrast the changes in Fe^{2+} 3d electronic transitions, local symmetry and visible color in the two phases, optical (solid UV-vis to near IR) absorbance spectra of the AFEP was compared to the literature reference spectrum for naturally occurring vivianite [133]. Compared to transmission

measurements of large (often thin, uniform and millimeter sized) natural vivianites, our synthetic vivianite samples, which were micrometer-sized platy florets (Figure A1F13, appendix I) yielded a much weaker signal-to-noise ratio due to non-uniform path length and partial scattering. Hence, literature spectrum for vivianite was used for comparison.

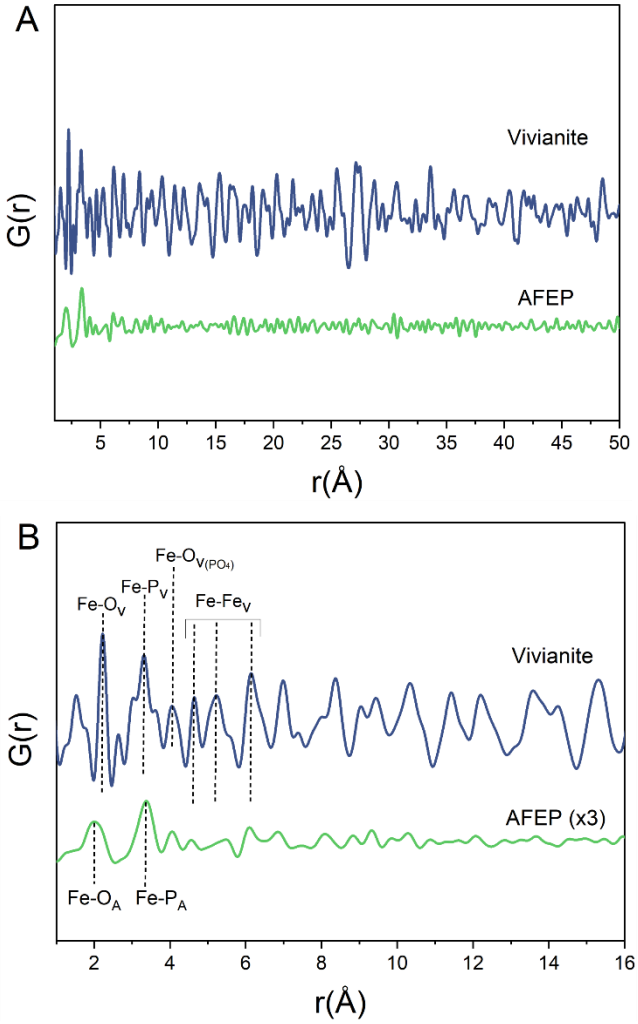

Figure 3.8. (A) G(r) for vivianite and AFEP. The G(r) decays rapidly with increasing r-values for AFEP, reflecting smaller coherently scattering domains than vivianite. (B) Zoom of lower r-values. Peak intensities for AFEP have been tripled (x3) so that small peaks are discernable. Subscripts: A for AFEP and V for vivianite.

Nevertheless, electronically, Fe^{2+} in perfectly octahedral high spin arrangement (S = 2) has the five *3d* orbitals split into three lower lying t_{2g} – like orbitals ($d_{x^2-y^2}$, d_{xz} and d_{yz}) and two upper lying e_g-like orbitals (d_{z^2} and d_{xy}) [135]. The splitting energy between the two e_g levels is directly proportional to the tetragonal distortion in the FeO_6 octahedron, with a large gap between the two-upper lying e_g orbitals translating to a highly distorted FeO_6 octahedron. In the measured range, the spin-allowed

Fe^{2+} *d-d* optical transition bands are observed for vivianite at 8200, 11655 and at 12220 cm^{-1} (Figure 3.9) [51, 133, 135]. These are attributed to electronic transitions from the lower lying $d_{x^2-y^2}$ to the upper lying e_g orbitals [135]. These multiple bands arise due to octahedrally distorted and structurally non-equivalent Fe^{2+} sites within its lattice [51, 135]. The optical bands at 11655 and 8200 cm^{-1} arise due to electronic transitions at Fe^{2+}(B) site, showing slight tetragonal distortion with calculated Fe-O distance variations of ± 0.04 Å from ideal octahedral geometry [135]. On the contrary, the largely tetragonally distorted Fe^{2+}(A) site shows a greater variation of Fe-O distances, reflecting a greater splitting of the two e_g- like orbitals.

This appears as a strong band at 12220 cm^{-1} and a theoretically calculated band at ~ 4000 cm^{-1} [51, 133, 135]. In contrast, the experimental optical spectrum of AFEP is characterized by a single band corresponding to spin-allowed Fe^{2+} *d-d* electronic transition at 10255 cm^{-1} (Figure 3.9). This single band arises due to electronic excitations from lower lying $d_{x^2-y^2}$ to the two-upper lying degenerate e_g orbitals, indicating a perfectly symmetrical octahedral crystal field. This, confirms the presence of a less distorted FeO_6 octahedra within the AFEP structure, agreeing with the pre-edge XANES fitting results (Figure 3.5, Figure A1F10 – appendix I).

Since samples were extremely sensitive to Fe oxidation, partial oxidation of the samples was inevitable as the optical measurements were performed outside the anaerobic chamber. Visually, the pristine samples were observed to be pale blue (vivianite) and pale green (AFEP). However, upon aerial exposure, the color of the precipitates darkened due to an increase in the intensity of intra-valence charge transfer (IVCT) bands attributed to Fe^{2+} to Fe^{3+} electronic transfer, at ~ 15000 cm^{-1} in the natural vivianite [51] and ~ 14000 cm^{-1} in the AFEP pattern (this study). This change reflects and confirms the color perception in the blue and green visible regions respectively (600 – 700 nm absorbance).

The XANES, EXAFS, PDF and optical results together imply that AFEP undergoes significant changes in its local Fe bonding, structure and symmetry during its transformation to vivianite.

3.3.4. A crystallization driven by hydration

To evaluate the differences in group symmetry and bonding environment of the water and phosphate groups within the two phases, FTIR measurements were performed (Figure 3.10). The phosphate P-O stretching vibrations ν_1 (symmetric stretching) and ν_3 (asymmetric stretching) occur between 1100 – 930 cm^{-1} for the two phases (Figure 3.10). Our vivianite was characterized by three P-O stretching vibrations at 1034, 964 and 933 cm^{-1}, contrary to AFEP which showed a medium broad peak centered at 976 cm^{-1}. The ν_3 P-O stretching vibrations in AFEP appear merged, and therefore difficult to be

resolved from one another, producing a single broad peak centered at 976 cm^{-1}. In crystalline vivianite, the ν_3 P-O stretching vibrations are split into three components, which can be explained by lattice constraints [137], variable Fe (Fe in two distinct chemical environments) [48] and subsequently phosphate environments in its crystal structure.

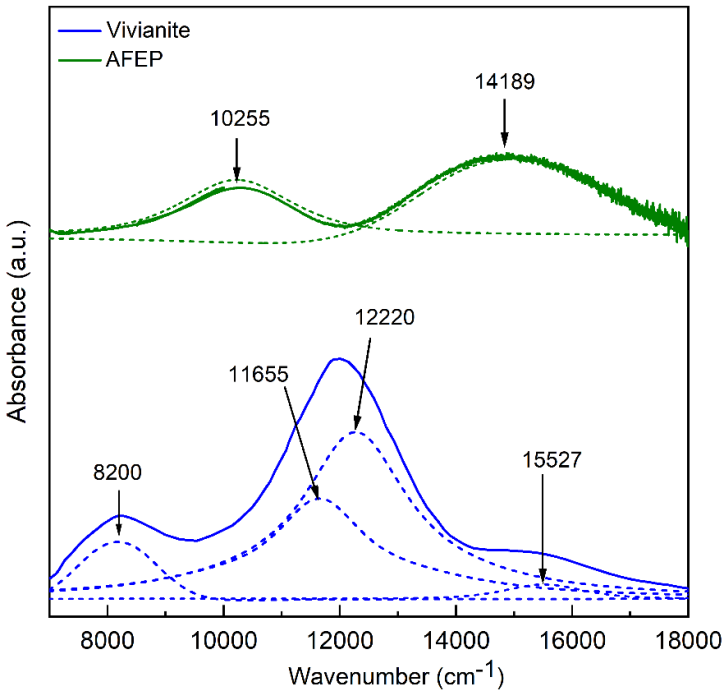

Figure 3.9. Optical spectra of AFEP and vivianite reference [60] (solid lines) and deconvoluted Pseudo-Voigt component (dotted lines). Arrows mark the optical absorption bands. Noise in AFEP spectrum at higher wavenumbers is an instrumental artefact.

Visually discernible decrease in the splitting of the ν_3 P-O stretching vibrations have been previously reported for other amorphous metal (Zn, Ca, Pb-NO_3) phosphate systems [31, 138-140]. Notably, in the case of lead nitrate phosphate crystals, the increase in ν_3 splitting in the crystalline phase has been attributed to higher distortions of the PO_4^{3-} ions compared to the isolated PO_4^{3-} ion, due to factor group splitting [140].

Therefore, changes in splitting features of the P-O stretching vibrations may indicate a decrease in average tetrahedral distortion [137, 140] in the AFEP, compared to crystalline vivianite, due to a lack of long-range structural arrangement of PO_4^{3-} units and absence of lattice constraints. The out-of-plane bending mode of the phosphate is visible as a distinct sharp peak at 534 cm^{-1} for vivianite. Furthermore, the O-H stretching vibration appears as a single broad peak centered at ~ 3260 cm^{-1} in the AFEP spectrum but it is split into two sharp peaks in vivianite at 3477 and 3110 cm^{-1} reflecting the

different water bonding environments in the vivianite crystalline lattice [48, 69]. Similar effects in O-H stretching vibrational bands have also been reported for amorphous and crystalline Zn-phosphates [31]. Another notable feature observed in the vivianite IR spectrum is the sharp peak at 810 cm^{-1}. This has been reported as a "librational water" stretching mode by Frost *et al.* [141], which arises due to hydrogen-bonded water molecules within the its structure [142]. The librational water bands in IR spectra of crystalline metal hydrates are affected by H_2O molecular deformation via H-bonding interactions [143-145]. Aquo-complexes of transition metal hydrates exhibit IR active water librational modes [144]. The librational IR water band appears distinctly at 810 cm^{-1} in the vivianite spectrum, however it is not distinguishable for AFEP (Figure 3.10). The reason may be because it is weak or is overshadowed by the broad P-O stretching peak at 976 cm^{-1}. Previous studies have reported that changes in strength of H-bonding within a crystal lattice causes changes in the intensity and frequency of the librational water bands in their IR spectra [144]. Therefore, the different intensity of this band in AFEP and vivianite, may imply differences in H-bonding network in the two phases. This may explain the changes in the surrounding local bonding environments which is corroborated by lack of long-range ordering as documented previously by its XRD (Figure 3.1), G(r) (Figure 3.8) and SAED (Figure 3.2-C) data. Overall, all the IR data, implies the establishment of a well-defined H-bonding network could accompany this transformation.

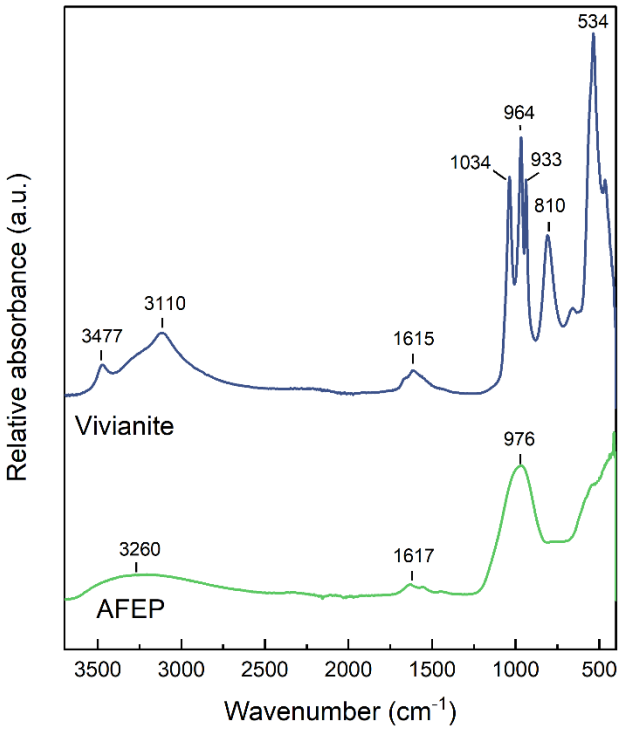

Figure 3.10. FTIR spectra of AFEP and vivianite with respective characteristic vibrational frequencies marked.

The variation in the water contents in our two phases, were quantified from the TGA data (Figures A1F11 and A1F12, appendix I). Calculations based on net percentage mass loss between 25 and 500℃ for repeat experiments yielded an approximate average composition of $Fe_3(PO_4)_2 \cdot 4.75\ H_2O$ for AFEP. The corresponding TGA data for vivianite (Figure A1F12, appendix I) showed a mass loss of 28.50 %, yielding a stoichiometric composition of $Fe_3(PO_4)_2 \cdot 7.98\ H_2O$. The vivianite water molar ratios matching well the expected stoichiometric composition i.e., $Fe_3(PO_4)_2 \cdot 8\ H_2O$. To minimize the contributions from surface-bound water removal, both the AFEP and crystalline vivianite were dried under vacuum for 6 to 24 h, prior to thermal analysis. The samples showed major water loss from 50 – 110˚C (Figures A1F11 and A1F12, appendix I). The TGA-DSC studies of amorphous calcium carbonate (ACC) [146, 147] have shown that ACC dehydrates in a series of steps, with significant water loss below 115℃ have been attributed to removal of weakly-bound or fluid-like mobile as well as restricted H_2O components from its structure.

Therefore, the calculated total water composition of AFEP may include stepwise contributions from both, rigidly-bound structural and weakly-bound H_2O molecules from AFEP. This data clearly revealed that AFEP has a lower total water content than vivianite, demonstrating that AFEP undergoes a net hydration during its crystallization to vivianite.

This was also supported by the beam-induced damage in the two phases when analyzed by TEM (Figure A1F14, appendix I). During exposure of the vivianite platelets to the focused TEM beam, it was more easily beam damaged, than the aggregated AFEP nanoparticles. Such differences, in reaction to the same beam conditions, in materials containing different water contents has been documented before. For example, when observing quartz of similar composition and variable water contents [148], the presence of higher amount of water lead to greater beam damages through permanent atomic displacement. Hence, our FTIR and TGA data confirmed the pivotal role of water in the crystallization of vivianite from AFEP. We could document that only structural rearrangement and incorporation of water molecules within the AFEP structure enables its crystallization to vivianite. This conclusion is also supported by the presented shorter average Fe-O distance (Figure 3.6, 3.7, 3.8; Table A1T2, appendix I) in the AFEP, as compared to vivianite. Overall, Fe-O(H_2O) bonds are slightly elongated as compared to Fe-O(PO_4) bonds owing to Fe → oxygen → phosphorus π back bonding interactions [149]. Therefore, a shorter average Fe-O bond length in AFEP, is expected due to its lower water content and its higher phosphate mass percentage than vivianite, based on calculated mass percentages from TGA data.

Our results show that an overall hydration of the AFEP nanoparticles occurs upon their transformation to vivianite. To experimentally verify this dried AFEP powder was suspended in anoxic ultrapure water in a sealed vial and equilibrated inside the anaerobic chamber for up to 5 d. Analysis of the solids after 24 h indicated no changes. However, after 5 d, FTIR analyses of the solids revealed presence of crystalline vivianite (Figure A1F15, appendix I) based on the strong characteristic phosphate $\nu_{P\text{-}O}$ (1034, 964 and 933 cm^{-1}), $\nu_{O\text{-}H}$ (3477 and 3110 cm^{-1}), $\delta_{H\text{-}O\text{-}H}$ (1615 cm^{-1}) and H_2O libration (810 cm^{-1}) peaks. Since the solubility of AFEP is not known, we cannot ascertain its saturation index in this system. A slower rate of its transformation in pure deionized water (> 24 h) may be due to supersaturation changes. SEM micrographs of the solids recovered after 5 d (Figures 3.11-A and A1F15, appendix I) revealed large irregular-shaped vivianite crystals with AFEP nanoparticles attached on their surface. In nearly all regions, the formed vivianite showed a surface texture of spherical nanoparticles resembling the starting AFEP uniformly distributed on its surface as shown in Figure 3.11-A and Figure A1F15 (appendix I).

The texture of spherical nanoparticles could be distinguished from the loosely attached aggregated AFEP particles, based on size, shape and distribution. Although the morphology solely cannot be a conclusive proof of the formation mechanism, such nanoparticulate surface textures resembling the dimensions of initial the amorphous intermediates (ACC) are evidences for solid-state transformations in Ca-CO_3 systems [30, 150-152], wherein crystalline phases exhibit irregular surface textures bearing resemblances to their former nanoparticulate precursors.

These differ from the smooth faceted vivianite crystals obtained at a high supersaturation (Figure 3.11-B) which may have formed via ionic attachment [152], that did not show such a texture within instrumental detection limits, suggesting concurrent pathways of growth and transformation. Several previous studies reporting the transformation of an amorphous precursor to a crystalline phase in sparingly soluble salt systems most often evidenced a dehydration-induced crystallization pathway. For example, in the Ca-CO_3 system the pathway from the hydrated metastable amorphous calcium carbonate (ACC) to thermodynamically more stable crystalline polymorphs such as anhydrous calcite or aragonite proceeds via loss of water [16, 17, 89, 110, 153, 154]. This dehydration step is energetically favorable and exothermic, irreversibly driving the crystallization process [89]. Similarly, hydrous, amorphous calcium phosphate (ACP) nanoparticles undergo dehydration prior to apatite crystallization [155, 156, 157].

On the other hand, in the calcium sulfate system, structural rearrangement, hydration and particle aggregation of sub 3-nm primary anhydrous but nanocrystalline species is the driving force for gypsum ($CaSO_4.2H_2O$) crystallization [23].

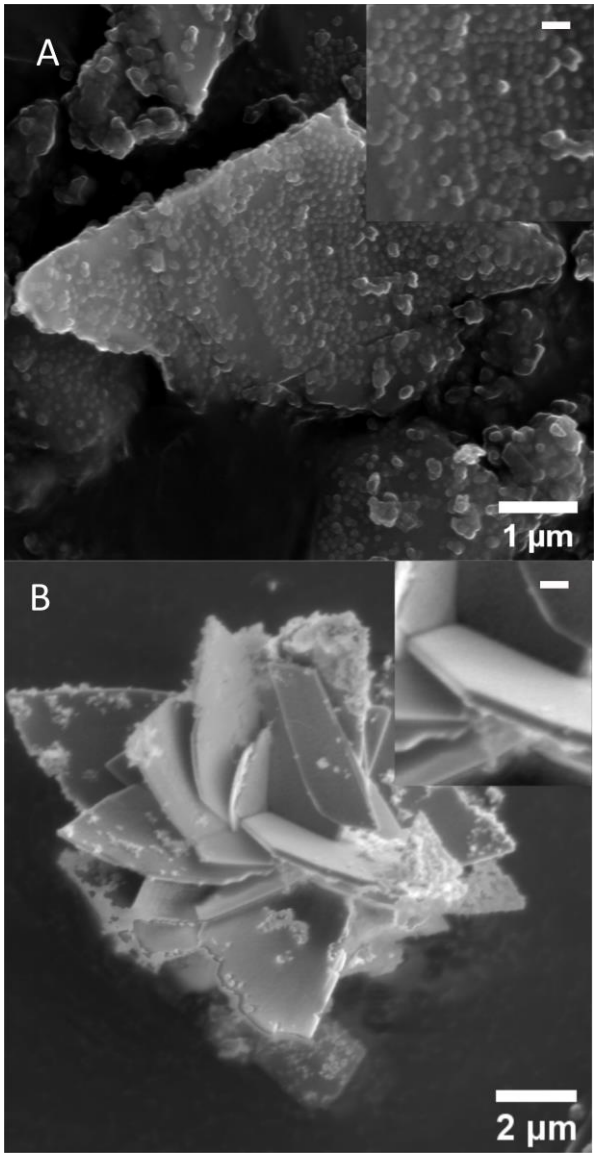

Figure 3.11. SEM micrographs, (A) showing the spherical nanoparticulate texture on the surface of AFEP transformed to vivianite in water after 5 d. (B) Vivianite crystal radial florets showing feature-less and smooth surface texture at 1 h (SI 10.19); *Insets* show zooms of the textures with white scale bar of 100 nm.

We clearly document that in the ferrous phosphate system, hydration of the nanoparticulate amorphous precursor phase is the driving force for the crystallization. The incorporation of structural water and rearrangement of parent ions (Fe^{2+} and PO_4^{3-}) favors the transition from dissolved ions to amorphous intermediate to the stable polymorph vivianite. We hence documented that in the ferrous phosphate system on enrichment of water, and not dehydration, leads to the transformation of amorphous intermediates to hydrated crystalline polymorphs. Overall, all the results presented indicate a lower distortion from ideal octahedral and tetrahedral geometries in the local structure of

AFEP, as compared to vivianite. Typically, deviations from regular octahedral geometries, as suggested in case of vivianite, have kinetic costs due to higher molecular strain (Jahn-Teller distortion) [158]. This factor may kinetically favor the initial formation and stabilization of the less distorted AFEP precursor phase.

3.4. Conclusions

We have shown that hydrated ferrous phosphate (vivianite) crystallizes via a transient nanoparticulate amorphous ferrous phosphate precursor – AFEP, that precipitates from a solution supersaturated with respect to vivianite. No solubility data for this precursor exists yet, but we have determined its local structure and average composition: $Fe_3(PO_4)_2 \cdot 4.75\ H_2O$ and showed that this intermediate is less enriched in water than crystalline vivianite. The water associated with the AFEP nanoparticles structurally rearranges, leading to formation of a defined H-bonding network, playing a pivotal role in the AFEP transformation to vivianite. Both our *ex* and *in situ* analyses cross-correlated and confirmed that vivianite forms via a predominantly solid-state hydration-driven reaction via AFEP, as opposed to dehydration-driven crystallization, at moderately high to low vivianite supersaturations (SI ≤ 10.19).

We suggest that multiple vivianite formation pathways could be present concurrently in a system, as reported for crystallization mechanisms of calcium carbonates [17] and phosphates [113]. The dominant pathway depends on the systemic vivianite supersaturation. The overall rate of ferrous phosphate nucleation is enhanced and the induction period decreases with increasing Fe^{2+} and PO_4^{3-} concentrations. A solid-state transformation via the AFEP is favored at lower supersaturations (SI ≤ 10.19). At very high supersaturations (SI ≥ 12.86), the growth of vivianite occurs directly from solution via ionic attachment.

We showed that the lifetime of the AFEP increases at lower vivianite supersaturation and it remains stable once dried and kept anoxically. AFEP also has lower average distortions of its Fe-O octahedra and P-O tetrahedra, as compared to vivianite. This may be linked to its lack of a defined H-bonding network of water molecules and absence of lattice constrains. These factors may be steering this process via the more locally symmetric and kinetically accessible AFEP phase, via the non-classical route. Synthesis and stabilization of nanoparticulate (high surface area) material such as AFEP, may have several potential applications as a cathode material ($LiFePO_4$ batteries [118]) or slow release fertilizer [159]. Furthermore, the ferrous-phosphate system may serve as a model to investigate and draw conclusions for a wider range of hydrated phases with divalent metal ions (having similar hydration enthalpy and ionic radii to Fe^{2+}) and phosphates. These insights elucidate nucleation and growth

mechanisms of hydrated crystal phases and these may be applied to synthesize materials with distinctly different structural and chemical properties, compared to their crystalline counterparts.

Chapter 4. Kinetics of Vivianite Nucleation and Growth

ABSTRACT. The kinetics and non-classical nucleation and growth of vivianite ($Fe_3(PO_4)_2 \cdot 8H_2O$) from aqueous ions were studied experimentally using *in situ* small- and wide-angle X-ray scattering (SAXS-WAXS) at a range of environmentally relevant temperatures (10 - 60˚C). Our results reveal a two-stage process: in stage I we document the nucleation of spherical, amorphous ferrous phosphate (AFEP) nanoparticles, which rapidly grow in size and volume in the reacting solution. The AFEP growth rate and their total volume fraction were both directly proportional to temperature. In stage II, these spherical AFEP nanoparticles rapidly transform to a crystalline phase, that was identified based on the tie dependent growth of Bragg peaks of vivianite. The rate of vivianite growth was kinetically enhanced at higher temperature. We fitted the formation kinetics of vivianite using the Johnson – Mehl – Avrami − Kolmogorov model and evaluated a temperature dependent Avrami constant between 0.87 – 1.45, indicating a one-dimensional growth mechanism, and this yielded an associated activation energy of $E_a = 51 \pm 13$ kJ/mol. Concomitantly, we could document a temperature dependent change in the morphology of the formed vivianite crystals. Elevated temperature (40, 60˚C) favored a rosette-type crystal morphology over the sheaf-like structures seen at lower temperatures (21, 10˚C). We interpret this change as being a consequence of an increase in crystal splitting during the AFEP to vivianite transformation via the development of a more disordered H-bonding network at higher temperatures. Our results provide fundamental new insights into the fast and nonclassical nucleation, transformation and growth processes of hydrated mineral phases such as vivianite.

4.1. Introduction

Ferrous phosphate phases such as vivianite ($Fe_3(PO_4)_2 \cdot 8H_2O$) are widely distributed in natural [4-6] (e.g., freshwater/marine sediments, soils) and engineered environments [11, 13, 160] (e.g., waste water sludges, sewage, ground water treatment plants). Vivianite has several potential uses, because as a phosphate (P), it is part of a nutrient recovery chain for example from wastewaters and sewage sludges that are treated in order to reduce eutrophication of water bodies [11, 40-42, 59, 116]. The recovered vivianite can potentially be subsequently used as a slow-release phosphorus fertilizer [11, 41, 161]. Vivianite also acts as an important iron (Fe) and P sink in modern and ancient anoxic, ferruginous environments [6, 7] where its formation plays an important role in Fe-P cycling [5, 10]. Finally, vivianite is also an important economic starting material for $LiFePO_4$ material, that are used in battery cathode applications [162]. All these factors make vivianite an important phase from both an environmental and an economic perspective,

yet in the worlds literature there are several knowledge gaps about the mechanism and kinetics of vivianite formation from aqueous ions.

Our recent study has shown that vivianite nucleation occurs via a nonclassical pathway through a transient amorphous ferrous phosphate phase (AFEP) [163]. The AFEP has a different local structure, hydration ($Fe_3(PO_4)_2 \cdot 4.7H_2O$) and molecular symmetry compared to vivianite, and it transforms to vivianite in solution by undergoing a hydration and change in its local structure [163]. So far there only exist snapshots of this process (*ex situ* characterization) and the kinetics of this process remain unknown. It is difficult to follow fast crystallization reactions using *in situ* laboratory methods, therefore synchrotron X-ray scattering methods offer a good tool for a reliable signal-to-noise ratio for following such fast reactions in solution. *In situ* and time resolved synchrotron-based small- and wide-angle X-ray scattering (SAXS-WAXS) approaches have, in the last few decades, provided effective means for studying fast and complex multi-step nucleation and growth processes of sparingly soluble salts from solution [15, 16]. These span from carbonates [15, 16], to sulphates [37], to iron oxides [164] , to phosphates [21, 165] and iron sulfides [166].

Many of these studies have documented that the nucleation and growth of the stable end produce phase often proceeds via non-classical pathways. Similar to many such systems, the formation of vivianite has only recently also been shown to also proceed via a non-classical pathway that includes a transient amorphous ferrous phosphate (AFEP) phase, which nucleates from a solution supersaturated to vivianite [163]. Although it has been shown that the reaction proceeds via a complex multi stage transformation pathway [163], the kinetics and energetics of the nucleation, and growth of vivianite are so far lacking. To fill this gap, in this current study we describe a detailed experimental *in situ* X-ray scattering study where we followed the nucleation, growth and crystallization of vivianite at fast time scales and at different temperatures. We used the Johnson−Mehl−Avrami−Kolmogorov (JMAK) approach to model the reaction kinetics and the Arrhenius relation, to derive the temperature dependent rate constants and activation energy (E_a) for vivianite crystallization.

Our data may contribute to a better understanding of vivianite mineralization pathways, specifically at high supersaturation, which is particularly relevant to for example engineered systems of phosphorus recovery.

4.2. Experimental Methods

4.2.1. In situ SAXS and WAXS experimental design

The nucleation and growth of vivianite was investigated by time resolved and *in situ* SAXS and WAXS measurements on beamline I22 of the Diamond Light Source Ltd. (UK) using a monochromatic X-ray beam of 12.4 keV and with 2D scattered intensities recorded with two Dectris Pilatus 2M detectors. The sample to detector distance of 3.477 m allowed a (SAXS) usable *q*-range of 0.05 to 5 nm^{-1}. The SAXS detector was calibrated against Ag-behenate and dry collagen standards. The WAXS detector was calibrated against crystalline silicon (NIST SM 640C), synthetic vivianite and amorphous ferrous phosphate (AFEP) [163]. The reactions were performed inside a 500 ml temperature-stabilized, jacketed and air-tight glass reactor kept under constant Ar gas flow to maintain anaerobicity. The reactor temperature was stabilized via a circulating ethylene glycol/water bath (LAUDA-Brinkmann LP). The solutions were stirred at 400 rpm and circulated via a peristaltic pump (Gilson MiniPuls 3, flow ~ 100 ml per min) through a custom-built PEEK flow-through cell containing a glass capillary (diameter 0.9 mm, wall thickness ~ 0.1 mm) that was aligned perpendicular to the incoming beam. The experimental scheme is shown in the Appendix II figure A2S1. During measurement the sample was oscillated periodically along +/- *X-axis* to reduce beam-induced decomposition artifacts at any given point.

4.2.2. Solution preparation and experimental run

Mohr's salt (Sigma Aldrich, 99%) and sodium phosphate (Acros, 99%) stock solutions were prepared inside a water-tolerant glove box equilibrated with a high-purity nitrogen gas (99.9999 %, BIP®) atmosphere and using MilliQ water (18.6 MΩ). The concentrations of the starting solutions were calculated based on vivianite's saturation index (SI) in the mixed system The geochemical calculations of vivianite SI (Supporting information section S1) were performed on PHREEQC, Version 3 [119] using the Thermoddem database [120]. Two gas-tight glass syringes (Hamilton Company Ltd.) were used to transfer the two reacting solutions from the glovebox to the beamline, where 150 ml of the sodium phosphate solution (0.06 M) was transferred into the temperature stabilized glass reactor under Ar gas flow. This solution was equilibrated at a desired temperature using a circulating ethylene glycol/water bath (LAUDA-Brinkmann LP). The content of the second syringe containing a Mohr's salt solution (0.3 M) was transferred through a N_2-gas purged 3-way valve into a temperature stabilized stopped-flow injection system (Bio-Logic SFM-400). The final mixture consisted of an equimolar concentration of [Fe] = [P] = 50 mM, contrary to our previous study where [Fe] = [P] = 5 mM, a higher

concentration was used here to obtain a good signal-to-noise ratio. The saturation index of vivianite was calculated to be SI 12 – 13 in the system at different temperatures.

The vivianite crystallization reactions were remotely started by measuring SAXS/WAXS patterns of the initial phosphate solution in the reactor, while it was circulated through the capillary. Subsequently, 30 ml of the temperature stabilized Mohr's salt solution was injected into the reactor containing the phosphate solution by means of the fast-injection mode of the stopped-flow system (Bio-Logic SFM-400) to achieve a final concentration / supersaturation of 12-14, SAXS/WAXS patterns were continuously recorded at a rate of 3 sec/per frame for up to 60 minutes. The measurements were carried out at temperatures of 10, 21, 40 and 60˚C using the circulating water bath.

4.2.3. Data Analysis

The time-resolved SAXS data correction and processing was performed using the Data Analysis Workbench (DAWN) software package [167] and following I22 guidelines. Data correction included background subtraction using and capillary filled with MilliQ water. The SAXS data was fitted using McSAS [168] to derive particle size distributions as a function of time. The time resolved WAXS peaks were fitted to Pseudo-Voigt profiles using the Fityk software [127]. The final data fitting and plotting were performed using the Origin Pro software 2021 (OriginLab Corporation, Northampton, MA, USA).

4.2.4. Scanning electron microscopy (SEM)

SEM micrographs were acquired by filter quenching 0.5 ml aliquots from the reaction mixtures (section 4.1.2) at specified time points. The dried materials were prepared for SEM imaging and analyses by depositing the dry solid sample onto a carbon pad which was glued to an SEM aluminum stub. The samples were carbon coated (~ 20 - nm layer) using a Leica EM ACE600 high-vacuum sputter coater and SEM analysis was done on a FEI Quanta 3D FEG at a voltage of 20 kV and 22.6 nA current. The image analysis was performed on *Image J* software [169].

4.3. Results and Discussion

The results confirmed the geochemical calculations that with increasing temperature the solubility of vivianite increases. The scattering data confirmed that the crystallization reactions were faster and lasted ~ 300 seconds at 10˚C and ~ 50 seconds at 60˚C. Our previous work has shown that the vivianite forms via a transient amorphous ferrous phosphate (AFEP) phase [163] that precipitates instantaneously and converts to crystalline vivianite in solution with time. In both the SAXS and WAXS data and at all temperatures these reaction stages could be distinguished.

In the SAXS data an initial fast increase and subsequent decrease in scattering intensity at low angles ($q < 0.01$ nm^{-1}), showed the formation of a nanoparticulate material that aggregated with time (Figure 4.1 and 4.2). Conversely, in the WAXS patterns (Figure 4.3), initially no peaks were observed but concomitant with the SAXS pattern intensity decrease, the growth of vivianite Bragg peaks became evident. At higher temperatures, the crystallization reactions and transformation were kinetically faster.

4.3.1. In situ SAXS size modeling of nucleation of amorphous ferrous phosphate (AFEP) nanoparticles

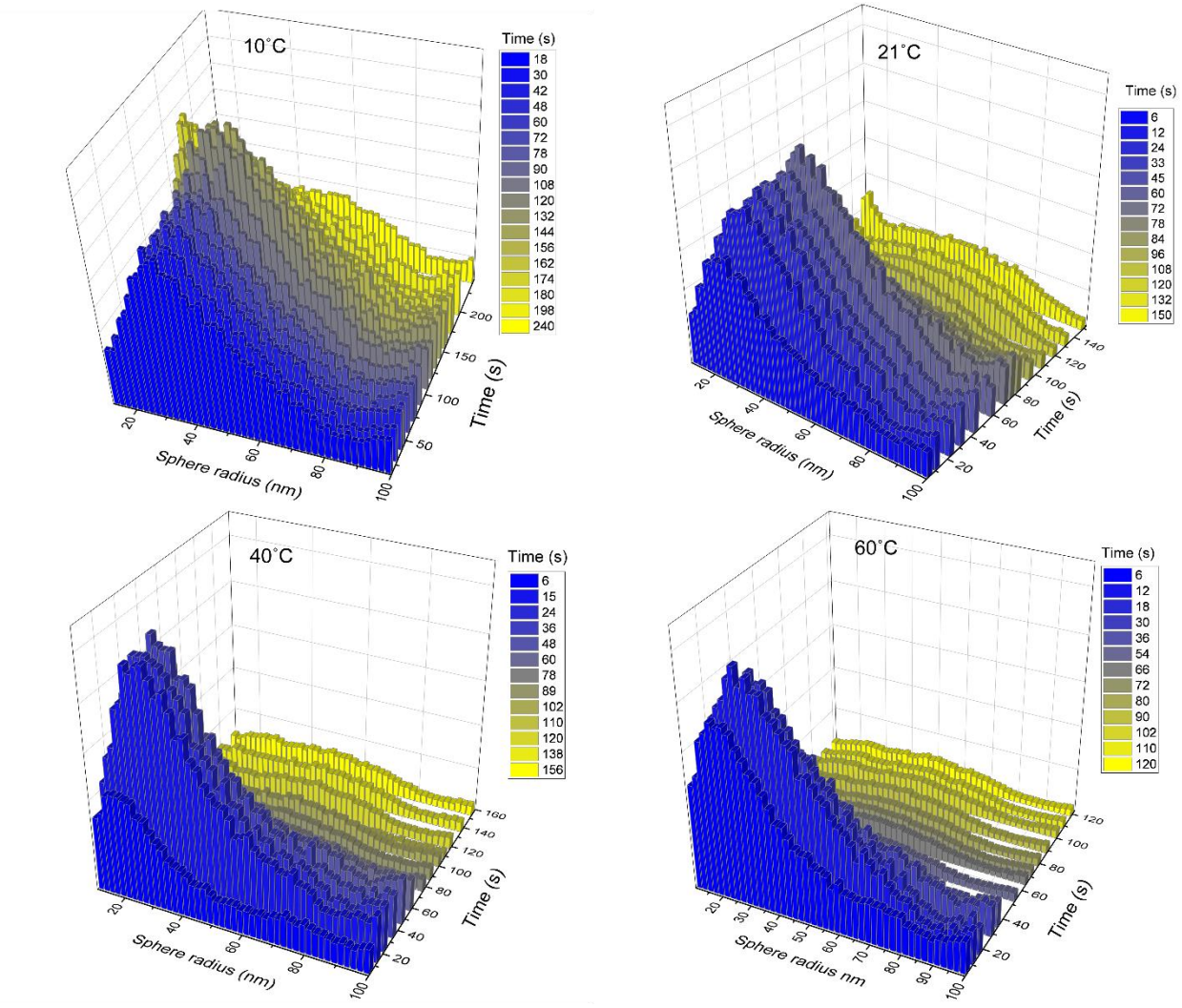

Figure 4.1. Volume weighed size distribution histograms associated with the *in situ* SAXS patterns acquired at different temperatures, during the vivianite precipitation experiments. The fitting was based on a spherical approximation model for the initial intermediate AFEP nanoparticles.

In situ SAXS patterns from the vivianite precipitation experiments revealed time-dependent changes such as an increase followed by a decrease in the relative intensity at values of q < 0.01 nm^{-1}, as a function of time (Figure A2S2 supporting information). Our previous work has shown that the nucleation of hydrated ferrous phosphate (vivianite) occurs via a transient amorphous ferrous phosphate (AFEP) phase [163] that ultimately converts to crystalline vivianite in solution with time. We have documented that the AFEP nanoparticles have a spherical morphology [163], and thus the *in situ* SAXS patterns could be fitted within the spherical model approximation [168] to derive the size distributions of the formed particles as a function of time and temperature (Figure 4.1). The distribution of particle volumes as a function of time and temperature is shown in this figure as a differential volume density distribution as a function of a sphere radius. The measured distribution can be described by a histogram of particles per unit volume with defined size bins, in this case, the size range of 0 – 100 nm (50 bins), which are shown as points in Figure 4.1.

The SAXS patterns fitted reasonably well within this approximation. This distribution of the particle volume is represented by a volume density distribution *v(r)* defined as

$$v(r) = \frac{dV}{dr}$$

Eq. 4.1

Where *r* is the particle radius, the total particle volume (V_t) in the system within range *0 – R* at time *t* is given by the following integral

$$V_t = \int_0^R v(r)dr.$$

Eq. 4.2

The latter can be approximated as the area under the volume size distribution histograms at a given time *t*, which reflects the total volume of the nanoparticles precipitated as a function of time. Noticeable is the fact that at higher temperatures of 40 and 60˚C, the size of the nanoparticles nearly doubled in initial radii within 12-15 s of the reaction (~ 20 → 37 nm), and within the first 120 s for lower temperatures of 10˚C. The growth of the nanoparticles in solution continued until a maximum intensity was observed, after which the nanoparticles decreased in radii and volume fraction until equilibrium was achieved (Figure 4.1).

When plotted as a 2-dimensional area vs time plot (eq. 2), the temperature dependent results show that the rate of nanoparticle growth is greatly enhanced at higher temperatures, with a concomitant decrease in lifetime (Figure 4.2). This volume reflects an estimate of total volume of nanoparticles formed in solution at each time point (Figure 4.2). The fitted *in situ* patterns revealed an initial increase in the total nanoparticle volume, immediately upon mixing the Fe^{2+} and phosphate precursor solutions (~ 6 s) due to instantaneous nucleation at the given supersaturation[15]. However, at lower temperature (i.e., 10˚C), a larger proportion of the initially formed nanoparticles remains, indicating a longer lifetime. However, the maximum volume fraction is nearly twice (in absolute units) at 60˚C at 12 s (~ 0.01 %), compared to 21˚C at 60 s (~ 0.005 %), showing that the 'amount' (number volume) of nucleated nanoparticles was much greater at higher temperatures. To summarize the results, the nucleation of nanoparticles upon mixing of the iron and phosphate solutions in our experiments progressed via two stages. The stage I encompasses the instantaneous nucleation of a huge volume of nanoparticles in solution and their subsequent growth, as a function of time. In that first fast stage (at all temperatures < 20 seconds), the distributions of the nanoparticles were nearly same for all temperatures (supersaturations) and the distribution curves did not vary much in terms of average nanoparticle radii, which were in the range of 20 – 40 nm for all temperatures.

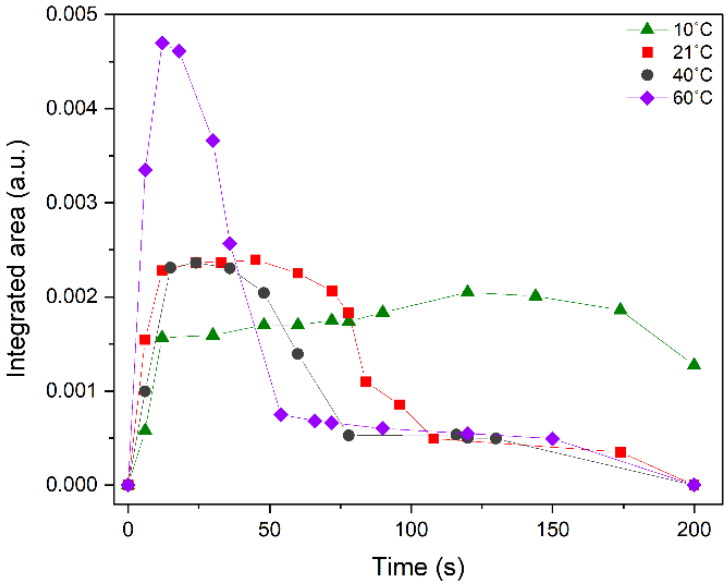

Figure 4.2. Plot of integrated area under the size distribution histograms at each time point reflecting the total relative volume (V_{total}) of the nanoparticles that grew at different temperatures as a function of time.

During stage II, we could observe the rapid decline in the volume fraction of the nanoparticles. The rate of this process also varied with temperature. At 60˚C, the majority of the nanoparticles decrease

in volume within the first 30 – 50 s, whereas at 21˚C the particles show a volume decrease within 75 – 100 s (Figure 4.2). The initial faster volume decrease is followed by a less pronounced minor decrease starting at ~ 100 s, till (~ 200 s) a nearly zero volume fraction was attained for 21, 40 and 60˚C. Furthermore, at 10˚C there were minor changes in the total volume fraction of the nanoparticles formed after stage I, reflecting the longer lifetime of the formed phase in stage II at this temperature. This represents the final equilibrium concentration of the nanoparticles in solution at 10˚C, which remained nearly constant for the total duration of this study (60 min). These results show that the lifetime and rate of disappearance of the formed nanoparticles in solution was inversely proportional to temperature. To understand the correlation of these two stages with the growth of vivianite crystals in solution, the *in situ* WAXS data and the crystallization of vivianite was further investigated.

4.3.2. The crystallization of vivianite

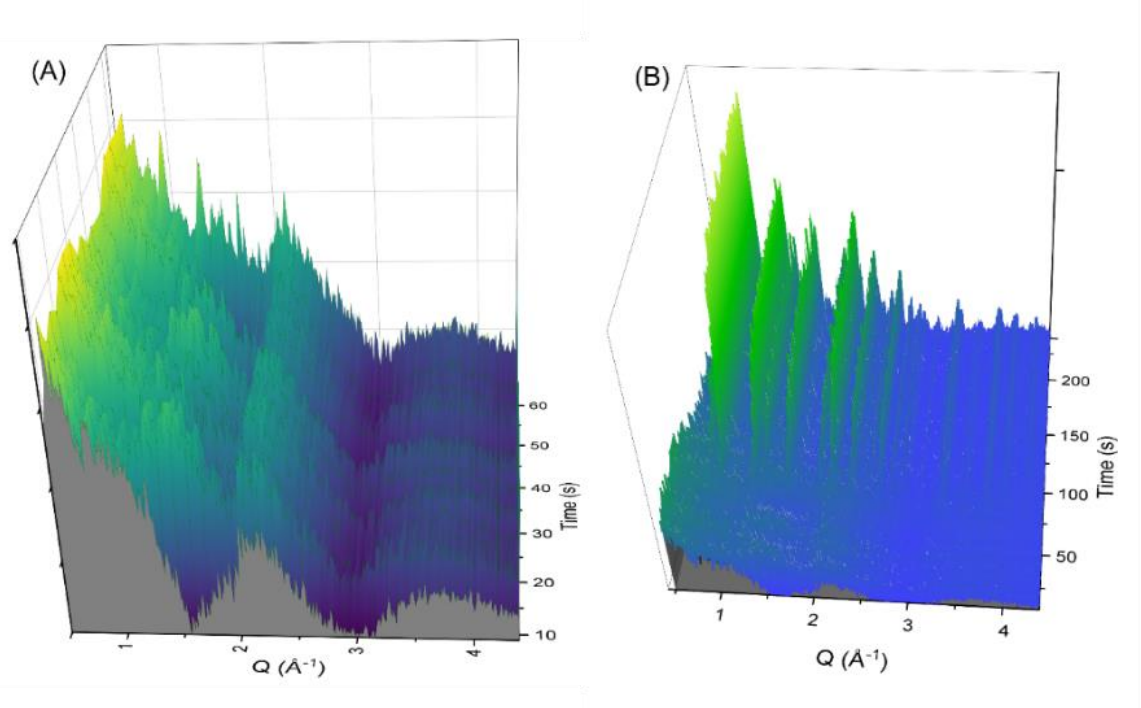

Figure 4.3. *In situ* WAXS patterns of vivianite precipitation at 21˚C (A) zoomed patterns at initial time points, (B) patterns at longer timeframes showing the onset and growth of Bragg peaks corresponding to crystalline vivianite.

The simultaneously collected *in situ* WAXS patterns were used to follow the growth of vivianite via the development of Bragg peaks in our experiments (Figure 4.3). Again, a two-stage process could be observed. In the first stage – and for about ~ 120 seconds (at 21˚C, see Figure 4.3 as an example), only

broad scattering features and no peaks were visible. This indicated the rapid nucleation of a large amount of a non-crystalline phase – in this case amorphous phase AFEP (Figure 4.3), a process that was as expected from our previous *ex situ* results [163]. Our previous powder XRD patterns [163] of AFEP matched the broad WAXS scattering features, centered at Q = ~ 2.15 $Å^{-1}$ and ~ 3.9 $Å^{-1}$ (Figure 4.3-A). As the reaction progressed the WAXS patterns revealed the onset of crystallization of vivianite starting at ~ 70 s at 21˚C, as evidenced by the prominent (020) and (200) Bragg peaks at Q values of 0.93 and 1.28 $Å^{-1}$ respectively. The peaks continued to grow until after ~ 200 seconds at 21˚C no more change was observed. We indexed the WAXS patterns (~ 300 s) from the existing vivianite *cif* file [163] and these matched well with purely crystalline vivianite.

To quantify the extent of the crystallization with time, the WAXS peak areas were integrated and normalized to derive the reaction progress (α) with respect to time (Figure 4.4). The induction period increased with reaction temperature: from ~ 17 s at 60°C, to ~ 120 s at 10 °C. After crystallization is complete, the curve reaches a plateau after ~ 118 s at 60 and after ~ 290 s at 10 °C. As a result, the rate of crystallization increases with the reaction temperature. The saturation index of vivianite also increases from 12.6 to 13.3. upon changing the temperature from 10 - 60˚C (Appendix II, section A2S1).

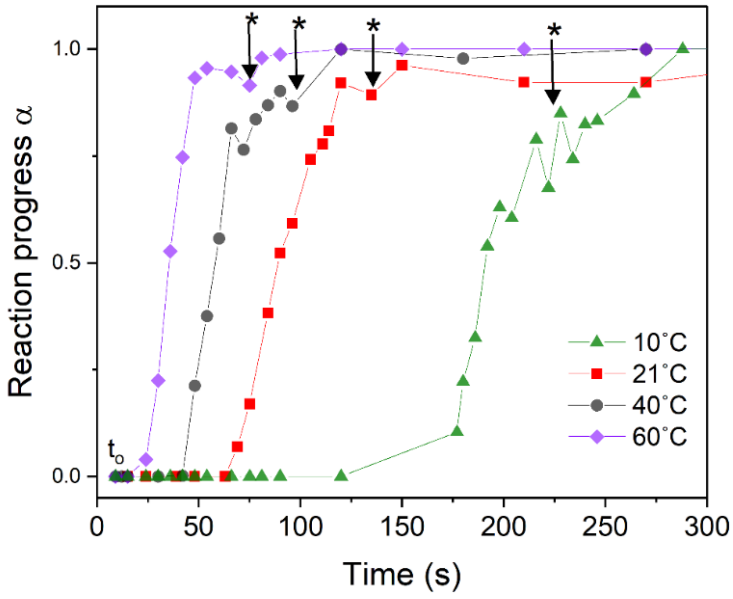

Figure 4.4. Plots of the *in situ* WAXS reaction progress (α) derived from normalized peak area integrals versus time, from vivianite precipitation experiments at different temperatures. The time point t_0 corresponds to the time of mixing the initial ferrous and phosphate precursor solutions and arrows represent the minor decrease in intensity.

All the curves showed the same qualitative features *i.e.*, initially no intensity followed by a rapid rise. Interestingly, once the maximum intensity was reached we observed a minor temporary decrease (arrows in Figure 4.4) followed by a second less pronounced rise, beyond which no further changes in the WAXS intensities were observed. It is very remarkable that at all temperatures, the rate of AFEP volume decrease after stage I coincided with the first major increase marking the onset of vivianite crystallization in the α versus time curves in stage II. For example, at 60˚C the decrease in the total volume fraction of the initial nanoparticles observed in the SAXS patterns (see Figure 4.2) and the first Bragg peak for crystalline vivianite occurred concomitantly at ~ 17 s; similarly, at ~ 35 s (40˚C), ~ 57 s (21˚C) and at ~ 120 s (10˚C) for different temperatures, showing that these two processes are inherently linked. A better visualization of this is available in Figure 4.5.

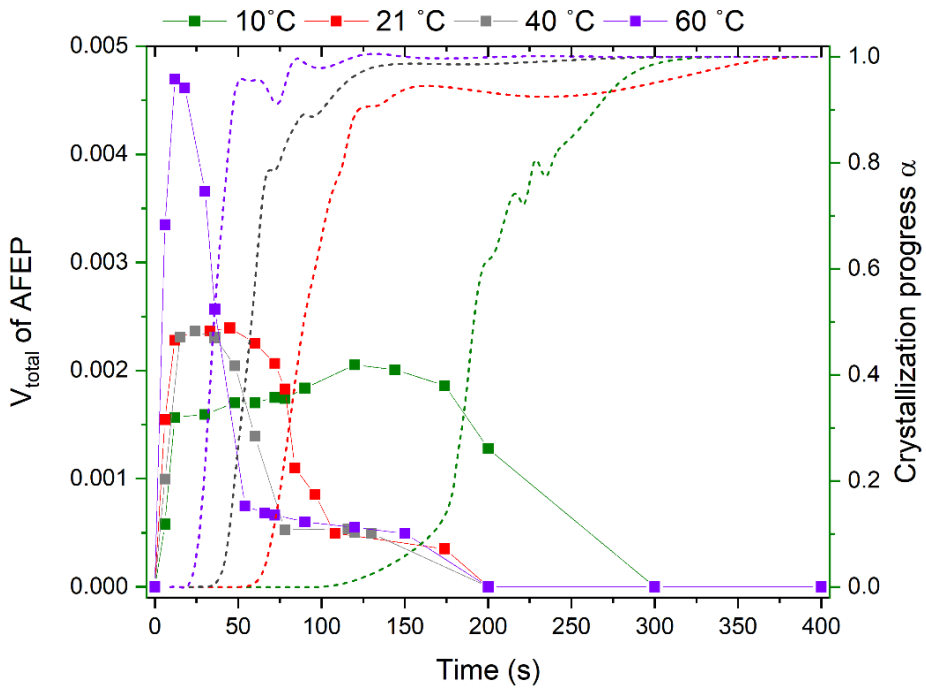

Figure 4.5. Plots of vivianite crystallization progress (α) modeled from *in situ* WAXS data (dashed lines) superimposed on total volume V_{total} of spherical AFEP nanoparticles estimated by *in situ* size distribution histograms from the modeled SAXS data (points).

Furthermore, the integral intensity of the WAXS peaks reached a constant plateau after achieving a maximum value at the end of stage I, however, concomitantly the AFEP particles in stage II exhibited a second minor decrease. This may imply that the particles could be undergoing aggregation to form structures, with sizes beyond the SAXS range, as observed in the Guinier region of Figure A2S2.

These results clearly indicated that the vivianite crystals grew in solution, at the cost of the AFEP nanoparticles, and these two processes are inherently linked. These results are in alignment with our previous *ex situ* studies [163] at ambient temperature and lower supersaturation (SI ~ 10) which showed that the intermediate AFEP phase transforms to crystalline vivianite with time.

Similar *in situ* SAXS-WAXS studies have been performed to understand nucleation and growth of $CaCO_3$ polymorphs, such as transformation of ACC → vaterite → calcite via a dissolution-reprecipitation pathway [16]. To understand the in-depth mechanism of this transformation and the associated activation energy of vivianite formation, the WAXS data was fitted with suitable literature growth models to derive the variation of the growth rate constant of vivianite with temperature.

4.3.3. Crystallization mechanism and activation energy of vivianite formation

Our results clearly documented that the rate of vivianite growth was directly proportional to temperature. To quantify this, we evaluated the associated rate constants (k) by applying the Johnson−Mehl−Avrami−Kolmogorov (JMAK) model. The JMAK model describes phase transformation reactions despite its limitations it has been widely used in a nucleation and growth studies from solution [15, 28, 37, 101] or in studies where homogeneous solid-state transformations were followed [170, 171]. The JMAK equation [172, 173] can be expressed as

$$\alpha = 1 - \ e^{-kt^n}$$

The above expression can be rearranged and expressed in the logarithmic form as

$$-\ln(1-\propto) = \ kt^n$$

Eq. 4.3.

where *α* denotes the amount of material that has undergone phase transformation, k is the rate constant of the reaction, t is the time elapsed since the initiation ($t_{induction}$) of the phase transformation ($t = t_{total} - t_{induction}$) and *n* describes the growth dimensionality, or the propagation mechanism of the transformation through the material [172, 173]. Generally, for bulk dominated nucleation and growth, a higher value of the dimensionality constant ($n > 2$) is expected [172-174]. The equation (1) can be rearranged to the following linear equation

$$\ln(-\ln(1-\propto)) = n\ln(t) + \ln(k)$$

Eq. 4.4.

If the data points can be fit according to the JMAK model. This fit can then be used to derive the variation of the rate constant (k) with temperature and the dimensionality constant of crystal growth. The *in situ* time resolved WAXS data was fitted to the JMAK equation and the fits are shown in Figure 6. The results of the JMAK fits are also summarized in table 1 and details are available in figure S3 (Supporting information). The fits showed linear trends and indicated a variation of the n parameter from 1.4 – 0.8 within the studied temperature range. The n parameter varied by approximately 0.5 units between the 10 and 60˚C experiments, indicating that the transformation/crystallization mechanism did not vary drastically over the studied temperature range.

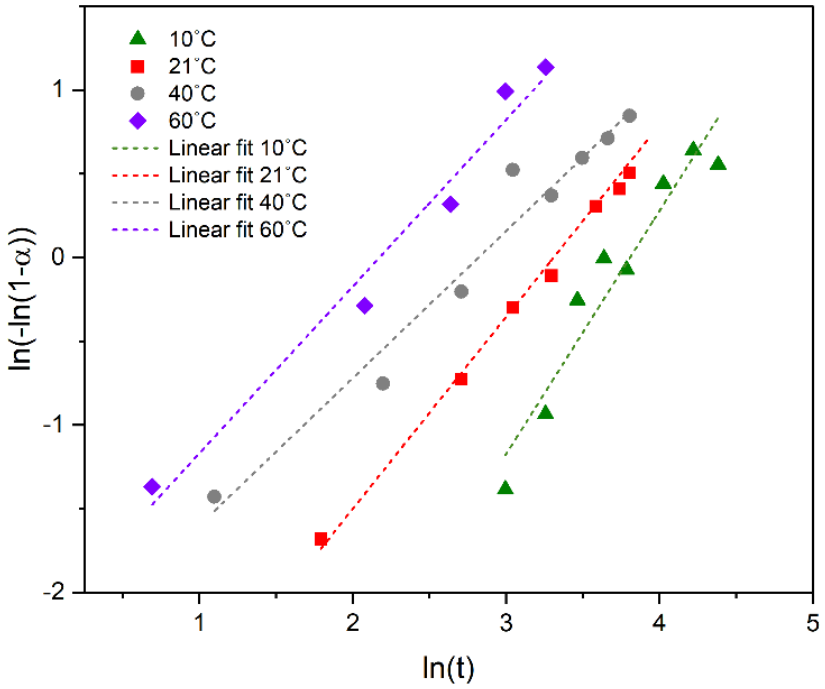

Figure 4.6. Plots of modified JMAK equation to determine the k and n parameters for crystallization of vivianite at different temperatures

Table 4.1. Avrami dimensionality constants (*n*) and reaction rate constants (*k*) extracted from fitting WAXS data sets from different temperatures with the JMAK model

Temperature (˚C)	*n*	*k* (s^{-1})
10	1.452 ± 0.169	0.003
21	1.145 ± 0.057	0.022
40	0.878 ± 0.070	0.083
60	0.995 ± 0.091	0.114

An *n* parameter of approximately 1 has been attributed to bulk nucleation and 1D propagation of this transformation front [170, 175], which may also be applicable for vivianite. The rate constants (k) also showed an increase with temperature, from 0.03 to 0.114 s^{-1}, as summarized in table 1. This directional proportional relation between k and temperatures was also observed for crystallization reactions in other sparingly soluble mineral systems like for example Ca-CO_3[176] and Ca-PO_4 [177] .

The Arrhenius equation is a simplified but accurate relation between the temperature and the rate constant for a chemical reaction. This has been used to model temperature variance of rate constants in various chemical reactions, including mineralogical transformation reactions [178 179]. Based on the derived rate constants from the JMAK fits, the temperature dependence of the rate constant for the crystallization of vivianite was modeled by the Arrhenius equation, which in its linear form can be expressed as

$$\ln(\mathrm{k}) = \ln(\mathrm{A}) - \frac{\mathrm{E_a}}{(\mathrm{R} \cdot \mathrm{T})}$$

Eq.4.5.

The term E_a denotes the activation energy of the crystallization, T is the absolute temperature, R is the universal gas constant and A is the pre-exponential factor. From eq (5), a plot of 'ln(k)' versus '1/RT' should yield a straight line with intercept ln(A) and slope ($-E_a$). As seen from Figure 4.6, the plot of 'ln k' vs '1/RT' for a range of temperatures from 10 – 60˚C exhibited a nearly linear trend for vivianite's crystallization, indicating that a nearly identical crystallization mechanism operates within the studied range of temperatures. The fit parameters are available in table A2S1 (appendix II). The apparent activation energy (E_a) for vivianite nucleation and growth was calculated from the slope of the curve in Figure 74. and is approximately E_a = 51 ± 13 kJ/mol, this is a value that is independent of reactant concentration.

It is interesting to note that Arrhenius plots of dissolution rates measured for oxide or carbonate minerals, whose dissolution is controlled by simple surface metal hydrolysis, are likely to generate true E_a. For example, the value of the apparent activation energy determined for magnesite dissolution/precipitation at near neutral conditions E_a = 46 kJ/mol, is consistent with the enthalpy of activation of the rate of exchange of water molecules in Mg^{2+} coordination sphere (ΔH* = 49 kJ/mol) [180].

Here, the apparent activation energy associated with vivianite crystallization is consistent with an E_a associated with dissolution precipitation reactions in minerals which range from 35 – 65 kJ/mol [180-182], which may shed light on the transformation mechanism of AFEP nanoparticles to vivianite, in solution, at stage II.

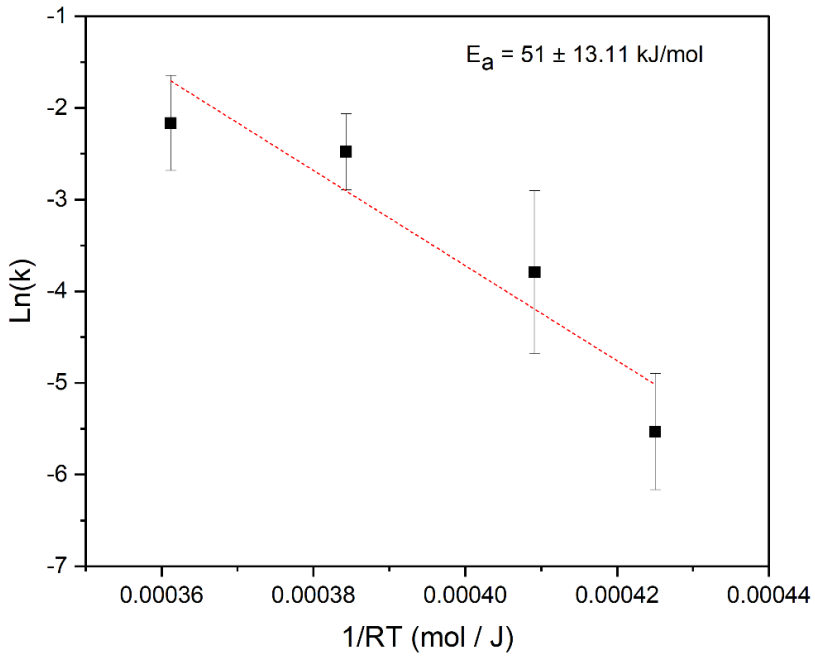

Figure 4.7. Plot of ln(k) versus 1/RT (where R = 8.314 J K^{-1} mol^{-1}) for estimation of the required activation energy (E_a) of vivianite crystallization, data (k and T) is taken from table 1 above. (Parameters of the linear fitting are available in Table S1, supporting information.

To assess how and if the end product vivianite varied as a function of reaction temperature, we used SEM imaging of materials from the end of each reaction at different temperatures. The data revealed that indeed morphologies of the final solids (Figure 4.8) varied. However, the initial solids from the reaction mixture filter quenched after 2-3 minutes from the 10 and 21˚C experiments were small and dispersed crystalline platelets (~ 50 – 100 nm) (Figure A2S5, appendix II). However, as time progressed, these small crystals transformed into a mixture of sheaf and rosette shaped crystals and when sampled at 10 min they grew to large micron sized crystals (Figure 8 a-d). The sheaf-like crystals were comprised of partially aligned rods having a thickness of 50 – 100 nm with radiating fantails linked at the center, resembling a 'wheat sheaf' (Figure 4.8 a, b). Some minerals like stilbite and aragonite tend to form these sheaf-like structures in nature [183].

On the other hand, the crystalline rosettes showed diameters of ~ 10 - 20 µm and were comprised of triangular blades emanating from a central core (Figure 4.8 - c,d). Sometimes these platelets crossed each other to form X-shaped configurations (Figure A2S4, appendix II). The precipitates at 10˚C mainly crystallized into a sheaf-like morphology (Figure 4.8-a). Interestingly, at 21˚C the crystals showed a mixture of both (sheaf-like and rosette) morphologies as shown in Figure 7b, wherein the triangular blades and nanorods emanated from a common core. At 40 and 60˚C, there were no sheaf-like crystals detected but only the rosettes (Figure 4.8-c,d). Therefore, it is clear from the above observations that lower temperatures tended to favor a sheaf-like morphology while higher temperatures, favored the formation of rosettes.

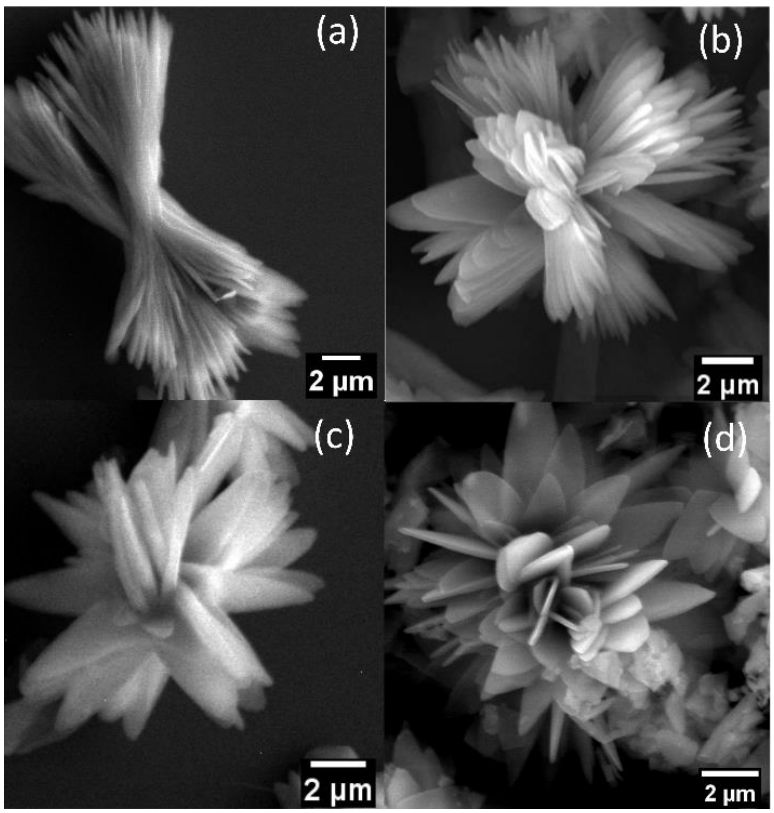

Figure 4.8. Time resolved SEM micrographs showing typical morphologies of vivianite crystals sampled at 10 mins from experiments at (a) 10˚C, (b) 21˚C, (c) 40˚C and (d) 60˚C. Varying morphologies from sheafs → rosettes observed with increasing temperature due to an increase in crystal splitting.

Crystal splitting is a phenomenon of the splitting of a single crystal into subunits during its growth. This splitting can be induced by defects, dislocations and disclinations that distort lattices locally, but this can produce global effects in the morphology [184]. Generally, a particular distorted crystal morphology can be understood by variation in the extent of crystal splitting, however the factors

controlling it are not entirely understood. The splitting ability of a crystal can vary with its structure or anisotropy, for example the crystal splitting of aragonite (orthorhombic) is higher than that of calcite (rhombohedral), which allows it to form split acicular structures [183]. In case of Bi_2S_3 crystals, the crystal splitting has been shown to increase with solution concentration, leading to development of increasingly split sheaf or flower-like structures [183]. Variations in sheaf and spherulitic morphology have also been attributed to changes in supersaturation in Ca-CO_3 systems [185].˚

The overall divergence of the crystals from an idealized monoclinic unit cell geometry for vivianite [47] is relatively lower for sheaf-like morphology than rosettes, therefore the sheaf-like crystals represent a lower degree of splitting. Overall, a lower = temperature leads to a greater preference for a sheaf-like morphology, which reflects a lower degree of crystal splitting during growth, as compared to the rosettes formed at higher temperatures (supersaturation). Based on its crystal structure, vivianite forms infinite sheets stretched along the (010) axis and these are held mainly by H-bonding interactions [48]. It is also known that small changes in the inter-layer stacking can induce faults, which can induce crystal twinning [186]. We have previously shown through *ex situ* experiments that the nucleation and growth of vivianite via AFEP was accompanied by an overall hydration and development of a well-defined H-bonding network [163]. Therefore, small changes in H-bonding interactions may lead to development of inter-layer stacking faults, which may be one of the factors promoting twinning and/or crystal splitting. As the rate of vivianite crystal growth increased with temperature, this could explain the greater likelihood of defects in the structure, which in turn could lead to crystal splitting and development of complex morphologies as documented shown in Figure 4.8.

4.4. Conclusions

We documented above the rates and mechanism of vivianite formation via *in situ* SAXS/WAXS experiments at different temperatures (10, 21, 40 and 60˚C) and at relatively high supersaturations (SI 12.6 – 13.3). The nucleation and growth of vivianite can be divided into two stages. In stage I, initially upon mixing of the starting Fe^{2+} and phosphate solutions, the *in situ* SAXS/WAXS data analysis showed that spherical particles of an amorphous phase (amorphous ferrous phosphate (AFEP)) rapidly nucleated and grew in size and volume in solution. No crystalline vivianite was present during this stage. The average radii of the AFEP nanoparticles were similar (20 – 40 nm) at all temperatures and their rate of growth was directly proportional to temperature. Once the nanoparticles reached a maximum size and volume, stage II follows, during which both the size and volume of the AFEP

nanoparticles steadily decreases while concomitantly the crystallization onset of vivianite was observed. The development of an H-bonding network enables the transformation of AFEP to vivianite, and at higher temperature there is a greater probability of molecular collisions, leading to a greater level of disorder in H-bonding and splitting during crystal growth (preference for rosette shape). The vivianite crystals grow rapidly, while the volume of AFEP steadily decreases, reaching an equilibrium value. Once all the AFEP had transformed into vivianite, the crystals remain stable in solution as evidenced by no further changes in the WAXS patterns. However, there was an observable minor decrease in the SAXS patterns at 21 and 10˚C, even after no changes were observed in the WAXS patterns, which may be due to aggregation of nanoscale particles at lower temperatures to form sheaf-like crystals.

We modeled the growth kinetics of vivianite from the stage II WAXS data using the JMAK model and could show that the value of the dimensionality constant (*n*, between 1.4 – 0.8 for all temperatures), indicates a one-dimensional propagation of the crystallization front within the bulk of the material. The derived rate constants were directly proportional to temperature and could be fitted with the Arrhenius model to evaluate the activation energy of vivianite crystallization E_a = 51.4 ± 13.11 kJ/mol, a value typical for dissolution-reprecipitation reactions mechanism of sparingly soluble salt systems. The SEM micrographs of the vivianite crystals formed at different temperatures showed marked differences in their morphologies. The preference for a sheaf-like morphology at 10 and 21˚C, transitioned at higher temperatures to a rosette morphology at 40 and 60˚C. This may be explained by changes in crystal splitting of vivianite during growth. Our results shed light on the fundamental mechanisms of fast non-classical crystallization reactions in solution.

Chapter 5. High-Temperature Induced Amorphization and Phase Transformation of Vivianite

ABSTRACT. The stability of ferrous phosphate geomaterials is fundamental for our understanding of iron and phosphorus cycling in modern and ancient natural systems and for improving industrial processes related to phosphate recovery. Here we report a temperature driven solid-state phase transformation reaction series where crystalline vivianite ($Fe_3(PO_4)_2 \cdot 8H_2O$, *C2/m*) breaks down to an amorphous phase that upon further heating transforms either to crystalline graftonite ($Fe_3(PO_4)_2$, *P21/c*) or to crystalline rodolicoite ($FePO_4$, *$P3_121$*). In the anoxic system, the reaction starts above 100˚C, when we observed the gradual dehydration of vivianite. Above 250˚C, vivianite transforms into an amorphous ferrous phosphate (a-$Fe_3(PO_4)_2$) through a pseudomorphic replacement retaining the initial vivianite morphology. When this amorphous $Fe_3(PO_4)_2$ phase is further heated it transforms either to graftonite at T ~ 502˚C when heated under anaerobic conditions a process that is following an exothermic reaction with a crystallization enthalpy (ΔH_{cryst}) of – 16.767 ± 0.26 kJ/mol. Conversely, when vivianite is heated in air it transforms to an amorphous phase (> 200˚C), oxidizes and transforms (700˚C) into a trigonal ferric phosphate phase - rodolicoite (*$P3_121$*) instead of crystalline graftonite, confirming that the transformation reaction follows variable pathways depending on the atmosphere of the system. Rietveld refinement-based calculations of the two crystalline end-members (vivianite and graftonite) evidenced a unit cell volume decrease of 3.11 ± 0.011%. This anaerobic transformation was also confirmed by *in situ* SEM analyses, where an overall shrinking of the initial vivianite crystals was observed. In addition, the time resolved images revealed changes in surface morphology including 'bubble'-like features during the transformation. Nevertheless, even after the full breakdown of the initial vivianite crystals into the amorphous phase, the overall shape of the initial vivianite crystals remained preserved, despite the net decrease in volume. *Ex situ* Fe-K XAS analyses indicate varying structural changes taking place in the vivianite to graftonite transformation. These new insights can be applied to understand, high-temperature and ambient pressure, phase transformations of ferrous phosphates.

5.1. Introduction

Phosphate phases consisting of ferric (Fe^{3+}) and ferrous (Fe^{2+}) ions are present in about 45% of the known phosphate bearing minerals [38]. Under anoxic aqueous conditions, at high phosphate and Fe^{2+} activities, the hydrated mineral vivianite ($Fe_3(PO_4)_2 \cdot 8H_2O$) is the most stable orthophosphate [1]. Vivianite occurs at low temperatures in ferruginous, and non-sulfidic, lake and river sediments [1, 4, 10]

and in waterlogged anoxic soils [5, 7]. It can be found in modern environments as well as in ancient ferruginous settings, wherein the availability of reduced aqueous iron is the crucial parameter controlling the cycling of phosphorus and its immobilization most often through vivianite precipitation [1]. Vivianite is also an economical precursor for synthesis of $LiFePO_4$, a Li-ion battery cathode material [118, 162]. The morphology of the initial vivianite precursor can have a significant impact on the morphology and electrochemical activity of the synthetic $LiFePO_4$ material [162].

On the other hand, graftonite is a phosphate mineral belonging to a series of minerals having a chemical composition of $(M)_3(PO_4)_2$, where M (= Mn^{2+}, Ca^{2+}, Fe^{2+}) is a divalent metal cation, which can exist as a mixed series [187]. In the environment, graftonite occurs as a typical phase in altered granitic pegmatites [61, 62, 188, 189]. Vivianite and graftonite show co-occurrences in altered granitic pegmatites that may have been subjected to varying hydrothermal conditions over time [61, 62, 189]. However, the origin of this graftonite in these pegmatite rocks cannot be ascertained [189] and the elucidation of alteration parameters (temperature and pressure) enabling the co-occurrence of vivianite and graftonite remain unclear. Synthetic graftonite can been prepared by heating a stoichiometric amount of ferrous phosphate for one month, in an evacuated and sealed silica tube at 800 ±10˚C [190].

Structurally, both the phases are remarkably different, vivianite crystallizes in a space group *C2/m* with two distinct Fe octahedral sites, Fe(1) being highly distorted and Fe(2) being comparatively more symmetrical [47]. Vivianite can undergo oxidation to metavivianite ($Fe^{2+}\,Fe^{3+}_2\,(PO_4)_2\,(OH)_2{\cdot}6\,H_2O$) in the presence of air, therefore anoxic conditions are required to stabilize its crystal structure [65]. This oxidation is also visually discernible as vivianite darkens to a shade of dark indigo upon such aerial exposure, due to crystal structure changes. On the other hand, graftonite is pale gray to salmon pink in color, is resistant to Fe oxidation and crystallizes in the *P21/c* space group [191]. In this present work, we describe an experimental study of the heat-induced structural transformations of vivianite by different *in situ* and *ex situ* techniques.

The results of our analyses provide a fundamental understanding on how vivianite dehydrates into an amorphous material a-$Fe_3(PO_4)_2$ phase and subsequently undergoes an exothermic, solid-state rearrangement to form the thermodynamically stable end product - graftonite. We also highlight the impact of changing atmosphere (presence of oxygen) on the pathway and results of this transformation.

5.2. Experimental Section

5.2.1. Vivianite synthesis

Vivianite was synthesized at room temperature inside an anaerobic chamber (Coy Laboratory Products, Inc., 97 % N_2 and 3 % H_2 gas mixture) following our previously reported synthetic protocol [163]. Ultrapure water (~ 18.2 M Ω·cm) was degassed by purging with CO_2-free Ar gas and heating (at ~ 80˚C) for 6 hours. This was used to prepare a Mohr's salt solution (0.1 mol L^{-1}, 50 mL, 99.95 % purity, Alfa Aesar GmbH), which was reacted for 1 hour and under constant stirring with a mixture of dibasic sodium phosphate (0.0505 mol L^{-1}, 25 mL, Sigma Aldrich, 99.98 %) and monobasic potassium phosphate (0.0494 mol L^{-1}, 25 mL, Sigma Aldrich). The precipitation reaction was carried out in a 250 mL perfluoroalkoxy alkane (PFA) reactor. The suspension was capped and aged in a closed PFA reactor for a week inside the anaerobic chamber. The resulting precipitates were vacuum filtered through a 0.2 µm polycarbonate membrane filter (Nucleopore), and washed with ultrapure water (30 mL) to remove any adsorbed ions or salts. The resulting vivianite was a pale blue solid that was dried via overnight evaporation, inside the anaerobic chamber and transferred into a crimp seal vial for further anaerobic storage.

5.2.2. Characterization and instrumental methods

Thermogravimetry and differential scanning calorimetry (TGA-DSC)

Determination of thermal properties of vivianite upon heating and its phase transformation behavior was followed via thermal gravimetric analyses (TGA) and differential scanning calorimetry (DSC). Important to note is that the synthesized vivianite samples were stored under nitrogen gas and analyzed under argon gas in corundum crucibles to avoid oxidation. The TGA-DSC spectra were simultaneously recorded on a thermobalance Themys One$^+$ instrument (Setaram, Caluire, France), at a heating rate of 10 K/min, and up to a maximum temperature of 700°C. Temperature and energy calibrations were performed by measuring the melting temperatures and enthalpy of fusion of pure metal standards in corundum crucibles. The metals In, Al, Ag, Au, Ni were used for temperature calibration and In, Sn, Al, Ag, Au, for energy calibrations. The data was evaluated with the Themis One$^+$ software (Setaram, Caluire, France). At the end of each measurement, the resulting solids were retrieved for further characterization.

Powder X-ray diffraction (XRD)

The phase identification and structural analyses were performed via powder X-ray diffraction (XRD) measurements. All samples were transferred into quartz glass capillaries (Hilgenberg 80 x 0.5 mm), that were sealed with a gum sealant (Cristaseal Sealant Tray, Hawksley & Sons Ltd.) inside the anaerobic chamber. Diffraction patterns were recorded on a STOE STADI P (STOE & Cie GmbH, Germany) diffractometer equipped with curved Ge(111) monochromator, DECTRIS MYTHEN2 R detectors in Debye-Scherrer geometry operating at 40 kV and 40 mA using Ag K_α radiation (λ = 0.55941 Å) with a 0.015° step size / 2500 s per step.

An empty capillary measured under the same experimental conditions, was used as the background. The calculated XRD patterns were obtained using the Vesta software [52]. Qualitative phase identification was done using the QUALX2 software (version 2.1) [192] .

Rietveld refinements from powder XRD data

Rietveld analyses were performed on GSAS-II software [193] starting with initial models for vivianite [121] and Fe-graftonite [194]. Background estimation was done via Chebyschev polynomial fitting and samples were modelled as pure phases. The unit cell parameters, micro-strain, grain size, thermal displacement and atomic coordinates were the refined parameters. NIST 660c LaB_6 standard was used to calibrate the instrument line profile.

In situ high temperature XRD (HT-XRD)

In situ HT- XRD measurements were performed using a STOE furnace accessory where a sealed capillary containing powdered vivianite could be heated, and patterns collected, over a temperature range. For these experiments, the capillary was prepared and sealed inside the anaerobic chamber. Finely powdered vivianite was transferred into quartz glass capillaries, and the end was sealed with a quick-sealing glue (Bolton Adhesives). The furnace accessory was temperature-calibrated by using KNO_3 (Alfa Aesar, > 99%) and KCl (Sigma Aldrich, > 99%) standards at a heating rate of 10˚C/min. The calibration curves are available as Figure S1, appendix II. Vivianite heating experiments/ measurements were done in 4 ranges (at 10˚C/min), optimize the total acquisition time, these were (I) 25 – 400˚C (range 1) and (II) 400 – 550 ˚C (range 2) and (III) 450 – 550 ˚C (range 3) and (IV) 550 – 600 ˚C (range 4). XRD patterns were recorded in Debye Scherrer mode from 0 to 73˚, with a 0.015˚ step size (180 s per step) as a function of temperature. The XRD patterns from the different ranges were compiled to construct *in situ* plots from 25 – 600˚C. The relative intensities of the patterns were scaled to increase *signal-to-noise* ratio, such that the Bragg peaks could be discernible. An empty capillary measured in the furnace accessory at room temperature was used for background

subtraction. The *in situ* XRD patterns at different temperatures were refined via Rietveld analyses on GSAS-II software [193] starting with initial models for vivianite [121] and Fe-graftonite [194] via phase fraction analyses at fixed histogram scale factors (= 1). The normalized factors (α) were then plotted as a function of temperature.

Infrared spectroscopy (IR)

The samples were analyzed using IR spectroscopy to gain insights into the bonding environment and functional group compositions. Fourier transform IR patterns of the dried solids, were measured in attenuated total reflection (ATR) mode on a Nicolet iD5 spectrometer (Thermo Fischer Scientific, USA) with a single bounce iD7 ATR accessory. For each pattern 16 scans were averaged and data was recorded at a resolution of 4 cm^{-1}.

Scanning electron microscopy (SEM)

The morphologies and qualitative elemental composition of the synthesized initial vivianite and the solid products following the TGA-DSC runs were imaged and analyzed using a field emission gun scanning electron microscope (FEG-SEM, FEI Quanta 3D, run at a voltage of 20 kV and 83.3 pA current) coupled to an energy dispersive X-ray spectrometer (EDX, Octane Elect EDAX detector). Prior to insertion into the microscope the solids were dispersed onto sticky carbon pads that had been glued to the SEM aluminum stubs and carbon coated (~ 20 nm layer) with a Leica EM ACE600 high-vacuum sputter coater. The SEM-EDX relative peak areas were analyzed by EDAX-TEAM software (AMETEK Inc.). *In situ* SEM experiments were performed using a TKD (DENS Solutions) dedicated specimen holder by depositing vivianite powder on a heating chip and imaging transformations at acceleration voltage of 20 kV, 1 mbar of N_2, and at a heating rate of 10 ˚C / min from 23 - 700 ˚C.

Transmission electron microscopy (TEM) – electron energy loss spectroscopy (EELS)

High resolution imaging and analyses of the solids was done by transmission electron microscopy (TEM, TECNAI F20 XTWIN, operated at 200 kV), with a field emission gun electron source and a Gatan Imaging Filter (GIF) Tridiem™ EDAX X-ray analyzer (EDX). TEM EELS-analyses were performed using a Themis Z (3.1) scanning transmission electron microscope equipped with a Continuum 1065 spectrometer on powders of crystalline ferric phosphate, amorphous ferrous phosphate and graftonite which were drop cast onto a lacey carbon film supported by Cu grid.

Heat induced transformation of vivianite in air

To study the oxidation behavior of vivianite, ~ 1 g of the sample was placed on a ceramic crucible and heated inside a Thermolyne bench-top muffle oven (Thermo ScientificTM) to 700˚C for 2 hours. At the end, a reddish-yellow colored powder was obtained, and analyzed by powder XRD and IR spectroscopy.

X-ray Absorption Spectroscopy (XAS)

The Fe K-edge X-ray absorption spectroscopy (XAS) data were collected on the P65 undulator beamline of DESY German Electron Synchrotron (HASYLAB, DESY PETRA III, Hamburg, Germany). The spectra were recorded at room temperature in transmission mode to a reciprocal space value of ~14.5 $Å^{-1}$. The details of sample preparation, protocols to prevent oxidation during sample transport and XAS beamline details are described in the appendix II – section A3S1. Spectra were aligned, averaged and background subtracted using the Athena software [126]. The normalized X-ray absorption near edge structure (XANES) were exported to OriginPro software (Origin Labs©, 2021). Shell-by-shell fits were performed on the k^3-weighted extended X-ray absorption fine structure (EXAFS) using the SIXpack software [128] based on algorithm derived from IFFEFIT [195].

5.3. Results and Discussion

5.3.1. High-temperature induced phase transformations of vivianite upon anoxic heat treatment

The synthesized vivianite was a pale blue solid characterized via powder XRD and IR analysis. Its XRD pattern showed crystalline Bragg reflections, which could be indexed (Figure A3S2, appendix III) based on the existing crystal structure of vivianite [121]. The anoxic TGA-DSC analysis of this sample from 25 to 700˚C, revealed step-wise loss of the volatile component (H_2O) from its structure (Figure 5.1). The results of inert TGS-DSC analysis of the vivianite sample ($Fe_3(PO_4)_2 \cdot 8\ H_2O$) showed a major mass loss of ~ 18 % between 100 - 200˚C representing a loss of 3/4th stochiometric H_2O of vivianite (~ 5 mol), highlighted as the grey regime in Figure 1. These results suggest that vivianite undergoes a major mass loss step involving the reaction $Fe_3(PO_4)_2 \cdot 8H_2O \rightarrow Fe_3(PO_4)_2 \cdot 3H_2O + 5H_2O$ between 100 - 200˚C. This mass loss is accompanied by a sharp endothermic DSC signal, typical for a dehydration process [159].

There is a lower rate of H_2O mass loss (~ 27 %) continuing up to ~ 450˚C, representing its complete dehydration (~ 8 mol H_2O) of vivianite, giving rise to a final material having the composition of $Fe_3(PO_4)_2$. With continued heating, there were no further observable changes in the TGA pattern from 450 ˚C till 700˚C (end of TGA-DSC run) showing that the $Fe_3(PO_4)_2$ material remained stoichiometrically

intact. These findings are consistent with the TGA-DSC analysis of natural vivianite by Frost *et al* [196]. However, it is surprising to notice an exothermic peak in the DSC curve between ~ 500 - 530˚C, unaccompanied by mass loss, suggesting a spontaneous structural modification. Similar exothermic effects in TGA-DSC spectra have been attributed to transformation of anhydrous amorphous calcium carbonate (ACC) → calcite in the Ca-CO_3 system [197] and anhydrous amorphous calcium phosphate (ACP) → HAP (hydroxyapatite) in the Ca-PO4 system [198].

The presence of this exothermic peak may therefore imply a solid-solid transformation [198] and recrystallization of the dehydrated vivianite into a material whose composition may be expressed as $Fe_3(PO_4)_2$. Furthermore, the DSC data could be used to calculate the molar enthalpy of this transformation (ΔH_{cryst}) as – 16.767 ± 0.26 kJ/mol from the pre-calibrated DSC data.

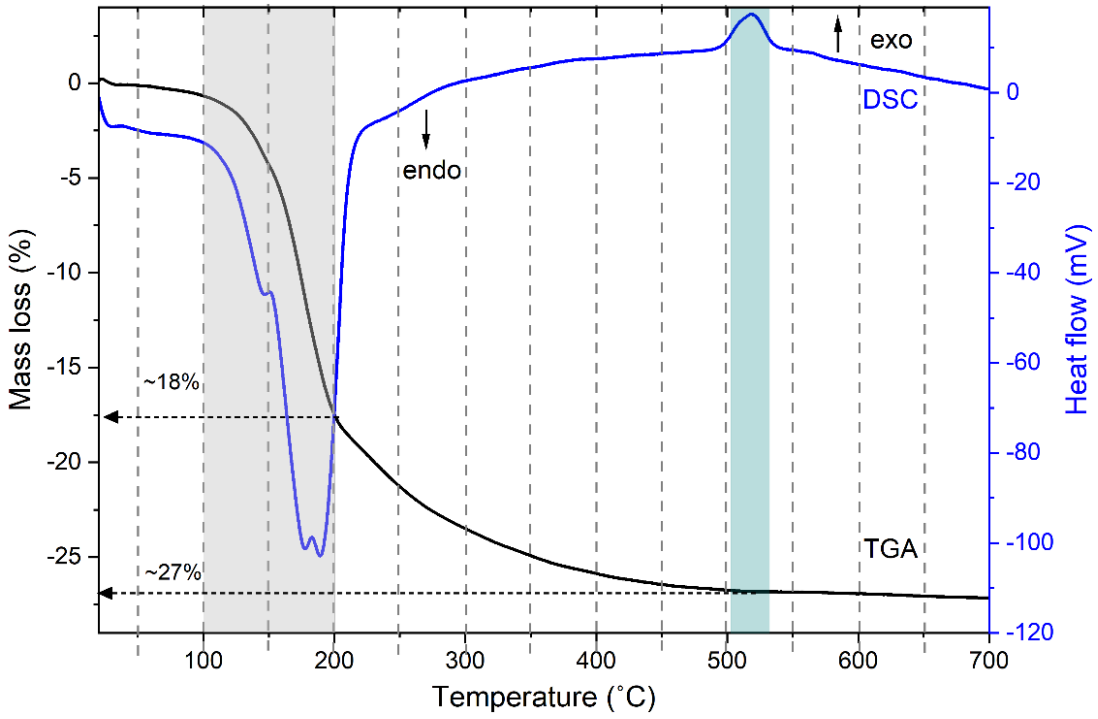

Figure 5.1. TGA (black) and DSC (blue) curves of vivianite for a heating rate of 10°C/min from 25 to 700 °C. The grey area indicates the major endothermic mass loss step (~ 18 %) between 100 – 200 °C, and the blue area indicates the exothermic peak (~ 27 %) between 500 – 540 °C (with no observable mass loss)

To determine the structural changes accompanying this transformation, *in situ* powder XRD was performed. The patterns revealed presence of pure crystalline vivianite between 25 - 120˚C. Upon continued heat treatment, a gradual decrease in the relative intensities of vivianite's Bragg reflections

was observed as a result of dehydration (Figure 5.2) as inferred from TGA-DSC data. At ~ 200˚C all the Bragg reflections corresponding to crystalline vivianite, including and the most visually prominent (020) reflection at 0.95 $Å^{-1}$, could no longer be discernible, indicating a collapse of the crystal structure. These results are consistent with the TGA-DSC data exhibiting the major loss of the bulk of structural water ongoing up to ~ 200˚C. The *in situ* XRD patterns between ~ 200 - 500˚C showed broad scattering features indicating an amorphous material (Figure 5.2) this also correlates to the *ex situ* pattern of the solids harvested at 400˚C, from the heated crucible under Ar (Figure 5.3).

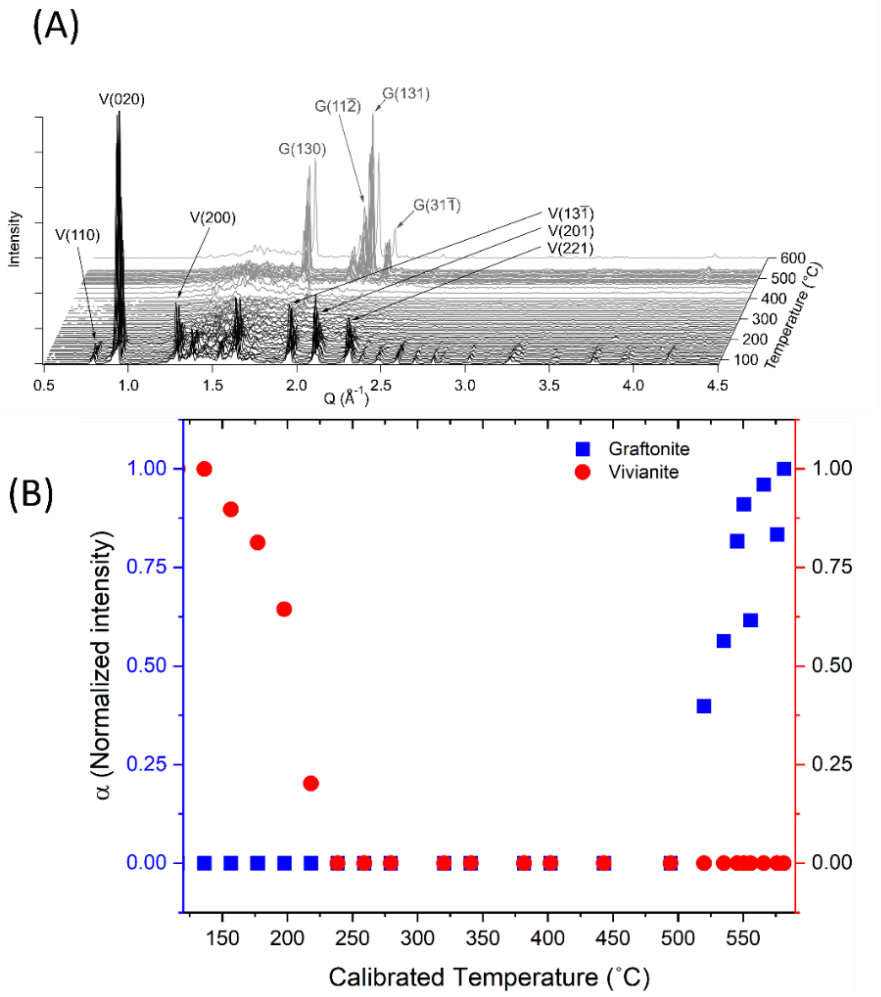

Figure 5.2. (A) *In situ* powder XRD diffractograms showing the initial breakdown of vivianite to an amorphous phase and its subsequent re-crystallization into graftonite. The respective Bragg reflections have been assigned to vivianite (V) and Fe-graftonite (G), respectively; (B) Plots of α (normalized phase fractions (PF) via Rietveld refinements) as a function of (calibrated) furnace temperature. Colored schemes: red – vivianite and blue – graftonite).

At ~ 510˚C, the first evidences of thermally-induced crystallization were documented from the XRD patterns as a rapid increase in sharp crystalline Bragg peaks (Figure 5.2). These Bragg reflections were assigned to graftonite structure reported by Henry et al. [194]. The most relatively intense (130) and (131) Bragg reflections of graftonite were initially observed at Q values of 1.83 and 2.20 $Å^{-1}$ (Figure 5.2) starting at ~ 500 ˚C, followed by their steady growth. The Bragg peaks increased in normalized intensity with temperature, a process which continued till no further changes in the XRD patterns were observed and crystallization was complete. These results agreed with our TGA-DSC data, since the composition of the graftonite is $Fe_3(PO_4)_2$, which is also documented by the TGA mass loss. This supports the recrystallization process observed as an exothermic peak in the TGA-DSC curves. It is noteworthy that despite the potential formation of another crystalline ferrous phosphate phase *e.g.* sarcopside $Fe_3(PO_4)_2$ [199], the formation of graftonite is specifically observed.

The *in situ* XRD data clearly showed the breakdown of vivianite crystal structure, into an amorphous material, followed by crystal nucleation and growth of domains of graftonite in the solid-state. The *signal-to-noise* ratio of the measurement was not satisfactory enough for exact phase identification and determination, therefore *ex situ* XRD data was used for quantitative Rietveld refinements and structural analyses of the two crystalline end-members.

5.3.2. Rietveld refinements for quantification of cell parameter changes during this transformation

The *ex situ* room-temperature XRD patterns of initial vivianite and the material collected from its anoxic TGA-DSC runs after 400 and 700˚C are shown in Figure 5.3, it is evident that the *signal-to-noise* ratio was much better than *in situ* measurements, due to a longer acquisition period and absence of thermally induced artefacts present while measuring *in situ* XRD patterns within the furnace accessory.

From the *ex situ* patterns, the phase at 400˚C was amorphous with broad X-ray scattering features and the one at 700˚C was Fe-graftonite [194]. Rietveld refinement was used to quantitatively determine the unit cell parameters of the crystalline end-members, *i.e.* vivianite and graftonite. The Rietveld refinement of the crystalline graftonite following the TGA-DSC experiment at 700˚C as well as that for the initial crystalline vivianite gave both good fits when we started with the pure phase models for Fe-graftonite by Henry *et al.* (2003) [194] and vivianite by Fejdi *et al.* (1980) [121] respectively. The Rietveld refinement results (Table 5.1) for vivianite and graftonite as derived from the XRD data (Figure 5.4)

revealed that although vivianite and graftonite both crystallize as centrosymmetric monoclinic Bravais lattices, they show variations in their space groups. Structurally, vivianite crystallized in *C2/m* while graftonite in the *P21/c* space group, respectively.

Rietveld refinements evidenced that the unit cell volume decreases by 3.11 ± 0.011 %, upon heat induced dehydration of vivianite, followed by amorphization to anhydrous $Fe_3(PO_4)_2$ and its crystallization to Fe-graftonite structure. This also implies a density change. Theoretical calculations from literature values of unit cell volumes from the structural models of vivianite Fejdi *et al.* (1980) [121] and Fe-graftonite Henry *et al.* [194] (2003) predict a volume decrease of 3.19 %.

This approximately agrees to the calculated volume change from our Rietveld analyses (Table 1). Additionally, there are also changes in coordination environments of the two crystalline end-phases, Fe^{2+} changes from distorted octahedrally coordinated in vivianite (coordination no. (CN) = 6), to a mixture of trigonal bipyramidal and distorted octahedral (CN = 5 and 6) in graftonite. The local structure of the intermediate anhydrous amorphous $Fe_3(PO_4)_2$ is not known because Rietveld refinements cannot be performed for this phase due to its amorphous nature.

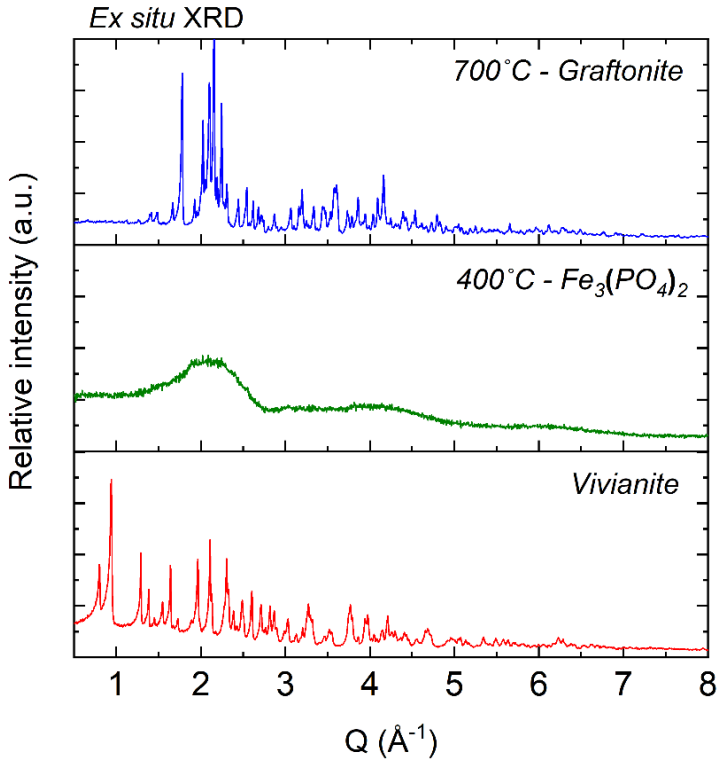

Figure 5.3. *Ex situ* XRD patterns of vivianite and powders collected from TGA-DSC crucibles (under Ar gas) at 400 (amorphous phase) & 700˚C (graftonite).

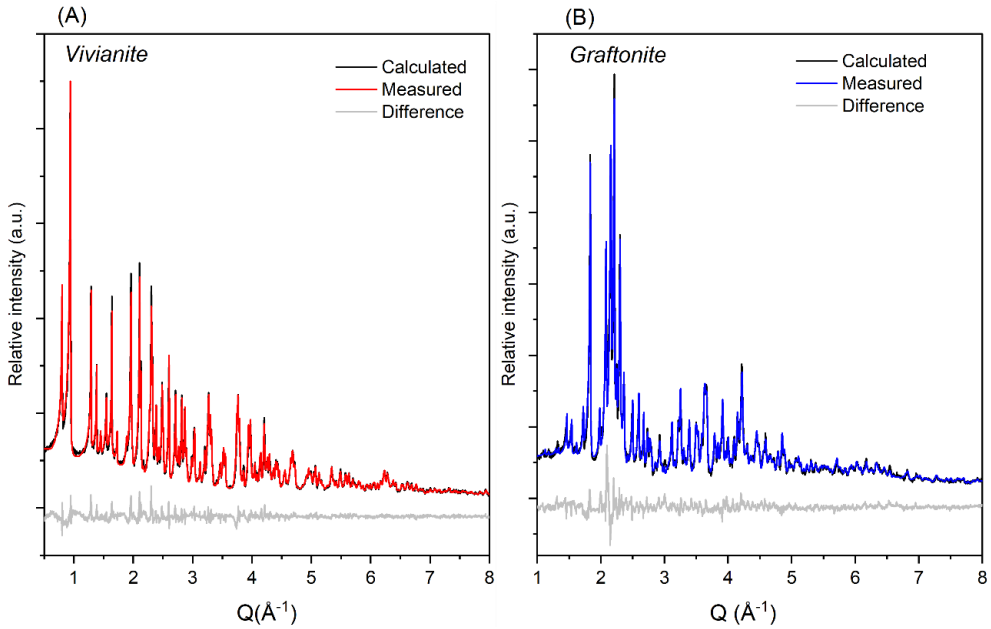

Figure 5.4. Rietveld refinement results for (A) synthetic vivianite – red trace and (B) graftonite – blue trace (anoxically heat treated vivianite harvested from TGA-DSC run up to 700˚C) showing the measured, calculated and difference powder XRD patterns.

Table 5.1: Details of Rietveld refinements of powder XRD data for synthetic vivianite and graftonite from this work

Phase	Space group	a (Å)	b (Å)	c (Å)	β (˚)	Volume (Å ^{3})	R_{wp} (%)
Vivianite	*C 2/m*	10.09 (17)	13.43 (6)	4.70 (4)	104.30 (28)	618.94 (5)	5.45
Graftonite	*P21/c*	8.87 (18)	11.16 (10)	6.13 (10)	99.33 (6)	599.60 (12)	7.56

The following sections will explore this transformation *ex situ*, in terms of local bonding environments (IR spectroscopy), EDS analyses (chemical composition) and morphology.

5.3.3. Structural and morphological changes upon HT- treatment of vivianite

The IR spectra provided structural insights into the difference in water and phosphate stretching and bending regions for the initial vivianite and all solids recovered after the TGA-DSC runs (Figure 5.5) and indicated that all three phases differ in structure and hydration. For the initial vivianite, the water hydroxyl stretching (v_1) region (~ 3500 - 2500 cm^{-1}) reveals more than one vibrational peak indicating

the different water bonding environments in its crystal structure. The characteristic water bending mode ($\delta_{H\text{-}O\text{-}H}$) in vivianite appears as a medium and broad peak at ~ 1635 cm^{-1}, while the water librational mode is a sharp and intense peak at ~ 810 cm^{-1}, correlating well with its existing literature value [163]. The IR spectra of the materials obtained from the TGA-DSC runs at 400 and 700˚C indicate that these phases are indeed anhydrous due to the absence of stretching and bending vibrations due to the water molecules and nearly no absorbance in the specified O-H stretching and bending region.

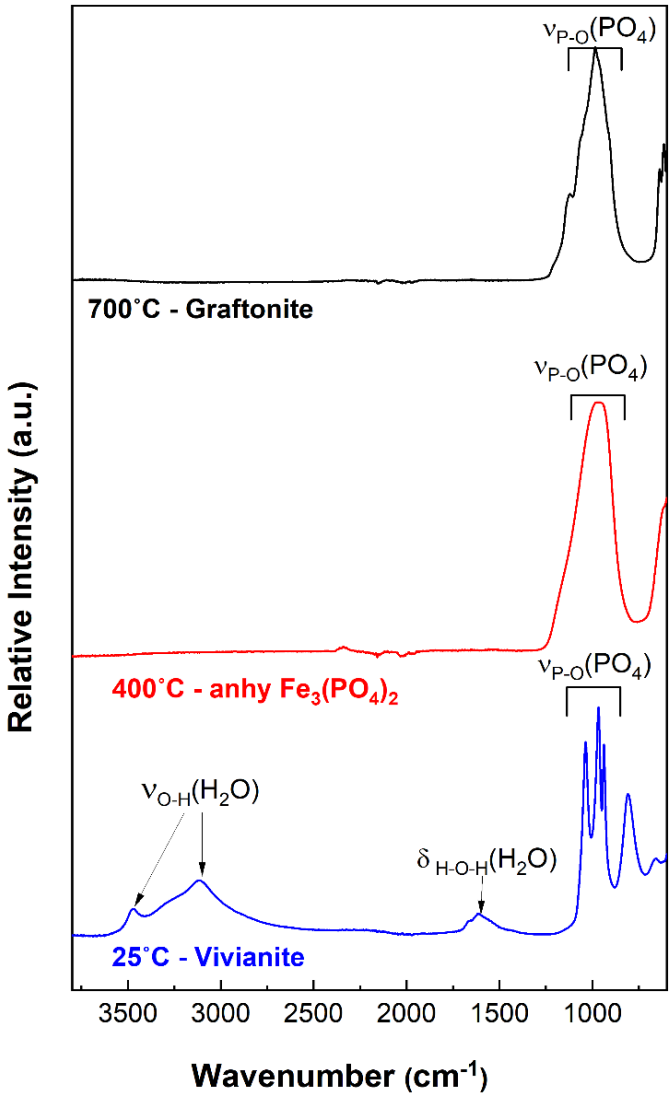

Figure 5.5. *Ex situ* temperature resolved IR spectra of vivianite – red trace, $Fe_3(PO_4)_2$ – green trace and graftonite – blue trace; the solid materials were harvested from anoxic TGA-DSC runs (under Ar gas) up to the specified temperatures and the arrows highlight characteristic IR vibrational modes for each phase.

The water librational mode at 810 cm^{-1} also disappears in case of anhydrous $Fe_3(PO_4)_2$ and Fe-graftonite, as expected from the loss of water from their local structure. The vibrational modes for phosphate (v_1 and v_3) are present in the same region for all three phases (~ 1050 – 800 cm^{-1}). However, differences in the bonding environments and structural arrangements are revealed by the changes in the splitting of these bands.

Vivianite has three sharp peaks for the phosphate group (1042, 966 and 945 cm^{-1}) due to the non-degeneracy of vibrational energy levels of the PO_4 groups in its crystal structure. Contrastingly, the a-$Fe_3(PO_4)_2$ solid retrieved after the TGA-DSC run at 400˚C, is characterized by a single, broad vibrational peak in which the antisymmetric (v_3) and symmetric (v_1) phosphate P-O stretching centered at 959 cm^{-1} are apparently visible as one band. Our previous results on IR analysis of the non-classical partially hydrated intermediate in vivianite nucleation *i.e.* amorphous ferrous phosphate (AFEP) ($Fe_3(PO_4)_2 \cdot \sim 4.7H_2O$), revealed a single broad P-O stretching peak centered at 976 cm^{-1} in its IR spectrum [163], which is ~ 23 cm^{-1} shifted to the lower wavenumber for the anhydrous phase (400˚C), revealing variations in local structure.

On the other hand, the IR spectrum of graftonite shows two sharp peaks for the P-O stretching vibrations, *i.e.* a strong peak centered at 987 cm^{-1} and a medium shoulder at 1124 cm^{-1}. The peaks were well pronounced, and not broad, reflecting its crystalline nature. These results confirm that the three phases (vivianite, anhydrous amorphous $Fe_3(PO_4)_2$ and Fe-graftonite) have a different (vibrational) local structures and bonding environments as expected from their XRD patterns (Figure 5.2 and 5.3).

To ascertain the nanoscale variation in atomic structure in these phases, *ex situ* TEM analysis coupled to SAED were performed. The solids collected at 400˚C showed a porous non-crystalline material based on broad scattering from its associated SAED pattern (Figure 5.6). The material harvested at 400˚C showed presence of non-uniform circular cavities or holes in its TEM micrographs. The material was nearly anhydrous prior to imaging and analysis (as shown from the TGA data) and there were no observable changes in the pore sizes upon prolonged exposure to the beam. Therefore, we can consider that there were no beam damages in this sample. On the other hand, TEM analysis of the samples harvested from the TGA-DSC run at 700˚C showed aggregated crystals of Fe-graftonite ~ 0.5 µm in sizes, which were also apparently resistant to beam damage. The associated selected area electron diffraction pattern (SAED) of the harvested solids at 700˚C (Figure 5.6-B, *inset*) from the TGA-DSC run (under Ar gas) revealed a mono-crystalline domain of graftonite (~ 0.3 µm in size) based on

the indexed pattern from a *cif* file of Fe-graftonite [194]. The TEM data for this sample agreed with the previous results of amorphous/crystalline nature of this sample from XRD and IR data. The pores were distributed non-uniformly within the sample and varied in terms of pore size diameters, with the surface having smaller pores and as compared to the bulk. At the vivianite-air interface, the minimization of surface energy (via smoothing/ reduction of pore-size) during heating may be a contributing factor to leading to variations in pore-size distribution within the sample, similar effects have been reported for heat-treated goethite [200].

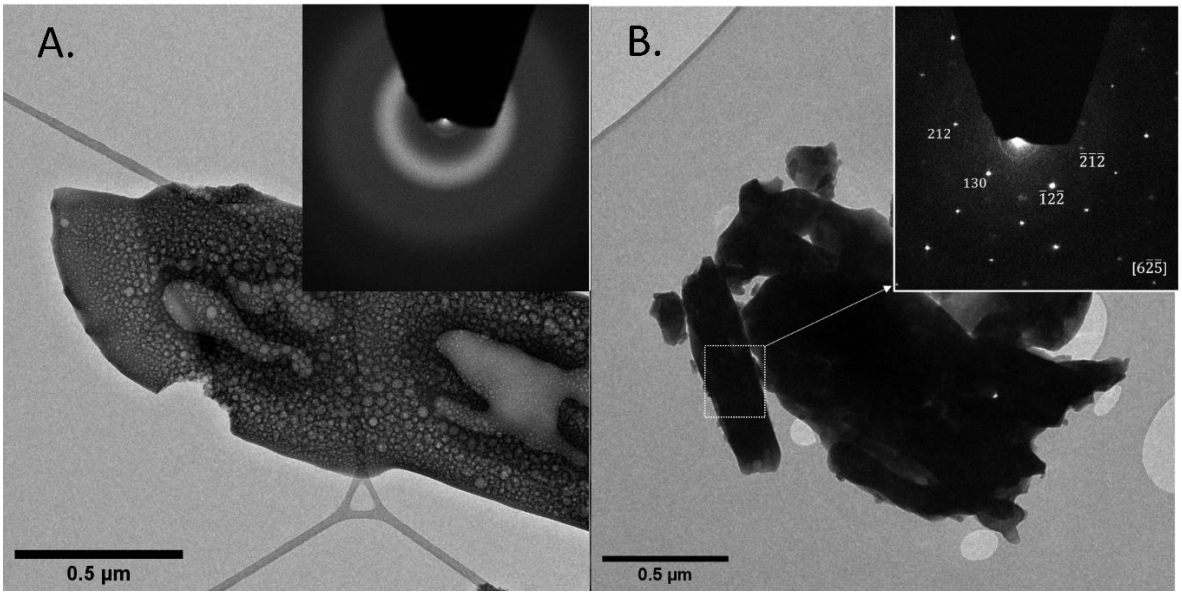

Figure 5.6. *Ex situ* TEM micrographs and associated indexed Selected Area Diffraction (SAED) patterns within *insets* for (A) amorphous $Fe_3(PO_4)_2$ (400˚C) and (B) graftonite (700˚C).

The morphologies and surface habits of the two crystalline end phases, vivianite and graftonite, when imaged *ex situ* via SEM (Figure A3S3, appendix III), revealed tabular crystals within a size range of 5 – 10 µm. Vivianite occurred as aggregated crystal platelets with the surface of each crystalline platelet being smooth. On the contrary, the surface morphology of the Fe-graftonite platelets was not smooth, but rough and porous. The presence of these surface features may be directly linked to the holes or "bubble" – like features in the amorphous anhydrous intermediate at 400˚C, as observed in TEM micrographs (Figure 5.6). During *in situ* SEM experiment (Figure A3S4, appendix III) we observed most of transformation effects detected by other *ex situ* methods (TEM, SEM), namely: cracks formation at the temperatures above 400° C, shrinking of particle agglomerates and formation of "bubble"- like contrast features at the surface. These features on the final graftonite surface show that the morphological features have been transferred from the amorphous → crystalline state, during this

(solid-solid) transformation. The outlines and shapes of the vivianite particles were preserved after heating (amorphization) and their volume shrunk rapidly via re-crystallization during transformation to graftonite. Note, that the temperatures of transformations are higher during *in situ* experiments, compared with *ex situ* experiments, because of less contact area of a sample with the heater causing a lower sample temperature on the imaged surface.

As expected from the collective data, both phases showed major peaks for Fe, P and O in their SEM-EDX profiles. Fe and P peaks in the EDX spectra (Figure A3S5, appendix III) show similar relative intensities, qualitatively verifying their expected chemical compositions. A calculated Fe:P ratio of 1.45 for vivianite, and 1.51 for Fe-graftonite, was obtained from the peak area integrals agreed with a calculated theoretical Fe:P ratio of ~ 1.5 for both these phases translating into a chemical composition of $Fe_3(PO_4)_2$.

5.3.4. Changes in the mineralogy of this transformation in the presence of oxygen

It is essential to note that all heating experiments, so far, were performed in the absence of oxygen and under an inert atmosphere (N_2 or Ar gas) to prevent a potential $Fe^{2+} \rightarrow Fe^{3+}$ oxidation in the initial vivianite sample. Once formed, our analyses of graftonite (a Fe^{2+} compound) showed that its crystal structure (XRD pattern) and local bonding environment (IR spectrum) remain unchanged even after prolonged aerial exposure (1 month), agreeing to literature results [201].

This suggests that once vivianite is anoxically heated and transformed to graftonite (~ 500 – 700 ˚C), the transformed product is no longer susceptible to aerial oxidation. To observe the effect of oxygen on this transformation pathway, we heated synthetic vivianite in an air furnace, up to 700˚C for 1 h. The oxic heat-treatment surprisingly yielded a crystalline yellow-colored powder, instead of the gray-colored graftonite. Qualitative XRD phase identification of the yellow powder gave agreeable fits with a pure crystalline ferric phosphate phase ($Fe^{3+}PO_4$) known as rodolicoite [202] (Figure 5.7) and graftonite was not present in the sample. This was indeed a surprising discovery because rodolicoite has a different structure than vivianite or graftonite. It has a tetrahedral coordination of Fe atoms and crystallizes in the $P3_121$ tetragonal space group, contrary to the monoclinic $P2_1/c$ space group of graftonite. Therefore, the XRD analysis reveals that Fe has completely oxidized to +3 oxidation state and it differs structurally from both vivianite and graftonite. Previous results of Huang *et al* showed that the transformation of amorphous ferric phosphate ($Fe^{3+}PO_4$) → rodolicoite, occurs upon heating the amorphous ferric phosphate (beyond 620˚C) in the presence of air [203]. Here, the starting material was vivianite, showing that the complete oxidation of $Fe^{2+} \rightarrow Fe^{3+}$ may have occurred prior to the

crystallization of rodolicoite. This can be understood by the oxidation of vivianite into triclinic metavivianite upon aerial exposure [65] and its potential transformation to rodolicoite during heat-up in the air furnace.

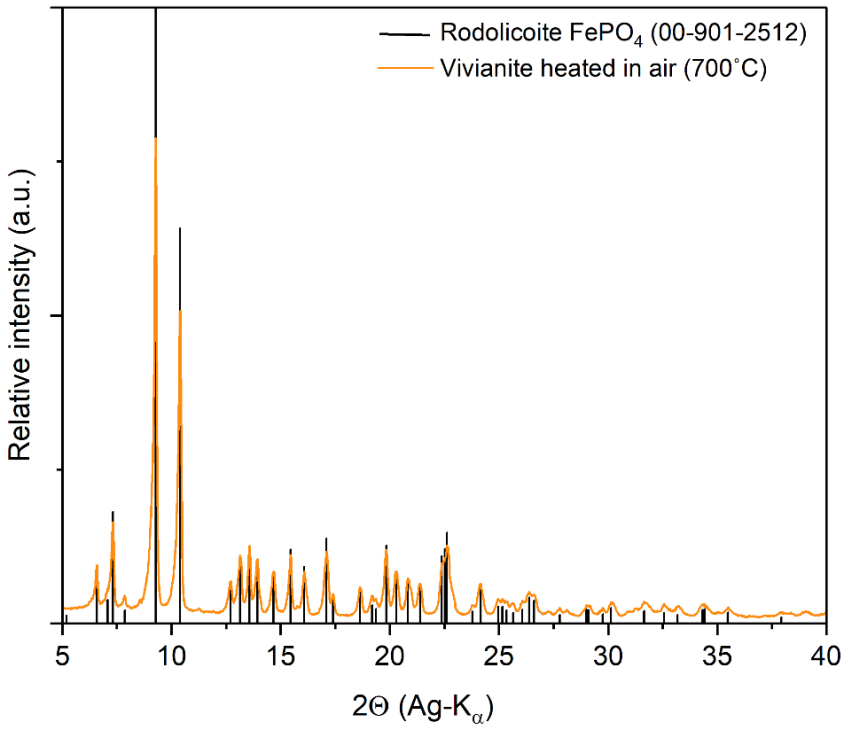

Figure 5.7. Measured XRD pattern of vivianite heated in an air furnace up to 700˚C for 1 h (orange trace) matching with a calculated XRD pattern of crystalline ferric phosphate (rodolicoite) from COD database (00-901-2512) – black bars.

To ascertain the oxidation states of iron in the different phases, XANES analysis at the Fe-K edge and TEM-EELS measurements were performed. The position of the first-derivative maximum of the Fe K-edge XANES spectra at ~7121 eV of gratonite indicates a bulk oxidation state of Fe^{2+}, matching the maxima of Fe(II)-bearing phases such AFEP and vivianite (Figure A3S6, appendix III). Furthermore, the shell-by-shell fitting of the Fe K-edge EXAFS spectra allowed determination of the local Fe bonding environment (coordination number, CN) and bond distances (*R*) of the different phases (see appendix III, Figure A3S7 and Table A3S3).

The first neighbor contribution to EXAFS spectra of the vivianite is best fitted with CN ~ 6.7 and an Fe-O bond distance ($R_{Fe\text{-}O}$) of 2.09 Å. In case of a-$Fe_3(PO_4)_2$ (400 °C), these parameters are best fitted with CN ~ 4.2 and $R_{Fe\text{-}O}$ of 2.03 Å, which can be understood as a dehydration and atomic rearrangement process. The CN and *R* values of a-$Fe_3(PO_4)_2$ are lower than those of the AFEP ($CN_{Fe\text{-}O} \approx 6.4$, $R_{Fe\text{-}O} = 2.13$

Å) [163], which is a partially hydrated phase. Similarly, the first shell Fe-O of graftonite (700 °C) has the lowest CN value of ~3.7 and a shorter $R_{Fe\text{-}O}$ of 1.99 Å. The lower amplitude (and thus CN value) of the transformed samples could be caused by potential destructive interferences with Fe-O scattering waves due to the large distortions in the three distinct Fe-O polyhedra. The decreasing $R_{Fe\text{-}O}$ upon heat treatment can be attributed to a greater mass percentage of phosphorus and therefore higher Fe → oxygen → phosphorus π back bonding interactions [163].

Figure S8 (appendix III) shows illustrative HAADF-STEM images of a-$Fe_3(PO_4)_2$, graftonite and rodolicoite (c-$FePO_4$, reference spectrum of Fe^{3+}) and corresponding the O-K and the Fe-$L_{2,3}$ edge spectra. The O-K edge shows a pre-peak feature (~ 531 eV) for rodolicoite, whereas the other two (mainly Fe^{2+} phases) graftonite and a-$Fe_3(PO_4)_2$ - lack this feature. This pre-peak feature corresponds to electronic transitions from the O *1s* (core state) → O (*2p*) – Fe (*3d*) (hybridized states) [204]. The height of the pre-peak is related to the occupancy of Fe 3d orbitals and Fe-O bond distances, Fe^{3+} phosphate ($FePO_4$) distinctly shows this feature at ~ 532 eV, whereas Fe^{2+} phase ($LiFePO_4$) lacks it [205]. The two major features of the Fe-$L_{2,3}$ are the strong white lines L_3 and L_2 due to the spin orbit splitting of the 2p core hole [205] and separated by about 12 eV. Rodolicoite (Fe^{3+} in the tetrahedral site) is characterized by an L_3 edge peak maximum at 711 eV, whereas a-$Fe_3(PO_4)_2$ and graftonite are characterized by an L_3 edge peak maximum at 709 eV. a-$Fe_3(PO_4)_2$ shows a shoulder feature at ~ 711 eV. These Fe- $L_{2,3}$ edges show a characteristic behavior with changing Fe oxidation states. Partial aerial oxidation of the vivianite sample can also lead to Fe^{3+} impurities in the annealed products. Therefore, to synthesize graftonite, special care must be taken to ensure anoxicity of the system.

The atmospheric-dependent pathways of this transformation can be explained by the oxidation of Fe^{2+} → Fe^{3+} in vivianite structure, which has been proposed to occur via two potential pathways. Firstly, by diffusion of oxygen through the parallel layers (*ac*) in its crystal structure followed by decomposition of the crystal lattice water into hydroxyl ions coordinated to the Fe^{3+} sites [64]. A second proposed pathway is via water auto – oxidation through decomposition of crystal water upon heating vivianite in vacuo under air [64]. The following chemical reaction summarizes the oxidation pathway of Fe^{2+} ions in the crystal structure, in the presence of oxygen

$$4\,Fe^{2+} + 2\,H_2O + O_2 \xrightarrow{\Delta} 4\,Fe^{3+} + 4\,OH^-$$

The above reaction may cause Fe^{2+} → Fe^{3+} oxidation and formation of a new ferric phosphate phase – rodolicoite, instead of graftonite, in the presence of oxygen. Furthermore, the stability of Fe-

graftonite and its resistance to Fe^{2+} oxidation may be understood by lack of a key chemical component for these two reactions i.e. H_2O molecules, in its structure. Thus, structural hydration may be linked to aerial $Fe^{2+} \rightarrow Fe^{3+}$ oxidation, and ultimately to crystal stability in the Fe^{2+}-PO_4^{3-} system. These results confirmed the HT-transformation of vivianite to graftonite occurs exclusively under anoxic conditions (N_2 or Ar gas), which prevent the initial oxidation of vivianite into ferric phosphate. Partial oxidation of the starting material (vivianite) may lead to formation of a mixture of the two phases *i.e.* graftonite and rodolicoite, depending on the extent of aerial exposure and other physical parameters of system (temperature and hydration).

5.4. Conclusions

Vivianite notably undergoes amorphization and recrystallization at T > 500˚C under N_2 / Ar gas (ambient pressure) to form graftonite, a crystalline $Fe_3(PO_4)_2$ phase. Upon heating beyond 500˚C, the crystallization of graftonite via amorphous ferrous phosphate (a-$Fe_3(PO_4)_2$) is thermodynamically feasible via an exothermic enthalpic release of – 16.767 ± 0.26 kJ/mol. Our results show the major variations in structural hydration, crystal symmetry, Fe coordination and morphology, induced by this HT-driven atomic rearrangement. The dehydrated/annealed samples (graftonite and a-$Fe_3(PO_4)_2$) show 'bubble'-like features in their electron micrographs and possess a porous structure, contrary to uniform and smooth surfaced vivianite crystals. The total volume of the initial vivianite is reduced by ~ 3 % after transforming to graftonite. However, the overall shape of the vivianite crystals is preserved despite their shrinking volume, as observed via *in situ* SEM analyses. Surprisingly, if the initial vivianite is heated in a furnace to 700˚C under air, it completely oxidizes to a stable ferric crystalline phosphate phase *i.e.* rodolicoite ($FePO_4$). Therefore, the transformation of vivianite can occur via different pathways depending on the atmospheric composition. These insights can be applied for a facile synthesis of thermodynamically stable iron phosphate materials (graftonite, rodolicoite, a-$Fe_3(PO_4)_2$) from synthetic vivianite, at ambient pressure. In a broader context, our work illuminates a direct link between crystal structures of vivianite and graftonite-rodolicoite, which offer novel insights into thermodynamic crystal stability in the Fe-PO_4 system.

Chapter 6. Summary and outlook

The results derived from this dissertation can be divided into three primary sections: (I) elucidation of the nucleation mechanism, (II) examination of growth kinetics, and (III) investigation into thermally induced phase transformations of vivianite. Each facet was scrutinized through laboratory-based experiments, aimed at understanding their intricate underlying mechanisms. The results revealed new insights on the fundamental nonclassical nucleation and growth pathways of vivianite, as well as elucidating phase transitions and the stability dynamics of ferrous phosphates.

6.1. Mechanism of non-classical nucleation pathway of vivianite formation via AFEP

Non-classical nucleation pathways have been known for many sparingly soluble mineral phases, and an understanding of the properties of amorphous intermediates in these systems — both chemical and physical — is critical to establishing the mineral crystal growth processes. Prior to this study, there was limited knowledge about the intermediates involved in vivianite formation. Vivianite is known for its low solubility (K_{sp} ~ 10^{-36}) [66] and occurrence in anoxic ferruginous systems, although the accuracy of equilibrium calculations regarding its precipitation has been questioned [3, 7, 9, 11, 13].

As elaborated upon in Chapter 3, the results of my laboratory experiments show that vivianite nucleates via an amorphous ferrous phosphate (AFEP) phase which precipitates from a solution oversaturated with vivianite. Initially, no vivianite is observed in these systems and only AFEP is detected, but as time progresses the AFEP nanoparticles hydrate, undergo changes in local structure and transform to vivianite in solution [66]. The *ex situ* analysis of the phases reveals notable distinctions in the local (bulk) structure between amorphous ferrous phosphate (AFEP) and vivianite. Specifically, AFEP exhibited a discernibly less distorted structure when compared to vivianite, as evidenced by thorough structural analyses [66]. Traditionally, the transformation of amorphous intermediates to crystalline phases is often associated with dehydration processes, a phenomenon commonly observed in various mineral transformations, such as the conversion of amorphous calcium carbonate (ACC) to calcite [146] and amorphous calcium phosphate (ACP) to hydroxyapatite [206]. However, contrary to prevailing notions, the present study unearthed evidence suggesting that hydration may play a role in the amorphous-to-crystalline transformation process of AFEP to vivianite. The increase of water content or hydration levels observed during this transformation was found to exert a profound influence, potentially hindering the impeding the subsequent crystallization of vivianite. The interplay

between water molecules and the structural dynamics of AFEP is a pivotal determinant governing the transformational pathway from AFEP to vivianite, thus underscoring the multifaceted role of water in mediating mineral phase transitions.

In various environmental systems, occurrences of amorphous ferrous phosphate phases have been documented, exemplified by notable instances such as anoxic sewage infiltrated aquifer (Massachusetts, USA) [13]. Likewise, within anoxic meadow soils (Denmark), analogous observations have been made, where a spongy or amorphous material was discerned and subsequently identified as ferrous phosphate [7]. Notably, this amorphous phase coexists partially alongside vivianite within the soil matrix [7]. In both cases, the origin of this amorphous Fe^{2+} phase was not fully understood. Drawing from the findings in Chapter 3, there exists a possibility that the aforementioned ferrous phosphate material may indeed correspond to the AFEP phase, serving as a metastable intermediate/precursor in the transition towards stable crystalline vivianite. It is imperative to acknowledge that phosphate-containing wastewaters are discharged on a global scale. Given the widespread distribution of iron in soils, the formation of vivianite and AFEP, may be a widespread phenomenon within anoxic environmental contexts. A subsurface transport process of this AFEP phase could have significant implications regarding the movement of reactive pollutants (toxic trace metals and radionuclides) in groundwater or soils. Therefore, it is necessary to understand its properties and reactivity.

6.2. Kinetics of vivianite growth investigated as a function of temperature

Synchrotron-based time-resolved X-ray scattering is a powerful tool for *in situ* characterization and evolution of the reaction products for aqueous precipitation reactions. Specifically, temporal progression revealed the emergence of discernible vivianite crystalline Bragg peaks, concomitant with a pronounced reduction in the volume fractions of amorphous ferrous phosphate (AFEP) particles within the solution, as elucidated through meticulous SAXS-WAXS modeling. The results also showed that the total lifetime of AFEP nanoparticles was inversely proportional to the systemic temperature. Such revelations amplify the scope of its occurrence and implications within environmental and geological systems.

These results also show the direct link between the nucleation and growth processes of vivianite. The rate of the transformation reaction is directly proportional to temperature. By applying the JMAK model, the growth process of vivianite from AFEP was characterized, revealing an apparent activation energy of approximately 51 kJ/mol using the Arrhenius model.

Another interesting discovery was the difference in the vivianite morphology, particularly crystal splitting – at different temperatures. The fast growth rate (60˚C) produced radial floret-like morphology, as opposed to a mixture of sheaf-like/radial floret morphology at lower temperatures (10˚C). This variability in crystal splitting suggests that growth processes are linked to crystal morphology, providing insights that can be applied to understand vivianite growth in natural systems under different environmental conditions.

The findings presented in Chapter 5 constitute a pivotal contribution towards elucidating the intricate thermal behavior and phase transformations exhibited by vivianite under elevated temperatures extending up to 700˚C. While previous studies have endeavored to probe the thermal characteristics of vivianite through thermal analysis techniques such as thermogravimetric analysis coupled with differential scanning calorimetry (TGA-DSC), notable discrepancies in the reported outcomes underscore the need for further investigation. For instance, Waerenborgh *et al.* reported an intriguing sequence of phase transformations occurring during the heating of vivianite in air, wherein an amorphous intermediate material transitions successively to a transitional cristobalite-type ferric orthophosphate before stabilizing into the berlinite-type phase characterized by a compositional arrangement of Fe_3PO_7 [207]. Conversely, Frost *et al.* observed a distinct thermal profile through their TGA-DSC coupled with mass spectrometry analyses, noting a sequential loss of water content up to 450˚C followed by subsequent oxygen loss from the structural matrix extending up to 1000˚C [196]. Such divergent findings highlight the complexity inherent in vivianite's thermal behavior and show the necessity for a comprehensive examination thereof.

The results from Chapter 5 show that vivianite undergoes dehydration during heat-treatment upto ~ 400˚C under inert gas (Ar or N_2) to give an amorphous material, this finding agreed with the previous results [196, 207]. The phase at 400˚C is identified in this work as an anhydrous amorphous ferrous phosphate based on XAS (Fe-K edge) and TEM-EELS data. This intermediate converts to crystalline graftonite ($Fe_3(PO_4)_2$) starting at ~ 500˚C and this transformation is accompanied by an exothermic enthalpy release and decrease in initial unit cell volume. Graftonite has a distinctly different structure ($P2_1c$) than vivianite ($C2/m$) and varying Fe coordination (mixture of five-and six-fold), but its Fe:P ratio is identical to vivianite and amorphous ferrous phosphate, showing that there are no redox processes involved but only dehydration. Furthermore, the *in situ* temperature-resolved SEM experiments revealed that this is a pseudomorphic transformation, and a shrinking of the crystals was observed, which agreed with the Rietveld refinements of the crystalline end-members.

Notably, these findings contrast with existing literature [196, 207], as no prior investigations have documented the anoxic transformation pathway of vivianite to graftonite. Notably, the experimental conditions employed herein, were conducted under an inert gas atmosphere, likely precluded the oxidation of Fe^{2+} → Fe^{3+}. Conversely, contrasting outcomes were observed in heating experiments conducted in air, wherein an amorphous intermediate phase emerged at 450˚C, subsequently transitioning into rodolicoite—a distinct crystalline ferric phosphate phase characterized by a $P3_12_1$ space group. This transformation aligns with the berlinite-type phase elucidated by Waerenborgh et al [207]. Collectively, these observations reveal the critical influence of the experimental atmosphere — whether inert or aerial — on the oxidation dynamics of iron species (Fe^{2+} to Fe^{3+}), consequently dictating the resultant composition and crystalline phase attained.

These novel results offer insights into the high-temperature induced phase transformation behavior of vivianite under different environmental conditions, with implications for materials science and the synthesis of iron-phosphates. Understanding these pathways enhances our comprehension of vivianite's behavior in various systems, whether anoxic or oxygenated, contributing to broader knowledge in the field.

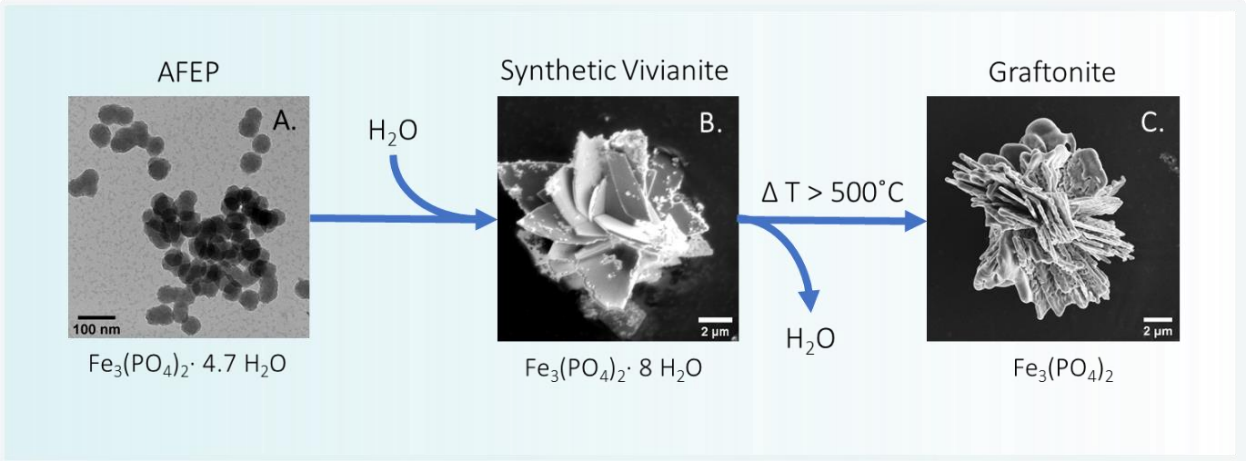

Figure 6.1. Summary of nucleation and phase transformation of vivianite under anoxic conditions; (A) TEM micrograph of AFEP- which hydrates in solution to give (B) radial florets of crystalline vivianite (SEM micrograph), when subjected to heating > 500˚C undergoes dehydration and transformation to (C) crystalline graftonite (SEM micrograph).

6.3. Future Perspectives

The results of this study have generated novel insights into the mechanism of nucleation, growth and transformation phenomena of vivianite. However, it is important to acknowledge that several crucial questions arise from these findings.

Chapter 3 and 4 provided fundamental knowledge of the structure, chemical bonding environment, properties and mechanism/kinetics of AFEP transformation. Nevertheless, the solubility of the AFEP phase is of particular interest for establishing the chemical composition of the environment at the time of precipitation. Further studies need to be performed to predict its supersaturation in different environmental conditions. The thermodynamic stability of AFEP remains an unexplored aspect requiring further investigation. Theoretical methods, such as density functional theory (DFT) and *ab initio* calculations, offer valuable tools for probing the thermodynamic properties of AFEP in detail. These computational approaches hold promise for elucidating the energetics and stability of AFEP under varying environmental conditions.

Furthermore, in natural systems, particularly iron-rich acidic soils (pH < 7) or phosphate-rich alkaline soils (pH > 7), it is difficult to ascertain the resulting kinetics/mechanism of this transformation due to changing pH. Organic additives such as bicarbonates, citrates and humic acids are widely present in soils and they can function as complexing agents, which may affect the stability and transformation kinetics of AFEP. Experimental studies need to be performed to analyze the effect of pH and organic additives on the mechanism of nucleation and growth of vivianite, as well as the stability of AFEP, for a wider range of systems. The presence of AFEP may also be a widespread phenomenon, therefore its occurrence in environmental systems (such as anoxic soils, lakes groundwater streams and sewage sludge) could be further explored via fieldwork studies, showing the larger impact of this metastable phase on contaminant (toxic trace metals and radionuclides) and nutrient (Fe and P) cycling.

Chapter 5 reports a novel atmosphere-dependent amorphization and recrystallization of vivianite, which is very interesting from a structural perspective. However, the *in situ* experiments have only been performed for anoxic systems, it would be very interesting to observe the transformation of vivianite → amorphous ferric phosphate → rodolicoite by aerial *in situ* experiments (*i.e.* XRD, TGA-DSC). Moreover, from a fundamental perspective, it is intriguing to investigate the reversibility of this transformation, specifically the potential for the conversion of graftonite → vivianite under anoxic aqueous conditions at elevated temperatures. Such experimentation holds promise for elucidating the thermodynamic feasibility and kinetic pathways associated with this transformational process,

thereby contributing to a deeper understanding of the phase behavior and stability of iron-phosphate minerals in dynamic environmental settings. This may explain the geological co-occurrence of vivianite (secondary) and graftonite (primary) phases in altered granitic pegmatites, which may have been subjected to late-stage hydrothermal fluid leaching and alteration [60].

In conclusion, while this study represents a significant step towards unraveling the complexities of vivianite's nucleation, growth, and transformation phenomena, it also emphasizes the need for continued research to address remaining questions and further advance our understanding of this important mineral phase. This research holds the potential to enhance our comprehension of geochemical processes occurring within contemporary environments such as lakes, soils, and wastewater systems, as well as ancient ferruginous systems. The widespread occurrence of vivianite shows its significance in influencing biogeochemical cycling and mineralogical transformations. The findings of this study may offer valuable contributions to our understanding of the key processes and factors driving Fe^{2+} and phosphate environmental dynamics.

Appendix I

Section AS1. Preparation of sodium phosphate buffer solution

Preparation of sodium phosphate buffer solution was performed by mixing calculated amounts of NaH_2PO_4 and Na_2HPO_4 solids in the required volume of water to achieve a particular pH and concentration of phosphate in solution. The calculations were based on Henderson Hasselbalch equation taking the second dissociation constant of phosphoric acid as $K_2 = 6.2 \cdot 10^{-8}$

$$K_2 = \frac{[H^+][HPO_4^{2-}]}{[H_2PO_4^-]}$$

The calculated $pK_2 = 7.21$ for the chosen range for vivianite precipitation (pH 6 – 8). Hence, the following equation can be used to calculate the amount of di- and mono-basic phosphates to prepare the buffer solution of required pH

$$X_{NaH_2PO_4} = \frac{X_{PO_4}}{10^{(pH-7.21)} + 1}$$

Where $X_{NaH_2PO_4}$ is the calculated concentration with the input parameters of required final phosphate concentration (X_{PO_4}) and pH. Substituting the calculated amount of $X_{NaH_2PO_4}$ from the above equation, the amount of $X_{Na_2HPO_4}$ can be calculated as

$$X_{Na_2HPO_4} = X_{PO_4} - X_{NaH_2PO_4}$$

Therefore, to prepare 250 mL of 10 mM phosphate buffer of pH 7.2, the di-basic phosphate reagent Na_2HPO_4 (Sigma Aldrich, 99.98 %, anhydrous; 150.1 mg) and monobasic NaH_2PO_4 powder (Alfa Aesar, 99.8 %; 175 mg) were weighed and transferred to the anaerobic chamber in a 250 mL volumetric flask and degassed O_2-free Milli-Q water (18.2 MΩ·cm) was added to it, the flask was closed and shaken to dissolve the salts to obtain a homogeneous solution. The phosphate buffer solution was stored inside the anaerobic chamber inside an acid cleaned and rinsed polypropylene (PP) bottle until further use.

Section A1S2. Thermodynamic modeling of the system

Thermodynamic modeling of the system based on calculations on PHREEQC software (Version 3) [119] using the Thermoddem database [120]

The solubility of vivianite in water can be expressed by the following chemical equilibrium:

$$Fe_3(PO_4)_2 \cdot 8H_2O + 2\,H^+ \rightarrow 3\,Fe^{2+} + 2\,HPO_4^{2-} + 8\,H_2O$$

The solubility product of vivianite is $10^{-35.767}$ and its saturation index (SI) is defined as [66]:

$$SI_{Vivianite} = log \frac{[a_{Fe^{2+}}]^3 \cdot [a_{HPO4^{2-}}]^2}{[H^+]^2 \cdot K_{sp(vivianite)}}$$

At pH 7.2 and a temperature of 25˚C, p_e of -1 (anoxic system) and 1 atm pressure, the system composition was input as:

Species	SI 1 (10^{-3} mol L^{-1})	SI 2 (10^{-3} mol L^{-1})	SI 3 (10^{-3} mol L^{-1})
Fe^{2+}	5	0.5	50
HPO_4^{2-}	5	0.5	50
NH_4^+	10	1	100
SO_4^{2-}	10	1	100
Na^+	5	0.5	50

The following were the calculated solid SI at different concentrations:

Phase	SI 1	SI 2	SI 3
Melanterite ($FeSO_4 \cdot 7H_2O$)	-3.22	-4.55	-2.16
Vivianite	10.19	7.16	12.86

Table A1T1. ICP-OES data for instrumental parameters and quality control (QC) solutions

ICP-OES data for quality control (QC) solutions prepared from purely elemental standards (Merck, CentiPur). The mean results of n replicate analyses are given with standard deviation (SD) and relative standard deviations (RSD)

Parameters	**Fe (mg L^{-1})**	**P (mg L^{-1})**
Wavelength	261.382 nm	213.618 nm
Instrumental limits		
Limit of detection (LoD)	$0.014 \cdot 10^{-3}$	0.0040
Limit of quantification (LoQ)	0.002	0.013
Quality Control (QC)		
QC verify (n = 5)	0.406	0.205
SD	0.008	0.005
RSD	2.0%	2.5%
2RSD	4.1%	5.1%
Reference value	0.406	0.205
Deviation from reference value	0.01%	0.05%

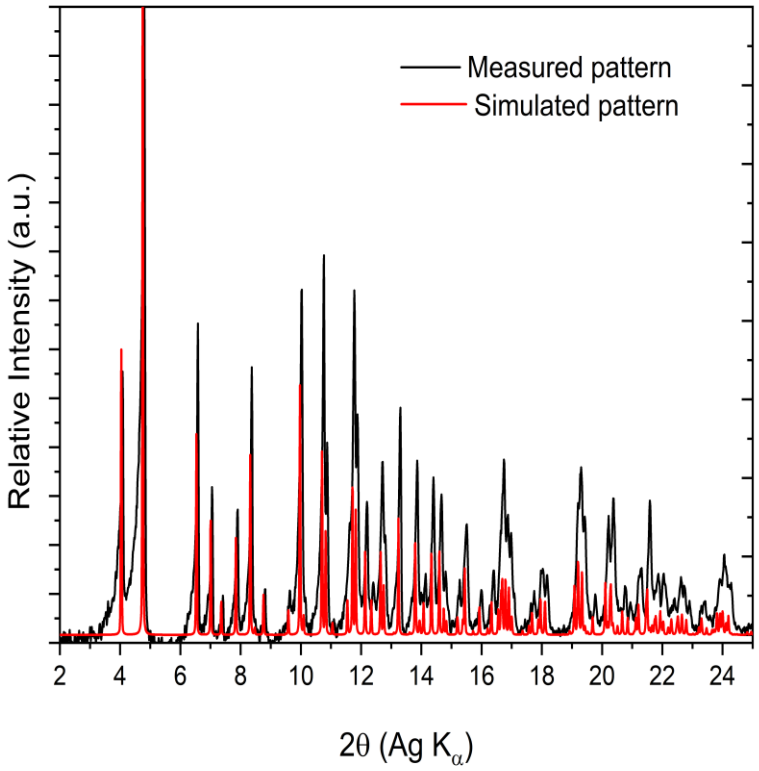

Figure A1F1. Powder X-ray diffraction (XRD) pattern of the collected precipitates (black) and calculated XRD pattern for crystalline vivianite [48] (red). SI 10.19 (1 h)

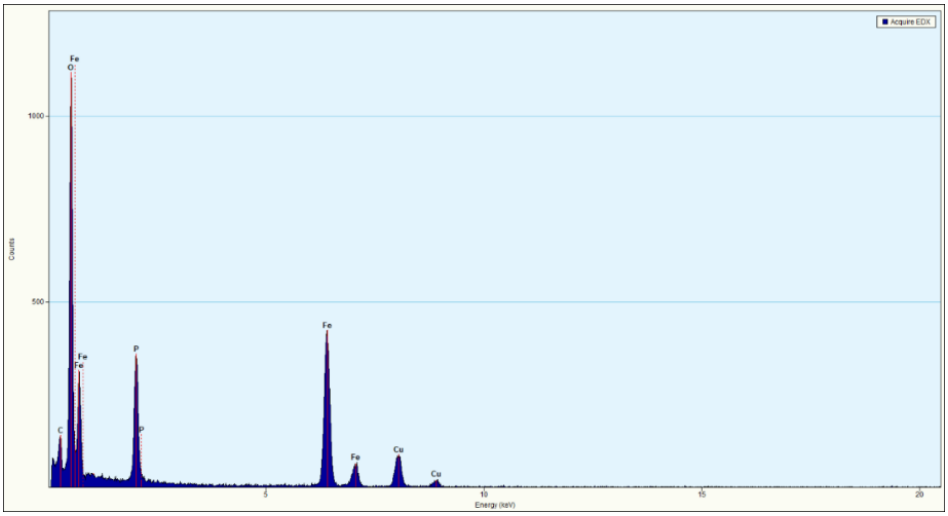

Figure A1F2. STEM-EDS analysis of precursor indicating an iron phosphate phase (SI 10.19), the Cu signal comes from the copper grid background. SI 10.19 – 30 s.

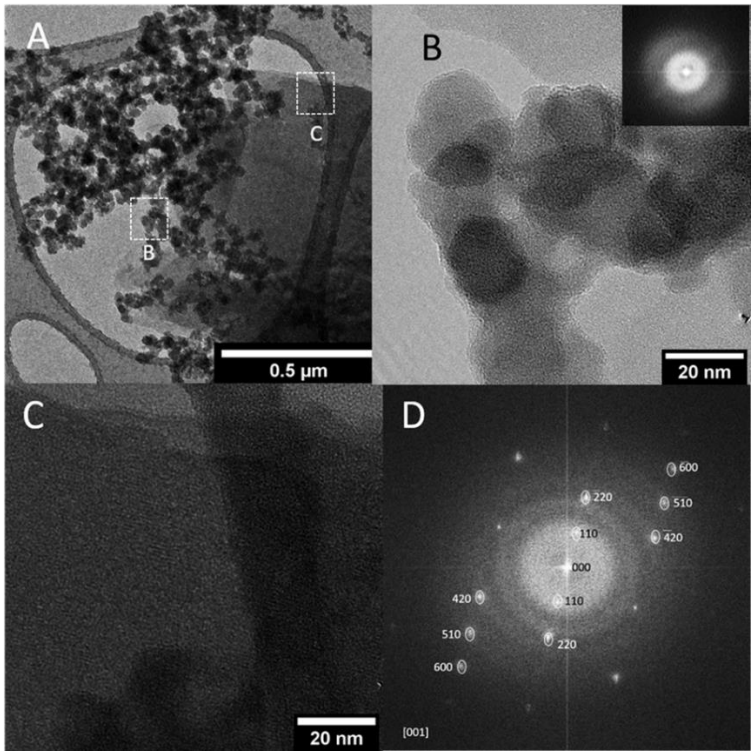

Figure A1F3. (A) TEM micrograph of solids obtained from batch reaction at 100 s with squared areas representing the locations of HRTEM analysis for B and C; (B) HR-TEM of area B showing amorphous intermediate (*inset* FFT pattern); (C) HR-TEM of area C with corresponding crystalline FFT pattern for vivianite indexed in (D). SI 10.19.

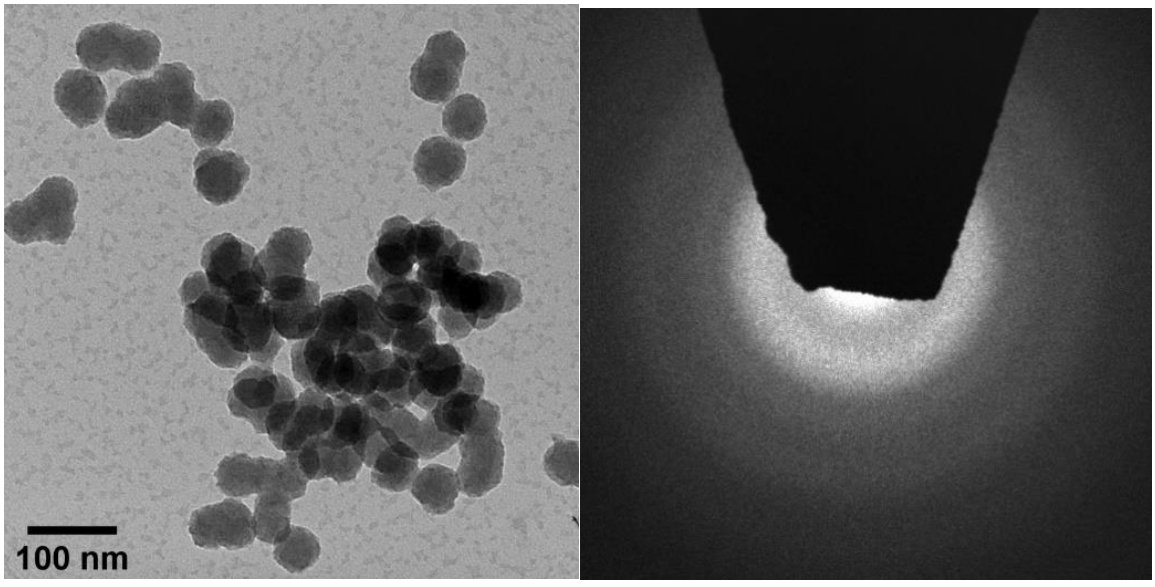

Figure A1F4. *Ex situ* TEM micrographs of solids from a vivianite precipitation experiment at a SI of 7.16: 20 min showing spherical aggregated nanoparticles (~ 50 nm in diameter) and corresponding SAED pattern showing diffuse rings characteristic of an amorphous material.

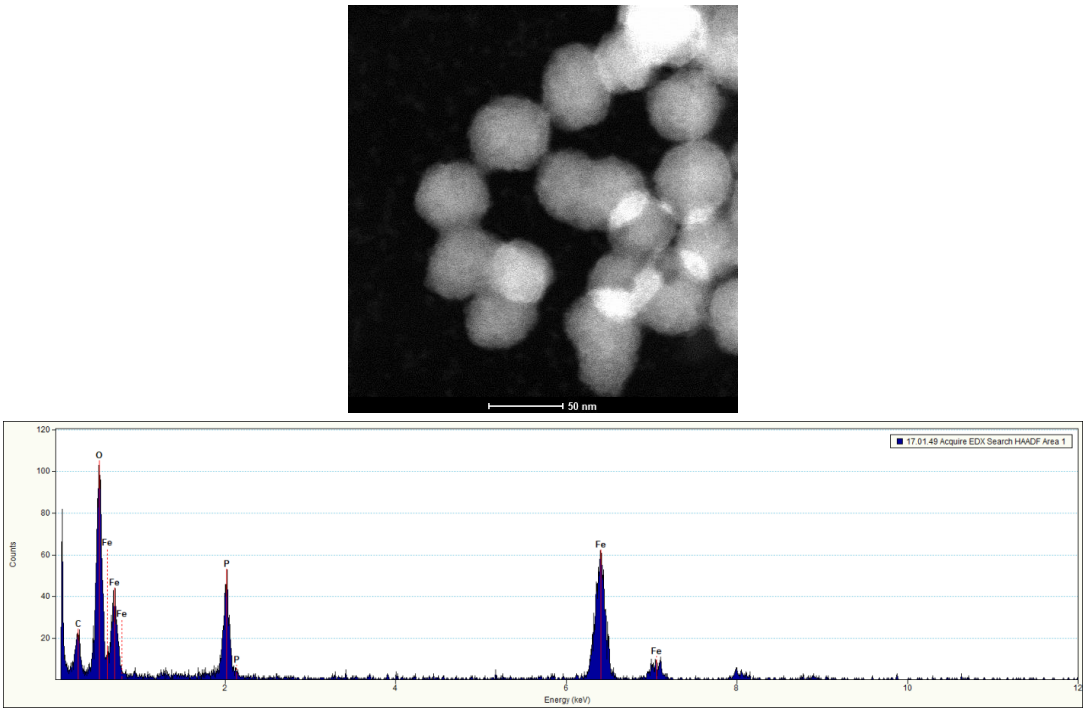

Figure A1F5. STEM-EDS analysis showing aggregated spherical nanoparticles of iron phosphate (SI 7.16) at 20 min.

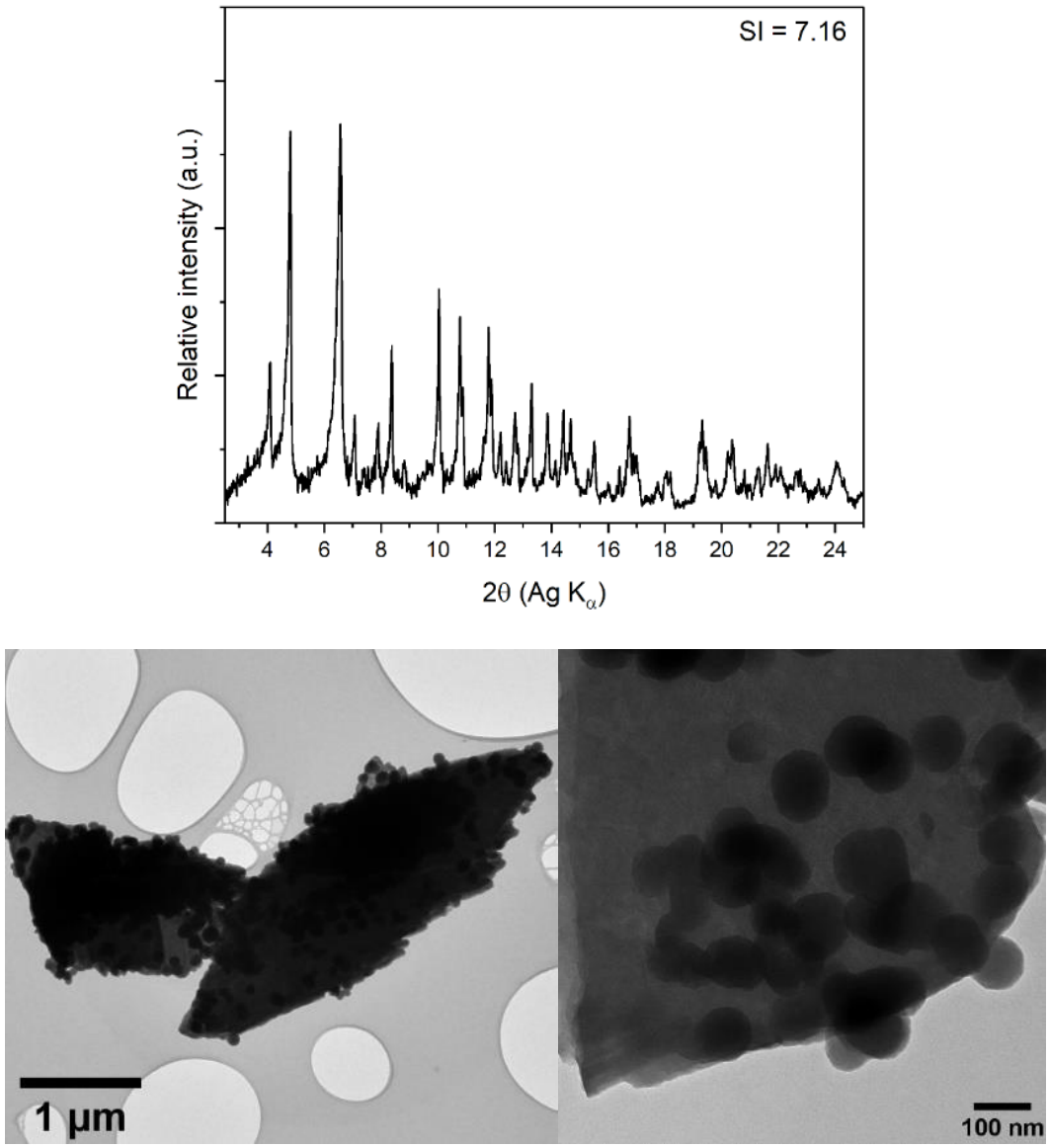

Figure A1F6. XRD pattern of solids from a vivianite precipitation experiment at SI 7.16 48 h after filter quenching (*above*). TEM micrographs of the solids from the reaction mixture at 48 h showing vivianite crystals with aggregated amorphous precursor on its surface (*below*).

Section A1S3: *In situ* pH metric measurements of vivianite precipitation at different super-saturations

Due to the protonated speciation of the phosphate (HPO_4^{2-} and $H_2PO_4^-$) at pH 6.5 – 8.0 [1], the precipitation of vivianite near neutral pH leads to a release of protons and causes a decrease in the total solution pH [11]. The rate of the initial decrease can reflect the rate of initial nucleation of ferrous phosphate phases. At higher supersaturation (SI 12.86) nucleation was almost instantaneous with an induction period of ~ 5 s, observed as a sudden and steep decrease in pH curve. At lower supersaturation (SI 7.16) there was an increase in the induction period (~ 12 s) , as expected [208]. The fast-initial decrease at each supersaturation was proportional to the amount of ferrous phosphate precipitated (H^+ released) in solution.

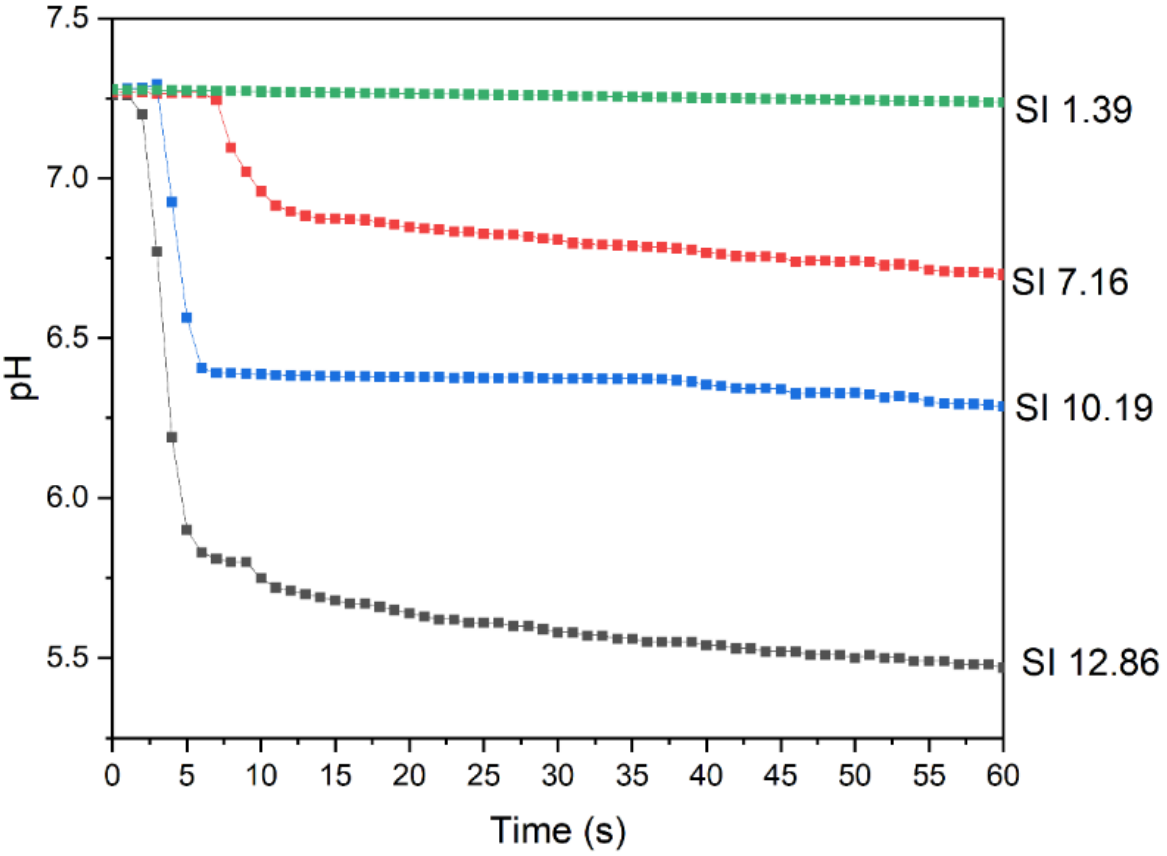

Figure A1F7. In situ time resolved pH metric measurements of vivianite precipitation at different supersaturations at pH 7.2.

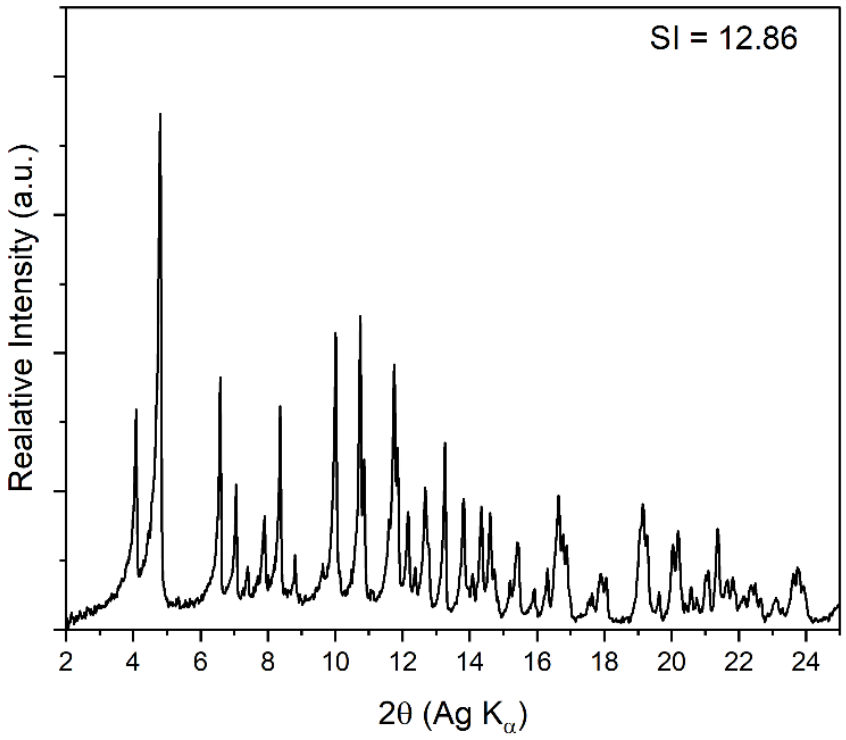

Figure A1F8. XRD pattern of solids from a vivianite precipitation experiment at SI 12.86 immediately after filter quenching, time taken for filtration ~ 20 s.

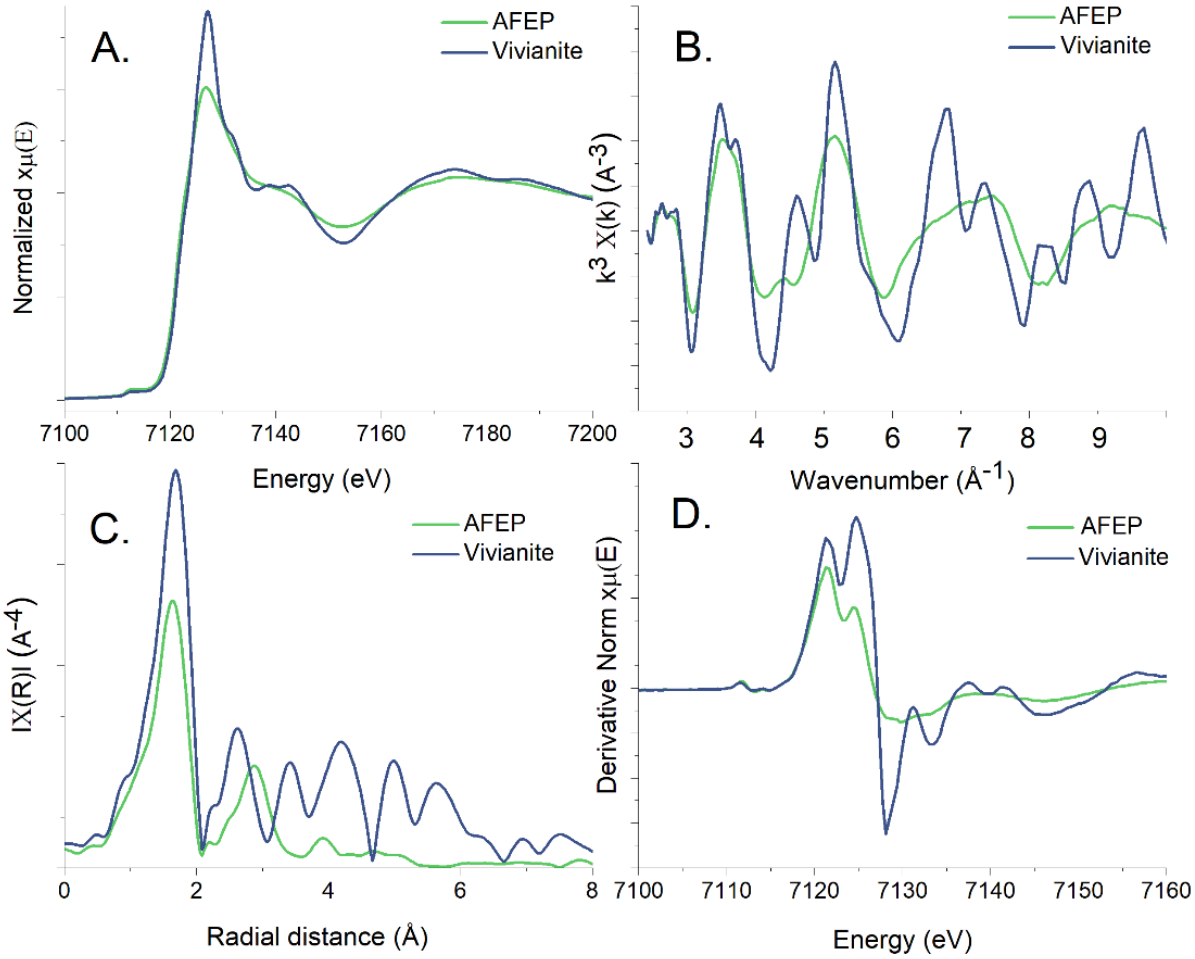

Figure A1F9. (A) Normalized Fe K-edge XANES; (B) k^3-weighted χ(k) EXAFS spectra; (C) Radial distribution function via FT-EXAFS spectra; (D) First derivative of χ(k); for AFEP and vivianite respectively.

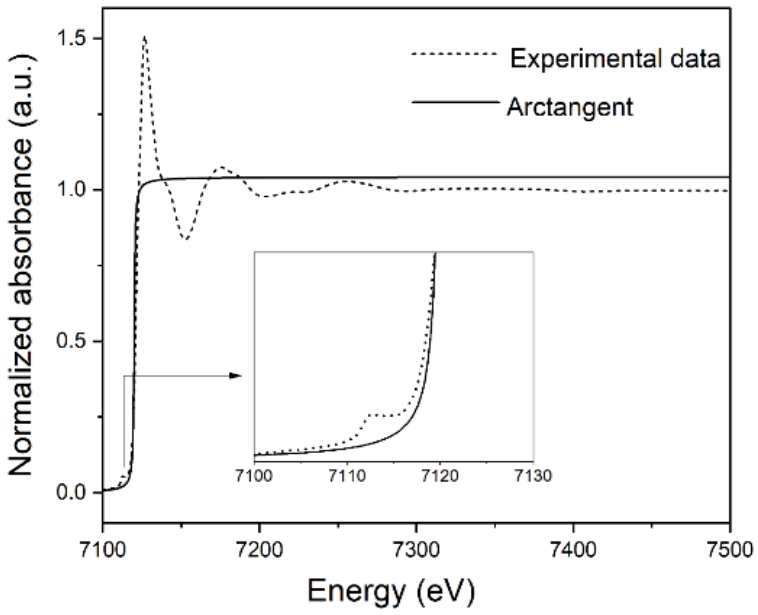

Figure A1F10. Pre-edge extraction [72] from Fe-K edge XANES spectrum of AFEP via subtraction of a modeled arctangent function

Table A1T2.

Fe-K edge XANES pre-edge fitting results for AFEP via Fityk software [127] for Pseudo-Voigt fits (50:50) and Levenberg-Marquradt (least squares) method.

Component type	Component position (eV)	Height	Area [b]	WSSR [c]
Peak 1	7112.70	0.01811	0.0416	-
Peak 2	7112.24	0.00445	0.0056	-
Peak 3	7114.44	0.00703	0.0110	-
Cumulative peak fit [a]	7112.95	-	0.0578 [d]	0.98809

[a] 'Cumulative peak fit' corresponds to the centroid position

[b] Integrated area under the peak (OriginPro (2021) software (OriginLab Corporation, Northampton, MA, USA)

[c] WSSR denotes weighted sum of squared residuals

[d] Represents total area of the cumulative peak fit

Table A1T3. EXAFS analysis via shell-fit results obtained by fitting Fe-K edge EAXFS of synthesized AFEP sample

Path	CN[a]	R (Å)[b]	σ^2 (Å^2)[c]	ΔE_0 (eV)[d]	Red. χ^2 [e]	R-factor
Fe-O	5.4 (0.5)	2.10 (0.01)	0.010 (0.001)	3.4 (0.9)	21.2	0.027
Fe-P	3.5 (1.0)	3.34 (0.01)	0.011 (0.003)			

Best fit value reported with uncertainty in statistical fit for the last digit as shown in parenthesis.

[a] Coordination numbers

[b] Mean half-path length

[c] Debye-Waller factor

[d] Energy-shift parameter

[e] Reduced χ^2 as using the SIXPack interface to the IFEFFIT XAFS analysis package [128]

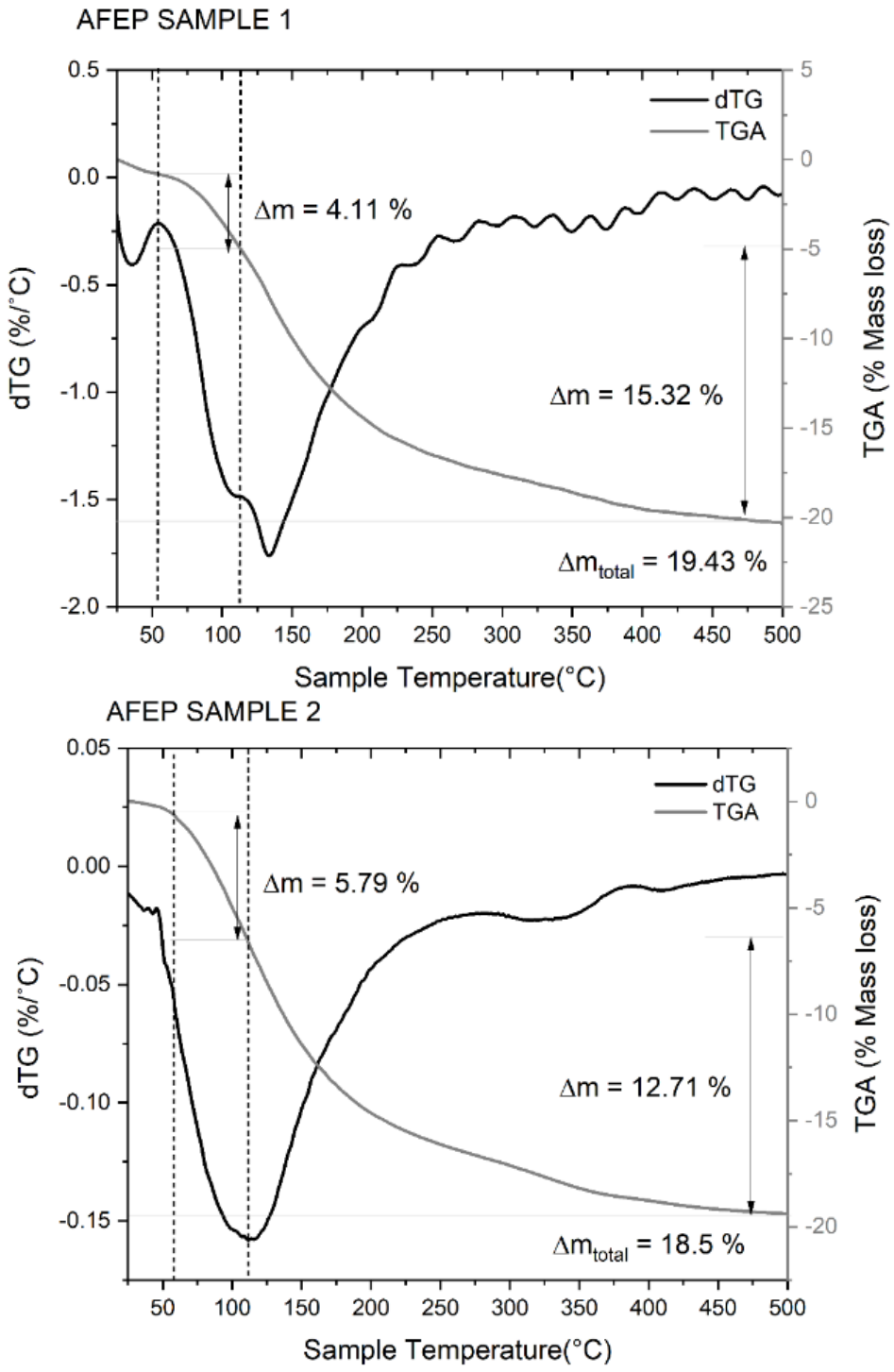

Figure A1F11. Thermogravimetric (TGA) measurement and the first derivative of the TGA plot (dTG) of two AFEP samples under Ar gas flow. Sample 1 was dried under vacuum for 6 h and sample 2 was dried for 24 h, prior to analysis.

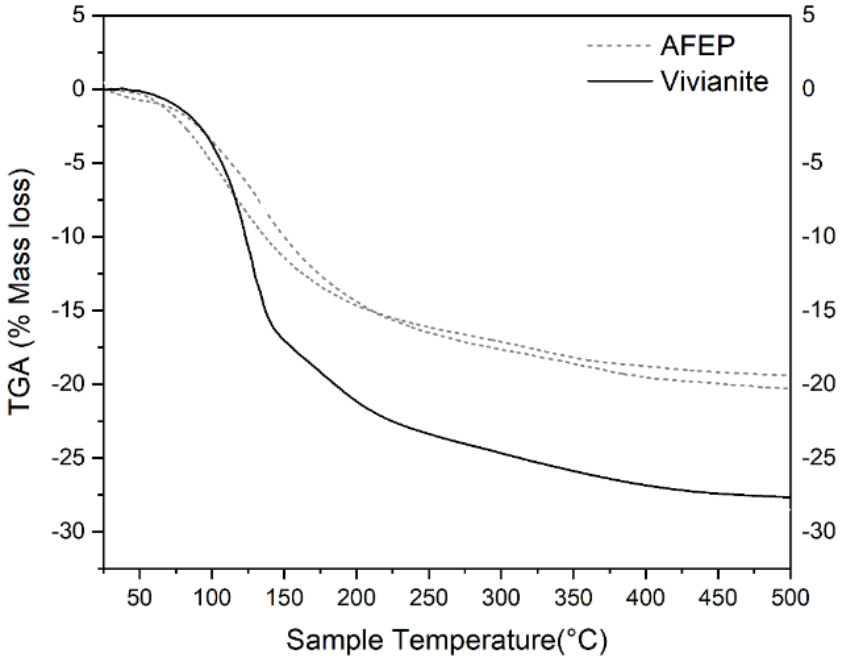

Figure A1F12. Thermogravimetric (TGA) measurement of AFEP (repeat) and vivianite samples under Ar gas flow.

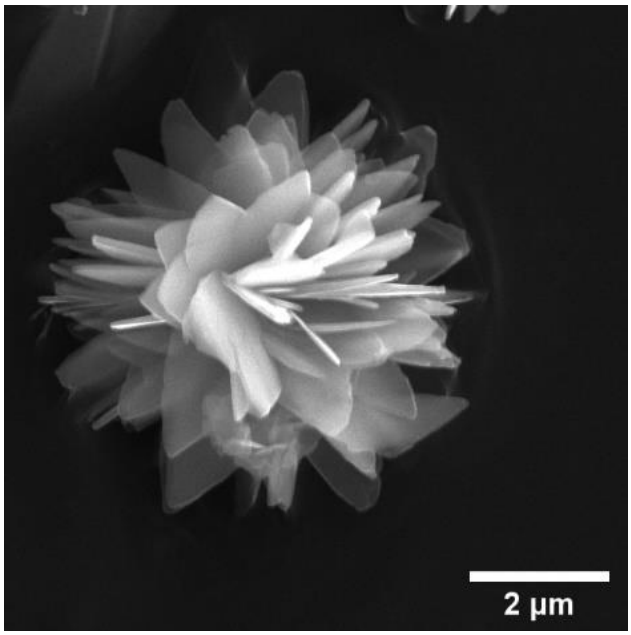

Figure A1F13. SEM micrograph of synthetic vivianite collected from an experiment at SI 12.86 (20 ± 10 s) showing micrometer ranged platy rosette

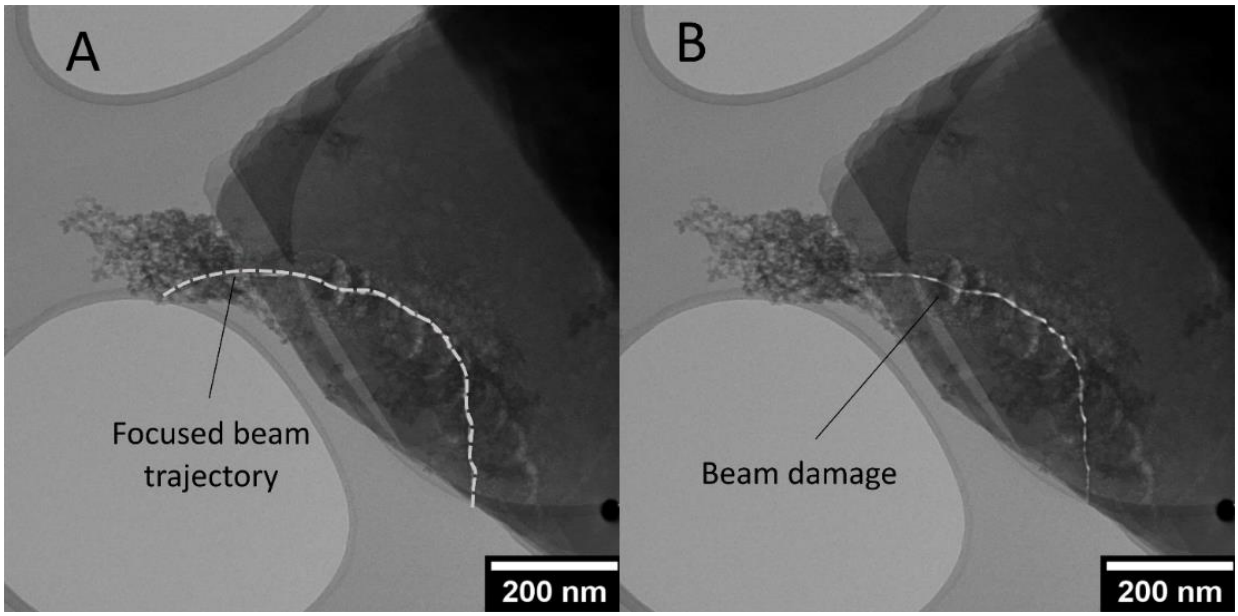

Figure A1F14. (A) TEM micrograph of aggregated AFEP nanoparticles and crystalline vivianite showing the manually focused electron beam trajectory represented by a white dashed line (dose rate 1170 e $Å^{-2}$ s^{-1}). **(B)** TEM micrograph showing the observed beam damage, indicating greater beam damage for crystalline vivianite as compared to AFEP nanoparticles. SI 10.19.

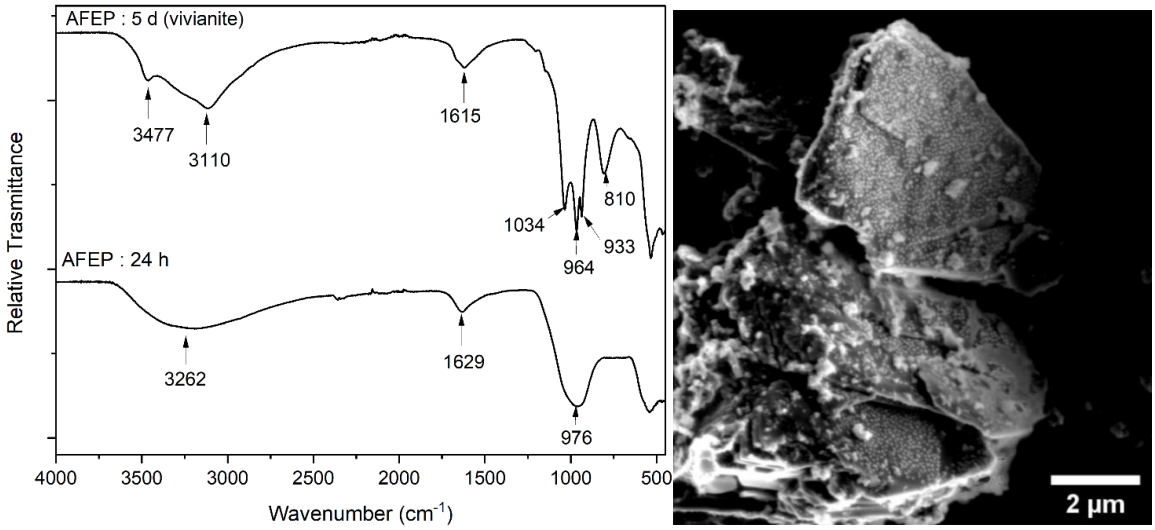

Figure A1F15. FTIR spectra of dried solid obtained after suspending AFEP (10 mg) in 50 ml anoxic deionized water in crimped vials inside the anaerobic chamber after 24 h and 5 d. Sample at 24 h showed no observable changes but presence of vivianite was observed after 5 days (*left*), SEM micrographs of solids after suspending AFEP for 5 d in anoxic DI water showing crystalline vivianite with nanoparticulate texture on their surface (*right*).

Appendix II

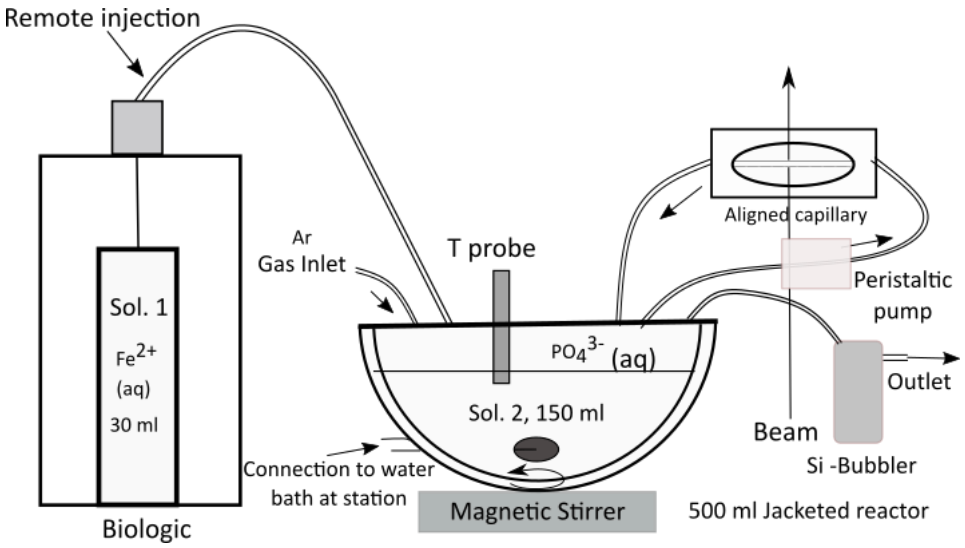

Figure A2S1. Experimental scheme of the *in situ* SAXS WAXS experiments performed at beamline I22 at the Diamond Light Source. UK. Components: (1) Ar gas inlet (2) temperature probe inlet (3) tubing inlet and outlet for closed loop circulation of the reaction mixture from the vessel to the beam-aligned capillary (4) Ar gas outlet and connection to the Si-oil gas-bubbler.

Section A2S1. Thermodynamic geochemical modeling of the system

Thermodynamic modeling of the system based on calculations on PHREEQC software (Version 3) [119] using the Thermoddem database [120].

At pH 7.2 and p_e of -1 (anoxic system) and 1 atm pressure, the system composition was input as:

Species	Concentration (10^{-3} mol L^{-1})
Fe^{2+}	50
HPO_4^{2-}	50
NH_4^{+}	100
SO_4^{2-}	100
Na^{+}	50

The following were the calculated solid saturation indices at different temperatures between 10 - 60˚C

Phase	10˚C	21˚C	40 ˚C	60 ˚C
Melanterite ($FeSO_4 \cdot 7H_2O$)	-1.91	-2.10	-2.38	-2.61
Vivianite ($Fe_3(PO_4)_2 \cdot 8H_2O$)	12.63	12.80	13.07	13.31

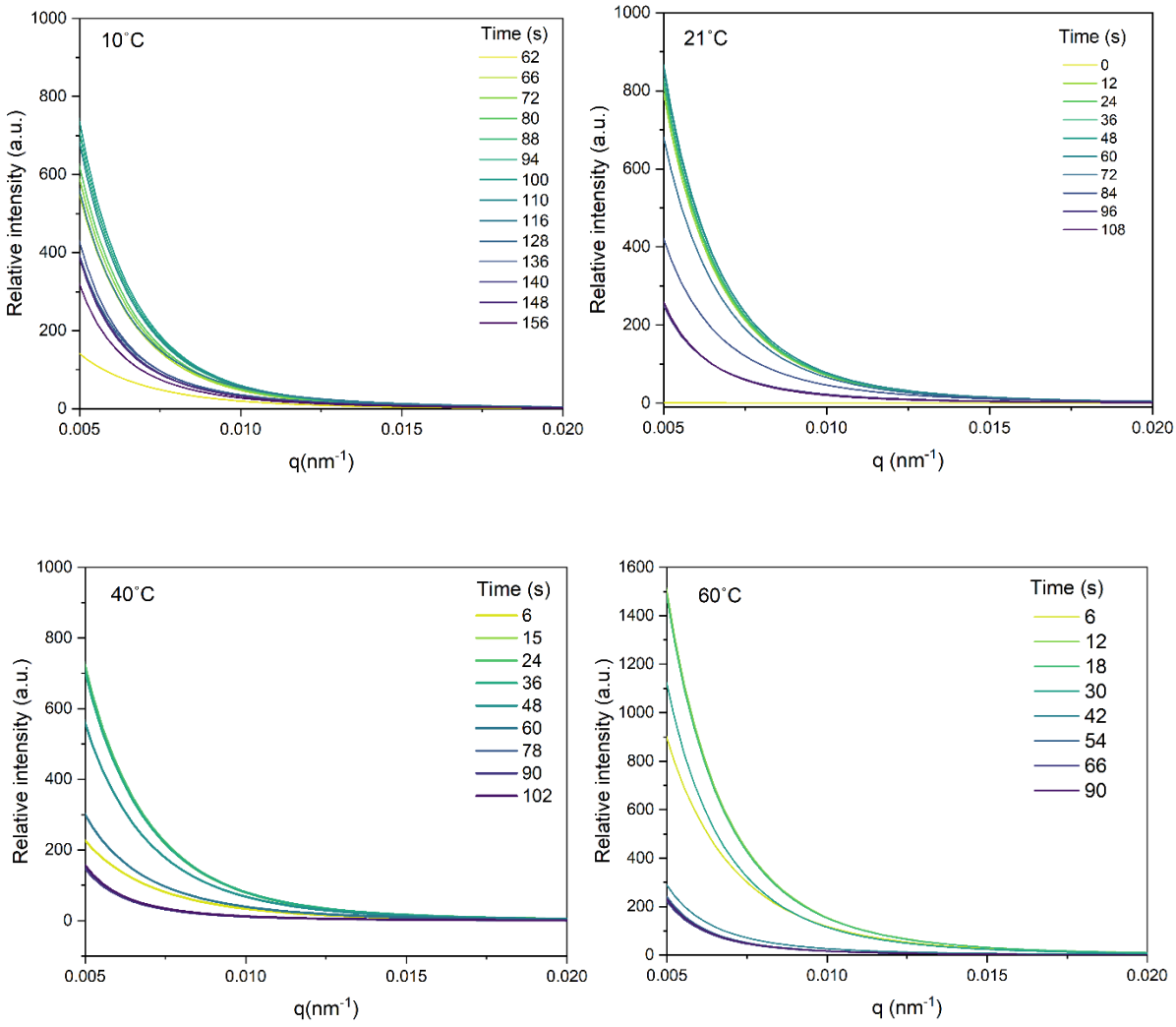

Figure A2S2. *In situ* SAXS patterns from a vivianite precipitation experiment at 21˚C.

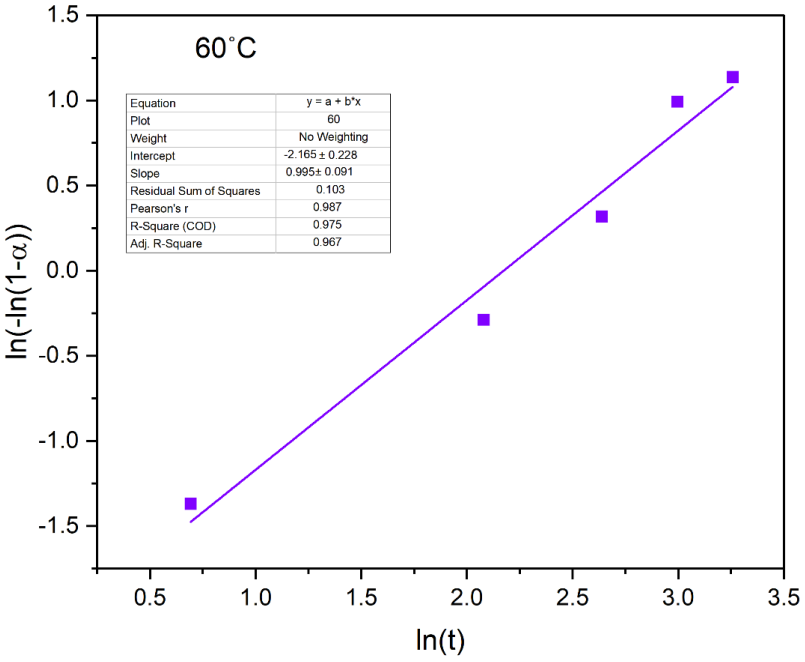
60˚C
Equation y = a + b*x
Plot 60
Weight No Weighting
Intercept -2.165 ± 0.228
Slope 0.995± 0.091
Residual Sum of Squares 0.103
Pearson's r 0.987
R-Square (COD) 0.975
Adj. R-Square 0.967
ln(-ln(1-α))
ln(t)

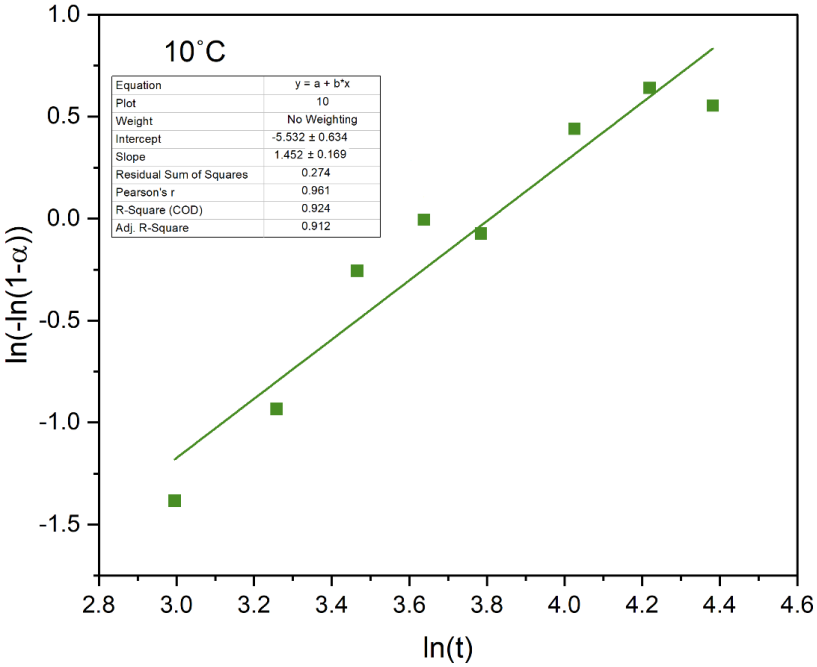
10˚C
Equation y = a + b*x
Plot 10
Weight No Weighting
Intercept -5.532 ± 0.634
Slope 1.452 ± 0.169
Residual Sum of Squares 0.274
Pearson's r 0.961
R-Square (COD) 0.924
Adj. R-Square 0.912
ln(-ln(1-α))
ln(t)

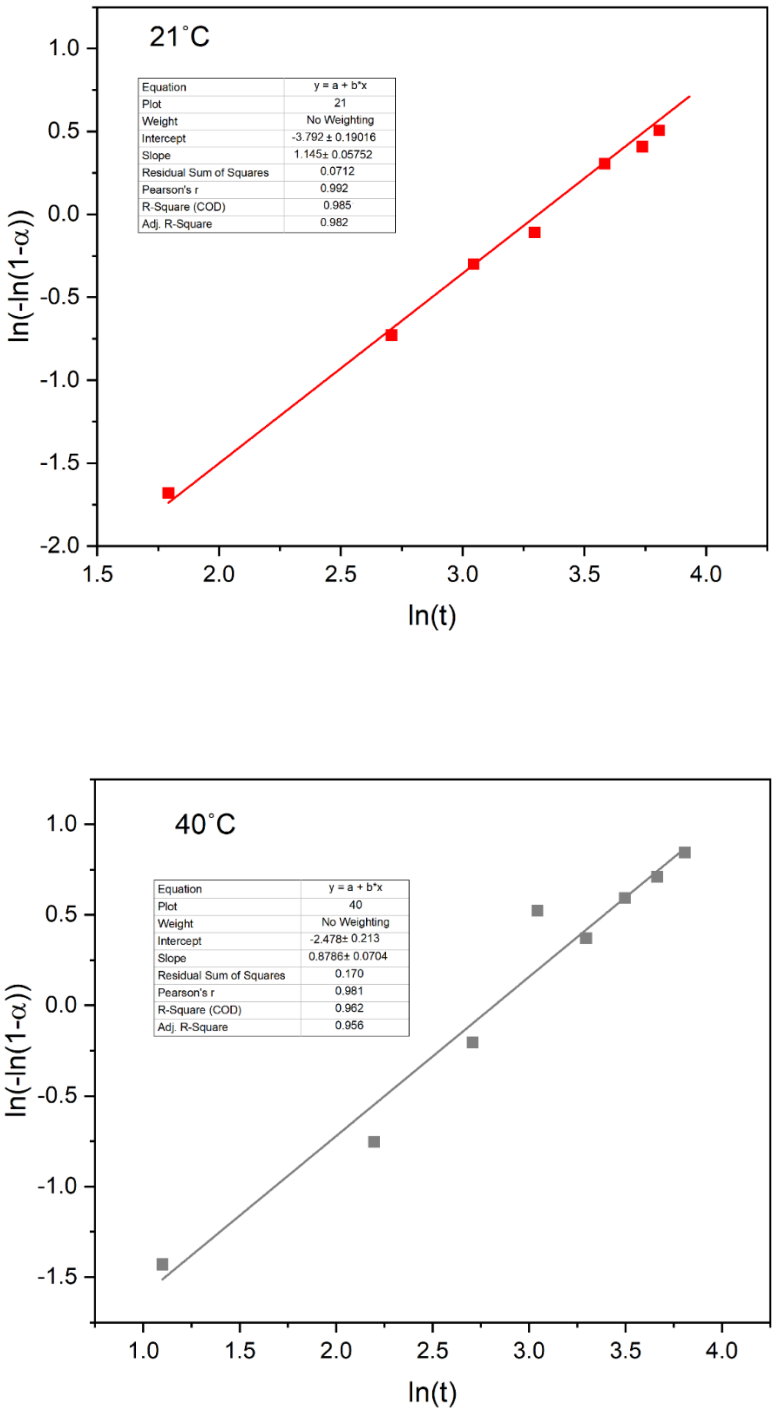

Figure A2S3. Details of linear JMAK fits obtained from the WAXS data at different temperatures

Table A2S1. Arrhenius fitting parameters for the temperature dependent growth of vivianite, data from table 1 in the main manuscript

Equation	y = a + b*x
Plot	ln k
Weight	Instrumental (=1/ei^2)
Intercept	1.805 ± 0.875
Slope	-12972.037 ± 2244.496
Residual Sum of Squares	0.473
Pearson's r	-0.971
R-Square (COD)	0.943
Adj. R-Square	0.915

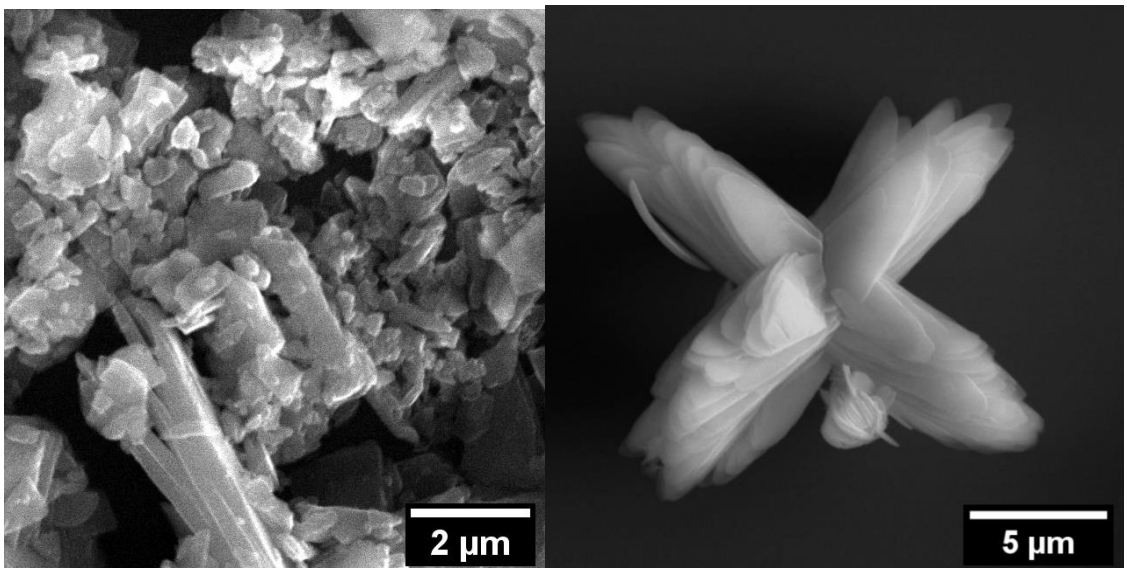

Figure A2S4. Time resolved SEM micrographs showing vivianite crystals sampled from experiments: 10˚C at 3 min – small platelets (left) and at 21˚C at 10 min – X-shaped configuration (right).

Appendix III

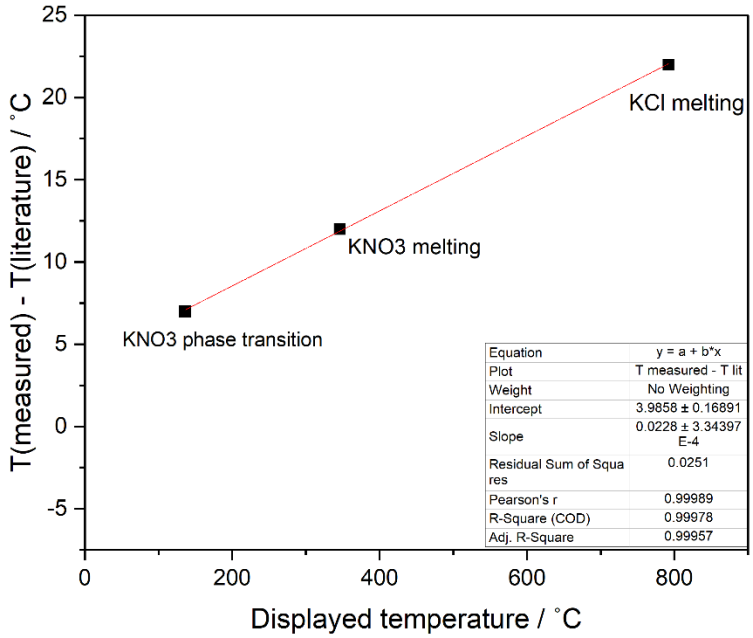

Section A3S1. Figure S1. Calibration curve with phase transitions / melting points for a STOE high-temperature XRD furnace accessory, a heating rate of 10˚C/min.

Preparation samples for Fe-K edge XAS spectroscopy

Pellet preparation and protocol for preventing sample oxidation

Pellets were prepared in a glovebox (97% N_2, 3% H_2) at GFZ Potsdam by mixing powder samples with cellulose based on calculations using XAFSmass software.[209] Pellets were sealed inside 2 layers of single-sided 70-µm thick Kapton® polyimide tape, and then fixed into the custom sample holder for the beamline. The samples were put inside airtight Mylar® bags and sealed with an impulse heat sealer inside the glovebox. The bags were transported to the beamline inside an anaerobic jar (Oxoid™ AnaeroJar™, Thermo Fischer Scientific). Samples were only taken out just before XAS measurement.

Details of As K-edge XAS data collection

Iron K-edge XAS data were collected on the P65 undulator beamline of DESY German Electron Synchrotron (HASYLAB, DESY PETRA III, Hamburg, Germany). Incoming photon flux energy was modulated with a Si(111) double crystal monochromator, with an energy resolution of ~0.6 eV at the Fe K-edge and a beam size of 0.3 × 1.5 mm^2. The effective suppression of higher harmonics was achieved using Si-plane mirrors. The data were collected from -160 eV below the edge to +800 eV above. Spectra of the samples were acquired in transmission mode at room temperature, concomitantly with the spectrum of an Fe foil for energy calibration and alignment. Meanwhile, the spectra of the reference phases were collected at 20 K in an earlier beamtime session [163]. Multiple scans were collected for each sample depending on data quality (at least 3 scans). Changes in line shape and peak position indicative of beam-induced photoreduction were examined and no beam damage was observed during spectra collection. The first inflection point in the first derivative of the adsorption threshold

of the Fe foil was calibrated at 7112 eV. X-ray absorption near-edge structure (XANES) data handling and edge analyses were done on Athena software [126].

Shell-by-shell fitting procedure

Shell-by-shell fits of the EXAFS spectra of the samples (k-range = 2-11.5 Å^{-1}) and amorphous Fe phosphate references (k-range = 2-12.5 Å^{-1}) were performed from 1 to 3.5 Å in R+ΔR-space, while those for the crystalline Fe phosphate phases (k-range = 2-12.5 Å^{-1}) were conducted from 1 to 6.5 Å. All fits were performed using the SIXPack software[210] based on algorithms derived from IFEFFIT.[211] The fits included the interatomic distance (R), the coordination number (CN), the mean squared atomic displacement parameter (σ^2), and the change in threshold energy (ΔE_0) for one sample. Phase and amplitude functions for single and multiple scattering paths were calculated using FEFF6 [212] and included Fe-O, Fe-Fe, Fe-P and Fe MS paths derived from the structure of goethite[213], strengite[214] and vivianite[48]. In preliminary fits, the CN and σ^2 were found to be highly correlated, which produced high fit-derived standard errors in these fitting parameters. We constrained σ^2 to 0.01 and 0.009 Å^2 in the second shell fits of Fe-Fe and Fe-P paths for the samples to reduce the high correlations as done in a previous work [215]. For the crystalline vivianite samples, the σ^2(Fe-Fe) paths were constrained at 0.006 Å^2 [215]. Consistent with previous work, the passive electron reduction parameter (S_0^2) in each fit was set to 0.9 [134]. The goodness-of-fit was assessed based on the R-factor, which is defined as the mean square difference between the fit and the data on a point-by-point basis: R-factor = $\sum_i (\text{data}_i - \text{fit}_i)^2 / \sum_i (\text{data}_i)^2$. An R-factor < 0.05 is considered to reflect a reasonable fit [216]. The validity of the addition of all scattering paths was evaluated using the F-test for EXAFS [217].

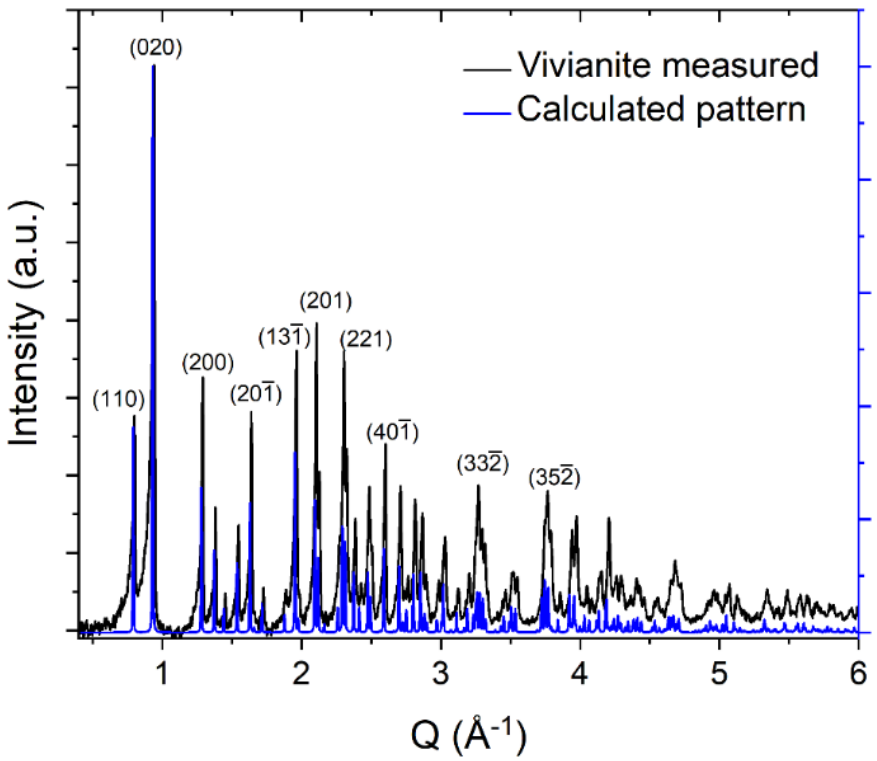

Figure A3S2. Indexed powder XRD pattern of synthetic vivianite from a *cif* file. [48]

Table A3S1. Atomic parameters of vivianite unit cell from Rietveld refinements

Atom	x	y	z	U_{iso}
Fe(1)	0.00000	0.00000	0.00000	0.0187(12)
Fe(2)	0.00000	0.38971(17)	0.00000	0.0137(8)
P(1)	0.3152(4)	0.00000	0.3744(10)	0.0125(12)
O(1)	0.1547(8)	0.00000	0.3678(19)	0.0298(29)
O(2)	0.3902(10)	0.00000	0.7038(20)	0.029(3)
O(3)	0.3409(5)	0.0966(5)	0.2176(12)	0.0325(21)
O(4)	0.1040(5)	0.1184(4)	0.7986(11)	0.0182(20)
O(5)	0.3986(6)	0.2245(4)	0.7107(13)	0.0189(20)

Table S2. Atomic parameters of graftonite unit cell from Rietveld refinements

Atom	x	y	z	U_{iso}
Fe(1)	0.9271(9)	0.1147(8)	0.8669(12)	0.0174(25)
Fe(2)	0.7233(9)	0.0793(7)	0.3361(16)	0.0230(28)
Fe(3)	0.3615(9)	0.1943(7)	0.1167(14)	0.0164(23)
P(4)	0.0962(15)	0.1382(10)	0.3943(25)	0.009(4)
P(5)	0.6034(15)	0.0887(10)	0.7962(22)	0.001(3)
O(6)	0.0699(31)	0.0581(25)	0.175(5)	0.008(9)
O(7)	0.48665	0.18172	0.82108	0.0206
O(8)	0.95193	0.20663	0.40837	0.0071
O(9)	0.70576	0.13144	0.62498	0.0161
O(10)	0.226(4)	0.2267(30)	0.376(6)	0.037(12)
O(11)	0.7275(31)	0.0845(27)	0.009(5)	0.008(9)
O(12)	0.1220(27)	0.0598(26)	0.594(5)	0.000(8)
O(13)	0.53020	0.03050	0.76400	0.0550

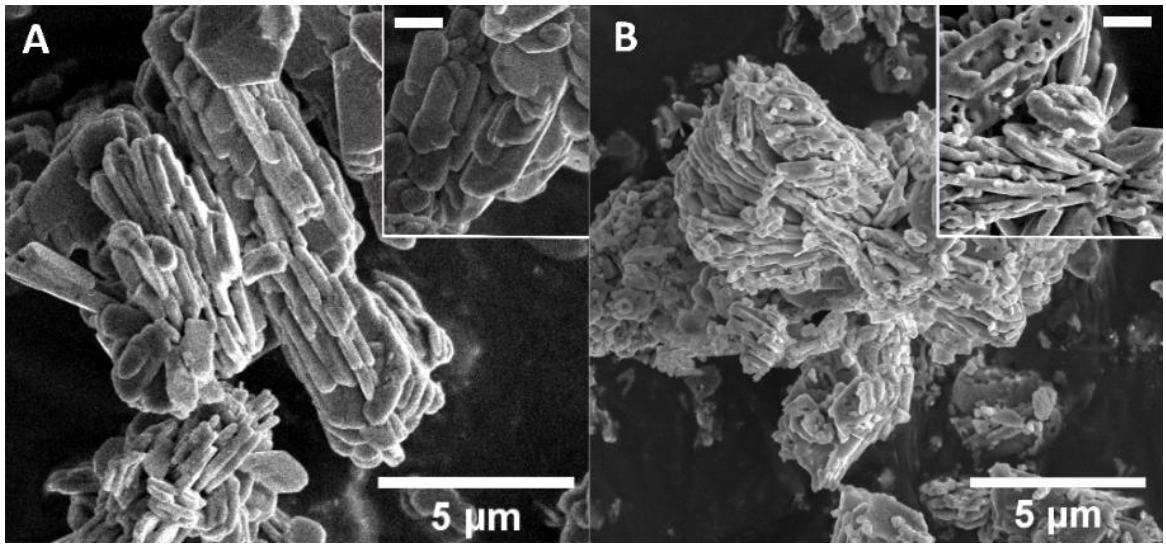

Figure A3S3. *Ex situ* SEM micrographs of (a) vivianite and (b) graftonite, with *insets* showing a zoom of textures and a white bar representing a scale bar of 100 nm

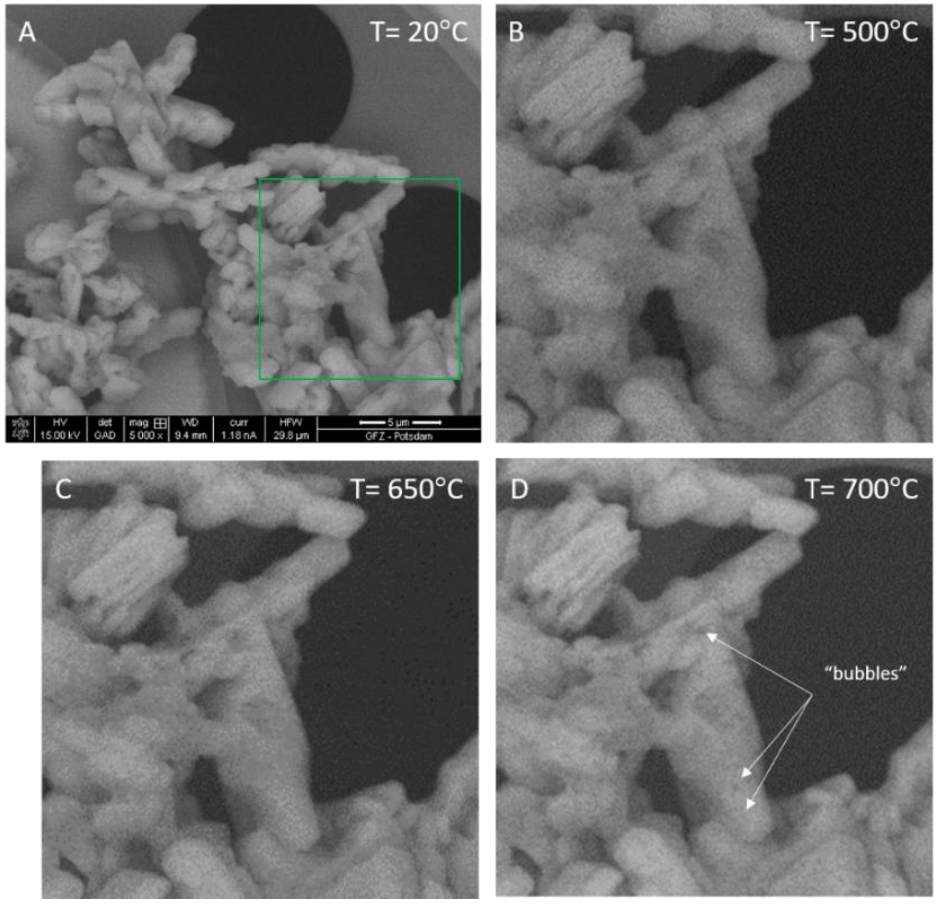

Figure A3S4. (A) SEM image before *in situ* experiment. (B-D) zoomed images at different temperatures from the area marked in (A). White arrows point out on to "bubble"- like features; T = display stage temperature. Heating rate is 10˚C/min

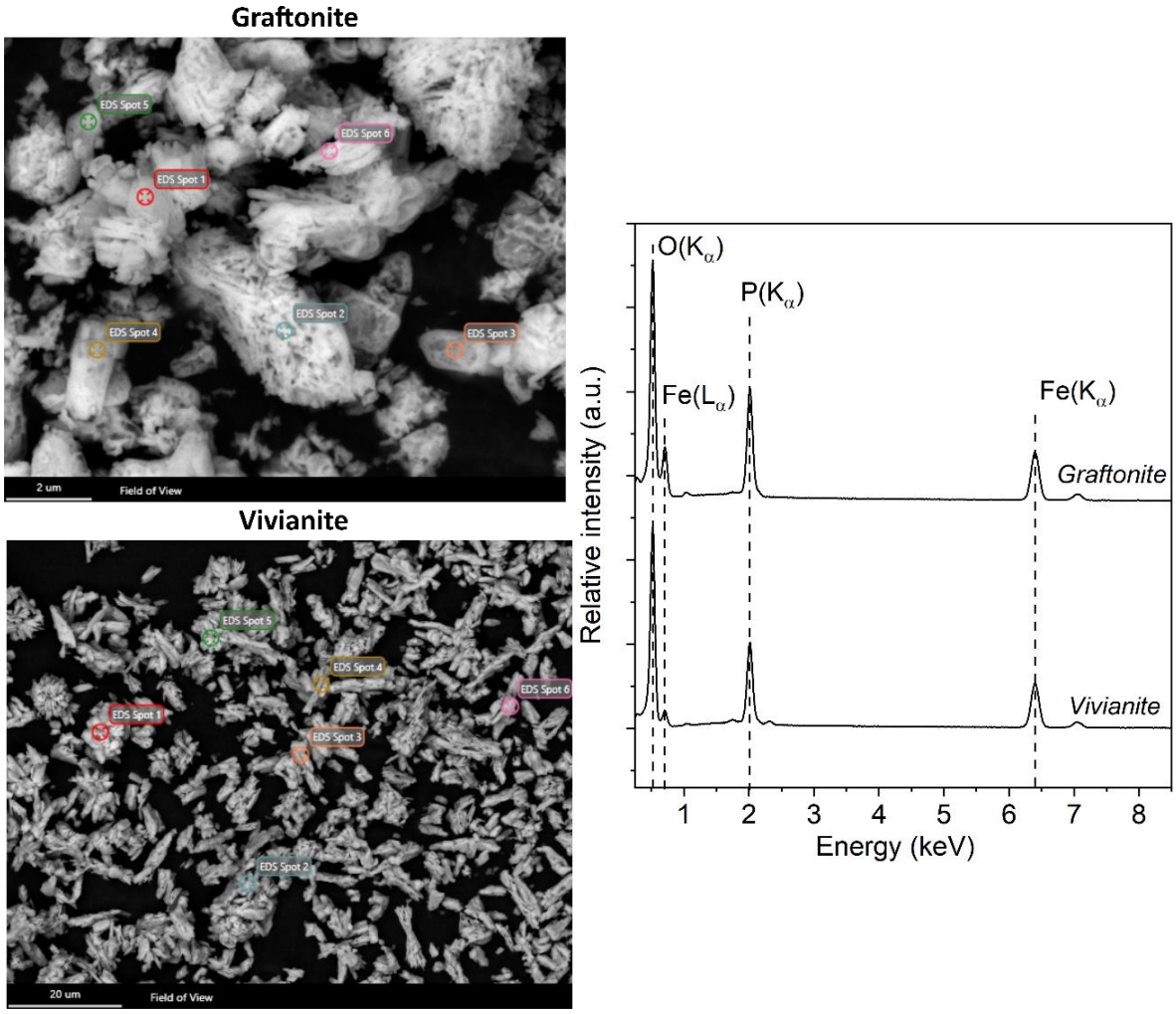

Figure A3S5. SEM-EDX spectra of vivianite and graftonite, the EDX spectrum corresponds to a total of the EDX analysis from 5 different points

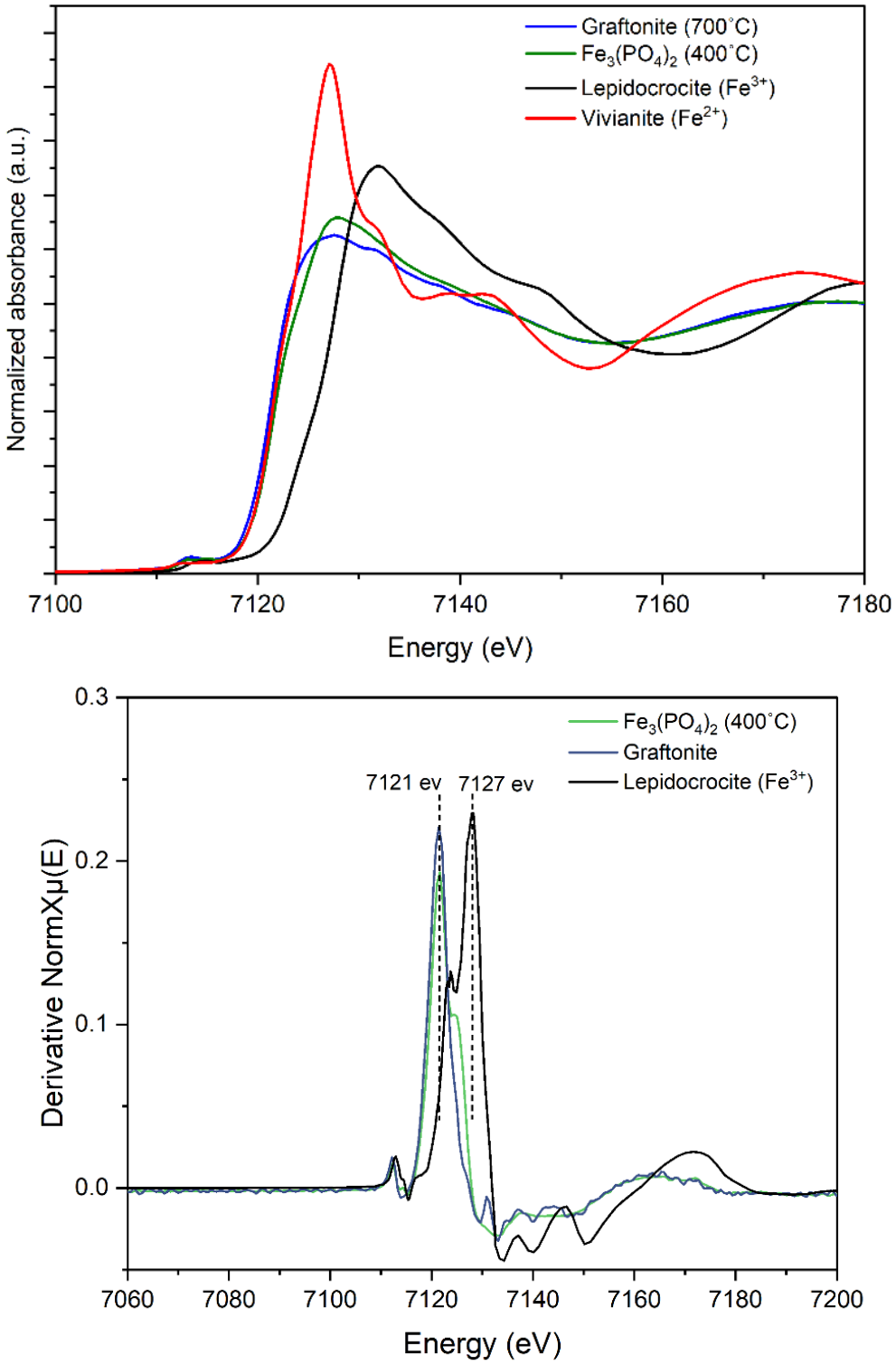

Figure A3S6. Normalized Fe K-edge XANES spectra collected for lepidocrocite (γ-Fe(O)OH (Fe^{3+} reference)), amorphous ferrous phosphate (a-$Fe_3(PO_4)_2$) and vivianite; First derivative of χ(k) for a-$Fe_3(PO_4)_2$ (400˚C), graftonite (mainly Fe^{2+}) and lepidocrocite (Fe^{3+} reference)

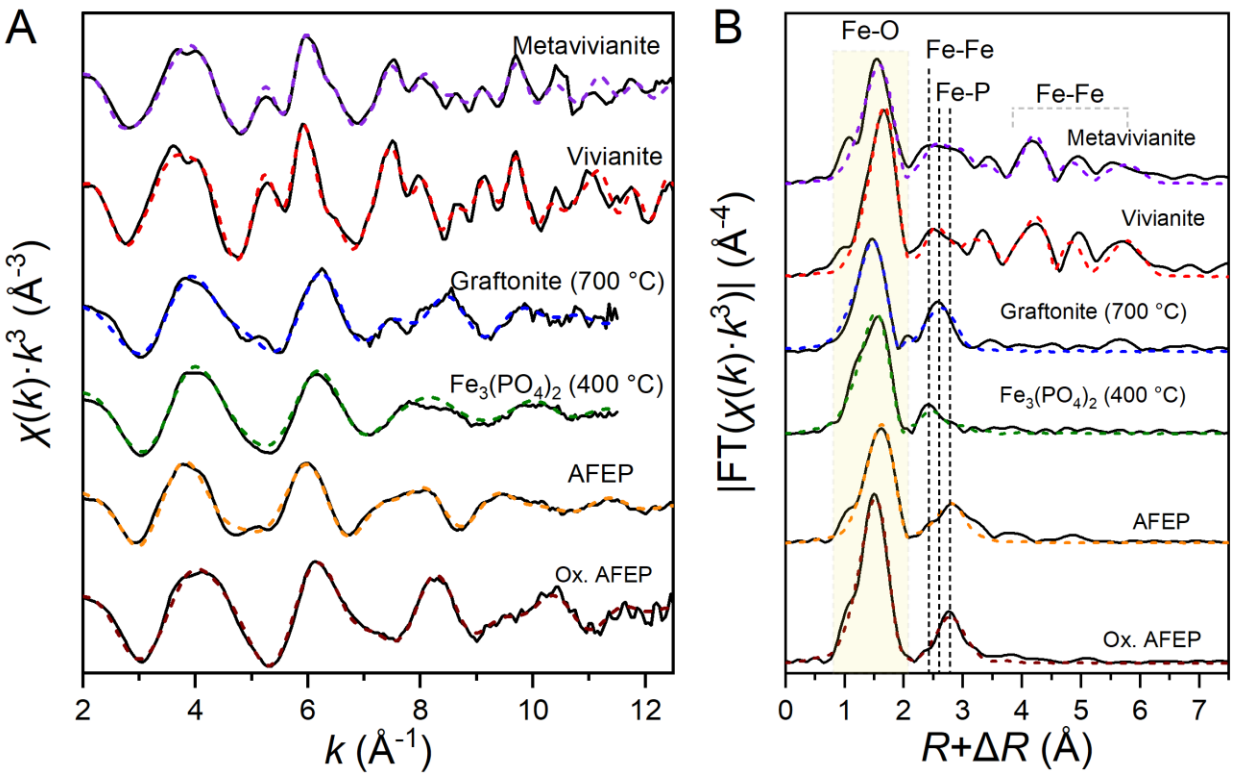

Figure A3S7. Fe K-edge XAS data for the graftonite (700 °C) – *blue trace* and $Fe_3(PO_4)_2$ intermediate (400 °C) – *green trace* at RT and reference phases (metavivianite – *purple trace*, vivianite – *red trace*, AFEP ($Fe_3(PO_4)_2 \cdot 4.7H_2O$) [163] – *green trace* and oxidized AFEP – *brown trace*) at 20 K: (a) k^3-weighted EXAFS spectra and (b) Fourier-transformed EXAFS spectra. The shell-by-shell fitting output (red dashed lines) are superimposed on the experimental data (black solid lines). See Table S1 for fitting results

Table A3S3. Shell-by-shell fits of k^3-weighted EXAFS spectra of graftonite and the $Fe_3(PO_4)_2$ intermediate.

Sample	Atomic pair	*CN*	*R* (Å)	σ^2 (Å^2)	ΔE_0 (eV)	n_{idp}/n_{var}	χ_ν^2	R_f
Graftonite (700 °C)	Fe-O	3.7 (0.5)	1.99 (0.01)	0.012 (0.002)	-3.9 (1.4)	15/8	39	0.019
	Fe-Fe1	0.7 (0.4)	3.02 (0.03)	*0.010*				
	Fe-P	1.1 (0.6)	3.21 (0.04)	*0.008*				
a-$Fe_3(PO_4)_2$ (400 °C)	Fe-O	4.2 (0.6)	2.03 (0.01)	0.012 (0.002)	0.4 (1.4)	15/8	175	0.023
	Fe-Fe	0.7 (0.3)	3.01 (0.03)	*0.010*				
	Fe-P	0.8 (0.4)	3.35 (0.05)	*0.008*				
Reference phases								
$Fe_3(PO_4)_2{\cdot}4.7H_2O$ (AFEP)	Fe-O	5.5 (0.6)	2.10 (0.01)	0.010 (0.001)	3.6 (1.0)	17/7	381	0.018
	Fe-P	3.7 (1.1)	3.34 (0.01)	0.011 (0.003)				
Oxidized AFEP	Fe-O	6.4 (0.5)	1.99 (0.01)	0.009 (0.001)	-0.5 (0.8)	17/7	32	0.008
	Fe-P	2.5 (0.6)	3.29 (0.01)	0.006 (0.002)				
Vivianite, $Fe_3(PO_4)_2{\cdot}8H_2O$	Fe-O	6.4 (0.6)	2.13 (0.01)	0.008 (0.001)	2.0 (0.9)	36/18	150	0.027
	Fe-Fe1	1.1 (0.3)	3.03 (0.02)	*0.006*				
	Fe-P	1.7 (0.6)	3.34 (0.03)	*0.008*				
	Fe-O2	5.9 (1.7)	3.98 (0.02)	σ^2 (Fe-O1)				
	Fe-O-O	6.3 (2.6)	4.45 (0.04)	σ^2 (Fe-O1)				
	Fe-Fe2	4.8 (0.8)	4.69 (0.01)	σ^2 (Fe-Fe1)				
	Fe-Fe3	4.2 (0.9)	5.22 (0.01)	σ^2 (Fe-Fe1)				

	Fe-Fe4	7.5 (1.5)	6.25 (0.01)	σ^2 (Fe-Fe1)				
	Fe-O	6.7 (0.9)	2.09 (0.01)	0.013 (0.002)	1.0 (1.1)	36/16	123	0.049
	Fe-Fe1	0.6 (0.3)	3.00 (0.02)	*0.006*				
Metavivianite,	Fe-P	2.3 (0.6)	3.29 (0.02)	*0.008*				
$Fe^{II}_{3-x}Fe^{III}_{x}(PO_4)_2(OH)_x$	Fe-O2	7.1 (2.4)	4.00 (0.03)	σ^2 (Fe-O1)				
$\cdot(8-x)H_2O$	Fe-Fe2	3.4 (0.6)	4.66 (0.01)	σ^2 (Fe-Fe1)				
	Fe-Fe3	5.8 (1.7)	5.22 (0.02)	$2\sigma^2$ (Fe-Fe1)				
	Fe-Fe4	9.1 (3.0)	6.26 (0.03)	$2\sigma^2$ (Fe-Fe1)				

Note: CN – coordination number, R – interatomic distance, σ^2 – mean-squared displacement, ΔE_0 – change in threshold energy, n_{idp} – no. of independent data points, n_{var} – no. of variables, χ_ν^2 – reduced CHI square, and R_f – R-factor. Values given without fit uncertainty (in parenthesis) were fixed. The amplitude reduction factor (S_0^2) was set to 0.9 in all fit

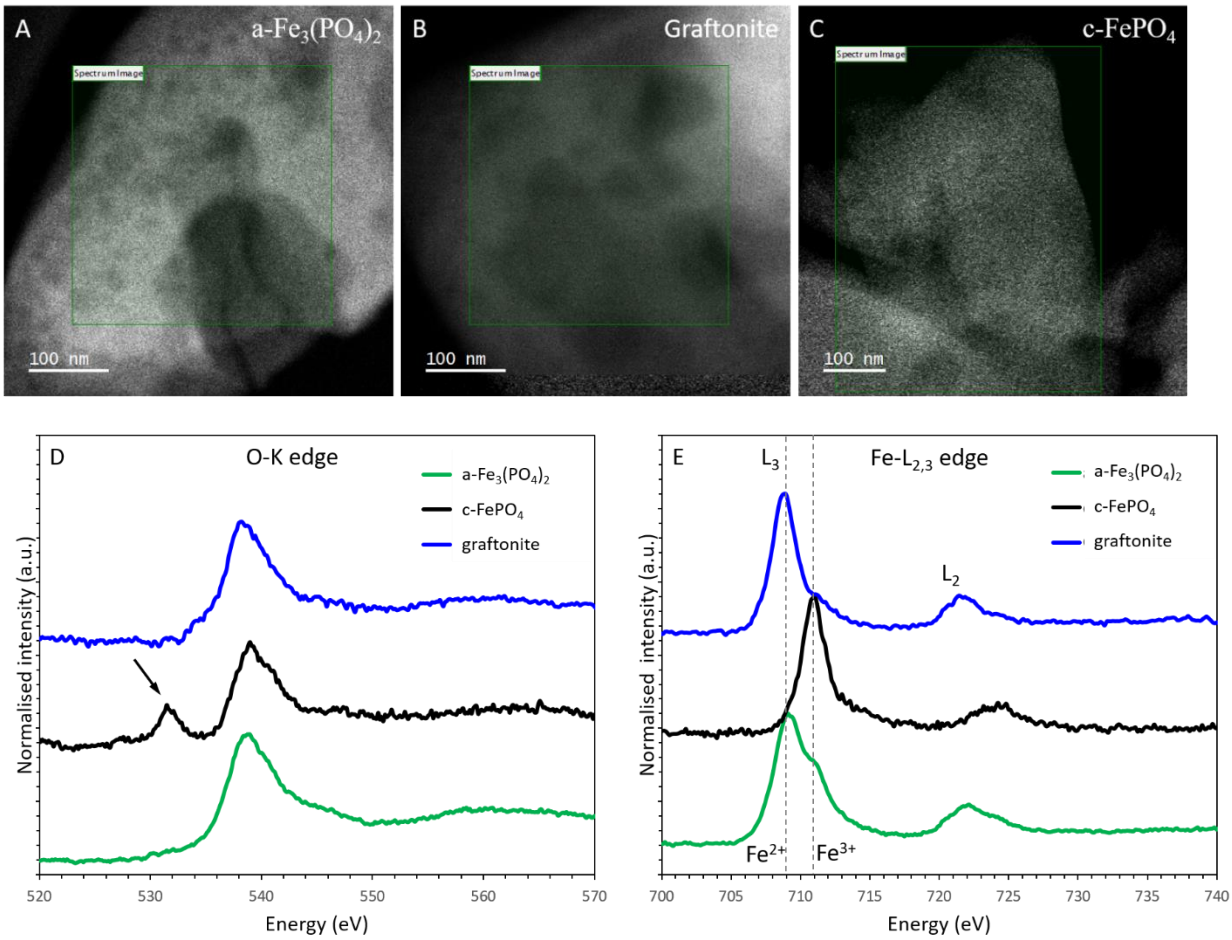

Figure A3S8. O-K edge and Fe-$L_{2,3}$ spectra of the amorphous a-$Fe_3(PO_4)_2$, graftonite and rodolicoite (c-$FePO_4$, Fe^{3+} reference). The corresponding spectrum images were collected from areas marked with green contours. The black arrow in (D) marks the visible pre-edge feature in O-K edge EELS spectrum of c-$Fe^{3+}PO_4$ (a characteristic of Fe^{3+} compounds)

Appendix IV

Adapted from the published article: Authigenic minerals reflect microbial control on pore waters in a ferruginous analogue

A. Vuillemin, M. Morlock, A. Paskin, L. G. Benning, C. Henny, J. Kallmeyer, J. M. Russell, and H. Vogel

Geochem. Persp. Let. 2023, 28, 20–26

DOI: 10.7185/geochemlet.2339

ABSTRACT. Ferruginous conditions prevailed in the oceans through much of Earth's history. However, minerals testifying to these conditions remain difficult to interpret in terms of biogeochemical processes prior to lithification. In Lake Towuti, Indonesia, ferruginous sediments are deposited under anoxic sulphate-poor conditions similar to the Proterozoic oceans, allowing the study of mineralogical (trans)formations during microbial diagenesis. Comprehensive pore water geochemistry, high-resolution geochemical core profiles and electron microscopy of authigenic minerals revealed in-situ formation of magnetite, millerite, and abundant siderite and vivianite along a 100-m-long sequence. Framboidal magnetites represent primary pelagic precipitates, whereas millerite, a sulphide mineral often overlooked under sulphate-poor conditions, shows acicular aggregates entangled with siderite and vivianite resulting from saturated pore waters and continuous growth during burial. These phases act as biosignatures of microbial iron and sulphate reduction, fermentation and methanogenesis, processes clearly tractable in pore water profiles. Variability in metal and organic substrates attests to environment-driven processes, differentially sustaining microbial processes along the stratigraphy. Geochemical profiles resulting from microbial activity over 200 kyrs after deposition provide constraints on the depth and age of mineral formation within ferruginous records.

Introduction

Ferruginous conditions (iron-rich, sulphate-poor) were widespread in the Archean and Proterozoic oceans and resulted in the deposition of ancient iron formations (Canfield et al., 2008). Precambrian iron formations are composed of diverse iron oxides and carbonates thought to have formed as primary pelagic precipitates from the recrystallization of ferric-ferrous iron (oxyhydr)oxides (Halevy et al., 2017). Sulphides are also occasionally reported to occur, but only in minor quantities due to the scarcity of seawater sulphate at the time (Fakhraee et al., 2019). Although the Proterozoic Earth was an essentially microbial world, mineral phases precipitated by microbial biogeochemical cycling of

iron, sulphur and carbon remain poorly constrained in terms of early diagenetic imprints prior to sediment lithification (Posth et al., 2014). Characterizing and identifying such mineral phases is therefore paramount in order to employ their signatures as recorders of past ferruginous environments and as tracers of microbial processes of the Earth's early oceans (Tosca et al., 2019).

Modern analogues to Earth's early oceans (Swanner et al., 2020) that allow the study of both modern pore water geochemistry and short-term diagenetic evolution of ferruginous sediments are scarce.

One such environment are the ferruginous sediments deposited in the Malili Lakes (Russell et al., 2016), a chain of five interconnected tectonic lakes hosted in variably weathered (ultra)mafic rocks on Sulawesi, Indonesia (Figs. 1a-1b). Lateritic erosion of the catchment supplies considerable amounts of iron (oxyhydr)oxides, but little sulphate to the lakes (Morlock et al., 2018). Lake Towuti (2.5° S, 121° E), with a maximum water depth of ca. 200 m, is presently oxygen-depleted below 130 m depth (Fig. 1c) displaying a persistent monimolimnion wherein primary ferric iron phases, mostly ferrihydrite ($Fe_2O_3 \cdot 0.5H_2O$), undergo reductive dissolution (Bauer et al., 2020). Subsequent sediment (trans)formation during early diagenesis (Vuillemin et al., 2019, 2020) precipitates secondary mineral phases, such as siderite ($FeCO_3$) and vivianite ($Fe_3[PO_4]_2 \cdot 8H_2O$). Geomicrobiological investigations have shown that iron-, sulphur- and methane-related biogeochemical processes coexist in Lake Towuti sediments (Vuillemin et al., 2016, 2018). Due to extremely low sulphate concentrations (<20 µM), sediment organic matter (OM) remineralization proceeds mainly through methanogenesis (Friese et al., 2021). These sedimentary conditions make Lake Towuti a unique ferruginous analogue in which to study the evolution of pore water geochemistry under the influence of microbial reduction and mineral (trans)formations prior to sediment lithification (Vuillemin et al., 2023).

Here, we analyze one 100-m-long sediment sequence to establish the link between putative microbial processes and geochemical gradients under which authigenic minerals precipitate. We present detailed pore water geochemistry and high-resolution geochemical core surface profiles down to a basal age of at least ~1 Myr (Russell et al., 2020). Using transmitted light and scanning electron microscopy (SEM), we illustrate characteristic authigenic mineral phases, namely magnetite (Fe_3O_4), millerite (NiS), siderite and vivianite, which occur in varying quantities throughout the stratigraphy. Together these data document the direct precipitation of successive phases from pore waters, highlight microbial processes of sediment remineralization underlying reductive diagenesis, and allow to establish mineral biosignatures in ferruginous records.

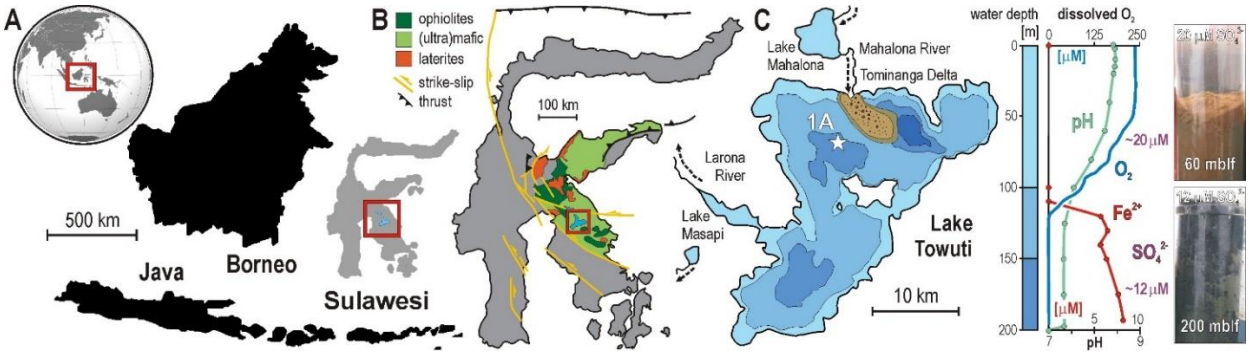

Figure A4.1 Site description of Lake Towuti. **(a)** World map displaying the location of Sulawesi Island, with close-up on the Indonesia archipelago and location of the Malili Lake System. **(b)** Map of Sulawesi illustrating the ultramafic and lateritic geology of the Malili Lake catchment. **(c)** Bathymetric map of Lake Towuti with position of drill site TDP-1A (156 m water depth); dissolved oxygen, iron and pH profile of Lake Towuti's water column (Bauer et al., 2020); gravity cores retrieved from 60 and 200 m water depth illustrating sulfate concentrations and redox conditions at the water-sediment interface.

Methods

The Towuti Drilling Project (TDP) coring operations were carried out by the International Continental scientific Drilling Program (ICDP) in spring-summer 2015, using the Deep Lakes Drilling System (Russell et al., 2016). Hole TDP-1A (156 m water depth) was drilled with a contamination tracer to aid geomicrobiological sampling (Friese et al., 2017). In the field, pristine core sections were transferred into an anaerobic chamber for pore water extraction, using Rhizon samplers for soft sediment, and an IODP-style titanium cylinder and hydraulic press for compact samples deeper than 10 m below lake floor (mblf). Alkalinity, pH, and Fe^{2+}, $Mn^{2+}$and PO_4^{3-} concentrations were determined via colorimetric titration, potentiometry and spectrophotometry, respectively. Dissolved inorganic carbon (DIC) was calculated by solving the carbonate system using the pH and alkalinity profiles and borehole temperatures. Major dissolved elements and volatile fatty acids (VFAs) were analyzed by ion chromatography. Pore water trace metals were quantified by ICP-MS. Potential sulphate reduction rates (pSRR) rates were determined by sediment incubation with radioactive $^{35}SO_4^{2-}$ (Friese et al., 2021).

All cores from TDP site 1 were split and scanned at the National Lacustrine Core Facility (LacCore), described macroscopically and microscopically to determine their stratigraphy and composition. A composite core was established based on visual alignment of lithologic features and magnetic susceptibility measurements (Russell et al., 2020). The upper 100 m of the composite cores were scanned at 5 mm resolution on an XRF core scanner (ITRAX, Cox Ltd.) equipped with chromium and

molybdenum X-ray tubes to resolve high atomic mass elements (Morlock et al., 2021). The remainder of core TDP-1A was subsampled for heavy mineral extraction (≥2.9 g × cm^{-3}) via density and magnetic separation. Heavy mineral extracts were fixed onto SEM aluminum stubs and carbon-coated (~ 20 nm layer), using a Leica EM ACE600 high-vacuum sputter coater. Morphological investigation and elemental point analyses were performed on a Zeiss Ultra 55 Plus field SEM and FEI Quanta 3D FEG, both coupled to energy dispersive X-ray spectrometers (EDX). All methods are detailed in the appendix IV.

Results and Discussion

Authigenic mineral shapes and compositions can be employed to trace changes in redox-controlled variations in water and pore fluid geochemistry associated with microbial processes in the upper sediment sequence. If mineral precipitation continues during burial, their signatures deviate from the stratigraphic context.

Pore water geochemical evolution and mineral precipitation

Reducible iron oxides in sediments originate from lateritic weathering of Towuti's (ultra)mafic catchment (Morlock et al., 2019) and authigenic oxidation of ferrous iron in the water column (Sheppard et al., 2019). Consequently, alternating red and green sediments reflect variations in the composition, abundance and changes in iron oxidation state through time (Russell et al., 2020). During settling, particulate iron undergoes partial reductive dissolution in the monimolimnion (Bauer et al., 2020), precipitating pelagic framboidal magnetites (Fig. A4-2a). As bottom waters contain ca. 20 to 12 mM sulphate (Vuillemin et al., 2016), potential sulphate reduction rates (SRR) are highest at the sediment-water interface (SWI) and drastically drop within the upper 20 cmblf (Fig. A4-3a).

Compared to euxinic conditions under which Fe sulphides (*e.g.* mackinawite) act as the primary Ni-hosting phases (Mansor et al., 2019), iron sulphides were not observed. Under the present ferruginous conditions, sulphate reduction with organic carbon as the reductant produces sulphide that reacts with nickel (Fig. A4-4) and precipitates millerite (NiS). The habits of millerites identified at 0.2 mblf and deeper suggest both pelagic precipitation and post-depositional growth at the SWI and in shallow sediments during active sulphate reduction (Fig. A4-2b).

Due to stratification in ferruginous Lake Towuti, the main terminal electron acceptors (*i.e.* O_2, NO_3^-, SO_4^{2-}) are rapidly depleted in the sediment (Figs. A4-1 and 3a), which implies that anaerobic OM degradation should proceed via mineral ferric iron and CO_3^{2-} reduction.

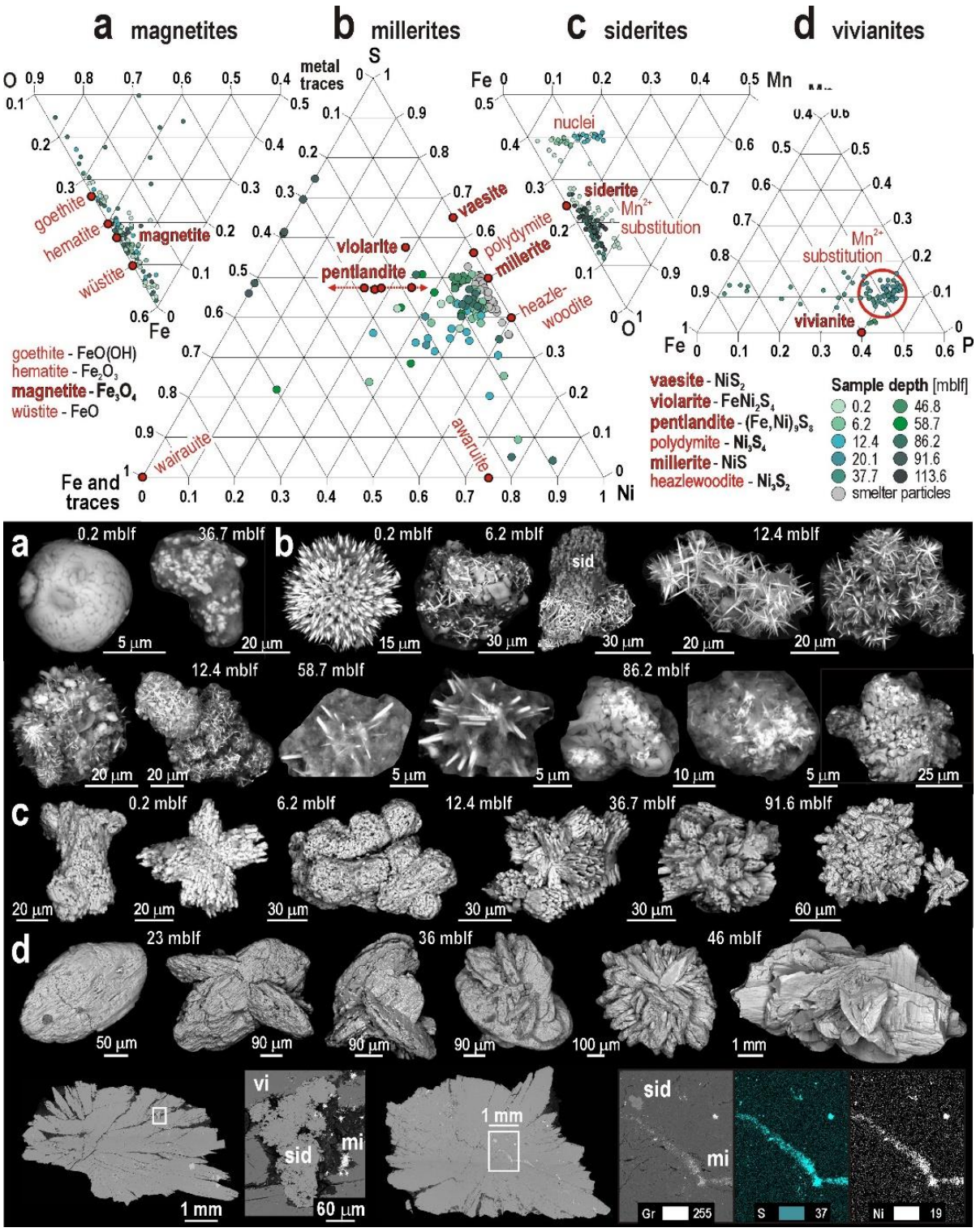

Figure A4.2 EDX point analyses and SEM images of diagenetic minerals. **(Top)** Ternary plots show: **(a)** magnetites and coextracted iron oxides (goethite, wüstite); **(b)** millerites with incorporation of Fe^{2+} traces; **(c)** siderites and **(d)** vivianites with substitution of Mn^{2+} for Fe^{2+}. Smelter particles represent airborne contaminants from the nearby mine. **(Bottom)** Magnetites **(a)** in framboidal habits; millerites **(b)** in acicular spherules and aggregates,

sometimes entangled and overgrown by siderites; siderites **(c)** aggregating into twins and mosaic monocrystals; **(d)** vivianites in tabular habit developing into rosettes. The crystal section shows inclusions of millerite and siderite.

Reductive dissolution of hydrous ferric oxides (*e.g.* ferrihydrite) continues in shallow sediments releasing substantial amounts of Fe^{2+} to the pore water (Fig. A4-3a). Below 50 cmblf, as mostly goethite and magnetite remain as reducible ferric phases (Figs. A4-2a and A5.S-1), fermentation is preferentially performed over microbial respiration of less reactive substances (Friese et al., 2021). Nevertheless, steadily increasing metal concentrations in pore water (Mn, As, Co) suggests that Fe reduction concomitant with fermentation (Fig. A4-3a) continues at slow rates, promoting the dissolution of less reactive ferric-ferrous phases during burial. From 1 to 10 mblf, pore water NH_4^+, PO_4^{3-} and VFAs concentrations provide concomitant evidence of microbial OM degradation (Fig. A4-3a). Between 30 cmblf and 5 mblf, formate, lactate, acetate and butyrate concentrations vary with metabolic production and consumption (*i.e.* acidogenesis, acetogenesis). Below 5 mblf, persistently low VFA concentrations (<20 M) indicate complete remineralization to methane (Friese et al., 2021) accompanied by a decrease in microbial uptake of PO_4^{3-}. Such stepwise fermentation and steady increase in DIC delimit the depth at which pore waters reach siderite saturation (Vuillemin et al., 2019). The pore water pH (7.1-7.5) implies that this biogenic DIC reacts in the form of HCO_3^- with dissolved Fe^{2+} to consistently precipitate siderite between 50 cmblf and 5 mblf (Table S-1), whereas CO_2 fixation via hydrogenotrophic methanogenesis subsequently reduces DIC activity in pore waters (Fig. A4-3b). Pore water Na^+, Ca^{2+} and Mg^{2+} concentrations increasing with depth (Fig. A4-3) indicate that ultramafic sheet silicates (*e.g.* serpentine) partially dissolve after burial.

Their presence in pore water could exert control over the onset of vivianite precipitation (Fig. A4-2d) after siderite (Vuillemin et al., 2020). Ca^{2+} and Mg^{2+} concentrations drop around 15 mblf, suggesting that PO_4^{3-} supplants CO_3^{2-} for precipitation with Fe^{2+} and Mn^{2+} available in pore water (Fig. 3). Pore water geochemical profiles in Lake Towuti's upper sediment column stem from microbial activity and dissolution-precipitation of specific mineral phases (Figs. A4-2-3). We observe a characteristic succession of authigenic mineral precipitation as a function of chemical equilibration of ferruginous pore waters (Jiang and Tosca, 2019) during anaerobic respiration of terminal electron acceptors and sediment OM remineralization. Namely, magnetite, millerite, siderite and vivianite represent biosignatures of microbial iron and sulphate reduction, fermentation and methanogenesis lasting 200 kyrs after deposition.

Geochemical gradient and continuous mineral overgrowth

Based on the geochemical gradient that developed in Lake Towuti's upper 25 m of sediment (Fig. A4-3a) and pH-Eh stability fields for authigenic minerals (Fig. 3b), we estimated that the initial environments of formation for magnetite, millerite, siderite and vivianite correspond to the monimolimnion, SWI, shallow (<1 to 5 mblf) and deep sediments (>15 mblf), respectively. These precipitation stages, which are inherent to microbial processes, can overlap according to the geochemical gradient that develops in anoxic sediments (Fig. A4-3a-b).

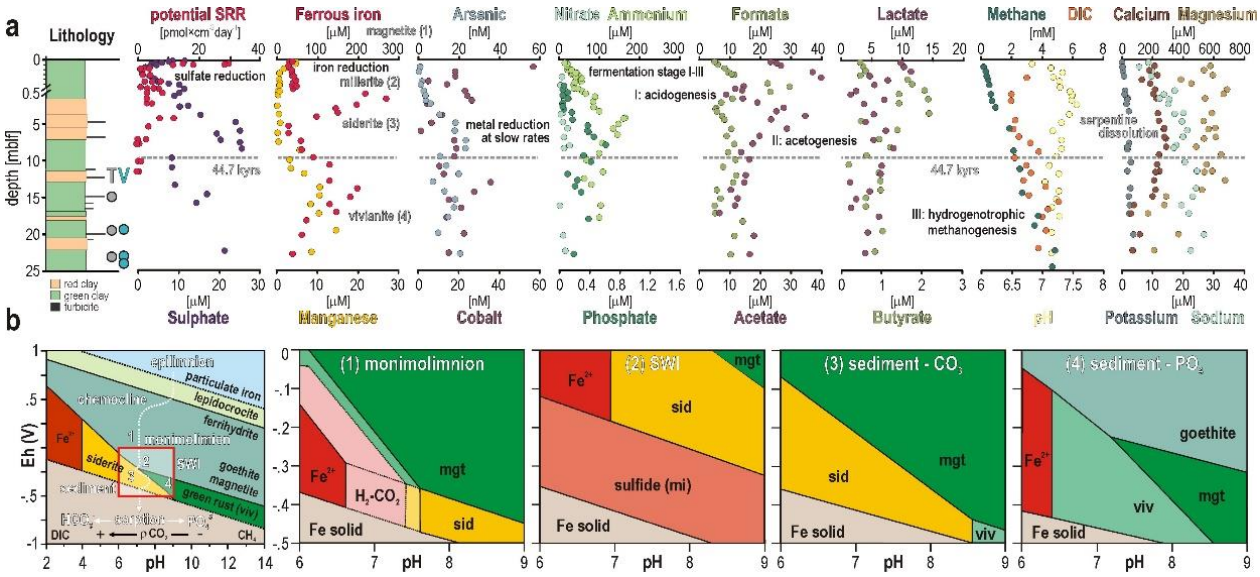

Figure A4.3 Depth profiles for pore water geochemistry and stability diagrams for Fe-bearing phases. **(a)** Lithology of Lake Towuti's upper 25 mblf including tephras (T) and vivianites (V); potential sulphate reduction rates (SRR); pore water concentrations for sulphate, ferrous iron, manganese, arsenic, cobalt, nitrate, ammonium, phosphate, formate, acetate, lactate, butyrate, methane, dissolved inorganic carbon (DIC), pore water pH, calcium, magnesium, potassium and sodium. Data points represent averaged triplicates (reproducibility <5%). The dotted line signifies the base of the ^{14}C ages, *i.e.* 44.7 kyrs (Russell et al., 2020). **(b)** Stability diagram tracing the measured pH and decreasing eH during sedimentation and burial, successively focusing on conditions (red square) observed during *in vitro* microbial Fe^{3+} reduction (Maher et al., 2003) corresponding to: (1) the monimolimnion (Roh et al., 2003); (2) sediment-water interface (SWI) wherein millerite replaces pyrite (Craw and Bowell, 2014); (3) shallow and (4) deep sediments under carbonate- (Zachara et al., 2002) and phosphate-saturated conditions (Morton and Edwards, 2005).

In Lake Towuti, some framboidal magnetites form as pelagic precipitates in the chemocline (Fig. A4.1C) during periods of water column stratification (Bauer et al., 2020) and are preserved as such in the sediment (Fig. A4-2a).

Even at low sulphate concentrations (< 20 M), microbial sulphate reduction in the vicinity of the SWI produces HS^- in pore water which preferentially reacts with Ni^{2+} over Fe^{2+} to form millerite,

incorporating minor Fe and trace metals (Figs. A4-2b, A5.S-2 and S-3). The spherical habits fused into acicular aggregates of authigenic millerites originating from microbial sulphate reduction appear in places with early siderite phases, or fully overgrown by siderite (Figs. A4-2b and A5.S-3). Furthermore, millerite aggregates within siderite-rich zones suggest increased millerite precipitation in sediment layers with greater sulfate availability derived from either sedimentary OM or tephra layers.

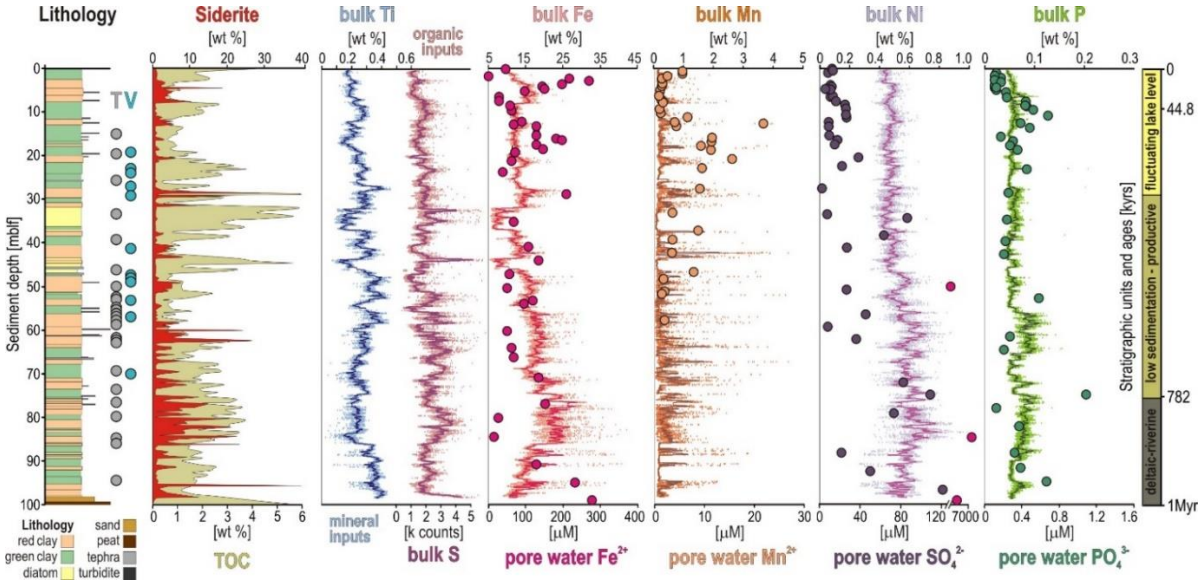

Figure A4.4 Depth profiles for bulk sediment, and pore water geochemistry. **(Left to right)** Stratigraphy of site TDP-1A with tephras (T) and vivianites (V); siderite concentration based on coulometry; total organic carbon (TOC); XRF core-scanning profiles for Ti, S, Fe, Mn, Ni, and P in bulk sediment overlain by pore water concentrations for Fe^{2+}, Mn^{2+}, SO_4^{2-}, and PO_4^{3-}. XRF core-scanning profiles represent punctual analyses with moving averages at 5 mm and 2 cm resolution, respectively. Data points represent averaged triplicates (reproducibility <5%).

Crystallization of successive phases from pore waters and the entangled habits that we observe (Fig. A4-2) reveal a certain degree of Ostwald ripening where smaller precursor crystals dissolve and re-precipitate allowing larger crystal nuclei to further grow over time of burial (Benning and Waychunas, 2008). As demonstrated for redox (trans)formation of green rust (Halevy et al., 2017), pore water solutions become saturated with ferrous colloids (Moens et al., 2021) that react with either carbonate or phosphate ions over time to form siderite monocrystals (Vuillemin et al., 2019) and vivianite nodules (Vuillemin et al., 2020). Siderite SEM images document diagenetic growth from micritic phases into twins and aggregates, forming spherules of mosaic monocrystals (Fig. A4-2c) promoted by saturated pore water conditions during burial.

Similarly, vivianite SEM images reveal crystal growth from tabular habits into rosettes (Fig. 2d), forming macroscopic crystals due to diagenetic diffusion during burial, indicating that vivianite constitutes an important sink for Fe^{2+}, Mn^{2+} and Mg^{2+} in pore waters that reached saturation in specific sedimentary layers. Millerite and siderite inclusions identified in a vivianite crystal cross-section suggest that these phases precipitated first (Fig. A4.2d). Finally, EDX results (Figs. A4.2 and A5.S-2) show that magnetites have minor trace metal concentrations, millerites incorporate some Fe^{2+}, siderites substitute Mn^{2+} in their initial growth phase.

Mineral biosignatures in their recent and ancient stratigraphic context

The mineralogy of Lake Towuti presents an alternation of dark green to reddish-grey clays, considered to reflect detrital iron fluxes to the lake, stratification regimes, and redox conditions at the SWI (Russell et al., 2016 and 2020). While XRF core profiles (*e.g.* Ti, S) attest to climate- and tectonic-driven processes along the sediment stratigraphy (Fig. A4.4), variations in the burial of ferric iron and OM, their availability as substrates and pore water geochemistry ensuing microbial breakdown can imprint different mineral biosignatures during early diagenesis (Morlock et al., 2021). Each of these minerals, whether forming in the water column, near-surface sediments or from pore waters, acts as a discrete sink for selective solutes (*i.e.* Ni^{2+}, Mn^{2+}, Fe^{2+}, CO_3^{2-}, HS^-, PO_4^{3-}). Pore water profiles thereby provide constraints on the depth of formation and age difference with the stratigraphy. Yet their abundance along the stratigraphic record results from past depositional modes and redox biogeochemistry.

Iron inflows deposited under oxygenated conditions formed reddish clays containing abundant, but poorly reactive, detrital magnetites and diagenetic siderites (Vuillemin et al., 2023). Millerites were also found in red clays in which slightly more sulfate was available for microbial reduction at the time of deposition (*i.e.* ~20 Mya). These magnetites and millerites were progressively overgrown by diagenetic siderite during burial. While framboidal magnetites and spherical millerites represented pelagic precipitates forming under stratified conditions, vivianites nucleated from diffusive pore waters in greenish clays.

To conclude, we could show that millerite precipitates in ferruginous anoxic waters and shallow sediments at sulfate levels relevant to sulfur cycling in Earth's early oceans (Farquhar et al., 2010). Whereas vivianite preservation over geologic scale is compromised, continuous precipitation of siderite from saturated pore waters forms spheroids that can coalesce into lithified bands as seen in red beds.

References for Appendix IV

Bauer, K.W., Byrne, J.M., Kenward, P., Simister, R., Michiels, C.C., Friese, A., Vuillemin, A., Henny, C., Nomosatryo, S., Kallmeyer, J., Kappler, A., Smit, M.A., Francois, R., Crowe S.A. (2020) Earth and Planetary Science Letters 549, 116495.

Benning, L., Waychunas, G. (2008). Kinetics of Water-Rock Interaction. Springer, New York,

Canfield, D.E., Poulton, S.W., Knoll, A.H., Narbonne, G.M., Ross, G., Goldberg, T., Strauss, H. (2008) Science 321, 949-952.

Craw, D., Bowell, R. (2014). The Characterization of Arsenic in Mine Waste. Reviews in Mineralogy and Geochemistry 79, 473-505.

Fakhraee, M., Hancisse, O., Canfield, D.E., Crowe, S.A., Katsev S. (2019) Proterozoic seawater sulfate scarcity and the evolution of ocean-atmosphere chemistry. Nature Geoscience 12, 375-380.

Farquhar, J., Wu, N., Canfield, D.E., Oduro, H. (2010) Connections between sulfur cycle evolution, sulfur isotopes, sediments, and base metal sulfide deposits. Economic Geology 105, 509-533.

Friese, A., Kallmeyer, J., Kitte, J.A., Montaño Martínez, I., Bijaksana, S., Wagner, D., the ICDP Lake Chalco Drilling Science Team, the ICDP Towuti Drilling Science Team (2017) Limnology and Oceanography: Methods 15, 200-211.

Friese, A., Bauer, K.W., Glombitza, C., Ordoñez, L.G., Ariztegui, D., Heuer, V.B., Vuillemin, A., Henny, C., Nomosatryo, S., Simister, R., Wagner, D., Bijaksana, S., Vogel, H., Melles, M., Russell, J.M., Crowe, S.A., Kallmeyer, J. (2021) Nature Communications 6, e2216.

Halevy, I., Alesker, M., Schuster, E.M., Popovitz-Biro, R., Feldman, Y. (2017) Nature Geoscience 10, 135–139.

Jiang, C.Z., Tosca, N.J. (2019) Earth and Planetray Science Letters 506, 231-242.

Maher, B.A., Alekseev, A., Alekseeva, T. (2003) Palaeogeography, Palaeoclimatology, Palaeoecology 201, 321-341.

Mansor, M., Winkler, C., Hochella, M.F.J., Xu, J. (2019) Frontiers in Earth Sciences 7, 151.

Moens, C., Montalvo, D., Smolders, E. (2021). European Journal of Soil Sciences 72, 2199-2214.

Morlock, M.A., Vogel, H., Nigg, V., Ordoñez, L.G., Hasberg, A.K.M., Melles, M., Russell, J.M., Bijaksana, S. Journal of Paleolimnology, 61, 279-295.

Morlock, M.A., Vogel, H., Russell, J.M., Anselmetti, F.S., Bijaksana, S. (2021). Journal of Quaternary Sciences 36, 1040-1051.

Morton, S.C., Edwards, M. (2005) Critical Reviews in Environmental Science and Technology 35, 333-364.

Posth, N.R., Canfield, D.E., Kappler, A. (2014) Biogenic Fe (III) minerals: from formation to diagenesis and preservation in the rock record. Earth-Science Reviews, 135, 103–121.

Roh, Y., Zhang, C.-L., Vali, H., Lauf, R. J., Zhou, J., Phelps, T. J. (2003). Clays and Clay Minerals 51, 83-95.

Russell, J.M., Bijaksana, S., Vogel, H., Melles, M., Kallmeyer, J., Ariztegui, D., Crowe, S.A., Fajar, S., Hafidz, A., Haffner, D., Hasberg, A., Ivory, S., Kelly, C., King, J., Kirana, K., Morlock, M., Noren, A., O'Grady, R., Ordoñez, L., Stevenson, J., von Rintelen, T., Vuillemin, A., Watkinson, I., Wattrus, N., Wicaksono, S., Wonik, T., Bauer, K., Deino, A., Friese, A., Henny, C., Imran, Marwoto, R., Ngkoimani, L. O., Nomosatryo, S., Safiuddin, L. O., Simister, R., Tamuntuan, G. (2016) The Towuti Drilling Project: Scientific Drilling, 21, 29–40.

Russell, J.M., Vogel, H., Bijaksana, S., Melles, M., Deino, A., Hafidz, A., Hasberg, A., Morlock, M., von Rintelen, T., Sheppard, R., Stelbrink, B., Stevenson, J. (2020) The Late Palaeogeography, Palaeoclimatology, Palaeoecology 556, 109905.

Sheppard, R.Y., Milliken, R.E., Russell, J.M., Darby Dyar, M., Sklute, E.C., Vogel, H., Melles, M., Bijaksana, S., Morlock, M.A., and Hasberg, A.K.M. (2019). Chemical Geology 512, 11–30.

Swanner, E.D., Lambrecht, N., Wittkop, C., Harding, C., Katsev, S., Torgeson, J., Poulton, S.W. (2020) Earth-Science Reviews 211, 103430.

Tosca, N.J., Jiang, C.Z., Rasmussen, B., Muhling, J. (2019) Free Radical Biology and Medicine 140, 138-153.

Vuillemin, A., Friese, A., Alawi, M., Henny, C., Nomosatryo, S., Wagner, D., Crowe, S.A., Kallmeyer, J. (2016) Frontiers in Microbiology, 7, e1007. https://doi.org/10.3389/fmicb.2016.01007

Vuillemin, A., Horn, F., Friese, A., Winkel, M., Alawi, M., Wagner, D., Henny, C., Orsi, W.D., Crowe, S.A., Kallmeyer, J. (2018). Environmental Microbiology, 20, 4297-4313.

Vuillemin, A., Wirth, R., Kemnitz, H., Schleicher, A.M., Friese, A., Bauer, K.W., Simister, R., Nomosatryo, S., Ordoñez, L., Ariztegui, D., Henny, C., Crowe, S.A., Benning, L.G., Kallmeyer, J., Russell, J.M., Bijaksana, S., Vogel, H., the Towuti Drilling Project Science Team (2019) Geology 47, 540-544.

Vuillemin, A., Friese, A., Wirth, R., Schuessler, J.A., Schleicher, A.M., Kemnitz, A., Lücke, A., Bauer, K.W., Nomosatryo, S., von Blanckenburg, F., Simister, R., Ordoñez, L.G., Ariztegui, D., Henny, C., Russell, J.M., Bijaksana, S., Vogel, H., Crowe, S.A., Kallmeyer, J., the Towuti Drilling Project Science Team (2020). Biogeosciences 17, 1955-

Vuillemin, A., Mayr, C., Schuessler, J.A., Friese, A., Bauer, K.W., Lücke, A., Heuer, V.B., Glombitza, C., Henny, C., von Blanckenburg, F., Russell, J.M., Bijaksana, S., Vogel, H., Crowe, S.A., Kallmeyer, J. (2023). GSA Bulletin 135, 504-522.

Zachara, J.M., Kukkapadu, R.K., Fredrickson, J.K., Gorby, Y.A., Smith, S.C. (2002) Geomicrobiology Journal 19, 179-207.

Appendix V

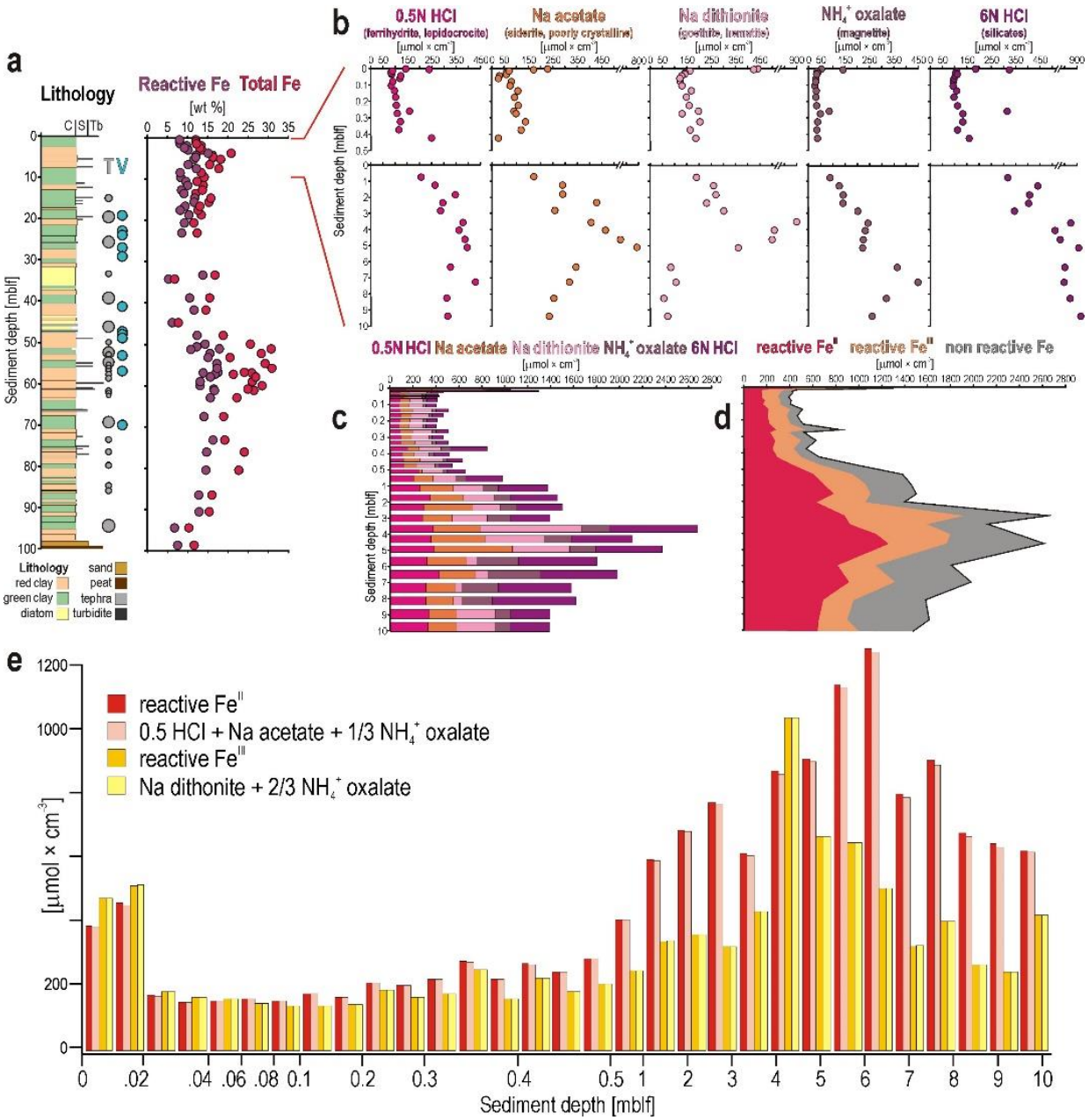

Figure A5S1. Additional depth profiles for bulk iron and sequentially extracted iron phases. (a) Stratigraphy of site TDP-1A and reactive and total iron; (b) separate and (c) cumulative plots for iron fractions sequentially extracted with solutions of 0.5 N HCl, sodium acetate adjusted to pH 4.5, sodium dithionite adjusted to pH 4.8, 0.2 M ammonium oxalate with 0.17 M oxalic acid adjusted to pH 3.2, and near boiling 6 N HCl; (d) Iron speciation was determined spectrophotometically. Note that Fe^{III} within the 0.5N HCl fraction was below detection, so that the reactive Fe^{III} pool is entirely composed of the sodium dithionite (*e.g.* goethite, hematite) and ammonium oxalate (*e.g.* magnetite) fractions;

and (e) and close-up of the cumulative plot for sequentially extracted iron fractions (modified from Friese et al., 2021).

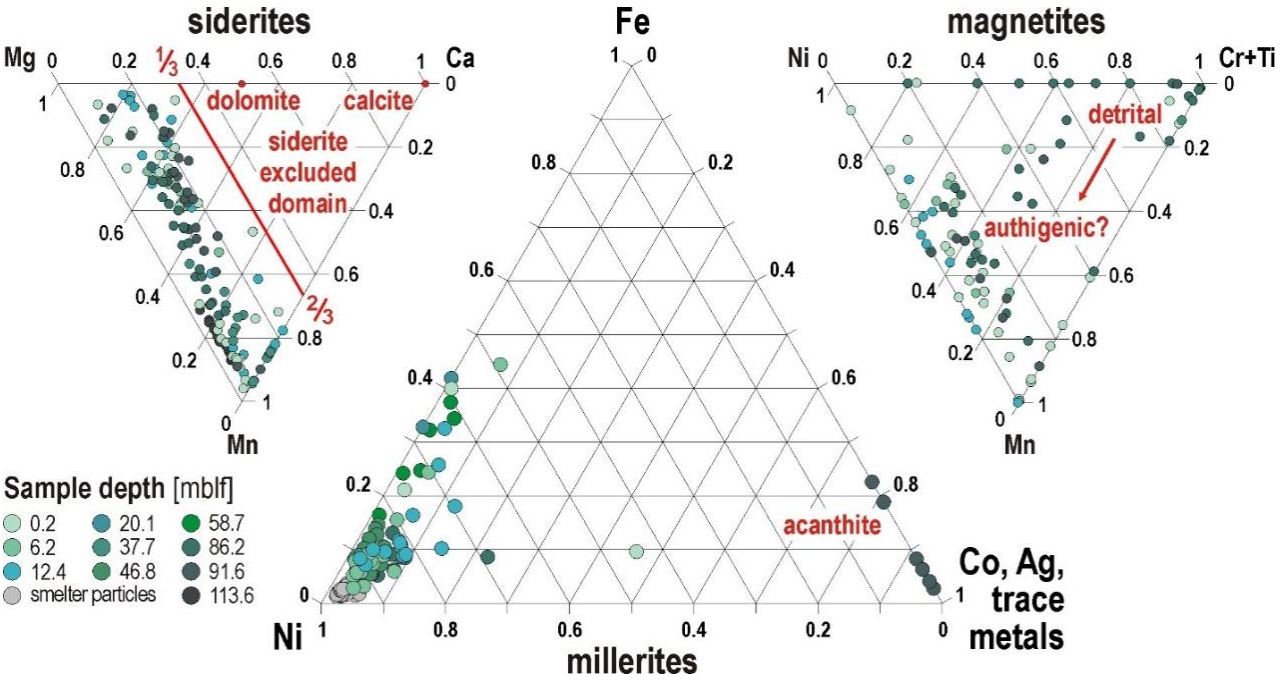

Figure A5S2. Elemental EDX punctual analyses. The ternary plots show that millerites include minor Fe^{2+} traces (center). Acanthite (ac) was also identified in deep sediments (see Figure S-9). Siderites (left) substitute Mn^{2+} for Fe^{2+} in the initial growth phase, incorporating variable amount of Mg^{2+} but constant Ca^{2+} traces in crystal rims. Magnetites (right) show some indication of trace metal incorporation related to microbial reduction. Although trace elements (e.g., Ni, Mn, Ti, and Cr) are common in magmatic magnetites, increased Mn and Ni contents potentially point to neoformation of magnetites in the water column (Bauer et al., 2020) and sediment (Vuillemin et al., 2019a).

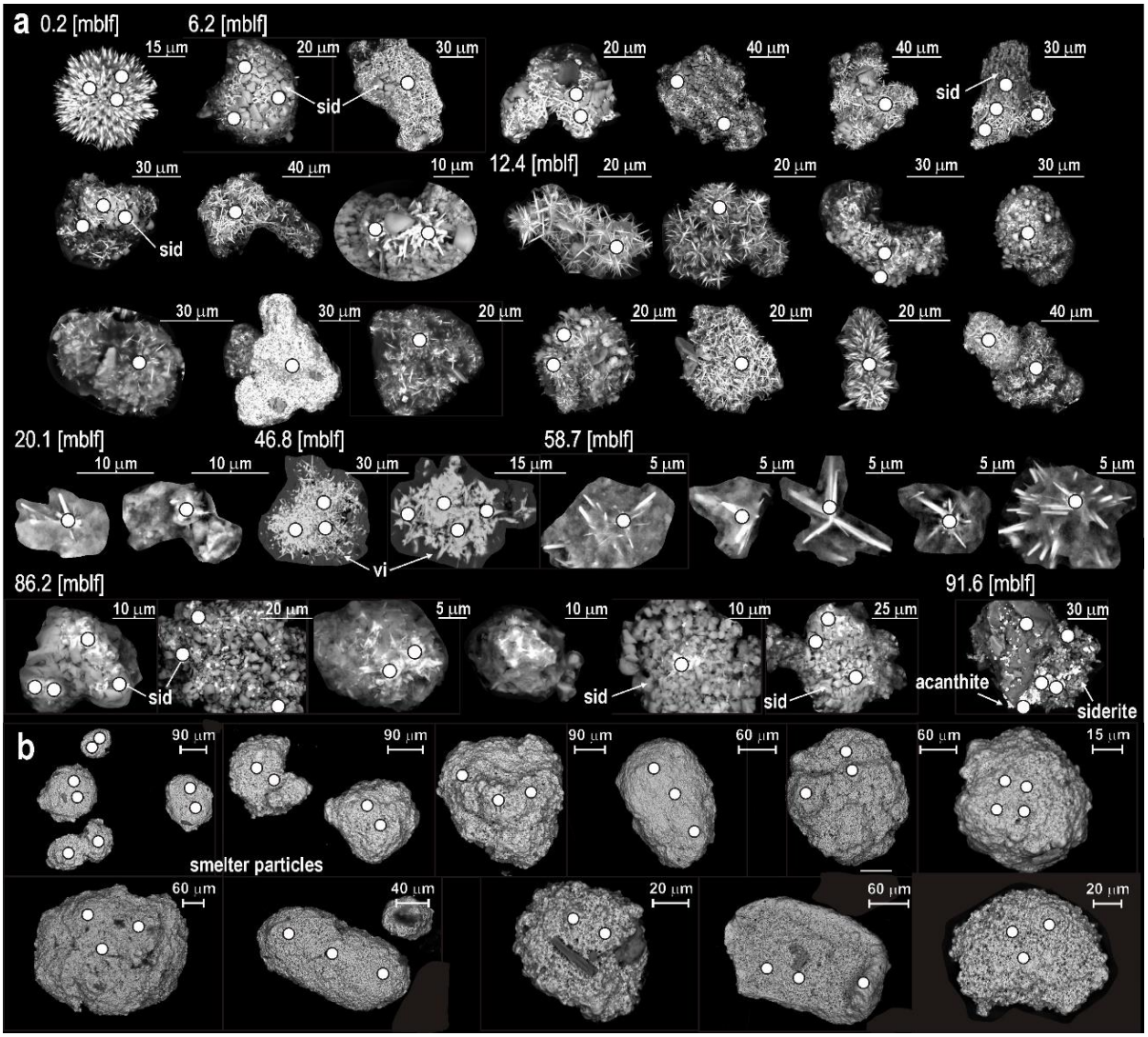

Figure A5S3. SEM images of millerites and corresponding points of EDX analyses. (a) Millerite crystals identified in dense fractions, sometime entangled with siderite or as inclusions in vivianites, and corresponding points of EDX analyses. (b) Millerite dust contaminants (i.e. smelter particles) derived from Sorowako's nickel mine smelter and corresponding points of EDX analyses.

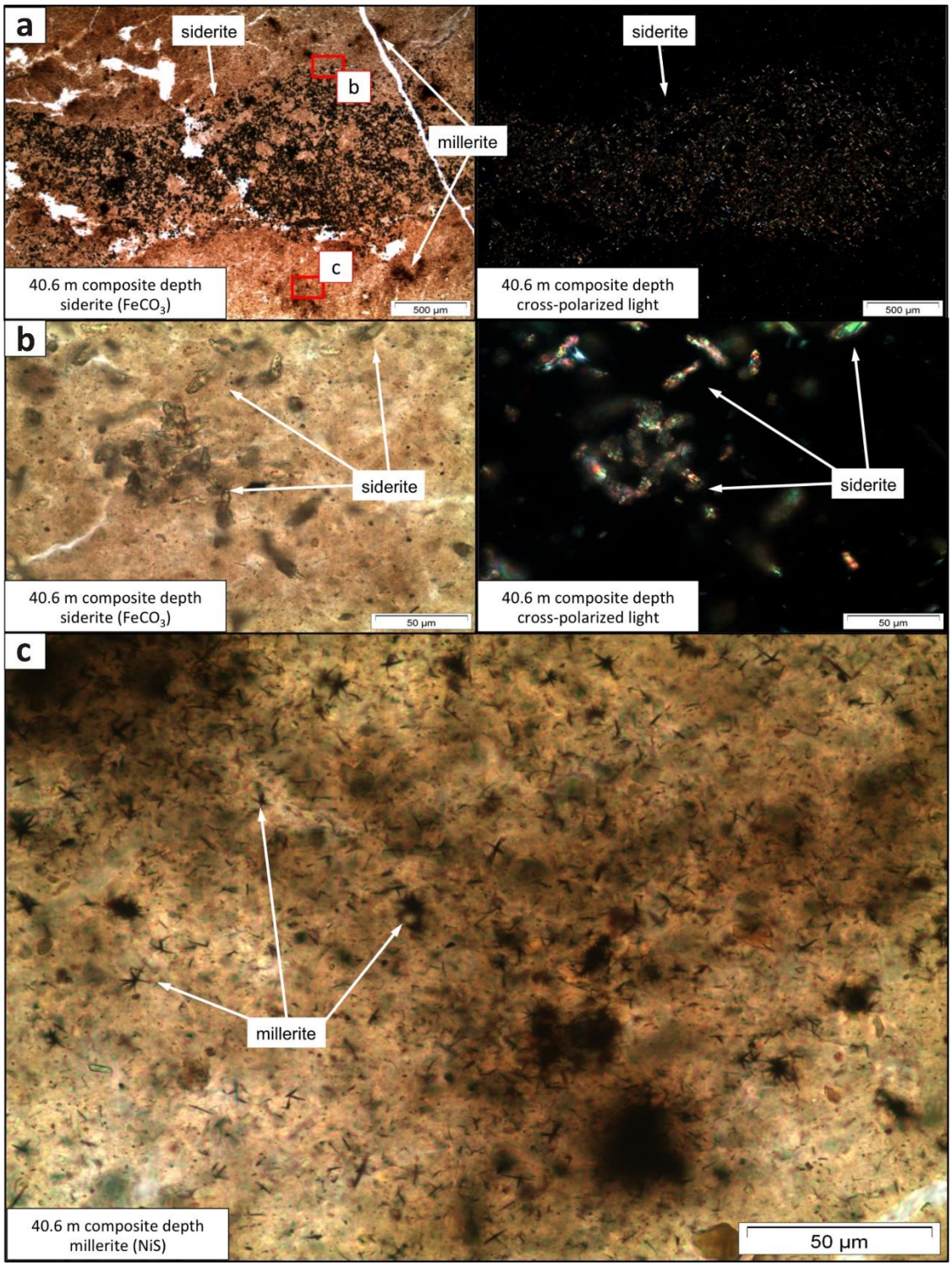

Figure A5S4. Optical images of sediment smear slides in natural and polarized light. The density of siderite and millerite crystals in the vicinity of micro-cracks in the sediment argue for secondary precipitation from pore water associated with the additional pore space accommodated during seismic events with (a-c) close-ups to millerite crystals.

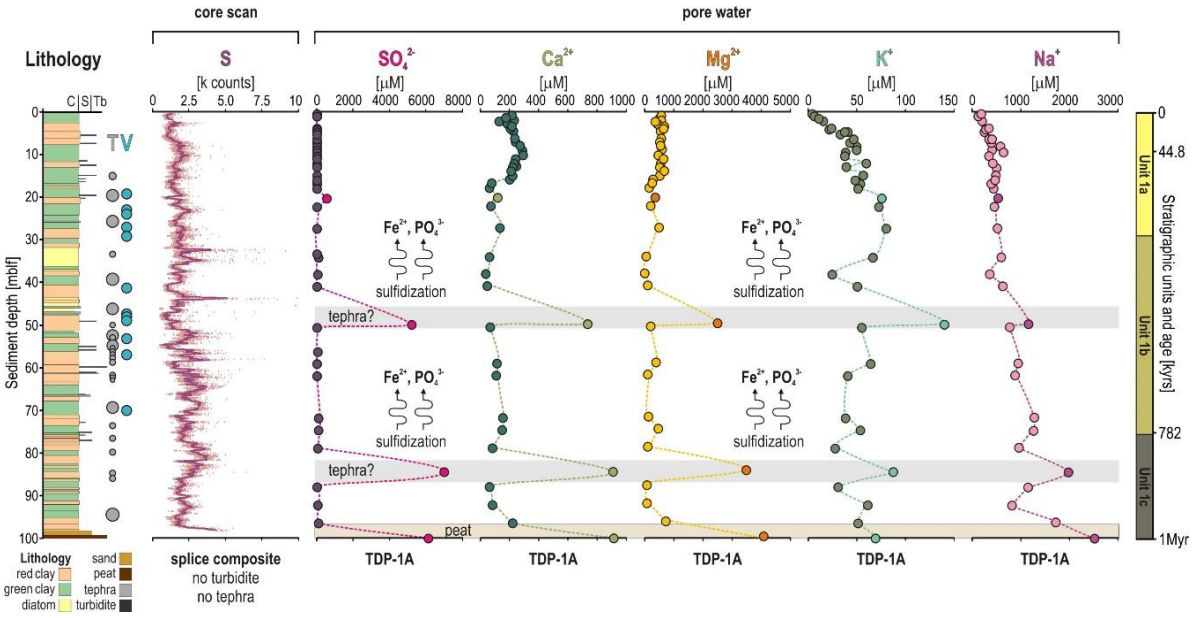

Figure A5S5. Depth profiles for bulk sediment, and pore water geochemistry. (Left to right) Stratigraphy of site TDP-1A; XRF core-scanning profile for total S; pore water concentrations for SO_4^{2-}, Ca^{2+}, Mg^{2+}, K^+ and Na^+. The outliers in pore water concentrations may be explained by sporadic tephra and dissolution of anhydrite ($CaSO_4$) and sanidine ($KAlSi_3O_8$). An additional source of sulphate to the lake could result in sulphidization of iron oxides (*e.g.* goethite, hematite), with subsequent release and diffusion of pore water Fe^{2+} and PO_4^{3-} that would promote saturated conditions with respect to vivianite. Similarly, microbial acid-sulphate weathering of basaltic tephra could (trans)form ferric minerals, *e.g.* jarosite [$(K, Na, H_3O)Fe^{3+}_3(SO_4)_2(OH)_6$], to release sulphate (Sekerci and Balci, 2022). Stratigraphic units correspond to: (Unit 1c) lake initial stage with basin subsidence and regular riverine-deltaic inflows; (Unit 1b) a productive phase with low sedimentation rates; and (Unit 1a) hydrological changes and lake level fluctuations during the Late Pleistocene (Russell et al., 2020; Vuillemin et al., 2023).

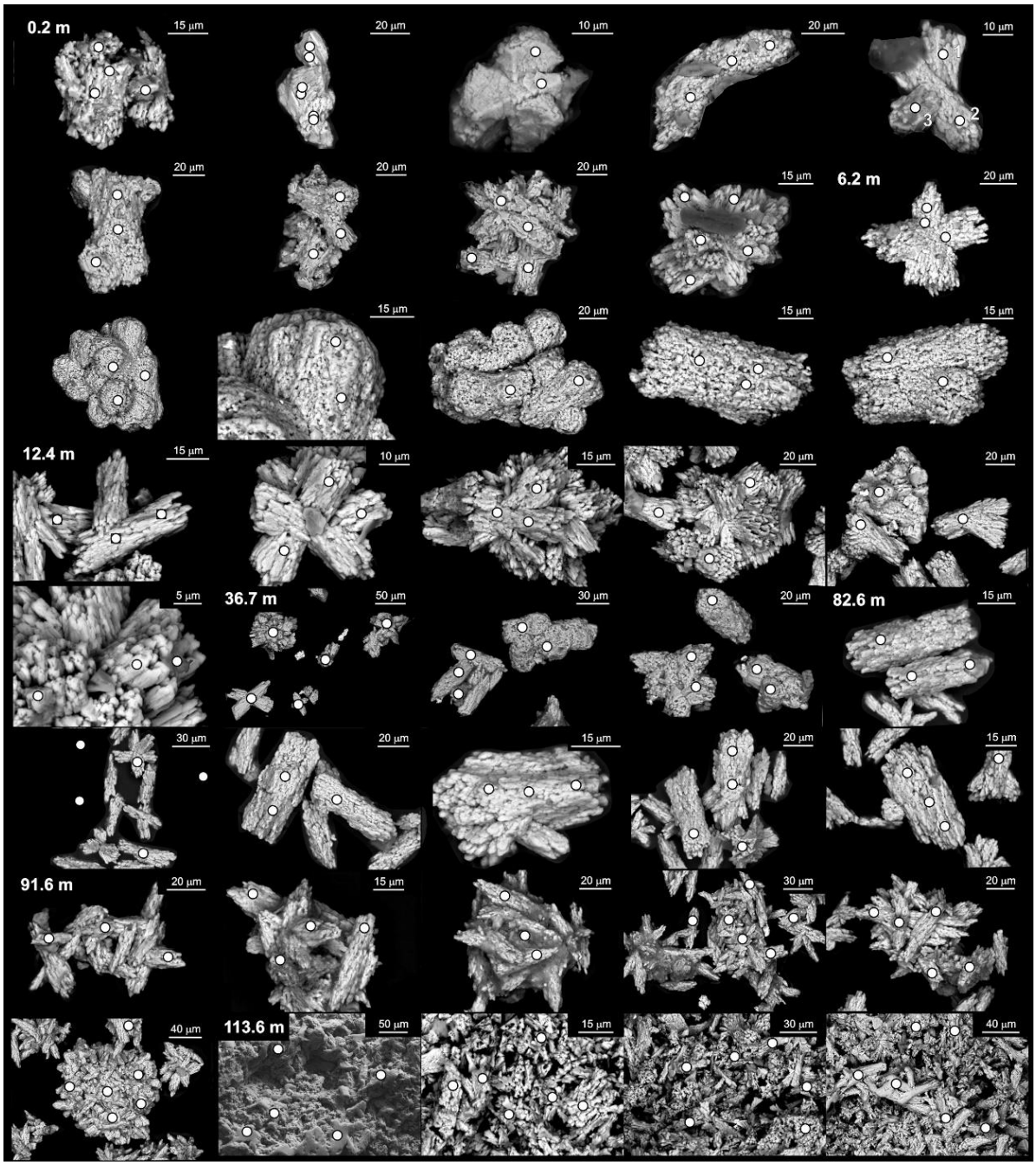

Figure A5S6. SEM images of siderites and corresponding points of EDX analyses.

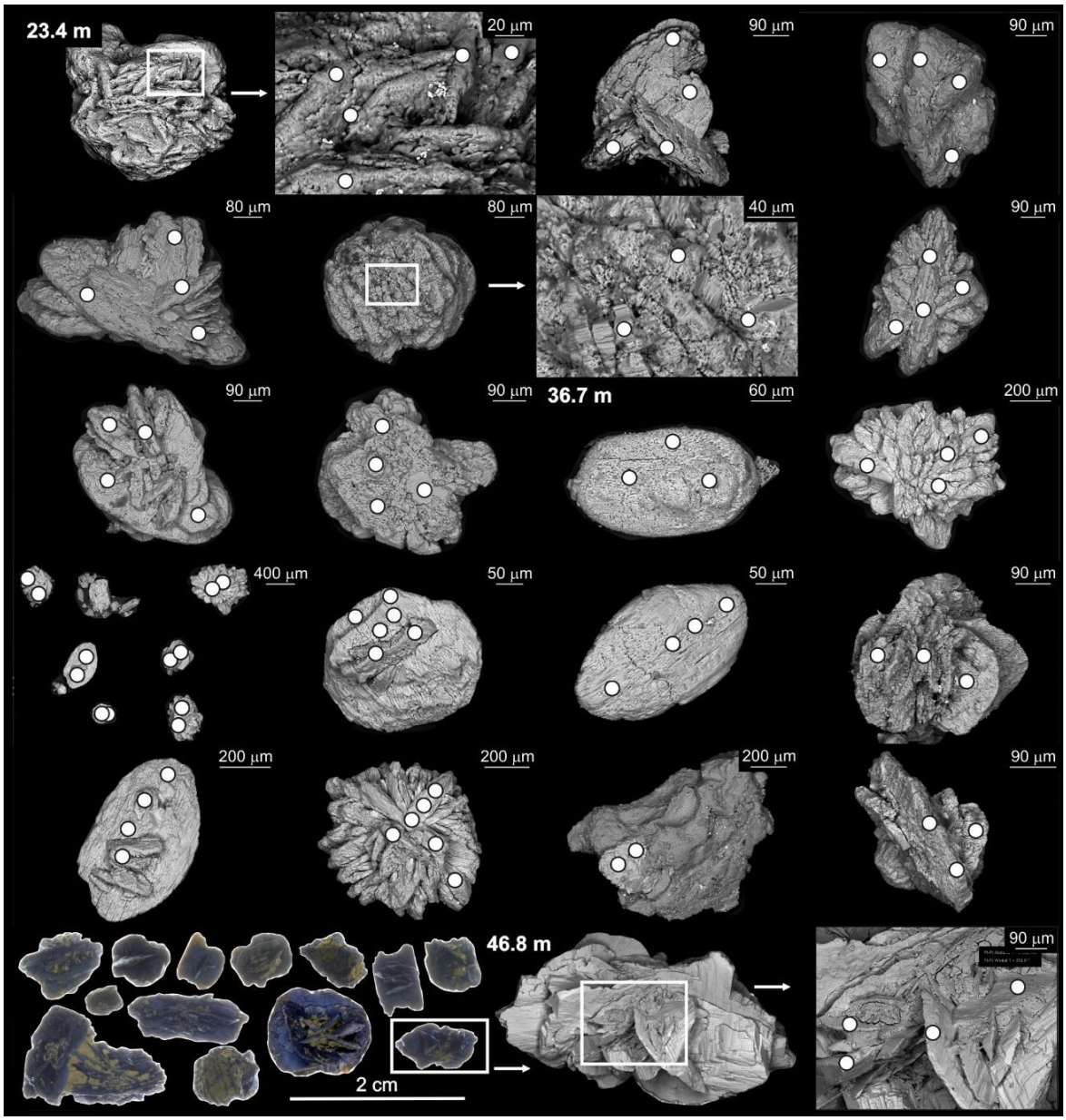

Figure A5S7. SEM images of vivianites and corresponding points of EDX analyses.

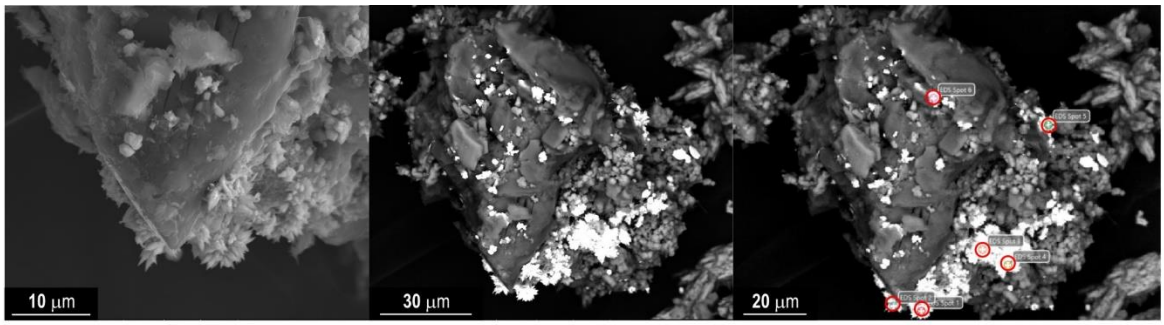

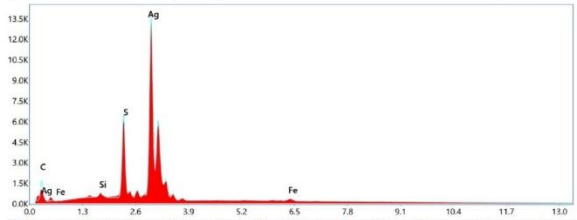

Element	Weight %	MDL	Atomic %	Net Int.	Error %	R	A	F
C K	13.6	0.58	52.0	470.1	12.4	0.7458	0.0897	1.0000
Si K	0.4	0.09	0.7	240.3	13.5	0.7972	0.4811	1.0202
S K	10.0	0.09	14.4	5722.3	4.9	0.8087	0.6786	1.0377
Fe K	1.1	0.29	0.9	214.5	17.9	0.8660	0.8709	1.0630
Ag L	74.9	0.29	32.0	13880.4	3.6	0.8233	0.7691	1.0038

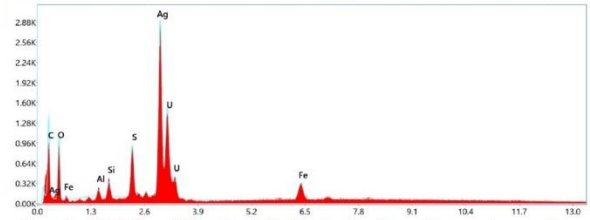

Element	Weight %	MDL	Atomic %	Net Int.	Error %	R	A	F
C K	33.2	0.64	59.1	695.9	11.1	0.8393	0.1274	1.0000
O K	22.0	0.55	29.5	606.9	12.3	0.8535	0.0652	1.0000
Al K	0.4	0.13	0.3	77.0	20.6	0.8806	0.4314	1.0088
Si K	0.7	0.12	0.5	184.9	11.1	0.8854	0.5504	1.0133
S K	3.0	0.10	2.0	771.7	5.6	0.8944	0.7379	1.0276
Fe K	4.1	0.37	1.6	365.3	7.9	0.9342	0.9311	1.0667
Ag L	34.0	0.31	6.7	2921.5	3.5	0.9054	0.8436	1.0047
U M	2.7	1.38	0.2	191.8	9.6	0.9081	0.8582	1.0176

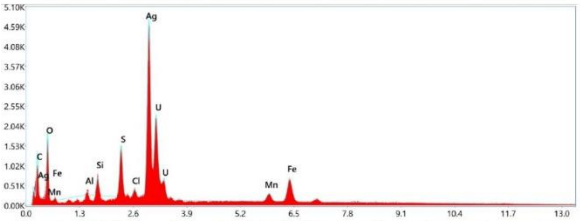

Element	Weight %	MDL	Atomic %	Net Int.	Error %	R	A	F
C K	23.3	0.72	47.2	635.1	11.7	0.8258	0.1114	1.0000
O K	24.1	0.55	36.7	1045.5	11.5	0.8403	0.0689	1.0000
Al K	0.3	0.13	0.2	78.4	23.3	0.8686	0.4056	1.0092
Si K	1.0	0.12	0.9	382.8	9.1	0.8736	0.5256	1.0140
S K	3.3	0.10	2.5	1235.8	5.8	0.8831	0.7176	1.0295
Cl K	0.1	0.14	0.1	41.4	61.8	0.8876	0.7669	1.0448
Mn K	2.0	0.29	0.9	285.2	12.3	0.9215	0.9071	1.0582
Fe K	6.4	0.36	2.8	834.0	5.3	0.9257	0.9255	1.0604
Ag L	38.2	0.31	8.6	4808.8	3.5	0.8947	0.8293	1.0049
U M	1.3	1.03	0.1	130.7	16.7	0.8977	0.8453	1.0219

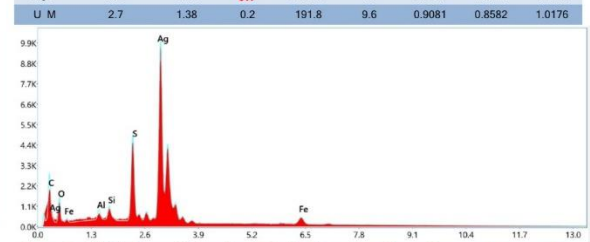

Element	Weight %	MDL	Atomic %	Net Int.	Error %	R	A	F
C K	28.7	0.52	60.2	1246.1	11.1	0.8152	0.1003	1.0000
O K	13.2	0.44	20.9	822.5	12.3	0.8299	0.0559	1.0000
Al K	0.8	0.08	0.8	447.7	10.9	0.8589	0.4212	1.0113
Si K	0.9	0.07	0.8	618.0	8.1	0.8641	0.5360	1.0174
S K	6.6	0.07	5.2	4471.7	4.5	0.8739	0.7240	1.0334
Fe K	2.2	0.20	1.0	513.0	9.4	0.9187	0.9142	1.0647
Ag L	47.5	0.21	11.1	10438.0	3.2	0.8860	0.8166	1.0039

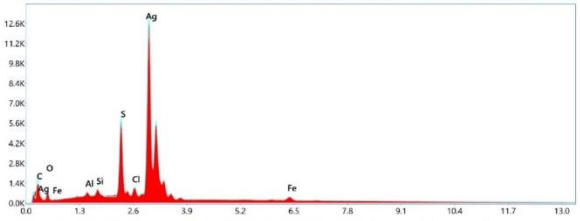

Element	Weight %	MDL	Atomic %	Net Int.	Error %	R	A	F
C K	17.0	0.58	50.5	657.2	12.0	0.7724	0.0915	1.0000
O K	7.3	0.49	16.2	395.7	13.2	0.7872	0.0502	1.0000
Al K	0.5	0.10	0.6	235.8	15.6	0.8181	0.3840	1.0122
Si K	0.7	0.08	0.9	420.4	10.4	0.8238	0.4986	1.0190
S K	8.3	0.08	9.2	5243.6	4.8	0.8348	0.6933	1.0365
Cl K	0.5	0.13	0.5	280.6	16.2	0.8401	0.7188	1.0552
Fe K	1.5	0.26	0.9	319.3	15.8	0.8876	0.8873	1.0635
Ag L	64.3	0.26	21.2	13268.3	3.5	0.8486	0.7854	1.0038

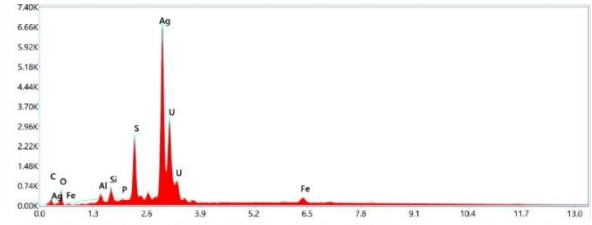

Element	Weight %	MDL	Atomic %	Net Int.	Error %	R	A	F
C K	4.4	0.77	18.1	87.7	17.4	0.7429	0.0947	1.0000
O K	10.5	0.66	32.4	295.5	13.5	0.7572	0.0521	1.0000
Al K	0.6	0.16	1.1	128.1	17.8	0.7884	0.3517	1.0109
Si K	1.0	0.14	1.8	287.4	11.5	0.7943	0.4631	1.0166
P K	0.0	0.10	0.1	8.9	73.8	0.8002	0.5652	1.0263
S K	7.6	0.13	11.7	2276.0	5.5	0.8059	0.6601	1.0322
Fe K	2.4	0.42	2.2	265.2	13.6	0.8636	0.8705	1.0640
Ag L	69.7	0.39	32.0	7036.8	3.8	0.8205	0.7683	1.0041
U M	3.8	1.60	0.8	318.8	11.6	0.8244	0.7848	1.0169

Figure A5S8. SEM images of acanthite and corresponding points of EDX analyses.

Appendix VI – Conference contributions and synchrotron work

Conference lectures

- Presentation title: 'Multi-Step Crystallization Pathway of Vivianite'
  Alice Paskin, T. Couasnon, J. P. H. Perez, S. S. Lobanov, R. Blukis, S. Reinsch, and L. G. Benning
  GeoMinKöln 2022, Cologne, Germany. Date: 12th September 2022
  (Entire costs were covered by the European Association of Geochemistry: Student Sponsorship grant awarded to A. Paskin.)
- Presentation title: 'Nucleation and crystallization of vivianite via nanoparticulate amorphous ferrous phosphate: a combined spectroscopic and microscopic study'
  Alice Paskin, T. Couasnon, J. P. H. Perez, S. S. Lobanov, R. Blukis, S. Reinsch, and L. G. Benning
  Goldschmidt Lyon 2023, France. Date: 14th July 2023

Synchrotron Beamtime

- Funded successful synchrotron beamtime, including travel expenses, awarded for *in situ* SAXS/WAXS (I22 beamline) at Diamond Light Source, UK from 8 - 12th December 2022.

  Proposal authors: **Alice Paskin**, T. Couasnon, L. G. Benning

References

(1) Nriagu, J. O. Stability of vivianite and ion-pair formation. *Geochimica et Cosmochimica Acta* **1972**, *36* (4), 459-470. DOI: https://doi.org/10.1016/0016-7037(72)90035-X.

(2) Rosenqvist, I. T. Formation of vivianite in holocene clay sediments. *Lithos* **1970**, *3* (4), 327-334. DOI: https://doi.org/10.1016/0024-4937(70)90039-3.

(3) Rothe, M.; Frederichs, T.; Eder, M.; Kleeberg, A.; Hupfer, M. Evidence for vivianite formation and its contribution to long-term phosphorus retention in a recent lake sediment: a novel analytical approach. *Biogeosciences* **2014**, *11* (18), 5169-5180. DOI: 10.5194/bg-11-5169-2014.

(4) Rothe, M.; Kleeberg, A.; Hupfer, M. The occurrence, identification and environmental relevance of vivianite in waterlogged soils and aquatic sediments. *Earth-Science Reviews* **2016**, *158*, 51-64.

(5) Slomp, C. P. Vivianite blues. *Nature Geoscience* **2023**, *16* (5), 394-394. DOI: 10.1038/s41561-023-01174-7.

(6) Vuillemin, A.; Friese, A.; Wirth, R.; Schuessler, J. A.; Schleicher, A. M.; Kemnitz, H.; Lücke, A.; Bauer, K. W.; Nomosatryo, S.; von Blanckenburg, F.; et al. Vivianite formation in ferruginous sediments from Lake Towuti, Indonesia. *Biogeosciences* **2020**, *17* (7), 1955-1973. DOI: 10.5194/bg-17-1955-2020.

(7) Walpersdorf, E.; Koch, C. B.; Heiberg, L.; O'Connell, D. W.; Kjaergaard, C.; Hansen, H. C. B. Does vivianite control phosphate solubility in anoxic meadow soils? *Geoderma* **2013**, *193-194*, 189-199. DOI: 10.1016/j.geoderma.2012.10.003.

(8) Mortimer, C. H. The Exchange of Dissolved Substances Between Mud and Water in Lakes. *Journal of Ecology* **1941**, *29* (2), 280-329. DOI: 10.2307/2256395.

(9) Hearn, P. P.; Parkhurst, D. L.; Callender, E. Authigenic vivianite in Potomac River sediments; control by ferric oxy-hydroxides. *Journal of Sedimentary Research* **1983**, *53* (1), 165-177. DOI: 10.1306/212F817F-2B24-11D7-8648000102C1865D

(10) Nriagu, J. O.; Dell, C. I. Diagenetic formation of iron phosphates in recent lake sediments. *American Mineralogist* **1974**, *59* (9-10), 934-946.

(11) Goedhart, R.; Müller, S.; van Loosdrecht, M. C. M.; van Halem, D. Vivianite precipitation for iron recovery from anaerobic groundwater. *Water Research* **2022**, *217*, 118345. DOI: https://doi.org/10.1016/j.watres.2022.118345.

(12) Liu, J.; Cheng, X.; Qi, X.; Li, N.; Tian, J.; Qiu, B.; Xu, K.; Qu, D. Recovery of phosphate from aqueous solutions via vivianite crystallization: Thermodynamics and influence of pH. *Chemical Engineering Journal* **2018**, *349*, 37-46. DOI: https://doi.org/10.1016/j.cej.2018.05.064.

(13) Gschwend, P. M.; Reynolds, M. D. Monodisperse ferrous phosphate colloids in an anoxic groundwater plume. *Journal of Contaminant Hydrology* **1987**, *1* (3), 309-327. DOI: https://doi.org/10.1016/0169-7722(87)90011-8.

(14) Mer, V. K. L. Nucleation in Phase Transitions. *Industrial & Engineering Chemistry* **1952**, *44* (6), 1270-1277.

(15) Bots, P.; Benning, L. G.; Rodriguez-Blanco, J.-D.; Roncal-Herrero, T.; Shaw, S. Mechanistic Insights into the Crystallization of Amorphous Calcium Carbonate (ACC). *Crystal Growth & Design* **2012**, *12* (7), 3806-3814. DOI: 10.1021/cg300676b.

(16) Rodriguez-Blanco, J. D.; Shaw, S.; Benning, L. G. The kinetics and mechanisms of amorphous calcium carbonate (ACC) crystallization to calcite, viavaterite. *Nanoscale* **2011**, *3* (1), 265-271, DOI: 10.1039/C0NR00589D.

(17) Nielsen, M. H.; Aloni, S.; De Yoreo, J. J. In situ TEM imaging of CaCO3 nucleation reveals coexistence of direct and indirect pathways. *Science* **2014**, *345* (6201), 1158-1162. DOI: 10.1126/science.1254051

(18) Teng, H. H.; Dove, P. M.; Orme, C. A.; De Yoreo, J. J. Thermodynamics of calcite growth: Baseline for understanding biomineral formation. *Science* **1998**, *282* (5389), 724-727. DOI: 10.1126/science.282.5389.724.

(19) Gower, L. B. Biomimetic Model Systems for Investigating the Amorphous Precursor Pathway and Its Role in Biomineralization. *Chemical Reviews* **2008**, *108* (11), 4551-4627. DOI: 10.1021/cr800443h.

(20) Eanes, E. D.; Gillessen, I. H.; Posner, A. S. Intermediate States in the Precipitation of Hydroxyapatite. *Nature* **1965**, *208* (5008), 365-367. DOI: 10.1038/208365a0.

(21) Boskey, A. L.; Posner, A. S. Conversion of amorphous calcium phosphate to microcrystalline hydroxyapatite. A pH-dependent, solution-mediated, solid-solid conversion. *The Journal of Physical Chemistry* **1973**, *77* (19), 2313-2317. DOI: 10.1021/j100638a011.

(22) Pan, H.; Liu, X. Y.; Tang, R.; Xu, H. Y. Mystery of the transformation from amorphous calcium phosphate to hydroxyapatite. *Chemical Communications* **2010**, *46* (39), 7415-7417, 10.1039/C0CC00971G. DOI: 10.1039/C0CC00971G.
(23) Stawski, T. M.; van Driessche, A. E. S.; Ossorio, M.; Rodriguez-Blanco, J. D.; Besselink, R.; Benning, L. G. Formation of calcium sulfate through the aggregation of sub-3 nanometre primary species. *Nature Communications* **2016**, *7*, 11177. DOI: 10.1038/ncomms11177.
(24) Van Driessche, A. E. S.; Benning, L. G.; Rodriguez-Blanco, J. D.; Ossorio, M.; Bots, P.; Garcia-Ruiz, J. M. The Role and Implications of Bassanite as a Stable Precursor Phase to Gypsum Precipitation. *Science* **2012**, *336* (6077), 69-72. DOI: 10.1126/science.1215648.
(25) Ossorio, M.; Stawski, T. M.; Rodriguez-Blanco, J. D.; Sleutel, M.; Garcia-Ruiz, J. M.; Benning, L. G.; Van Driessche, A. E. S. Physicochemical and Additive Controls on the Multistep Precipitation Pathway of Gypsum. *Minerals* **2017**, *7* (8). DOI: 10.3390/min7080140.
(26) Habraken, W. J.; Tao, J.; Brylka, L. J.; Friedrich, H.; Bertinetti, L.; Schenk, A. S.; Verch, A.; Dmitrovic, V.; Bomans, P. H.; Frederik, P. M.; et al. Ion-association complexes unite classical and non-classical theories for the biomimetic nucleation of calcium phosphate. *Nat Commun* **2013**, *4*, 1507. DOI: 10.1038/ncomms2490.
(27) Loh, N. D.; Sen, S.; Bosman, M.; Tan, S. F.; Zhong, J.; Nijhuis, C. A.; Král, P.; Matsudaira, P.; Mirsaidov, U. Multistep nucleation of nanocrystals in aqueous solution. *Nature Chemistry* **2017**, *9* (1), 77-82. DOI: 10.1038/nchem.2618.
(28) Rodriguez-Blanco, J. D.; Shaw, S.; Benning, L. G. A route for the direct crystallization of dolomite†. *American Mineralogist* **2015**, *100* (5-6), 1172-1181. DOI: 10.2138/am-2015-4963
(29) DeVol, R. T.; Sun, C.-Y.; Marcus, M. A.; Coppersmith, S. N.; Myneni, S. C. B.; Gilbert, P. U. P. A. Nanoscale Transforming Mineral Phases in Fresh Nacre. *Journal of the American Chemical Society* **2015**, *137* (41), 13325-13333. DOI: 10.1021/jacs.5b07931.
(30) Gal, A.; Kahil, K.; Vidavsky, N.; DeVol, R. T.; Gilbert, P. U. P. A.; Fratzl, P.; Weiner, S.; Addadi, L. Particle Accretion Mechanism Underlies Biological Crystal Growth from an Amorphous Precursor Phase. *Advanced Functional Materials* **2014**, *24* (34), 5420-5426, https://doi.org/10.1002/adfm.201400676. DOI: https://doi.org/10.1002/adfm.201400676
(31) Bach, S.; Celinski, V. R.; Dietzsch, M.; Panthofer, M.; Bienert, R.; Emmerling, F.; Schmedt auf der Gunne, J.; Tremel, W. Thermally highly stable amorphous zinc phosphate intermediates during the formation of zinc phosphate hydrate. *Journal of the American Chemical Society* **2015**, *137* (6), 2285-2294. DOI: 10.1021/ja5103663.
(32) Bach, S.; Panthöfer, M.; Bienert, R.; Buzanich, A. d. O. G.; Emmerling, F.; Tremel, W. Role of Water During Crystallization of Amorphous Cobalt Phosphate Nanoparticles. *Crystal Growth & Design* **2016**, *16* (8), 4232-4239. DOI: 10.1021/acs.cgd.6b00208.
(33) Sun, S.; Gebauer, D.; Colfen, H. Alignment of Amorphous Iron Oxide Clusters: A Non-Classical Mechanism for Magnetite Formation. *Angew Chem Int Ed Engl* **2017**, *56* (14), 4042-4046. DOI: 10.1002/anie.201610275.
(34) Baumgartner, J.; Dey, A.; Bomans, P. H. H.; Le Coadou, C.; Fratzl, P.; Sommerdijk, N. A. J. M.; Faivre, D. Nucleation and growth of magnetite from solution. *Nature Materials* **2013**, *12* (4), 310-314. DOI: 10.1038/nmat3558.
(35) Yuwono, V. M.; Burrows, N. D.; Soltis, J. A.; Penn, R. L. Oriented Aggregation: Formation and Transformation of Mesocrystal Intermediates Revealed. *Journal of the American Chemical Society* **2010**, *132* (7), 2163-2165. DOI: 10.1021/ja909769a.
(36) Montes-Hernandez, G.; Renard, F. Time-Resolved in Situ Raman Spectroscopy of the Nucleation and Growth of Siderite, Magnesite, and Calcite and Their Precursors. *Crystal Growth & Design* **2016**, *16* (12), 7218-7230. DOI: 10.1021/acs.cgd.6b01406.
(37) Davidson, L. E.; Shaw, S.; Benning, L. G. The kinetics and mechanisms of schwertmannite transformation to goethite and hematite under alkaline conditions. *American Mineralogist* **2008**, *93* (8-9), 1326-1337. DOI: 10.2138/am.2008.2761
(38) Moore, P. B. Crystal chemistry of the basic iron phosphates. *American Mineralogist* **1970**, *55* (1-2), 135-169.
(39) Egger, M.; Jilbert, T.; Behrends, T.; Rivard, C.; Slomp, C. P. Vivianite is a major sink for phosphorus in methanogenic coastal surface sediments. *Geochimica et Cosmochimica Acta* **2015**, *169*, 217-235. DOI: https://doi.org/10.1016/j.gca.2015.09.012.

(40) Wilfert, P.; Dugulan, A. I.; Goubitz, K.; Korving, L.; Witkamp, G. J.; Van Loosdrecht, M. C. M. Vivianite as the main phosphate mineral in digested sewage sludge and its role for phosphate recovery. *Water Research* **2018**, *144*, 312-321. DOI: 10.1016/j.watres.2018.07.020.
(41) Wang, S.; An, J. K.; Wan, Y. X.; Du, Q.; Wang, X.; Cheng, X.; Li, N. Phosphorus Competition in Bioinduced Vivianite Recovery from Wastewater. *Environmental Science & Technology* **2018**, *52* (23), 13863-13870. DOI: 10.1021/acs.est.8b03022.
(42) Li, C.; Sheng, Y.; Xu, H. Phosphorus recovery from sludge by pH enhanced anaerobic fermentation and vivianite crystallization. *Journal of Environmental Chemical Engineering* **2021**, *9* (1), 104663. DOI: https://doi.org/10.1016/j.jece.2020.104663.
(43) Millet, R. a. Mössbauer Spectroscopy of Synthetic Oxidized Vivianite. *Hyperfine Interactions* **1993**, *77*.
(44) Watson, T. L. The Color change in Vivianite and its effect on the Optical Properties. *American Mineralogist* **1918**, *3* (8), 159-161.
(45) Figueiredo, M. O.; Silva, T. P.; Veiga, J. P. The blue of iron in mineral pigments: a Fe K-edge XANES study of vivianite. *Applied Physics A* **2010**, *99* (2), 357-361. DOI: 10.1007/s00339-010-5637-9.
(46) Ito, T. Structure of Vivianite and Symplesite. *Nature* **1949**, *164* (4167), 449-450. DOI: 10.1038/164449b0.
(47) Mori, H.; Ito, T. The structure of vivianite and symplesite. *Acta Crystallographica* **1950**, *3* (1), 1-6. DOI: doi:10.1107/S0365110X5000001X.
(48) Capitelli, F.; Chita, G.; Ghiara, M. R.; Rossi, M. Crystal-chemical investigation of vivianite minerals. *Zeitschrift Fur Kristallographie-Crystalline Materials* **2012**, *227* (2), 92-101. DOI: 10.1524/zkri.2012.1442.
(49) Cosmidis, J.; Benzerara, K.; Morin, G.; Busigny, V.; Lebeau, O.; Jézéquel, D.; Noël, V.; Dublet, G.; Othmane, G. Biomineralization of iron-phosphates in the water column of Lake Pavin (Massif Central, France). *Geochimica et Cosmochimica Acta* **2014**, *126*, 78-96. DOI: https://doi.org/10.1016/j.gca.2013.10.037.
(50) Faye, G. H.; Manning, P. G.; Nickel, E. H. The polarized optical absorption spectra of tourmaline, cordierite, chloritoid and vivianite: Ferrous-ferric electronic interaction as a source of pleochroism1. *American Mineralogist* **1968**, *53* (7-8), 1174-1201.
(51) Taran, M. N.; Platonov, A. N. Optical absorption spectra of iron ions in vivianite. *Physics and Chemistry of Minerals* **1988**, *16* (3), 304-310. DOI: 10.1007/BF00220700.
(52) Momma, K.; Izumi, F. VESTA: a three-dimensional visualization system for electronic and structural analysis. *Journal of Applied Crystallography* **2008**, *41*, 653-658. DOI: 10.1107/S0021889808012016.
(53) Zelibor, J. L.; Senftle, F. E.; Reinhardt, J. L. A proposed mechanism for the formation of spherical vivianite crystal aggregates in sediments. *Sedimentary Geology* **1988**, *59* (1), 125-142. DOI: https://doi.org/10.1016/0037-0738(88)90103-0.
(54) Fagel, N.; Alleman, L. Y.; Granina, L.; Hatert, F.; Thamo-Bozso, E.; Cloots, R.; André, L. Vivianite formation and distribution in Lake Baikal sediments. *Global and Planetary Change* **2005**, *46* (1-4), 315-336. DOI: 10.1016/j.gloplacha.2004.09.022.
(55) Nanzyo, M.; Onodera, H.; Hasegawa, E.; Ito, K.; Kanno, H. Formation and Dissolution of Vivianite in Paddy Field Soil. *Soil Science Society of America Journal* **2013**, *77* (4), 1452-1459. DOI: 10.2136/sssaj2012.0437n.
(56) Heiberg, L.; Koch, C. B.; Kjaergaard, C.; Jensen, H. S.; Hansen, H. C. B. Vivianite Precipitation and Phosphate Sorption following Iron Reduction in Anoxic Soils. *Journal of Environmental Quality* **2012**, *41* (3), 938-949, https://doi.org/10.2134/jeq2011.0067. DOI: https://doi.org/10.2134/jeq2011.0067
(57) Thali, M. J.; Lux, B.; Lösch, S.; Rösing, F. W.; Hürlimann, J.; Feer, P.; Dirnhofer, R.; Königsdorfer, U.; Zollinger, U. "Brienzi" – The blue Vivianite man of Switzerland: Time since death estimation of an adipocere body. *Forensic Science International* **2011**, *211* (1), 34-40. DOI: https://doi.org/10.1016/j.forsciint.2011.04.009.
(58) Postma, D. Formation of siderite and vivianite and the pore-water composition of a Recent bog sediment in Denmark. *Chemical Geology* **1980**, *31*, 225-244. DOI: https://doi.org/10.1016/0009-2541(80)90088-1.
(59) House, W. A. Geochemical cycling of phosphorus in rivers. *Applied Geochemistry* **2003**, *18* (5), 739-748. DOI: 10.1016/s0883-2927(02)00158-0.
(60) Guastoni, A.; Nestola, F.; Mazzoleni, G.; Vignola, P. Mn-rich graftonite, ferrisicklerite, stanekite and Mn-rich vivianite in a granitic pegmatite at Soe Valley, central Alps, Italy. *Mineralogical Magazine* **2007**, *71* (5), 579-585. DOI: 10.1180/minmag.2007.071.5.579.
(61) Vignola, P. New Evidence of alteration of graftonite-(Mn) from the Malpensata Pegmatite. *Canadian Mineralogist* **2018**, *56* (4), 645-656. DOI: 10.3749/canmin.1700066.

(62) Vignola, P.; Diella, V.; Ferrari, E. S.; Fransolet, A.-M. Complex Mechanisms of Alteration in a Graftonite + Sarcopside + Triphylite Association From the Luna Pegmatite, Italy. *The Canadian Mineralogist* **2011**, *49* (3), 765-776. DOI: 10.3749/canmin.49.3.765
(63) McCammon, C. A.; Burns, R. G. The oxidation mechanism of vivianite as studies by Möessbauer spectroscopy. *American Mineralogist* **1980**, *65* (3-4), 361-366.
(64) Hanzel, D.; Meisel, W.; Hanzel, D.; Gütlich, P. Mössbauer effect study of the oxidation of vivianite. *Solid State Communications* **1990**, *76* (3), 307-310. DOI: https://doi.org/10.1016/0038-1098(90)90843-Z.
(65) Sameshima, T.; Henderson, G. S.; Black, P. M.; Rodgers, K. A. X-ray diffraction studies of vivianite, metavivianite, and baricite. *Mineralogical Magazine* **1985**, *49* (350), 81-85. DOI: 10.1180/minmag.1985.049.350.11
(66) Alborno, A.; Tomson, M. B. The temperature dependence of the solubility product constant of vivianite. *Geochimica Et Cosmochimica Acta* **1994**, *58* (24), 5373-5378. DOI: 10.1016/0016-7037(94)90236-4.
(67) Nanzyo, M.; Yaginuma, H.; Sasaki, K.; Ito, K.; Aikawa, Y.; Kanno, H.; Takahashi, T. Identification of vivianite formed on the roots of paddy rice grown in pots. *Soil Science and Plant Nutrition* **2010**, *56* (3), 376-381. DOI: 10.1111/j.1747-0765.2010.00463.x.
(68) Taylor, K. G.; Hudson-Edwards, K. A.; Bennett, A. J.; Vishnyakov, V. Early diagenetic vivianite [Fe3(PO4)2·8H2O] in a contaminated freshwater sediment and insights into zinc uptake: A μ-EXAFS, μ-XANES and Raman study. *Applied Geochemistry* **2008**, *23* (6), 1623-1633. DOI: https://doi.org/10.1016/j.apgeochem.2008.01.009.
(69) Frost, R. L.; Martens, W.; Williams, P. A.; Kloprogge, J. T. Raman and infrared spectroscopic study of the vivianite-group phosphates vivianite, baricite and bobierrite. *Mineralogical Magazine* **2002**, *66* (6), 1063-1073. DOI: 10.1180/0026461026660077.
(70) Rennert, T.; Eusterhues, K.; De Andrade, V.; Totsche, K. U. Iron species in soils on a mofette site studied by Fe K-edge X-ray absorption near-edge spectroscopy. *Chemical Geology* **2012**, *332*, 116-123. DOI: 10.1016/j.chemgeo.2012.09.046.
(71) Figueiredo, M. O.; Silva, T. P.; Veiga, J. P. The blue of iron in mineral pigments: a Fe K-edge XANES study of vivianite. *Applied Physics a-Materials Science & Processing* **2010**, *99* (2), 357-361. DOI: 10.1007/s00339-010-5637-9.
(72) Wilke, M.; Farges, F.; Petit, P. E.; Brown, G. E.; Martin, F. Oxidation state and coordination of Fe in minerals: An FeK-XANES spectroscopic study. *American Mineralogist* **2001**, *86* (5-6), 714-730.
(73) Wilke, M.; Partzsch, G. M.; Bernhardt, R.; Lattard, D. Determination of the iron oxidation state in basaltic glasses using XANES at the K-edge. *Chemical Geology* **2004**, *213* (1-3), 71-87. DOI: 10.1016/j.chemgeo.2004.08.034.
(74) Frossard, E.; Bauer, J. P.; Lothe, F. Evidence of vivianite in FeSO4-flocculated sludges. *Water Research* **1997**, *31* (10), 2449-2454. DOI: https://doi.org/10.1016/S0043-1354(97)00101-2.
(75) Hansen, H. C. B.; Poulsen, I. F. Interaction of Synthetic Sulphate "Green Rust" with Phosphate and the Crystallization of Vivianite. *Clays and Clay Minerals* **1999**, *47* (3), 312-318. DOI: 10.1346/CCMN.1999.0470307.
(76) Madsen, H. E. L. Morphology and Optical Properties of Precipitated Vivianite. *Crystal Research and Technology* **2020**, *55* (6). DOI: 10.1002/crat.201900226.

(77) Bekker, A.; Holland, H. D.; Wang, P. L.; Rumble, D.; Stein, H. J.; Hannah, J. L.; Coetzee, L. L.; Beukes, N. J. Dating the rise of atmospheric oxygen. *Nature* **2004**, *427* (6970), 117-120. DOI: 10.1038/nature02260.
(78) Och, L. M.; Shields-Zhou, G. A. The Neoproterozoic oxygenation event: Environmental perturbations and biogeochemical cycling. *Earth-Science Reviews* **2012**, *110* (1), 26-57.
(79) Hood Ashleigh, V. S.; Wallace Malcolm, W. Marine cements reveal the structure of an anoxic, ferruginous Neoproterozoic ocean. *Journal of the Geological Society* **2014**, *171* (6), 741-744. DOI: 10.1144/jgs2013-099
(80) Kump, L. R.; Holland, H. D. Iron in Precambrian rocks: Implications for the global oxygen budget of the ancient Earth. *Geochimica et Cosmochimica Acta* **1992**, *56* (8), 3217-3223. DOI: https://doi.org/10.1016/0016-7037(92)90299-X.
(81) Poulton, S. W.; Canfield, D. E. Ferruginous Conditions: A Dominant Feature of the Ocean through Earth's History. *Elements* **2011**, *7* (2), 107-112. DOI: 10.2113/gselements.7.2.107.
(82) Poulton, S. W.; Raiswell, R. The low-temperature geochemical cycle of iron: from continental fluxes to marine sediment deposition. *American journal of science* **2002**, *302* (9), 774-805.

(83) Guilbaud, R.; Poulton, S. W.; Butterfield, N. J.; Zhu, M.; Shields-Zhou, G. A. A global transition to ferruginous conditions in the early Neoproterozoic oceans. *Nature Geoscience* **2015**, *8* (6), 466-470. DOI: 10.1038/ngeo2434.
(84) Burcar, B.; Castaneda, A.; Lago, J.; Daniel, M.; Pasek, M. A.; Hud, N. V.; Orlando, T. M.; Menor-Salvan, C. A Stark Contrast to Modern Earth: Phosphate Mineral Transformation and Nucleoside Phosphorylation in an Iron- and Cyanide-Rich Early Earth Scenario. *Angew Chem Int Ed Engl* **2019**, *58* (47), 16981-16987. DOI: 10.1002/anie.201908272.
(85) Planavsky, N. J.; Rouxel, O. J.; Bekker, A.; Lalonde, S. V.; Konhauser, K. O.; Reinhard, C. T.; Lyons, T. W. The evolution of the marine phosphate reservoir. *Nature* **2010**, *467* (7319), 1088-1090. DOI: 10.1038/nature09485.
(86) Volmer, M.; Weber, A. Keimbildung in übersättigten Gebilden. *Zeitschrift für Physikalische Chemie* **1926**, *119U* (1), 277-301. DOI: doi:10.1515/zpch-1926-11927.
(87) Frenkel, J. A general theory of heterophase fluctuations and pretransition phenomena. *The Journal of Chemical Physics* **1939**, *7* (7), 538-547.
(88) Ostwald, W. Z. Studien über die Bildung und Umwandlung fester Körper. *Zeitschrift für physikalische Chemie* **1897**, *22*, 289-330.
(89) Radha, A. V.; Forbes, T. Z.; Killian, C. E.; Gilbert, P.; Navrotsky, A. Transformation and crystallization energetics of synthetic and biogenic amorphous calcium carbonate. *Proceedings of the National Academy of Sciences of the United States of America* **2010**, *107* (38), 16438-16443. DOI: 10.1073/pnas.1009959107.
(90) Gebauer, D.; Volkel, A.; Colfen, H. Stable Prenucleation Calcium Carbonate Clusters. *Science,* **2008**, *322* (5909), 1819-1822. DOI: 10.1126/science.1164271.
(91) Habraken, W. J. E. M.; Tao, J.; Brylka, L. J.; Friedrich, H.; Bertinetti, L.; Schenk, A. S.; Verch, A.; Dmitrovic, V.; Bomans, P. H. H.; Frederik, P. M.; et al. Ion-association complexes unite classical and non-classical theories for the biomimetic nucleation of calcium phosphate. *Nature Communications* **2013**, *4* (1), 1507. DOI: 10.1038/ncomms2490.
(92) De Yoreo, J. J.; Gilbert, P.; Sommerdijk, N.; Penn, R. L.; Whitelam, S.; Joester, D.; Zhang, H. Z.; Rimer, J. D.; Navrotsky, A.; Banfield, J. F.; et al. Crystallization by particle attachment in synthetic, biogenic, and geologic environments. *Science* **2015**, *349* (6247). DOI: 10.1126/science.aaa6760.
(93) Addadi, L.; Raz, S.; Weiner, S. Taking advantage of disorder: Amorphous calcium carbonate and its roles in biomineralization. *Advanced Materials* **2003**, *15* (12), 959-970. DOI: 10.1002/adma.200300381.
(94) Mahamid, J.; Sharir, A.; Addadi, L.; Weiner, S. Amorphous calcium phosphate is a major component of the forming fin bones of zebrafish: Indications for an amorphous precursor phase. *Proceedings of the National Academy of Sciences* **2008**, *105* (35), 12748-12753. DOI: 10.1073/pnas.0803354105
(95) Jadzinsky, P. D.; Calero, G.; Ackerson, C. J.; Bushnell, D. A.; Kornberg, R. D. Structure of a thiol monolayer-protected gold nanoparticle at 1.1 angstrom resolution. *Science* **2007**, *318* (5849), 430-433. DOI: 10.1126/science.1148624.
(96) Mor, G. K.; Shankar, K.; Paulose, M.; Varghese, O. K.; Grimes, C. A. Use of highly-ordered nanotube arrays in dye-sensitized solar cells. *Nano Letters* **2006**, *6* (2), 215-218. DOI: 10.1021/nl052099j.
(97) Tobler, D. J.; Rodriguez-Blanco, J. D.; Dideriksen, K.; Bovet, N.; Sand, K. K.; Stipp, S. L. S. Citrate Effects on Amorphous Calcium Carbonate (ACC) Structure, Stability, and Crystallization. *Advanced Functional Materials* **2015**, *25* (20), 3081-3090. DOI: 10.1002/adfm.201500400.
(98) Sun, S.; Chevrier, D. M.; Zhang, P.; Gebauer, D.; Colfen, H. Distinct Short-Range Order Is Inherent to Small Amorphous Calcium Carbonate Clusters (<2 nm). *Angew Chem Int Ed Engl* **2016**, *55* (40), 12206-12209. DOI: 10.1002/anie.201604179.
(99) Whittaker, M. L.; Sun, W.; DeRocher, K. A.; Jayaraman, S.; Ceder, G.; Joester, D. Structural Basis for Metastability in Amorphous Calcium Barium Carbonate (ACBC). *Advanced Functional Materials* **2017**, *28* (2), 1704202. DOI: 10.1002/adfm.201704202.
(100) Rabizadeh, T.; Peacock, C. L.; Benning, L. G. Carboxylic acids: effective inhibitors for calcium sulfate precipitation? *Mineralogical Magazine* **2018**, *78* (6), 1465-1472. DOI: 10.1180/minmag.2014.078.6.13.
(101) Mulders, J. J. P. A.; Tobler, D. J.; Oelkers, E. H. Siderite nucleation pathways as a function of aqueous solution saturation state at 25 °C. *Chemical Geology* **2021**, *559*, 119947 - 119957. DOI: 10.1016/j.chemgeo.2020.119947.
(102) Lenders, J. J. M.; Mirabello, G.; Sommerdijk, N. Bioinspired magnetite synthesis via solid precursor phases. *Chem Sci* **2016**, *7* (9), 5624-5634. DOI: 10.1039/c6sc00523c.

(103) Cahn, J. W.; Hilliard, J. E. Free Energy of a Nonuniform System. III. Nucleation in a Two-Component Incompressible Fluid. *The Journal of Chemical Physics* **1959**, *31* (3), 688-699. DOI: 10.1063/1.1730447
(104) Gebauer, D.; Kellermeier, M.; Gale, J. D.; Bergström, L.; Cölfen, H. Pre-nucleation clusters as solute precursors in crystallisation. *Chemical Society Reviews* **2014**, *43* (7), 2348-2371, 10.1039/C3CS60451A. DOI: 10.1039/C3CS60451A.
(105) Van Santen, R. A. The Ostwald step rule. *The Journal of Physical Chemistry* **1984**, *88* (24), 5768-5769. DOI: 10.1021/j150668a002.
(106) Thanh, N. T. K.; Maclean, N.; Mahiddine, S. Mechanisms of Nucleation and Growth of Nanoparticles in Solution. *Chemical Reviews* **2014**, *114* (15), 7610-7630. DOI: 10.1021/cr400544s.
(107) Rodriguez-Blanco, J. D.; Shaw, S.; Benning, L. G. A route for the direct crystallization of dolomite. *American Mineralogist* **2015**, *100* (5-6), 1172-1181. DOI: 10.2138/am-2015-4963
(108) Albéric, M.; Bertinetti, L.; Zou, Z.; Fratzl, P.; Habraken, W.; Politi, Y. The Crystallization of Amorphous Calcium Carbonate is Kinetically Governed by Ion Impurities and Water. *Advanced Science* **2018**, *5* (5), 1701000, https://doi.org/10.1002/advs.201701000. DOI: https://doi.org/10.1002/advs.201701000
(109) Jensen, A. C. S.; Imberti, S.; Parker, S. F.; Schneck, E.; Politi, Y.; Fratzl, P.; Bertinetti, L.; Habraken, W. J. E. M. Hydrogen Bonding in Amorphous Calcium Carbonate and Molecular Reorientation Induced by Dehydration. *The Journal of Physical Chemistry C* **2018**, *122* (6), 3591-3598. DOI: 10.1021/acs.jpcc.7b10459.
(110) Koga, N.; Nakagoe, Y. Z.; Tanaka, H. Crystallization of amorphous calcium carbonate. *Thermochimica Acta* **1998**, *318* (1-2), 239-244. DOI: 10.1016/s0040-6031(98)00348-7.
(111) Politi, Y.; Batchelor, D. R.; Zaslansky, P.; Chmelka, B. F.; Weaver, J. C.; Sagi, I.; Weiner, S.; Addadi, L. Role of Magnesium Ion in the Stabilization of Biogenic Amorphous Calcium Carbonate: A Structure−Function Investigation. *Chemistry of Materials* **2010**, *22* (1), 161-166. DOI: 10.1021/cm902674h.
(112) Jiang, S.; Jin, W.; Wang, Y.-N.; Pan, H.; Sun, Z.; Tang, R. Effect of the aggregation state of amorphous calcium phosphate on hydroxyapatite nucleation kinetics. *RSC Advances* **2017**, *7* (41), 25497-25503, DOI: 10.1039/C7RA02208E.
(113) He, K.; Sawczyk, M.; Liu, C.; Yuan, Y.; Song, B.; Deivanayagam, R.; Nie, A.; Hu, X.; Dravid, V. P.; Lu, J.; et al. Revealing nanoscale mineralization pathways of hydroxyapatite using in situ liquid cell transmission electron microscopy. *Science Advances* **2020**, *6* (47), 7524. DOI: 10.1126/sciadv.aaz7524
(114) Van Driessche, A. E. S.; Benning, L. G.; Rodriguez-Blanco, J. D.; Ossorio, M.; Bots, P.; García-Ruiz, J. M. The Role and Implications of Bassanite as a Stable Precursor Phase to Gypsum Precipitation. *Science* **2012**, *336* (6077), 69-72. DOI: 10.1126/science.1215648
(115) Ann, Y.; Reddy, K. R.; Delfino, J. J. Influence of redox potential on phosphorus solubility in chemically amended wetland organic soils. *Ecological Engineering* **2000**, *14* (1-2), 169-180.
(116) Priambodo, R.; Shih, Y.-J.; Huang, Y.-H. Phosphorus recovery as ferrous phosphate (vivianite) from wastewater produced in manufacture of thin film transistor-liquid crystal displays (TFT-LCD) by a fluidized bed crystallizer (FBC). *RSC Advances* **2017**, *7* (65), 40819-40828, DOI: 10.1039/C7RA06308C.
(117) Li, R.; Li, Q.; Sun, X.; Li, J.; Shen, J.; Han, W.; Wang, L. Removal of lead complexes by ferrous phosphate and iron phosphate: Unexpected favorable role of ferrous ions. *Journal of Hazardous Materials* **2020**, *392*, 122509. DOI: https://doi.org/10.1016/j.jhazmat.2020.122509.
(118) Rao, S. R.; Varadaraju, U. V. Hydrothermal synthesis of LiFePO4 nanorods composed of nanoparticles from vivianite precursor and its electrochemical performance for lithium ion battery applications. *Bulletin of Materials Science* **2015**, *38* (5), 1385-1388. DOI: 10.1007/s12034-015-1025-6.
(119) Parkhurst, D. L., C.A.J. Appelo. *Guide to PHREEQC : a computer program for speciation, reaction-path, advective-transport, and inverse geochemical calculations*; Lakewood, Colo. : U.S. Dept. of the Interior, U.S. Geological Survey ; Denver
(120) Blanc, P.; Lassin, A.; Piantone, P.; Azaroual, M.; Jacquemet, N.; Fabbri, A.; Gaucher, E. C. Thermoddem: A geochemical database focused on low temperature water/rock interactions and waste materials. *Applied Geochemistry* **2012**, *27* (10), 2107-2116. DOI: https://doi.org/10.1016/j.apgeochem.2012.06.002.
(121) Fejdi, P. Affinement de la structure de la vivianite. *Bulletin de Minéralogie* **1980**, *103-1*, 135-138.
(122) Chupas, P. J.; Qiu, X.; Hanson, J. C.; Lee, P. L.; Grey, C. P.; Billinge, S. J. L. Rapid-acquisition pair distribution function (RA-PDF) analysis. *Journal of Applied Crystallography* **2003**, *36* (6), 1342-1347. DOI: doi:10.1107/S0021889803017564.

(123) Celina, M. C.; Quintana, A. Oxygen diffusivity and permeation through polymers at elevated temperature. *Polymer* **2018**, *150*, 326-342. DOI: https://doi.org/10.1016/j.polymer.2018.06.047.
(124) Jia, Y.; Luo, T.; Yu, X.-Y.; Jin, Z.; Sun, B.; Liu, J.-H.; Huang, X.-J. Facile one-pot synthesis of lepidocrocite (γ-FeOOH) nanoflakes for water treatment. *New Journal of Chemistry* **2013**, *37* (8), 2551-2556, DOI: 10.1039/C3NJ00509G.
(125) Stone, D. A.; Goldstein, R. E. Tubular precipitation and redox gradients on a bubbling template. *Proceedings of the National Academy of Sciences* **2004**, *101* (32), 11537-11541. DOI: 10.1073/pnas.0404544101 (acccessed 2023/01/30).
(126) Ravel, B.; Newville, M. Athena, Artemis, Hephaestus: data analysis for X-ray absorption spectroscopy using IFEFFIT. *Journal of Synchrotron Radiation* **2005**, *12*, 537-541. DOI: 10.1107/S0909049505012719.
(127) Wojdyr, M. Fityk: a general-purpose peak fitting program. *Journal of Applied Crystallography* **2010**, *43*, 1126-1128. DOI: 10.1107/S0021889810030499.
(128) Webb, S. M. SIXpack: a graphical user interface for XAS analysis using IFEFFIT. *Physica Scripta* **2005**, *T115*, 1011-1014.
(129) Hövelmann, J.; Stawski, T. M.; Freeman, H. M.; Besselink, R.; Mayanna, S.; Perez, J. P. H.; Hondow, N. S.; Benning, L. G. Struvite Crystallisation and the Effect of Co(II) Ions. *Minerals* **2019**, *9* (9), 503. DOI: 10.3390/min9090503.
(130) Dai, Z.; Zhang, F.; Kan, A. T.; Ruan, G.; Yan, F.; Bhandari, N.; Zhang, Z.; Liu, Y.; Lu, A. Y.-T.; Deng, G.; et al. Two-Stage Model Reveals Barite Crystallization Kinetics from Solution Turbidity. *Industrial & Engineering Chemistry Research* **2019**, *58* (25), 10864-10874. DOI: 10.1021/acs.iecr.9b01707.
(131) Fraser, S. J. The steady state and equilibrium approximations: A geometrical picture. *The Journal of Chemical Physics* **1988**, *88* (8), 4732-4738. DOI: 10.1063/1.454686
(132) Westre, T. E.; Kennepohl, P.; DeWitt, J. G.; Hedman, B.; Hodgson, K. O.; Solomon, E. I. A Multiplet Analysis of Fe K-Edge 1s → 3d Pre-Edge Features of Iron Complexes. *Journal of the American Chemical Society* **1997**, *119* (27), 6297-6314. DOI: 10.1021/ja964352a.
(133) Amthauer, G.; Rossman, G. R. Mixed valence of iron in minerals with cation clusters. *Physics and Chemistry of Minerals* **1984**, *11* (1), 37-51. DOI: 10.1007/BF00309374.
(134) Mikutta, C.; Schröder, C.; Marc Michel, F. Total X-ray scattering, EXAFS, and Mössbauer spectroscopy analyses of amorphous ferric arsenate and amorphous ferric phosphate. *Geochimica et Cosmochimica Acta* **2014**, *140*, 708-719. DOI: https://doi.org/10.1016/j.gca.2014.05.040.
(135) Grodzicki, M.; Amthauer, G. Electronic and magnetic structure of vivianite: cluster molecular orbital calculations. *Physics and Chemistry of Minerals* **2000**, *27* (10), 694-702. DOI: 10.1007/s002690000125.
(136) Dideriksen, K.; Frandsen, C.; Bovet, N.; Wallace, A. F.; Sel, O.; Arbour, T.; Navrotsky, A.; De Yoreo, J. J.; Banfield, J. F. Formation and transformation of a short range ordered iron carbonate precursor. *Geochimica et Cosmochimica Acta* **2015**, *164*, 94-109. DOI: 10.1016/j.gca.2015.05.005.
(137) Hezel, A.; Ross, S. D. Forbidden transitions in the infra-red spectra of tetrahedral anions—III. Spectra-structure correlations in perchlorates, sulphates and phosphates of the formula MXO4. *Spectrochimica Acta* **1966**, *22* (11), 1949-1961. DOI: https://doi.org/10.1016/0371-1951(66)80183-2.
(138) Vecstaudza, J.; Gasik, M.; Locs, J. Amorphous calcium phosphate materials: Formation, structure and thermal behaviour. *Journal of the European Ceramic Society* **2019**, *39* (4), 1642-1649. DOI: 10.1016/j.jeurceramsoc.2018.11.003.
(139) Ibsen, C. J. S.; Chernyshov, D.; Birkedal, H. Apatite Formation from Amorphous Calcium Phosphate and Mixed Amorphous Calcium Phosphate/Amorphous Calcium Carbonate. *Chemistry-a European Journal* **2016**, *22* (35), 12347-12357. DOI: 10.1002/chem.201601280.
(140) Vivekanandan, K.; Selvasekarapandian, S.; Kolandaivel, P. Raman and FT-IR studies of lead nitrate phophate crystal. *Materials Chemistry and Physics* **1995**, *39* (4), 284-289. DOI: https://doi.org/10.1016/0254-0584(94)01440-R.
(141) Frost, R. L.; Martens, W.; Williams, P. A.; Kloprogge, J. T. Raman and infrared spectroscopic study of the vivianite-group phosphates vivianite, baricite and bobierrite. *Mineralogical Magazine* **2018**, *66* (6), 1063-1073. DOI: 10.1180/0026461026660077.
(142) Corn, R. M.; Strauss, H. L. An infrared study of the dynamics of weakly bound water in crystalline hydrates. *The Journal of Chemical Physics* **1982**, *76* (10), 4834-4843. DOI: 10.1063/1.442802

(143) Diatto, P.; Martini, M.; Spinolo, G. Librational spectra of water molecules in Ni, Co and Fe dichloride hydrates. *Journal of Physics and Chemistry of Solids* **1988**, *49* (10), 1139-1144. DOI: https://doi.org/10.1016/0022-3697(88)90167-9.
(144) Gennick, I.; Harmon, K. M. Hydrogen bonding. VI. Structural and infrared spectral analysis of lithium hydroxide monohydrate and cesium and rubidium hydroxide hydrates. *Inorganic Chemistry* **1975**, *14* (9), 2214-2219. DOI: 10.1021/ic50151a037.
(145) Bruni, S.; Cariati, F.; Fermo, P.; Spinolo, G.; Martini, M. Raman and infrared spectra of Mn and Fe halides tetrahydrated. *Journal of Physics and Chemistry of Solids* **1998**, *59* (6), 845-857. DOI: https://doi.org/10.1016/S0022-3697(98)00042-0.
(146) Schmidt, M. P.; Ilott, A. J.; Phillips, B. L.; Reeder, R. J. Structural Changes upon Dehydration of Amorphous Calcium Carbonate. *Crystal Growth & Design* **2014**, *14* (3), 938-951. DOI: 10.1021/cg401073n.
(147) Radha, A. V.; Navrotsky, A. Direct Experimental Measurement of Water Interaction Energetics in Amorphous Carbonates MCO3 (M = Ca, Mn, and Mg) and Implications for Carbonate Crystal Growth. *Crystal Growth & Design* **2015**, *15* (1), 70-78. DOI: 10.1021/cg500878w.
(148) Martin, B.; Flörke, O. W.; Kainka, E.; Wirth, R. Electron irradiation damage in quartz, SiO2. *Physics and Chemistry of Minerals* **1996**, *23* (7), 409-417. DOI: 10.1007/BF00202027.
(149) Bianchini, C.; Laschi, F.; Masi, D.; Ottaviani, F. M.; Pastor, A.; Peruzzini, M.; Zanello, P.; Zanobini, F. A family of stable iron(I) .sigma.-alkynyl complexes. Synthesis, characterization, structure, and electron-transfer chemistry. *Journal of the American Chemical Society* **1993**, *115* (7), 2723-2730. DOI: 10.1021/ja00060a022.
(150) Von Euw, S.; Azais, T.; Manichev, V.; Laurent, G.; Pehau-Arnaudet, G.; Rivers, M.; Murali, N.; Kelly, D. J.; Falkowski, P. G. Solid-State Phase Transformation and Self-Assembly of Amorphous Nanoparticles into Higher-Order Mineral Structures. *Journal of the American Chemical Society* **2020**, *142* (29), 12811-12825. DOI: 10.1021/jacs.0c05591.
(151) Walker, J. M.; Marzec, B.; Nudelman, F. Solid-State Transformation of Amorphous Calcium Carbonate to Aragonite Captured by CryoTEM. *Angewandte Chemie International Edition* **2017**, *56* (39), 11740-11743, https://doi.org/10.1002/anie.201703158. DOI: https://doi.org/10.1002/anie.201703158
(152) Gal, A.; Weiner, S.; Addadi, L. A perspective on underlying crystal growth mechanisms in biomineralization: solution mediated growth versus nanosphere particle accretion. *CrystEngComm* **2015**, *17* (13), 2606-2615, 10.1039/C4CE01474J. DOI: 10.1039/C4CE01474J.
(153) Saharay, M.; Yazaydin, A. O.; Kirkpatrick, R. J. Dehydration-Induced Amorphous Phases of Calcium Carbonate. *Journal of Physical Chemistry B* **2013**, *117* (12), 3328-3336. DOI: 10.1021/jp308353t.
(154) Colfen, H.; Mann, S. Higher-order organization by mesoscale self-assembly and transformation of hybrid nanostructures. *Angewandte Chemie-International Edition* **2003**, *42* (21), 2350-2365.
(155) Lotsari, A.; Rajasekharan, A. K.; Halvarsson, M.; Andersson, M. Transformation of amorphous calcium phosphate to bone-like apatite. *Nature Communications* **2018**, *9* (1), 4170. DOI: 10.1038/s41467-018-06570-x.
(156) Kim, S.; Ryu, H.-S.; Shin, H.; Jung, H. S.; Hong, K. S. In situ observation of hydroxyapatite nanocrystal formation from amorphous calcium phosphate in calcium-rich solutions. *Materials Chemistry and Physics* **2005**, *91* (2), 500-506. DOI: https://doi.org/10.1016/j.matchemphys.2004.12.016.
(157) Ibsen, C. J. S.; Birkedal, H. Modification of bone-like apatite nanoparticle size and growth kinetics by alizarin red S. *Nanoscale* **2010**, *2* (11), 2478-2486, 10.1039/C0NR00488J. DOI: 10.1039/C0NR00488J.
(158) Piper, L. F. J.; Quackenbush, N. F.; Sallis, S.; Scanlon, D. O.; Watson, G. W.; Nam, K. W.; Yang, X. Q.; Smith, K. E.; Omenya, F.; Chernova, N. A.; et al. Elucidating the Nature of Pseudo Jahn–Teller Distortions in LixMnPO4: Combining Density Functional Theory with Soft and Hard X-ray Spectroscopy. *The Journal of Physical Chemistry C* **2013**, *117* (20), 10383-10396. DOI: 10.1021/jp3122374.
(159) Hövelmann, J.; Stawski, T. M.; Besselink, R.; Freeman, H. M.; Dietmann, K. M.; Mayanna, S.; Pauw, B. R.; Benning, L. G. A template-free and low temperature method for the synthesis of mesoporous magnesium phosphate with uniform pore structure and high surface area. *Nanoscale* **2019**, *11* (14), 6939-6951, 10.1039/C8NR09205B. DOI: 10.1039/C8NR09205B.
(160) Wu, Y.; Luo, J.; Zhang, Q.; Aleem, M.; Fang, F.; Xue, Z.; Cao, J. Potentials and challenges of phosphorus recovery as vivianite from wastewater: A review. *Chemosphere* **2019**, *226*, 246-258. DOI: 10.1016/j.chemosphere.2019.03.138.
(161) Azam, H. M.; Alam, S. T.; Hasan, M.; Yameogo, D. D. S.; Kannan, A. D.; Rahman, A.; Kwon, M. J. Phosphorous in the environment: characteristics with distribution and effects, removal mechanisms, treatment technologies,

and factors affecting recovery as minerals in natural and engineered systems. *Environ Sci Pollut Res Int* **2019**, *26* (20), 20183-20207. DOI: 10.1007/s11356-019-04732-y.
(162) Li, S.; Liu, X.; Mi, R.; Liu, H.; Li, Y.; Lau, W.-m.; Mei, J. A Facile Route To Modify Ferrous Phosphate and Its Use as an Iron-Containing Resource for LiFePO4 via a Polyol Process. *ACS Applied Materials & Interfaces* **2014**, *6* (12), 9449-9457. DOI: 10.1021/am501762x.
(163) Paskin, A.; Couasnon, T.; Perez, J. P. H.; Lobanov, S. S.; Blukis, R.; Reinsch, S.; Benning, L. G. Nucleation and Crystallization of Ferrous Phosphate Hydrate via an Amorphous Intermediate. *Journal of the American Chemical Society* **2023**, *145* (28), 15137-15151. DOI: 10.1021/jacs.3c01494.
(164) Vu, H. P.; Shaw, S.; Brinza, L.; Benning, L. G. Crystallization of Hematite (α-Fe_2O_3) under Alkaline Condition: The Effects of Pb. *Crystal Growth & Design* **2010**, *10* (4), 1544-1551. DOI: 10.1021/cg900782g.
(165) Karafiludis, S.; Kochovski, Z.; Scoppola, E.; Retzmann, A.; Hodoroaba, V.-D.; ten Elshof, J. E.; Emmerling, F.; Stawski, T. M. Nonclassical Crystallization Pathway of Transition Metal Phosphate Compounds. *Chemistry of Materials* **2023**, *35* (24), 10645-10657. DOI: 10.1021/acs.chemmater.3c02346.
(166) Matamoros-Veloza, A.; Stawski, T. M.; Benning, L. G. Nanoparticle Assembly Leads to Mackinawite Formation. *Crystal Growth & Design* **2018**, *18* (11), 6757-6764. DOI: 10.1021/acs.cgd.8b01025.
(167) Basham, M.; Filik, J.; Wharmby, M. T.; Chang, P. C. Y.; El Kassaby, B.; Gerring, M.; Aishima, J.; Levik, K.; Pulford, B. C. A.; Sikharulidze, I.; Data Analysis WorkbeNch (DAWN). *Journal of Synchrotron Radiation* **2015**, *22* (3)
(168) Bressler, I.; Pauw, B. R.; Thunemann, A. F. McSAS: software for the retrieval of model parameter distributions from scattering patterns. *Journal of Applied Crystallography* **2015**, *48* (3), 962-969. DOI: doi:10.1107/S1600576715007347.
(169) Schneider, C. A.; Rasband, W. S.; Eliceiri, K. W. NIH Image to ImageJ: 25 years of image analysis. *Nature Methods* **2012**, *9* (7), 671-675. DOI: 10.1038/nmeth.2089.
(170) Kirsch, B. L.; Richman, E. K.; Riley, A. E.; Tolbert, S. H. In-Situ X-ray Diffraction Study of the Crystallization Kinetics of Mesoporous Titania Films. *The Journal of Physical Chemistry B* **2004**, *108* (34), 12698-12706. DOI: 10.1021/jp036442p.
(171) Er-raji, O.; Rustam, L.; Kore, B. P.; Glunz, S. W.; Schulze, P. S. C. Insights into Perovskite Film Formation Using the Hybrid Evaporation/Spin-Coating Route: An In Situ XRD Study. *ACS Applied Energy Materials* **2023**, *6* (11), 6183-6193. DOI: 10.1021/acsaem.3c00698.
(172) Avrami, M. Kinetics of Phase Change. II Transformation-Time Relations for Random Distribution of Nuclei. *The Journal of Chemical Physics* **1940**, *8* (2), 212-224. DOI: 10.1063/1.1750631
(173) Avrami, M. Kinetics of Phase Change. I General Theory. *The Journal of Chemical Physics* **1939**, *7* (12), 1103-1112. DOI: 10.1063/1.1750380
(174) Avrami, M. Granulation, Phase Change, and Microstructure Kinetics of Phase Change. III. *The Journal of Chemical Physics* **2004**, *9* (2), 177-184. DOI: 10.1063/1.1750872
(175) Matsushita, K.; Sakka, S. Kinetic study on non-isothermal crystallization of glass by thermal analysis (commemoration issue dedicated to Professor Megumi Tashiro on the Occation of his retirement). *Bulletin of the Institute for Chemical Research, Kyoto University* **1981**, *59* (3), 159-171.
(176) Wiechers, H. N. S.; Sturrock, P.; Marais, G. v. R. Calcium carbonate crystallization kinetics. *Water Research* **1975**, *9* (9), 835-845. DOI: https://doi.org/10.1016/0043-1354(75)90143-8.
(177) Rodríguez-Lorenzo, L. M.; Vallet-Regí, M. Controlled Crystallization of Calcium Phosphate Apatites. *Chemistry of Materials* **2000**, *12* (8), 2460-2465. DOI: 10.1021/cm001033g.
(178) Petrou, A. L.; Economou-Eliopoulos, M. The activation energy values estimated by the Arrhenius equation as a controlling factor of platinum-group mineral formation. *Geochimica et Cosmochimica Acta* **2009**, *73* (6), 1625-1636. DOI: 10.1016/j.gca.2008.12.009.
(179) Francisco, P. C. M.; Sato, T.; Otake, T.; Kasama, T. Kinetics of Fe^{3+} mineral crystallization from ferrihydrite in the presence of Si at alkaline conditions and implications for nuclear waste disposal. *American Mineralogist* **2016**, *101* (9), 2057-2069. DOI: 10.2138/am-2016-5589.
(180) Lincoln, S. F.; Merbach, A. E. Substitution reactions of solvated metal ions. *Advances in inorganic chemistry* **1995**, *42*, 1-88.
(181) H. P. Vu, S. Shaw, L. Brinza and L. G. Benning, *Crystal Growth & Design* **2010** Vol. 10 Issue 4 Pages 1544-1551
(182) Schott, J.; Pokrovsky, O. S.; Oelkers, E. H. The Link Between Mineral Dissolution/Precipitation Kinetics and

Solution Chemistry. *Reviews in Mineralogy and Geochemistry* **2009**, *70* (1), 207-258. DOI: 10.2138/rmg.2009.70.6
(183) Tang, J.; Alivisatos, A. P. Crystal Splitting in the Growth of Bi2S3. *Nano Letters* **2006**, *6* (12), 2701-2706. DOI: 10.1021/nl0615930.
(184) Shtukenberg, A. G.; Punin, Y. O.; Gujral, A.; Kahr, B. Growth Actuated Bending and Twisting of Single Crystals. *Angewandte Chemie International Edition* **2014**, *53* (3), 672-699.
(185) Sand, K. K.; Rodriguez-Blanco, J. D.; Makovicky, E.; Benning, L. G.; Stipp, S. L. S. Crystallization of CaCO3 in Water–Alcohol Mixtures: Spherulitic Growth, Polymorph Stabilization, and Morphology Change. *Crystal Growth & Design* **2012**, *12* (2), 842-853. DOI: 10.1021/cg2012342.
(186) Dahmen, U.; Hetherington, C. J. D.; Radmilovic, V.; Johnson, E.; Xiao, S. Q.; Luo, C. P. Electron Microscopy Observations on the Role of Twinning in the Evolution of Microstructures. *Microscopy and Microanalysis* **2002**, *8* (4), 247-256. DOI: 10.1017/S1431927602020184
(187) Hawthorne, F. C.; Pieczka, A. Classification of the minerals of the graftonite group. *Mineralogical Magazine* **2018**, *82* (6), 1301-1306. DOI: 10.1180/minmag.2017.081.092.
(188) Vignola, P.; Diella, V.; Oppizzi, P.; Tiepolo, M.; Weiss, S. Phosphate assemblages from the Brissago granitic pegmatite, western Southern Alps, Switzerland. *Canadian Mineralogist* **2008**, *46*, 635-650. DOI: 10.3749/canmin.46.3.635.
(189) Vignola, P.; Diella, V.; Oppizzi, P.; Tiepolo, M.; Weiss, S. Phosphate Assemblages from the Brissago Granitic Pegmatite. *The Canadian Mineralogist* **2008**, *46* (3), 635-650. DOI: 10.3749/canmin.46.3.635
(190) Nord, A. G.; Ericsson, T. The cation distribution in synthetic (Fe,Mn)3(PO4)2 graftonite-type solid solutions. *American Mineralogist* **1982**, *67* (7-8), 826-832.
(191) Kostiner, E.; Rea, J. R. Crystal structure of ferrous phosphate, Fe3(PO4)2. *Inorganic Chemistry* **1974**, *13* (12), 2876-2880. DOI: 10.1021/ic50142a021.
(192) Altomare, A.; Corriero, N.; Cuocci, C.; Falcicchio, A.; Moliterni, A.; Rizzi, R. QUALX2.0: a qualitative phase analysis software using the freely available database POW_COD. *Journal of Applied Crystallography* **2015**, *48* (2), 598-603. DOI: doi:10.1107/S1600576715002319.
(193) Toby, B. H.; Von Dreele, R. B. GSAS-II: the genesis of a modern open-source all purpose crystallography software package. *Journal of Applied Crystallography* **2013**, *46* (2), 544-549.
(194) Henry, P. F.; Weller, M. T.; Wilson, C. C. Determination of the cation distribution in Fe2Ni(PO4)2 using isotopic substitution and powder neutron diffraction. *Journal of Applied Crystallography* **2003**, *36* (6), 1361-1367. DOI: doi:10.1107/S0021889803017515.
(195) Newville, M. IFEFFIT : interactive XAFS analysis and FEFF fitting. *Journal of Synchrotron Radiation* **2001**, *8* (2), 322-324. DOI: doi:10.1107/S0909049500016964.
(196) Frost, R. L.; Weier, M. L.; Martens, W.; Kloprogge, J. T.; Ding, Z. Dehydration of synthetic and natural vivianite. *Thermochimica Acta* **2003**, *401* (2), 121-130. DOI: https://doi.org/10.1016/S0040-6031(02)00505-1.
(197) Radha, A. V.; Forbes, T. Z.; Killian, C. E.; Gilbert, P. U. P. A.; Navrotsky, A. Transformation and crystallization energetics of synthetic and biogenic amorphous calcium carbonate. *Proceedings of the National Academy of Sciences* **2010**, *107* (38), 16438-16443. DOI: 10.1073/pnas.1009959107
(198) Uskoković, V.; Marković, S.; Veselinović, L.; Škapin, S.; Ignjatović, N.; Uskoković, D. P. Insights into the kinetics of thermally induced crystallization of amorphous calcium phosphate. *Physical Chemistry Chemical Physics* **2018**, *20* (46), DOI: 10.1039/C8CP06460A.
(199) Ericsson, T.; Nord, A. G. Strong cation ordering in olivine-related (Ni,Fe)-sarcopsides: a combined Mössbauer, X-ray and neutron diffraction study. *American Mineralogist* **1984**, *69* (9-10), 889-895.
(200) Pomiès, M. P.; Menu, M.; Vignaud, C. Tem observations of goethite dehydration: application to archaeological samples. *Journal of the European Ceramic Society* **1999**, *19* (8), 1605-1614. DOI: https://doi.org/10.1016/S0955-2219(98)00254-4.
(201) Stalder, M.; Rozendaal, A. Graftonite in phosphatic iron formations associated with the mid-Proterozoic Gamsberg Zn-Pb deposit, Namaqua Province, South Africa. *Mineralogical Magazine* **2002**, *66* (6), 915-927. DOI: 10.1180/0026461026660067 From Cambridge University Press Cambridge Core.
(202) Cipriani, C.; Mellini, M.; Pratesi, G.; Viti, C. Rodolicoite and grattarolaite, two new phosphate minerals from Santa Barbara Mine, Italy. *European Journal of Mineralogy* **1997**, *9* (5), 1101-1106.

(203) Huang, Y.; Zhang, X.; Chen, N.; Tian, R.; Zeng, Y.; Du, F. A Conformal Protective Skin Producing Stable Cathode-Electrolyte Interface for Long-Life Potassium-Ion Batteries. *Small* **2023**, 2302841, https://doi.org/10.1002/smll.202302841. DOI: https://doi.org/10.1002/smll.202302841
(204) Wang, C.; Baer, D. R.; Amonette, J. E.; Engelhard, M. H.; Antony, J.; Qiang, Y. Morphology and Electronic Structure of the Oxide Shell on the Surface of Iron Nanoparticles. *Journal of the American Chemical Society* **2009**, *131* (25), 8824-8832. DOI: 10.1021/ja900353f.
(205) Laffont, L.; Delacourt, C.; Gibot, P.; Wu, M. Y.; Kooyman, P.; Masquelier, C.; Tarascon, J. M. Study of the LiFePO4/FePO4 Two-Phase System by High-Resolution Electron Energy Loss Spectroscopy. *Chemistry of Materials* **2006**, *18* (23), 5520-5529. DOI: 10.1021/cm0617182.
(206) Xie, B.; Halter, T. J.; Borah, B. M.; Nancollas, G. H. Tracking Amorphous Precursor Formation and Transformation during Induction Stages of Nucleation. *Crystal Growth & Design* **2014**, *14* (4), 1659-1665. DOI: 10.1021/cg401777x.
(207) Waerenborgh, J. C.; Figueiredo, M. O. X-ray powder diffraction and57Fe Mössbauer spectroscopy study of the thermal breakdown of vivianite *Hyperfine Interactions* **1986**, *29* (1), 1101-1104. DOI: 10.1007/BF02399426.
(208) Nielsen, A. E. Nucleation and Growth of Crystals at High Supersaturation. *Kristall und Technik* **1969**, *4* (1), 17-38, https://doi.org/10.1002/crat.19690040105. DOI: https://doi.org/10.1002/crat.19690040105
(209) Klementiev, K.; Chernikov, R. XAFSmass: A program for calculating the optimal mass of XAFS samples. *J. Phys. Conf. Ser.* **2016**, *712*, 012008. DOI: 10.1088/1742-6596/712/1/012008.
(210) Webb, S. M. SIXpack: a graphical user interface for XAS analysis using IFEFFIT. *Phys. Scr.* **2005**, *T115* (T115), 1011-1014.
(211) Newville, M. IFEFFIT: Interactive XAFS analysis and FEFF fitting. *J. Synchr. Radiat.* **2001**, *8* (Pt 2), 322-324. DOI: 10.1107/s0909049500016964.
(212) Rehr, J. J.; Albers, R. C.; Zabinsky, S. I. High-order multiple-scattering calculations of X-ray-absorption fine structure. *Phys. Rev. Lett.* **1992**, *69* (23), 3397-3400. DOI: 10.1103/PhysRevLett.69.3397.
(213) Rakovan, J.; Becker, U.; Hochella, M. F. Aspects of goethite surface microtopography, structure, chemistry, and reactivity. **1999**, *84* (5-6), 884-894. DOI: doi:10.2138/am-1999-5-624
(214) Taxer, K.; Bartl, H. On the dimorphy between the variscite and clinovariscite group: refined finestructural relationship of strengite and clinostrengite, $Fe(PO_4)$. 2H2O. *Crystal Research and Technology* **2004**, *39* (12), 1080-1088. DOI: https://doi.org/10.1002/crat.200410293
(215) Bae, S.; Sihn, Y.; Kyung, D.; Yoon, S.; Eom, T.; Kaplan, U.; Kim, H.; Schäfer, T.; Han, S.; Lee, W. Molecular Identification of Cr(VI) Removal Mechanism on Vivianite Surface. *Environmental Science & Technology* **2018**, *52* (18), 10647-10656. DOI: 10.1021/acs.est.8b01614.
(216) Kelly, S. D.; Hesterberg, D.; Ravel, B. Analysis of Soils and Minerals Using X-ray Absorption Spectroscopy. In *Methods of Soil Analysis Part 5—Mineralogical Methods*, SSSA Book Series, 2008; pp 387-463.
(217) Downward, L.; Booth, C. H.; Lukens, W. W.; Bridges, F. A Variation of the F-Test for Determining Statistical Relevance of Particular Parameters in EXAFS Fits. *AIP Conference Proceedings* **2007**, *882* (1), 129-131. DOI: 10.1063/1.2644450.